3D-printed Synthetic Polymer Templates for Bone Tissue Engineering

Bulk Modifications and Osteoconduction Assessment

Mohamad Nageeb Hassan

Thesis for the degree of Philosophiae Doctor (PhD)
University of Bergen, Norway
2022

UNIVERSITY OF BERGEN

3D-printed Synthetic Polymer Templates for Bone Tissue Engineering
Bulk Modifications and Osteoconduction Assessment

Mohamad Nageeb Hassan

Thesis for the degree of Philosophiae Doctor (PhD)
at the University of Bergen

Date of defense: 21.10.2022

Year: 2022

Title: 3D-printed Synthetic Polymer Templates for Bone Tissue Engineering

Name: Mohamad Nageeb Hassan

Print: Skipnes Kommunikasjon / University of Bergen

" .... إِن أُريدُ إِلَّا الإِصلاحَ مَا استَطَعتُ ۚ
وَما تَوفيقي إِلّا بِاللَّهِ ۚ عَلَيهِ تَوَكَّلتُ وَإِلَيهِ أُنيبُ "

"…. I only intend reform to the best of my ability,
My success comes only through Allah,
In Him I trust, and to Him I turn"

(Quran 11:88)

Contents

Scientific environment

The work comprising this thesis was conducted at the Department of Clinical Dentistry (IKO), Faculty of Medicine, University of Bergen (UiB), over the course of five years (2017-2021), funded by UiB. At my group, the Tissue Engineering Group in IKO, all the main experiments were undertaken: bulk modifications, polymer blending, 3D-printing of templates, physical characterization, mechanical testing, scanning electron microscope examination, cell culture seeding, biological characterization, and processing and data analysis of the animal study samples.

The contact angle measurements, thermal analysis and the animal experiment in rabbits were conducted at my group collaborators: the Materials Science Department, Institute of Graduate Studies and Research (IGSR), Alexandria University, Egypt. FTIR and XRD characterization were conducted in collaboration with the Department of Chemical Engineering, Coimbatore Institute of Technology, India.

The principal supervisor of the thesis is Professor Kamal Mustafa. The co-supervisors are “Late” Associate Professor Harald Gjengedal, Post-doc. Mohamad Yassin, and Post-doc. Salwa Suliman. The experimental work done was co-funded by the Research Council of Norway (NFR) (BEHANDLING project, Grant no. 273551), Trond Mohn Research Foundation (Grant no. BFS2018TMT10) and Olav Thon foundation.

List of abbreviations

μCT	Micro-computed tomography
3D	Three dimensional
ADA	Available defect area
ALP	Alkaline phosphatase
AM	Additive manufacturing
ANOVA	Analysis of variance
AOI	Area of interest
BCP	Biphasic calcium phosphates
BG	Bioactive glass
BMP	Bone morphogenetic protein
BMSCs	Bone marrow-derived mesenchymal stem cells
BTE	Bone tissue engineering
Ca	Calcium
CAD	Computer-assisted design
CaP	Calcium phosphate
CBD	Calvarial bone defect
cDNA	Complementary DNA
CHA	Carbonated HA
co-Smad	Common-mediator Smad
COL1	Collagen type 1
CSi	Calcium silicate (Wollastonite)
CT	X-ray computed tomography
DCPD	Dicalcium phosphate dihydrate
dH_2O	distilled water
DNA	Deoxyribonucleic acid
DO	Distraction osteogenesis
ECM	Extracellular matrix
ECMVs	Extracellular matrix vesicles
EDTA	Ethylenediaminetetraacetic acid

EDX	Energy dispersive X-rays
ERK	Extracellular signal-regulated kinase
FDA	Food and drug administration
FGF	Fibroblast growth factor
GAPDH	Glyceraldehyde-3-phosphate dehydrogenase (gene)
GFs	Growth factors
GL	Gelatin
HA	Hydroxyapatite
hBMSCs	Human-BMSCs
I-Smads	Inhibitory Smad family
Mad	Mothers against decapentaplegic (Drosophila gene)
MAPK	Mitogen-activated protein kinase
Mg	Magnesium
MPa	Mega pascal
MPCs	Mesenchymal progenitor cells
MRI	Magnetic resonance imaging
mRNA	Messenger ribonucleic acid
MS	Multiple sclerosis
MSCs	Mesenchymal stem cells
NBA	New bone area
NZW	New Zealand white (rabbits)
OB	Osteoblast
OD	Optical density
P	Phosphate
PBS	Phosphate buffered saline
PCL	Polycaprolactone
PCR	Polymerase chain reaction
PDGF	Platelet derived growth factor
PDLLA	Poly(D,L-Lactide)
PDTEC	Poly(DTE carbonate)
PEEK	Polyetheretherketone

PGA	Poly(glycolide)
pH	Potential of hydrogen (scale)
PLA	Poly(lactic acid)
PLATMC	Poly(lactide-co-trimethylene carbonate)
PLGA	PLA and PGA copolymers
PLLA	Poly(L-Lactide)
PMMA	Polymethyl methacrylate
PPF	Poly(propylene fumarate)
PTMC	Poly(trimethylene carbonate)
qPCR	Quantitative PCR
R-Samds	Receptor-regulated Samds
ROI	Region of interest
RT	Room temperature
RT-PCR	Reverse transcription PCR
RUNX2	Runt-related transcription factor 2
SD	Standard deviation
SDF1	Stromal derived growth factor
Sma	Caenorhabditis elegans small protein
Smad	Intracellular signaling protein (Mad + Sma)
STL	Standard tessellation language
TCMP	Magnesium substituted β-TCP
TDA	Total defect area
TE	Tissue engineering
Tg	Glass transition temperature
TGF-β	Transforming growth factor-beta
Ti	Titanium
T_m	Melting temperature
US	United States of America
UV	Ultraviolet rays
VEGF	Vascular endothelial growth factor
Ø	Diameter

β-TCP	β-tricalcium phosphate
βGP	β-glycerol phosphate

List of tables

List of figures

List of publications

The thesis is based on the following scientific reports (studies) and will be referred to according to their Roman numbers:

Study I:

M. N. Hassan, M. A. Yassin, S. Suliman, S. A. Lie, H. Gjengedal, and K. Mustafa. “The bone regeneration capacity of 3D-printed templates in calvarial defect models: A systematic review and meta-analysis” *Acta Biomater.*, vol. 91, pp. 1–23, Jun. 2019.

Study II:

R. S. Azarudeen*, **M. N. Hassan***, M. A. Yassin, M. Thirumarimurugan, N. Muthukumarasamy, D. Velauthapillai, and K. Mustafa. “3D-printable polycaprolactone-gelatin blends characterized for *in vitro* osteogenic potency” *React. Funct. Polym.*, vol. 146, no. December 2019, p. 104445, Jan. 2020.

Study III:

M. N. Hassan, M. A. Yassin, A. M. Eltawila, A. E. Aladawi, S. Mohamed-Ahmed, S. Suliman, S. Kandil, and K. Mustafa. “Contact Osteogenesis by Biodegradable 3D-printed Poly(lactide-co-trimethylene carbonate)”. *Biomater. Res.,* (Accepted Sep. 2022)

Study IV:

M. N. Hassan, A. M. Eltawila, S. Mohamed-Ahmed, W. A. Ahmed, S. Suliman, S. Kandil, M. A. Yassin, and K. Mustafa. “3D-printed templates of hydroxyapatite blends: correlation between Ca release and osteoconduction *in vitro* and *in vivo*”. *Submitted Manuscript.*

* Shared contribution

The author has also contributed to the following work during the course of the PhD period, not included in this thesis:

1. M. Eltawila, **M. N. Hassan**, S. M. Safaan, A. Abd El-Fattah, O. Zakaria, L. K. El-Khordagui and S. Kandil. "Local treatment of experimental mandibular osteomyelitis with an injectable biomimetic gentamicin hydrogel using a new rabbit model" *J. Biomed. Mater. Res. Part B Appl. Biomater.*, vol. 109, no. 11, pp. 1677–1688, 2021.

2. S. Shanbhag, S. Suliman, S. Mohamed-Ahmed, C. Kampleitner, **M. N. Hassan**, P. Heimel, T. Dobsak, S. Tangl, A.I. Bolstad, and K. Mustafa, "Bone regeneration in rat calvarial defects using dissociated or spheroid mesenchymal stromal cells in scaffold-hydrogel constructs" *Stem Cell Res. & Ther.,* vol. 12, pp. 575, 2021.

3. S. Shanbhag, C. Kampleitner, S. Mohamed-Ahmed, M. A. Yassin, H. Dongre, D. E. Costea, S. Tangl, **M. N. Hassan**, A Stavropoulos, A.I. Bolstad, S. Suliman and K. Mustafa, "Ectopic Bone Tissue Engineering in Mice Using Human Gingiva or Bone Marrow-Derived Stromal/Progenitor Cells in Scaffold-Hydrogel Constructs" *Front. Bioeng. Biotechnol.,* vol. 9, pp. 1-14, 2021.

4. **M. N. Hassan**, R. S. Azarudeen, M. A. Yassin, M. Thirumarimurugan, N. Muthukumarasamy, D. Velauthapillai, and K. Mustafa. "The *in vitro* osteoconductive potential of 3D-printed and silk-fibroin coated polymer-based blends" *Manuscript under submission.*

Abstract in English

Synthetic polymer biomaterials are used in numerous biomedical applications providing biological inertness and ease of processing and shaping. Current research is directed towards boosting their biological activity, customized per application. 3D-printing is a promising technique for producing biomaterial templates with the required design parameters. The aim of the thesis was therefore to investigate the fabrication of osteoconductive 3D-printed synthetic polymer-based templates for bone tissue engineering (BTE). The investigation comprised three phases:

In phase I, a literature survey was conducted, to review factors of relevance in applying potentially-degradable 3D-printed templates and their influence on bone regeneration in the calvarial bone defect (CBD) model, across various animal species (Study I). A meta-analysis was undertaken to compare the yield of new bone for each type of template material (polymer, ceramic or composites/blends). The highest impact on new bone formation was associated with the blended polymers and bioceramics, and the interconnected porosity generated by the 3D-printing.

In parallel, an experimental study was undertaken on the functionalization of 3D-printed polycaprolactone (PCL) templates with gelatin (GL) due to its good biodegradation and biocompatibilty. Their physical and osteoconductive properties were tested *in vitro* (Study II). The biochemical compatibility contributed by GL (at 8 and 16%) improved the osteogenic differentiation of the seeded rat-BMSCs. However, this led to quite low tensile resistance and PCL/GL templates were therefore not studied in further *in vivo* trials.

In phase II, poly(lactide-co-trimethylene carbonate) (PLATMC) was compared to PCL, and revealed that PLATMC had better degradation and mechanical properties than PCL (Study III), with prominent osteoconductivity and mineralized extracellular matrix (ECM) deposition (*in vitro*). In a subcutaneous implantation model in rabbits (8 weeks), the host response to PLATMC was mild, with loose connective tissue interface and high cellular invasion. In contrast, PCL was characterized by dense fibrous tissue encapsulation. When both templates were implanted in CBD in rabbits, PLATMC

templates showed greater amount of new bone formation together with obvious contact osteogenesis presented on its surface, which was unique and unreported for a synthetic polymer before.

In phase III, PLATMC was blended with hydroxyapatite (HA), in several ratios: 10 % HA (HA10), 30 % (HA30) and 50 % (HA50). Printability, physical, mechanical, and biological properties were compared (Study IV). The disclosed tensile properties of all 3D-printed HA blends were reduced, compared to PLATMC. HA10 showed reduced degradation and mild Ca release rate, while the high degradation profile of HA30 and HA50 was accompanied by massive early Ca release rates.

On the biological aspect *in vitro*, using human-BMSCs seeded up to 28 days, HA10 disclosed higher mineralized ECM secretion at 14 and 21 days than PLATMC, while the osteoconductivity of HA30 and HA50 were markedly reduced and exhibited no advantages over pristine PLATMC templates. Moreover, HA30 and HA50, exhibited marked less osteoconductivity and reduced bone ingrowth when implanted in CBD. Thus high Ca release were correlated to reduced bone ingrowth and reduced osteoconduction, and the rate of Ca release should be considered in characterizing new HA-based templates.

In summary, 3D-printed PLATMC showed promising osteoconductive activity, stimulating abundant mineralized ECM secretion *in vitro*, and demonstrated contact osteogenesis *in vivo*. However, the addition of HA reduced its tensile properties and high Ca release rates exhibited less osteoconductive properties than PLATMC. The results of these studies support the application of 3D-printed PLATMC templates for BTE.

Abstract in Norwegian (Sammendrag)

Syntetiske polymerbiomaterialer er enkle å bearbeide, biologisk inerte og brukes derfor i en rekke biomedisinske applikasjoner. Forskning har i lang tid fokusert på å øke biologiske aktivitet til slike materialers, og å tilpasse egenskapene til ulike bruksområder. Tredimensjonal (3D)-printing er velegnet til framstille biomaterialmaler med stor presisjon etter bestemte designparametre. Målet med denne avhandlingen var å undersøke 3D-printede syntetiske polymermaler for bruk til dyrkning og regenerasjon av beinvev (BTE). Undersøkelsene bestod av tre faser:

Først ble det utført en systematisk litteraturundersøkelse for å analysere relevante faktorer ved bruk av 3D-printede, nedbrytbare maler og virkningen deres på beinregenerering i kraniale beindefekter hos ulike dyrearter (Studie I). En meta-analyse ble utført for å sammenligne nydannelse av bein for hver materialtype (polymerer, keramer eller komposítter). Man fant at effekten på beinregenereasjon var høyest hos kompositter bestående av polymerer og biokeramer, men også materialstrukturen gitt av 3D-printing.

Parallelt ble det utført en studie på funksjonalisering av 3D-printede polykaprolakton (PCL) maler med gelatin (GL) som ble testet *in vitro* (Studie II). Til tross for at økt mengde GL (ved 8 og 16%) forbedret osteogen differensieringen av stamceller (fra rotter) ble malene ikke videreført på grunn av materialets lave strekkfasthet.

I neste fase, ble poly(lactide-co-trimethylenecarbonate) (PLATMC) sammenlignet med PCL, og man fant at PLATMC hadde gunstigere både nedbrytnings- og mekaniske egenskaper enn PCL (studie III). I tillegg viste PLATMC seg bedre egnet for å fremme mineralisering av ekstracellulær matriks (ECM) fra humane stamceller *in vitro*. I en subkutan implantasjonsmodell i kanin (varighet 8 uker) var vertsresponsen på PLATMC mild, med innvekst av løst bindevevs og høy infiltrasjon av celler, der PCL bar preg av tett fibrøs vevsinnkapsling. Videre, når begge malene ble implantert i skallebensdefekter i kaniner, viste PLATMC-malene størst innvekst av bein. Det ble også funnet nydannelse av bein direkte på materialoverflaten, noe som hittil ikke beskrevet for syntetiske polymer.

I tredje fasen valgte man å modifisere PLATMC ved å kombinere polymeren med hydroksapatitt (HA), et mineral og en viktig komponent i beinmasse. 3D-printede blandinger med ulike andeler HA (10, 30 og 50 %) ble sammenlignet med umodifisert PLATMC og testet for fysiske og biologiske egenskaper (Studie IV). Man fant at tilsatt HA reduserte strekkfastheten sammenlignet med ren PLATMC. HA10 viste noe redusert nedbrytningshastighet og lave nivåer av frigitt kalsium, mens de høye nedbrytningsprofilene til HA30 og HA50 ble tidlig ledsaget av omfattende frigivelse av kalsium. Ved bruk av stamceller (fra menneske) (*in vitro*), fant man for HA10 høyere mineralisering av ECM etter 14 og 21 dager enn for PLATMC alene, mens HA30 og HA50 ikke fremmet mineralisering i like stor grad. I tillegg viste HA30 og HA50 markant mindre beininnvekst når de ble implantert i skallebeinsdefekter i kaniner.

Oppsummert fant man at umodifisert 3D-printet PLATMC fremmet mineralisering av ECM både *in vitro* og *in vivo*, men at man ved å tilsette HA i for store mengder, gjennom frigivelse av kalsium, forstyrrer denne prosessen i tillegg til å redusere materialets strekkfasthet. Resultatene fra disse studiene samlet støtter bruken av 3D-printede PLATMC-maler for beinregenerering.

1. Introduction

1.1. Bone formation and regeneration

Bone is a mineralized tissue with a major role in the structural support of the body. It is highly dynamic and in contrast to most other tissues, has a remarkable capacity to heal through regeneration of new functional tissue, for example after trauma or surgical intervention.

The cellular components of bone tissue do not exceed 10%, but produce extracellular matrix (ECM), which comprises around 90% of bone tissue volume. Mineralized bone ECM is composed of organic and inorganic matrix, around 35% and 65%, respectively. Collagen type 1 (COL1) is the most abundant component (> 90 %) of organic ECM. The mineralized inorganic matrix is derived mainly from the precipitation of hydroxyapatite (HA) crystals, which ultimately rely on COL1 fibrils for orientation [1] (Figure 1).

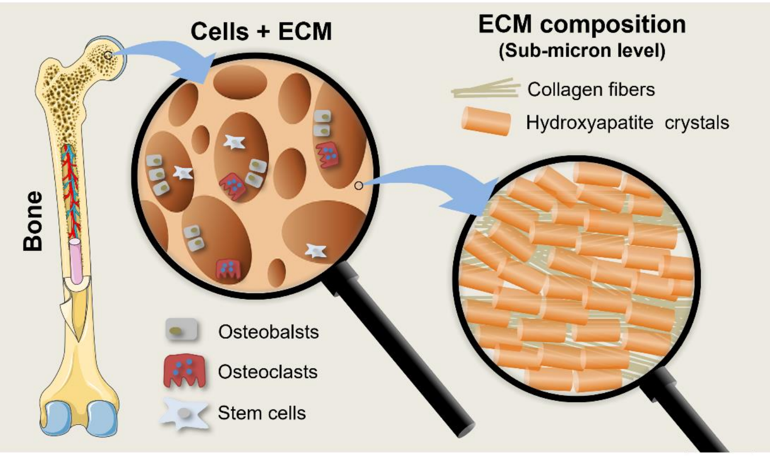

Figure 1: Schematic presentation to the general microstructure of bone tissues, including the major cellular components and ECM composition.

1.1.1. Bone biology and matrix deposition

Osteoblasts and osteoclasts are the bone cells primarily responsible for bone formation and resorption, respectively, and bone integrity of bone is maintained by osteoblast/osteoclast balance. Undifferentiated mesenchymal stem cells (MSCs) have a crucial role in bone regeneration, and their osteogenic differentiation into osteoblasts is regulated by specific signaling molecules and growth factors (GFs) [2].

Native bone tissues are also major storage sites for GFs (e.g. cytokines and hormones) in the form of proteins which are secreted by cells into the ECM and regulate cellular processes, including cell-cell interactions. Through specific trans-membrane receptors and other secondary reactions (signaling pathways) in the cell cytoplasm, GFs can transmit their message from extracellular level to inside the cell nucleus. This activates transcription factors that interact with DNA and give rise to signal transcription, represented as mRNA, followed by protein production by the cell [2].

Among the main GFs involved in skeletal osteogenic signaling pathways (induction of active osteoblasts) are transforming growth factor-beta (TGF-β), bone morphogenetic proteins (BMPs) and fibroblast growth factor (FGF). There are also crosstalks between these signaling pathways, accompanied by complex actions to coordinate osteogenesis [3].

TGF-β/BMP signaling has been widely recognized as a major pathway for bone formation and regulation during mammalian development. It acts through a heteromeric receptor complex at the cell surface, comprised of type I and type II receptors, that transduce intracellular signals via the Smad (intracellular signaling protein identified in invertebrates) complex, also known as the canonical pathway (Figure 2). The name Smad is a combination of the Drosophila gene 'mothers against decapentaplegic' (Mad) and the Caenorhabditis elegans small protein (Sma) [4].

In Smad-dependent (canonical) pathways, 8 different types of Smad proteins are involved. Smad 2 and 3 are activated by TGF-β extracellular signals, while Smad 1 and 5 or 8 are usually activated by BMP extracellular signals. These aforementioned receptor-regulated Samds (R-Samds), when activated in the cytoplasm, form a complex with common-mediator Smad (co-Smad, includes only Smad 4) and penetrates the nucleus to participate in transcription of the DNA promotor region. There are other classes of the inhibitory Smad family (I-Smads), including Smad 6 and 7, which negatively regulate BMP and TGF-β Smad-dependent signaling cascades, respectively [2] (Figure 2).

The non-canonical (Smad-independent), TGF-β signaling pathway is regulated through other cascades, including mitogen-activated protein kinase (MAPK) or extracellular signal-regulated kinase (ERK). The ERK-MAPK cascade is an important signaling component, stimulating proliferation of osteoprogenitor cells and promoting their differentiation into osteoblasts. Activation of this cascade was found to promote rapid bone expansion [5,6]. Thus, both Smad-dependent and -independent signaling pathways converge at transcription factors (e.g. RUNX2) to promote the differentiation of MSCs into osteoblasts [3].

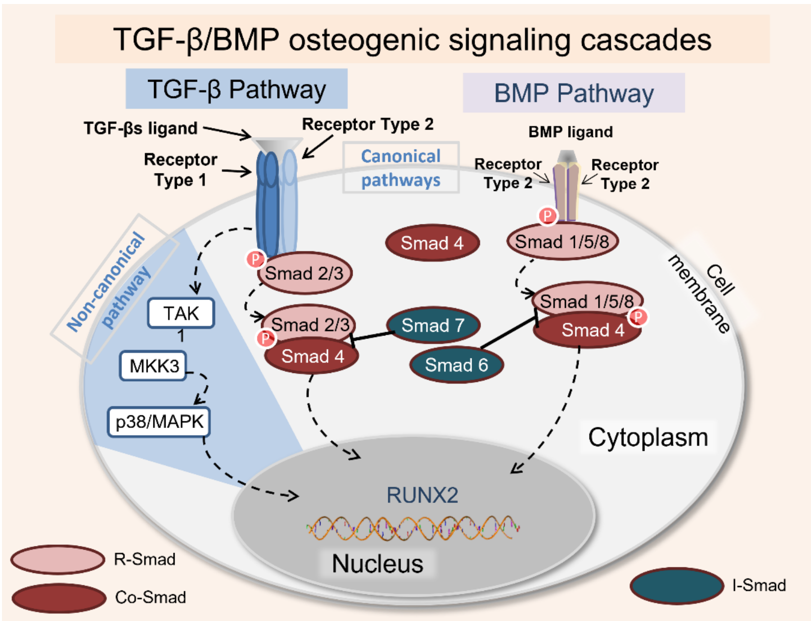

Figure 2: Schematic presentation of TGF-β/BMP signaling in MSCs, with canonical (Smad-dependent) pathways. Transforming growth factor (TGF-β) ligands activate signaling via TGF-β-specific receptors (type I and type II). Bone morphogenetic protein (BMP) ligands start signaling via the activation of two other receptors (BMP type I and BMP type II). Non-canonical pathway (Smad-independent) in TGF- β signaling is transmitted through MAPK. TAK: TGF-β activation kinase. Figure inspired from Chen G et al., 2012 [5].

Runt-related transcription factor 2 (RUNX2) is an early marker for osteogenesis and known to be the master regulator of MSCs differentiation into osteoblasts. It is an osteogenic transcription factor, mRNA, expressed in significant amounts by pre-osteoblasts, but its expression decreases during osteoblast maturation [7]. Mature osteoblasts secrete alkaline phosphatase (ALP) enzyme and lay down COL1 matrix, in addition to ECM vesicles (ECMVs) which concentrate calcium (Ca) and phosphate (P) ions (Figure 3).

In collagenous mineralized tissues (e.g. bone), initial biomineralization takes place within ECMVs, in the form of membrane-invested vesicles, released by budding from the surface of active osteoblasts. Calcium phosphates (CaP) are then actively accumulated within ECMVs and form HA crystals, which penetrate to outside the vesicle membrane and become proliferating calcification nodules in the ECM, within and between COL1 fibrils. However, the rate of crystal proliferation depends on other extracellular conditions, including concentration of Ca and P ions, pH, the presence of proteoglycans and non-collagenous ECM proteins [8].

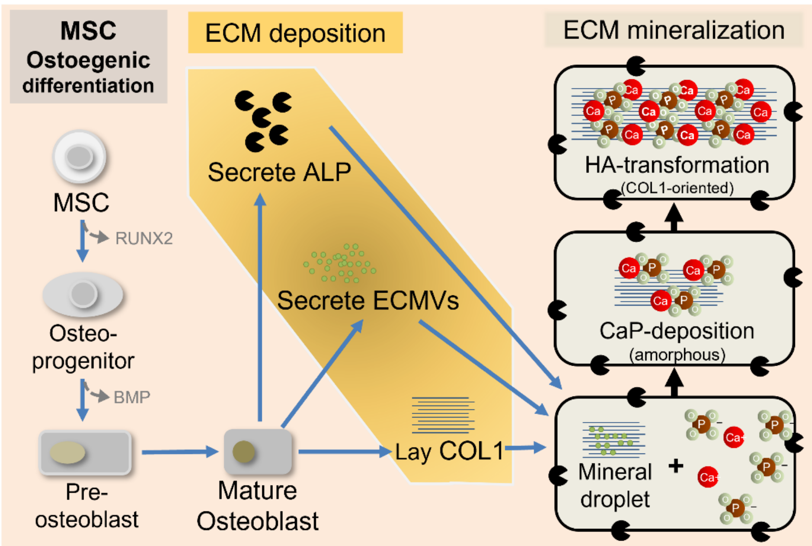

Figure 3: Schematic presentation of the stages of osteogenic differentiation of MSCs into osteoblasts, and their ECM deposition and biomineralization. ALP: Alkaline phosphatase enzyme; CaP: Calcium phosphates; COL1: Collagen type 1; ECM: Extracellular matrix; ECMVs: ECM vesicles; HA: Hydroxyapatite; MSC: Mesenchymal stem cell.

The role of ALP, an enzyme belonging to membrane-bound glycoproteins, is to cleave pyrophosphates that inhibit biomineralization in extracellular fluid, and remove phosphate groups from molecules, to allow biomineralization of ECM in alkaline medium [8]. Other important bone proteins are secreted by active secretory osteoblasts, e.g. osteopontin and bone sialoprotein, also referred to as secreted phosphoprotein, responsible for CaP crystal nucleation [9].

To imitate most of these conditions *in vitro,* osteogenic supplements are added to the basic culture medium to provide the essential factors needed to facilitate this osteogenic differentiation and matrix biomineralization process. The addition of Dexamethasone was found to stimulate osteogenic lineage commitment, RUNX2 expression, and secretion of ALP, while added L-ascorbic acid facilitate COL1 fibril assembly [10]. Disodium β-glycerol phosphate (βGP) was also added as the source of phosphates, converted by the secreted ALP, to potentiate calcification of collagenous ECM [11].

It is also important to note however, that in contact with synthetic substrates *in vitro*, the collagen compartment of the mineralized ECM is separated from the substrate surface by a continuous, submicron-thick layer involving individual, fused globules, known as globular accretions [12]. These globular accretions, Ø ≈ 1µm, were first described by John Davies et al., in the early 90's, as the primary event of mineralized ECM production by secretory osteoblasts on the synthetic substrates, preceding the deposition of overlying mineralizing collagen matrix [13].

1.1.2. From bone augmentation to tissue engineering

Despite the remarkable capacity of bone to heal through regeneration of new functional tissues, bone tissue is one of the most frequently transplanted/replaced tissues [14]. The process of bone regeneration depends on the interplay between potential osteogenic cells, mechanical and structural properties of the surrounding ECM and a microenvironment containing ions and GFs [15]. It should also be noted that bone regeneration is time dependent, and if local conditions are adverse, fibrous tissues can form instead or in addition to bone [16,17]. Thus in large bone defects, for example after trauma, surgical decompressive craniectomies or cancer resections, bone tissues cannot heal or regenerate spontaneously, and require surgical intervention for augmentation or restoration.

Autologous bone grafts (vascularized or non-vascularized) are currently the gold standard treatment. The procedure is inexpensive and does not usually induce adverse tissue reactions. However, there are a number of major limitations associated with the procedure, including donor site morbidity and limited availability of enough tissues to be transplanted [18], and there may associated tissue resorption [19]. This results in mental and physical distress for the patient and higher overall costs for the healthcare system.

Alternatively, allografts (fresh or frozen tissues from another matching patient), xenografts (tissues from another species) or alloplasts (synthetic non-degradable materials) have been used. However, inferior healing was observed in some allograft cases and a major drawback was availability, due to the shortage of donors [20]. Xenografts also have some limitations, including the risk of cross-contamination and immune rejection [21]. Alloplasts, including titanium (Ti) or polymethyl methacrylate (PMMA), on the other hand, are non-degradable, and this could lead to serious complications and high failure rates [22].

In the early 1960s, a process of distraction osteogenesis (DO) was refined and reported by Dr. Ilizarov G.A., using controlled mechanical strain to promote the self-healing capacity of the injured bone to create new bone volume [23]. This is regarded as the first attempt at bone tissue engineering (BTE) and was widely adopted in clinical orthopedics and maxillofacial surgery, with high impact and successful rates. However, it is not appropriate for all sites [24].

More recently, the general term of tissue engineering (TE) has been introduced as a general alternative approach to replace the lost or failing tissues. The classical foundations were described by Langer and Vacanti in the early 90's [25]. TE was defined as the tendency of the body to heal itself through the delivery of cells, biomolecules and supporting structures to the appropriate site. This was intended to provide the patients with the means to regenerate their own tissues, instead of only scar (fibrous tissue) repair [26]. It was hoped that this would overcome the massive limitations of organ or tissue transplantation through the interacting technology of stem cells, signaling systems and biomaterials to regenerate tissues [25]. Nevertheless, the biological influence defined by classical TE was limited to the loaded biological (e.g. cells) and/or pharmaceutical (e.g. GFs) agents: there was no major role for the biomaterial carrier, except as a totally inert vehicle [27].

1.1.3. Cell-based and GF-delivery approaches for BTE

Bone marrow-derived mesenchymal stem cells (BMSCs), and MSCs derived from other tissues (e.g. adipose tissue), have been shown to induce new bone formation [28,29]. In pre-clinical trials [30], and in non-controlled clinical studies [31,32], BMSCs loaded onto biomaterials were found to induce bone healing and biomineralization. However, the true significance was disclosed only on certain bone sites, when the treatment outcomes were meta-analyzed [33,34].

Nevertheless, the limitations of cell therapy need to be considered. Cell therapy is still under development, and considerable costs are incurred in the production, transportation, and quality controls of clinical grade MSCs. The cost of cell therapy is around 20,000 € per patient, compared with around 1,500 € for autologous bone grafting, charged by hospitals (K. Mustafa, personal communication, November 2021). Moreover, cell-based therapy has other disadvantages: relatively invasive isolation, limited availability of the donated amount, and limited multipotent ability after extensive passaging [28]. High cell seeding density is essential for effective bone regeneration outcomes [35,36]. The required cell transplants are in turn dependent on large-scale cell culture, followed by adequate seeding distribution in the 3D-matrix. Thus there are obvious financial and technical barriers to clinical translation of classical TE [37].

On the other hand, the use of purified auto-inductive proteins (e.g. GFs) or proteoglycans (e.g. heparan sulphate) in bone regeneration was considered to be a promising therapeutic approach, and was used as an alternative for cell transplantation [38]. The GFs used were BMP-2, TGF-β, FGF, vascular endothelial growth factor (VEGF), platelet-derived growth factor (PDGF), and stromal-derived growth factor

(SDF1) [39]. Moreover, the production of GFs in recombinant (synthetic) forms led to their application in numerous clinical trials [40].

BMPs, for instance, were first described by Urist 1965 [41], and generally characterized by their ability to auto-induce osteogenesis (bone formation) at ectopic sites (e.g. in muscles) from the ingrowing proliferating pluripotent cells of the host [41]. BMPs were named by Urist and Strates 1971 [42], and were later isolated from bovine bones and found to comprise different groups (14 types classified according their structure homology). Apart from BMP-1 which belongs to the TGF- superfamily, only a few BMPs (BMP-2, -4, -6, -7 and -9) were able to induce osteogenic factors and matrix biomineralization [43]. Moreover, the potential to achieve positive BMP-based bone growth is highly dependent on the BMP dose and method of delivery; either by delivery of DNA encoding the GFs, gene therapy or delivery of the protein itself through a carrier matrix. The latter was the most viable therapeutic approach, with the least safety concerns and production costs [44].

The use of 3D-templates to deliver BMPs, as a GF-delivery approach, was considered to be a cell-free approach targeting the recruitment the of the host's own stem cells [45]. Thus, of the BMPs used *in vivo* and in clinical trials, only BMP-2 and BMP-7 have been approved as osteoconductive GFs by the US Food and Drug Administration (FDA). These GFs are typically delivered through collagen sponges [46], despite the limitations of the collagen matrix itself (for instance, not injectable), in addition to the burst release instead of the required sustained release [44]. Thus, due to poor control over the distribution and timing of their delivery from the direct application of BMPs, the results were unsatisfactory. Various controlled delivery options were implemented for BMP, minimizing the dose required and enhancing the delivery processes [45,47,48]. However, with respect to the clinical use of BMPs, even with the controlled delivery systems, questions have arisen about the associated inflammation, the risk of tumor formation, or even life-threatening complications [49–51]. Hence, a strategic shift followed, intended to maximize dependence on osteoconductive biomaterials and patient-specific implants to replace lost bone tissues [15,37].

1.2. Functional templates for BTE

A biomaterial was defined as "a material intended to interface with biological systems to evaluate, treat, augment or replace any tissue, organ or function in the body" [52]. The BTE templates/scaffolds, used in 3D-porous form or in the form of sheets or hydrogels, could be fabricated from most of the available classes of biomaterials. In general, the main classes of biomaterials are metals, polymers, ceramics, or their blends/composites, which are widely used to promote bone regeneration for orthopedic and cranio-facial bone defects. This includes potentially-degradable metals, synthetic derived ceramics and polymers, as well as the naturally derived polymers and ceramics (Figure 4).

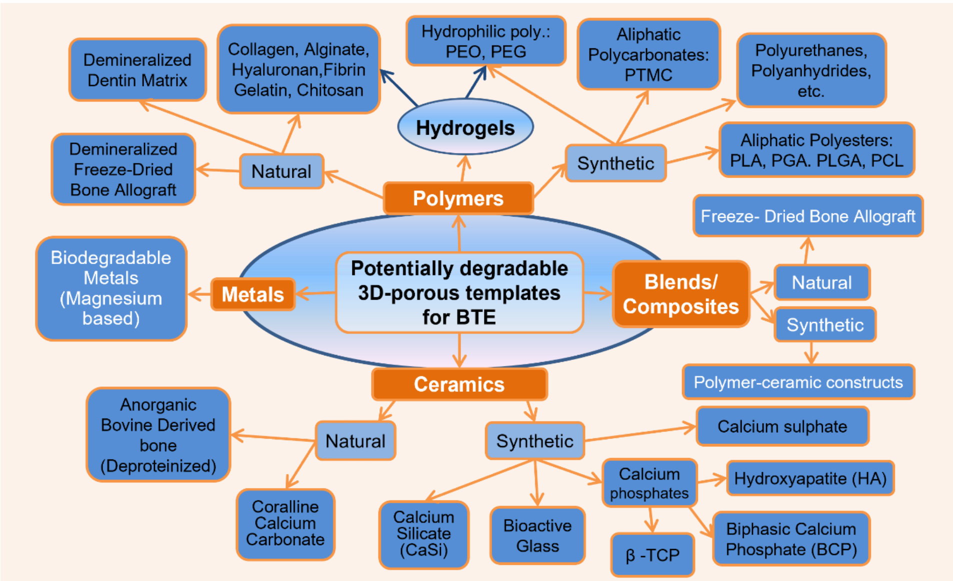

Figure 4: Schematic presentation of the general classification of the potentially-degradable biomaterials used for BTE. In addition, a sub-group of polymers denoted as hydrogels is shown in the classification. Abbreviations: PCL: Polycaprolactone, PEG: Poly(ethylene glycol), PEO: Poly(ethylene oxide), PGA: Poly(glycolide), PLA: Poly(lactic acid), PLGA: Poly(lactic-co-glycolic acid), PTMC: Poly(trimethylene carbonate), β-TCP: beta-tricalcium phosphate.

In the early attempts at TE, the use of a biomaterial scaffold (or template) was meant to provide temporary mechanical and structural support for the attachment of cells until they could produce their own skeletal ECM microenvironment [53]. However, as TE strategies have developed, the role intended by TE biomaterials has advanced: they are required to contribute dynamically to the regeneration process, and influence the course of the therapeutic procedure in human or veterinary medicine, alone or as a part of a complex system [52].

In addition to the typical requirements for BTE templates, such as biocompatibility, tailored biodegradation rate, adequate mechanical properties and 3D-porous structure, the ideal BTE template should offer osteoconduction on its surface. Moreover, for optimum commercial application of BTE templates, they should be sterilizable and available off-the-shelf, through an easy, cost-effective and reliable process [37]. Osteoconductive bone replacement grafts meet these requirements and are now materials of interest for fabrication of BTE templates.

1.2.1. Pore size and connectivity

Besides the characteristic osteoconductivity required from a BTE template, it is important to provide/maintain a space for tissue ingrowth and angiogenesis [54–56]. Tuning the intrinsic biomaterial properties through design, should support BTE. Bone formation cannot be observed on dense sintered ceramic which does not degrade *in vivo*; but bone can form on the same ceramic material when it is structured with pores that facilitate the invasion of blood vessels, allow exchange of nutrients and oxygen, and allow the osteogenic cells into the scaffold [57]. This maintained primary space can be achieved by using a design with appropriate pore size and distribution, without risking the mechanical resistance of the template structure [58]. However, interfering or blocking the pores reduces bone regeneration, even if cells or GFs are added [59].

The pore geometry of templates showed some impact on bone regeneration. When HA ceramic discs containing concavities of different dimensions were implanted in muscle tissues, bone formation was observed only in the concavities and never on the convexities [60]. The same was observed when biomimetic HA was tested in the form of concave microporous (foamed) versus orthogonal-patterned porous (3D-printed) structures [61,62]. Thus this concave geometry was believed to concentrate bone-forming molecules such as BMPs and stimulate angiogenesis, which induces bone formation [60].

Despite their osteoconductivity, the inherent brittleness of bioceramics is a major factor limiting their use in pure form as potential BTE templates [63]. To compromise between interconnected structural porosity and mechanical resistance, a porosity gradient design, based on finite element modeling, was developed to improve the flexural strength of 3D-printed bioactive glass (BG). Such porosity gradient templates possessed double the flexural strength of the grid-like templates, but did not enhance bone regeneration *in vivo* [64]. Therefore, the addition of synthetic polymers as the main support for bioceramics (BG, HA, β-TCP, etc.) was the most frequently documented and applied solution, due to their favorable inherent resilience.

The optimal pore size for osteogenic differentiation and bone ingrowth into 3D-printed templates varied across studies, ranging between 300 and 500 µm [65–68]. On the other hand, the creation of macro-pore channels within osteoconductive templates showed better *in vivo* bone regeneration [69,70] and less soft tissue ingrowth. These macro-porous structures were found to accommodate the ingrowing trabecular bone (Ø ≈ 100 - 250 µm) creeping onto the printed strands [68] (Figure 5).

In addition, the space regulated by the biodegradation rate of the template used (secondary space), was vital to new bone area (NBA) remodeling [71,72]. The rate of template biodegradation should match the space needed during the initial healing time for the organized and unrestricted inclusion of the BTE set-up. This healing period may differ across species and across the implantation sites, even within the same animal model [73]. Hence, hydrogels (e.g. β-TCP/collage/chitosan) showed superior bone regeneration, related to higher biodegradation rates than the control templates, even though the stiffness was less than optimum [74]. Moreover, better bone regeneration was directly proportional to the increase of *in vivo* biodegradation of printed templates [75–77].

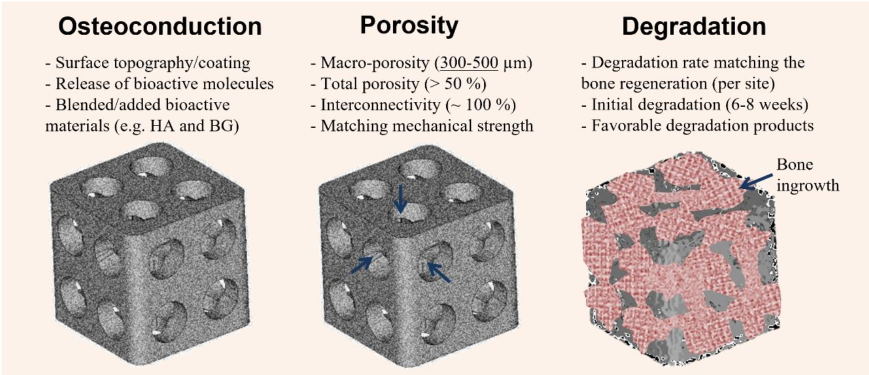

Figure 5: Schematic presentation of the requirements of the ideal BTE template.

1.2.2. Essential osteoconduction

An essential surface property of implantable materials for BTE is osteoconduction, defined as the biological activity of the surface, supporting the recruitment and migration of differentiating osteogenic cells to the implanted surface [78]. Ideally, this should be followed by the next healing phase, known as new (*de novo*) bone formation, whereby osteogenic cell activation and ECM deposition are initiated on the implant surface [78]. The combination of these two healing phases, osteoconduction and new bone formation, results in contact osteogenesis, commonly known as osseointegration. In endosseous Ti implants, this appears at the light microscopic level as direct bone contact to the implanted surface [79]. Consequently, the osteoconductivity of a biomaterial was defined clinically as the ability to conduct growing bone on its surface, with high surface contact ratio [37].

The desired features of osteoconductivity could be achieved or supported at the material/tissue interface, either by inherent or engineered physicochemical characteristics added to the biomaterial surface, or alternatively by the presence of attached molecules, or molecules intended to be released into the local host tissues [80].

Osteoconductive materials should be differentiated from bioactive and bioinert materials, which have higher or lower biological activity, respectively, than osteoconductive materials. Bioactive materials, e.g. BG, have more favorable interactive biological activity that is initiated with ion exchange, which elicits or modulates a specific biological response at the interface with bone tissues [81]. This results in the formation of a biological bond, shown as new bone collagen interdigitation with the chemically active implant surface [12], through osteoinduction [82]. Thus, osteoinduction was defined as the ability of the material to induce undifferentiated MSCs to the osteogenic lineage, to form osteoprogenitor cells [83]. The conclusive evidence for osteoinduction was the *in vivo* heterotopic bone formation by implantation of biomaterials in tissues where bone does not naturally form [57].

In contrast, the bioinert materials induce no adverse inflammatory reactions, either short- or long-term, but otherwise act to promote local fibrous tissue repair [80]. New bone could be formed through distance osteogenesis in relation to implanted bioinert materials, similar to physiologic appositional bone growth which encroaches on the implant surface. Hence, the bioinert (non-osteoconductive) implant becomes surrounded by bone through distance osteogenesis, but usually covered by fibrous connective tissue at the interface [12].

HA, for instance, is comprised mainly of Ca and P in a crystalline form ($Ca_{10}(PO_4)_6(OH)_2$), and has high osteoconductive and potential osteoinductive properties, although it has the lowest biodegradation rate among the CaP family members [84]. It occurs naturally as the main component of the ECM of bone (bone apatite): thus HA could be extracted from natural sources (e.g. deproteinized bovine-derived bone) or synthesized using various chemical and hydrothermal methods [84]. HA has been regularly used as a bone graft/template, alone or blended with different polymers, in different forms. HA particles of nano and submicron size were expected to exhibit more rapid biodegradation and biophysical characteristics closer to those of natural bone apatite [85].

By the mid-1980s, some products based on these osteoconductive or bioactive biomaterials reached clinical application in a variety of orthopedic and dental applications [84]. They have also been used routinely as porous implants, powders, and coatings on metallic prostheses to provide bioactive fixation with bone [14,86]. Currently, the biomaterial products are the most widely represented in the TE market. In a recent study, the biomaterials-based companies comprised 16 out of a total 49 TE-based companies identified as representing the TE industry in US from 2011 to 2018. However, during this period, the total biomaterials-based TE products accounted for 99% of total sales in the TE market in the US and only 1% of sales comprised cell-based and combined cell/biomaterials-based products [87].

1.2.3. Biological activity of synthetic polymers

In general, selection of synthetic polymers for biomedical applications was based on their bioinertness, which is defined as the inability to perform specific biological functions. The other families of "non-inert" synthetic polymers were undesirable in any application because they evoked a toxic biological response [88]. On the other hand, more recently, new synthetic polymers have emerged with specific functional bioactivity and outstanding anticancer [89], antibacterial [90], antifungal [91], and antiviral [92] properties, in the absence of any conjugated or encapsulated species. Bioactive synthetic polymers were found to bind with biomolecules (e.g. cell surface, proteins, and polysaccharides) through different non-covalent (e.g. electrostatic) interactions, or hydrogen bonds. Consequently the biological systems recognize these interactions and formulate targeted biological pathways [88]. Among these successful examples of bioactive synthetic polymers is glatiramer acetate, clinically approved for Multiple sclerosis (MS) treatment, because of its ability to compete with immunodominant basic proteins involved in the development of MS and to modulate T cell reactivity [93].

To be qualified as biologically active synthetic polymers for BTE, they should ideally induce/promote favorable tissue regeneration and osteoconduction, while modulating tissue response (anti-fibrotic) and avoiding adverse inflammatory reactions. However, to date, no synthetic polymers with inherent bioactivity/osteoconduction have been reported for BTE [94]. Various attempts have been made to boost the physical properties and bioactivity of synthetic polymers, customized per application through copolymerization, blending, and functionalized coatings [95]. Immunomodulation strategies have been suggested as a potential support for functional integration of synthetic polymers prior to implantation. This includes controlling the physical properties (e.g. surface roughness, or nano-scale topography), or loading of anti-inflammatory and/or pro-wound-healing molecules onto the top of the implanted synthetic biomaterials [94,96]. Hence, synthetic polymers were functionalized with mineralized and decellularized ECM [97–99] to be used as off-the-shelf bone osteoconductive templates.

1.3. Polymer-based templates for BTE

Polymer-based biomaterials used in medicine are either synthetic or natural (biologically-derived) polymers. They might also be classified into hydrolytically or enzymatically degraded polymers, respectively, according to their biodegradation and cleavage of sensitive bonds leading to polymer erosion [100]. Naturally-derived polymers used for BTE are polysaccharides (e.g. chitosan, alginate, and hyaluronic acid derivatives), or proteins (e.g. collagen, gelatin, and silk) [101]. Gelatin (GL), for instance, is a denatured form of collagen, which cells can recognize and bind to, and it degrades through enzymatic action. It has been used in different forms with different crosslinking mechanisms for GF-delivery [102] and BTE templates [101]. In addition, it could be added to synthetic polymers to enhance their affinity for cell attachment and controlled differentiation [103].

1.3.1. Synthetic polymers printed for BTE

The main advantages of synthetic polymers used in BTE are their mechanical properties (tensile strength and resilience) and their relatively simple processibility, degradation and bioinertness. The potentially-degradable synthetic polymers used in BTE possess hydrolytically labile chemical bonds presented in their chain backbone with functional groups (e.g. esters, anhydrides, carbonates, amides and urethanes). Aliphatic polyesters; also called poly(α-ester)s, are thermoplastic polymers with “hydrolytically” degradable aliphatic ester linkages, which have been extensively investigated in biomaterials science (Figure 6). Among the most extensively studied are poly(lactic acid) (PLA), poly(glycolide) (PGA) and polycaprolactone (PCL). The history of synthetic biomaterials used in medicine started with polymers, after the FDA first approved hydrolytically degradable PGA as a suture biomaterial in 1969 [100], followed by PLA and their copolymer (PLGA) at different ratios.

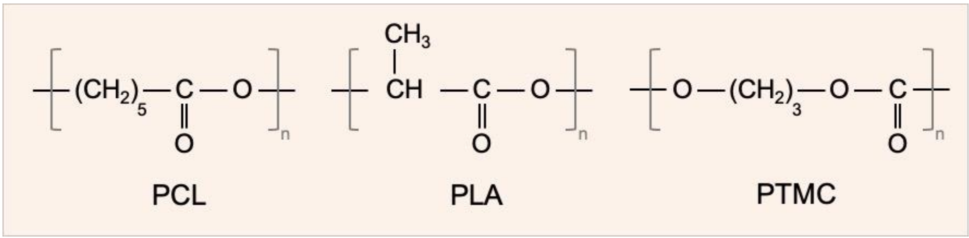

Figure 6: Representative sketch to the structure of selected (hydrolytically degradable) aliphatic polyesters (homopolymers) (e.g. PCL and PLA), and polycarbonates (e.g. PTMC)

1.3.2. PCL

PCL is a semi-crystalline polymer (aliphatic polyester), which usually takes 24 to 36 months for full biodegradation. It is highly processible due to its low melting point (55-60 ºC), very low glass transition temperature (Tg), around -60 ºC, and solubility in a wide range of organic solvents.

The earliest 3D-printed templates investigated for BTE in calvarial bone defect (CBD) were fabricated from PCL: PCL templates, seeded with calvarial osteoblasts (OBs) and mesenchymal progenitor cells, achieved a 60% higher calcification than either the unseeded templates or the empty CBD (negative controls) [104]. Furthermore, surface treatment of PCL/TCP templates with NaOH increased their surface roughness and exhibited better mechanical integration properties and better bone regeneration in CBD [105]. Following successful clinical trials [106,107], 3D-printed templates made of medical-grade PCL were approved by FDA for clinical use [38].

1.3.3. PLA

PLA is another subgroup of degradable aliphatic polyesters, which is broken down into lactic acid, and further into water and carbon dioxide by simple hydrolysis. PLA exists in two optically active forms; poly(L-Lactide) and poly(D,L-Lactide); known as PLLA and PDLLA, respectively. PLLA is a semi-crystalline polymer, with Tg ranges 60-65 ºC and melting temperature approximately 175 ºC. It has good tensile strength but a very low rate of biodegradation (> 3 years) *in vivo*. PDLLA is amorphous and characterized by lower Tg ranges (55-60 ºC), lower strength and more rapid biodegradation rates [100,108]. PLA is available in various molecular weights and in copolymer forms which have been widely used as surgical sutures, or dental and orthopedic fixation devices, or drug-delivery vehicles [109]. In addition, their biodegradation rates, mechanical, and physical properties are all dependent on PLA molecular weight and/or its copolymers [110].

1.3.4. Poly(trimethylene carbonate) and copolymers

Poly(trimethylene carbonate) (PTMC) is high molecular weight, amorphous polymer (aliphatic polycarbonates, which contain a carbonate ester group in their main chain) with excellent flexibility (Tg between -14 and -20 ºC), but low mechanical strength. PTMC has been investigated as a candidate implant material for soft tissue regeneration [111,112].

Unlike most aliphatic polyesters, PTMC undergoes surface degradation (surface erosion) [113], but a high rate of biodegradation was observed *in vivo* attributed to enzymatic degradation [114]. It produces no acidic degradation metabolites [111], however, the poor mechanical performance of the homopolymer significantly limits its application [100].

When evaluated in non-load bearing cranial defects (in sheep), porous (salt-leached) templates of PTMC, or blended with CaP particles, were found to degrade uneventfully and did not interfere with bone regeneration. However, the CaP content of the used templates were the key to enhanced bone regeneration. The addition of more pure β-TCP resulted in a greater amount of new bone formation than any of the other composites with PTMC [115].

Photo-crosslinked PTMC was fabricated (using stereolithography) and used for bone repair in CBD in rabbits, together with their composites with HA (PTMC/HA) with 20 and 40% HA. PTMC/HA composites showed superior osteoconduction, characterized by Alizarin red staining (*in vitro*) and by quantified histomorphometric bone healing (*in vivo*) [116]. On the other hand, PTMC was blended with high percentages of β-TCP, processed by stereolithography. This led to higher tensile strength and printing resolution [117]. Furthermore, Teotia et al. (2020) undertook a comparison of PTMC, PTMC/HA and PTMC/β-TCP *in vitro* and in critical size cranial defects in rabbits [21].

Compared to neat PTMC, blended-PTMC showed no major osteoconductivity advantages, except when functionalized with BMP. Moreover, due to the fabrication method (photo-crosslinking), all the test groups lacked any signs of biodegradation. Therefore, alternative copolymers (e.g. with PLA) and a better processing technique without crosslinking, were recommended to facilitate the fabrication of degradable templates for BTE applications [116].

Copolymer networks of PLA with PTMC (e.g. poly(lactide-co-trimethylene carbonate) (PLATMC)) were prepared, with PTMC content around 40 mol% or more, and were found to have tough, flexible, and elastomeric properties (Tg < room temperature), with shape-memory behavior, and high elongations at failure (up to 800%) [108,118,119]. In addition, they were found to degrade through bulk hydrolysis, autocatalyzed by the generated acidic end groups [120]. With respect to osteoconductivity, PLATMC stimulated the proliferation of cultured osteoblasts and preserved their normal phenotype [121]. PLATMC was recently used by the author's group with favorable osteoconductive applications [122,123].

1.4. 3D-printing for BTE

Various additive manufacturing (AM) techniques (including 3D-printing) have been used in diverse biomedical applications, from customizing dental guides in orthognathic surgery to reconstructive surgery stents [124], or as non-degradable prosthetic parts in cranioplasty [125]. This was facilitated by the various and endless options given and supported by AM, allowing the creation of 3D objects using data generated by computer-assisted design (CAD) software, or imported from 3D scanners (e.g. magnetic resonance imaging (MRI), or X-ray computed tomography (CT)) [126]. The CAD model is then converted to a standard tessellation language (STL) file, which directs the software system controlling the 3D-printer, followed by the generation of layer-by-layer modeling of the assigned design [127] (Figure 7).

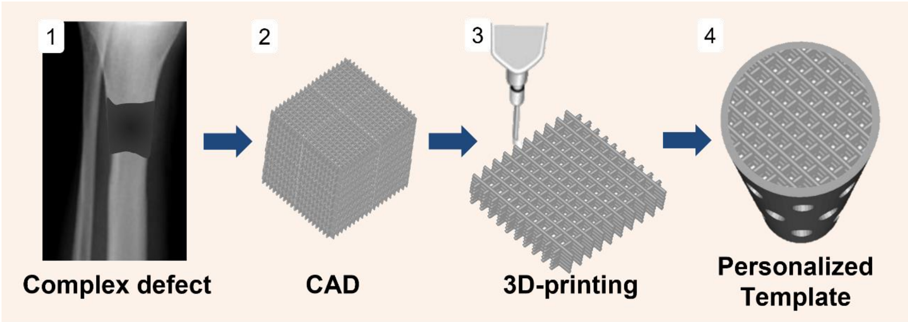

Figure 7: Schematic presentation of the major steps required in 3D-printing techniques to fabricate personalized templates for BTE.

A 3D-printer provides layer-by-layer fabrication of physical structures by selectively adding materials/inks from a feed print head, according to a programmed digital plan/model [128]. The 3D-printing based on material extrusion could be further classified into melting-extrusion (performed at high temperatures, using pellets), or aqueous/gel non-melting-extrusion that is known as direct writing. Thermoplastic polymers are usually printed through melting-extrusion and the first developed melting-extrusion platform was fused deposition modeling, referred as FDM, developed in the late 1980's. In FDM, the feed materials are supplied as filament (Ø = 1.7 mm), which is melted by deposition head, extruded through the heated nozzle, and moves horizontally to deposit the pattern for a given layer [129]. More recent melting-extrusion platforms were developed in which the used feed materials are in the form of powder or pellets. Therefore, 3D-printing could be done with a syringe (material reservoir) on which pneumatic pressure is applied directly onto the melted material to be extruded, or through a screw/plunger (under mechanical pressure) to extrude the material through the syringe nozzle/needle [130]. However, these techniques require the prefabrication of the polymer blends before being fed to the syringe to be printed.

In contrast, other types of screw extrusion printing are based on a homogeneous, continuous feeding process, and the application of high pressure, which allows smaller nozzles to be used [129]. Moreover, it allows fabrication of blended templates without their pre-fabrication in the form of pellets or filaments. However, agglomerations and nozzle clogging still occur because of the limited mixing capacity of the extruder at some points [131].

In melting-extrusion, the heat range is another critical factor which varies according to the material used. For semicrystalline polymers (e.g. PCL), the printing temperature should be kept at a range higher than its melting temperature (T_m). However, the printing temperature of amorphous polymers (e.g. PLATMC) should be well above the Tg and lower than its decomposition temperature [132]. Various techniques have been used for the fabrication of polymer-based templates for BTE, including salt-leaching, solvent-casting, phase separation, gas-foaming, and freeze-drying [133]. However, by comparison, 3D-printing offers a simple design and preparation process [134]. It can produce a highly porous structure with superior interconnectivity [135], and can rapidly and reproducibly fabricate custom templates with specific or complex anatomic shapes [136,137]. Moreover, it was observed that biologically, 3D-printed templates were outperforming non-printed porous templates [54,138]. Hence, the customization of design and sub-structures, including the interconnected macro-porosity created by 3D-printing, was crucial for BTE templates, favoring bone ingrowth within the template [139].

1.5. 3D-printing toward BTE clinical translations: state-of-the-art

The aim of biological assessment of new therapeutic approaches and technologies is to understand the basis of their efficacy or complications. Thus, it is crucial to translate the reported successes observed *in vitro* or in small animals (*in vivo*) to preclinical studies, in relevant large animal models, to facilitate progression to clinical translation [140]. Moreover, the preclinical animals used should closely reflect clinical conditions, in order to explore the challenges and limitations [141]. In this context, various large-animal species were manipulated as preclinical models including goat (caprine), sheep (ovine) [141], dog (canine) [62], pig (swine) [142] and non-human primates [60,133].

There are many case studies of 3D-printed customized devices made from non-degradable biomaterials (e.g. Ti, PMMA, Polyetheretherketone (PEEK)) [124,125]. In the following section however, only studies of potentially-degradable and 3D-printed BTE templates are discussed.

1.5.1. First generation 3D-printed BTE templates

In 2000, the first generation of 3D-printed templates for BTE was fabricated from PCL and evaluated and patented by an interdisciplinary group at the National University of Singapore. Among those early trials in non-load bearing defects, 3D-printed PCL porous templates were applied in the reconstruction of orbital-wall defects in pigs [142,143]. At this time, 3D-printed templates revolutionized the outcomes compared with the commercially available products, PLA and PLGA (non-porous) sheets, which were used as full-body implants (sheets or membranes), on which bone is allowed to grow only along their surface [143]. After 3 months, relatively higher amounts of new bone were detected within the porous PCL, compared to the familiar PLA sheets. Moreover, when PCL templates were coated with bone-marrow immediately before implantation, a significant increase in the amount of new bone was observed [142,143].

These 3D-printed PCL templates were FDA approved in 2006 [38] and commercialized as Ostoepore ™. 3D-printed PCL templates have since been evaluated in non-load bearing bone defects; as orbital wall and orbital floor reconstructions, burr hole plugs in cranioplasty, or to augment the iliac crest after an autograft [144]. Despite some drawbacks, in most such applications, alloplastic non-degradable biomaterials were used and are still being used (e.g. polyethylene (Medpore) or Ti mesh) [124,125]. Meanwhile 3D-printed PCL templates showed advanced healing properties and perfect adaptation and integration to defects, and were considered promising in future BTE [144].

Osteopore templates were further used successfully in clinical trials with apparently good outcomes. Shantz et al. 2006, used 3D-printed PCL templates as burr hole plugs (Ø = 14 mm) in cranioplasty (5 case studies), immediately after trephination of the skull to relieve subdural hematoma [106]. The implanted plugs revealed good integration to the surrounding calvarial bone. New bone, characterized by µCT was observed within the templates at 12 months. However, histologically there was no evidence of direct bone contact with the PCL surface *in vivo*, and a fine fibrous connective tissue interface was always present. Moreover, no follow-up studies have been reported of the long-term fate or biodegradation of the inserted templates.

1.5.2. Second generation 3D-printed BTE templates

In the second generation of 3D-printed templates for BTE applications, PCL was blended with CaP (including PCL/HA and PCL/β-TCP) to develop more favorable mechanical, biochemical, and biodegradation kinetics, for more advanced clinical applications [38]. A case report by Probst et al. (2010) reported the use of a patient-specific 3D-printed PCL/β-TCP template, with apparently good bone integration (assessed by μCT), after 6 months [107].

On the other hand, the treatment of load-bearing defects (e.g. mandibular or long bone defects) was a major challenge for BTE using degradable 3D-printed templates, where tens of parameters are crucial and critical [144]. Berner et al. (2013), studied the effect of 3D-printed PCL/β-TCP templates (Osteopore) combined with autologous or allogenic seeded mesenchymal progenitor cells (MPCs) in ovine, critical-sized segmental bone defects. In this study, unseeded 3D-printed PCL/β-TCP templates and autogenous bone grafts served as negative and positive control groups, respectively. After 12 weeks, no significant biomechanical differences were observed between the cell-seeded groups and the unseeded PCL/β-TCP templates. The unseeded group showed slightly less volume of bone regeneration than the two seeded groups, but significantly less bone volume than the autogenous bone graft group [145].

Extensive further attempts using copolymers and bioceramic blends to produce an osteoconductive 3D-printed templates for an exclusively template-based BTE approach, have to date not been clinically successful. Full bone regeneration within critical-sized defects in pre-clinical models using 3D-printed Osteopore (PCL/β-TCP) templates could not be achieved without a combination of hydrogels and doses of BMPs [146]. Kobbe et al. (2020) reported a successful clinical case study on treatment of long bone (femoral) defects, which was successful only when an autogenous bone graft (cancellous bone) was combined with BMP-2, using a patient-specific 3D-printed Osteopore template [147].

New design features were added to PCL templates through electro-writing processing, using an AM technique combined with electrospinning, for skeletal repair of long bones. Black et al. (2020), studied the pre-clinical efficacy of BMSCs loaded onto PCL tubular templates fabricated with electro-writing in two models [140]. In the *ex-vivo* model (femoral defect of embryonic chick), bone bridging and partial repair were observed in the BMSCs/PCL template group, but on the unseeded PCL template, no new bone outgrowth was observed at the cut ends. This indicated the crucial role of seeded BMSCs to activate bone regeneration in association with their direct potential for bone and cartilage formation, or their paracrine effects, which recruit periosteal skeletal precursor cells [140]. In the other critical-sized segmental tibial defect in the preclinical (ovine) model, no significant differences in new bone forming activity were observed between the groups. Several contributing factors were proposed: the limited regeneration of the vasculature required for new bone formation or the limited effect of the number of seeded cells, especially with reference to the observed lack of proliferation of the seeded cells [140].

Jakus et al. (2016), introduced 3D-printed PLGA/HA (referred to as hyperelastic bone) templates and tested them in rat spinal fusion [133]. Although these templates showed promising mechanical and processing properties, and apparent new bone formation within the porous templates, templates loaded with BMP-2 showed twice the amount of new bone formation. When these PLGA/HA hyperelastic bone templates were applied in a single case study in baboon (primates) CBD (4 x 4 cm), some bone ingrowth was observed at the defect interface after 4 weeks, but the template was invaded with soft tissues [133]. On the other hand, in a recent pilot study in a segmental defect in a sheep model, an axial vascular pedicle was essential, combined within the structure of a 3D-printed CaP template, to disclose an obvious increase in the amount of bone regeneration [63]. With reference to development of the next-generation of BTE templates, there are multiple challenges, not least the need to maximize the osteoconductivity of the templates, and to control pore size/structure and biodegradation and mechanical properties.

1.6. Rationale

Although TE is intended to solve the tissue donor shortage, at present the cell-based or GF-delivery strategies are hindered by various technical, financial and safety challenges, which limit their widespread and efficient application. Biomaterials are essential to support BTE through the production of well-designed, osteoconductive and off-the-shelf templates.

The effect of pore size and connectivity on BTE needs to be identified and clarified. The osteoconductivity of new copolymers and blends needs to be studied and/or boosted. Moreover, in addition to being degradable and easy to process, BTE templates should also have adequate mechanical strength.

Among the current options for processing biomaterials, 3D-printing shows promise, with advanced and accurate control of the pore structure, balanced with the mechanical resistance of the material. This provides the advantage of versatility of the materials used and reproducibility in production, even of complex structures.

2. Aim of the thesis

The overall focus of this thesis was to fabricate 3D-printed templates from selected polymers, with enhanced osteoconductivity. The selected polymers (PCL or PLATMC) were blended with other components (e.g. GL or HA) at different ratios in order to increase their osteoconductivity. Physical properties were tested for each of the fabricated templates, while the *in vitro* biological assessment aimed to compare their osteoconductivity using BMSCs. Furthermore, the *in vivo* model included host response assessment in the subcutaneous model, while the bone regeneration assessments was based on CBD in rabbit, as a non-load bearing defect in a relatively large animal model.

Specific goals:

1. To review the impact of 3D-printed templates, made of different biomaterials and their pore structures, on bone regeneration in CBDs (Study I).
2. To boost the osteoconductivity of 3D-printed PCL templates, by blending with GL at various ratios (Study II).
3. To compare the osteoconductive potential of 3D-printed PLATMC and PCL (Study III).
4. To enhance the osteoconductivity of 3D-printed PLATMC, by blending with HA at various ratios (Study IV).
5. To characterize the bone regeneration capacity of the 3D-printed polymer-based templates in the CBD model in rabbit (Studies III and IV).

3. Materials and methods

3.1. Methodological considerations and workflow

The approach in the thesis was to fabricate 3D-printed polymers, modified for BTE, based on the best-defined parameters. After a systematic literature review, the proper 3D-structure parameters and materials properties required for an effective BTE template were recorded, while the role of various biomaterials was defined [126].

Two synthetic polymers were selected, to be modified, printed and tested. PCL, with adequate mechanical properties and facile printability, was found to be the most successfully printed template for BTE: it was blended with GL at different ratios. On the other hand, in comparison with PCL, PLATMC was found to have higher mechanical properties and potential to support MSC attachment and proliferation. 3D-printed templates of PLATMC blended with HA, at different ratios, were developed. All the templates were assessed for their osteoconductive potential *in vitro*.

For *in vivo* assessment, the CBD model was the *in vivo* model most frequently cited in the literature for testing the osteoconductive potential of BTE templates: the lack of direct mechanical stresses [77] and accessibility (simple application) make it reproducible [126]. The rabbit model was chosen, as a relatively large animal model compared with the frequently used rodents, with abundance of reports in the literature of bone regeneration outcomes [126]. 3D-printed PCL, PLATMC and PLATMC/HA templates were tested for their host response in the subcutaneous model and for their osteoconductive potential in CBD in rabbits. The three main phases of this project and the corresponding four studies formulated from the collected data are summarized in Figure 8.

3.2. Materials

All the materials used in this thesis project are listed in Table 1, while the devices used are listed in Table 2.

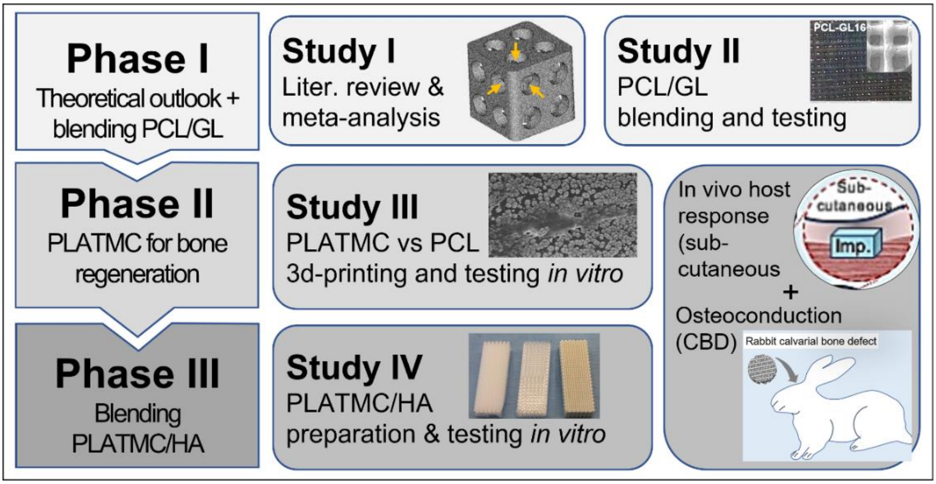

Figure 8: Schematic summary of the study design followed in the thesis.

Table 1: List of the materials used in the thesis project

Materials	Specifications	Supplier	Study
Acid Fuchsin stain	2% solution, pH = 6	Merk, Germany	Study IV
AlamarBlue reagent	Cell viability reagent	Invitrogen, USA	Study III
Alizarin-Red S		Sigma-Aldrich	Study II-IV
Calcium Assay Kit	ab102505	abcam, UK	Study IV
cDNA Rev. transc. kit	High-Capacity cDNA	Applied Biosystems	Study III
Cetylpyridinium Chl.	C0732-100G	Sigma-Aldrich	Study II-IV
Dexamethasone		Sigma-Aldrich	Study II-IV
Dimethyl sulphoxane	(DMSO)	Sigma-Aldrich	Study IV
EDTA solution (10%)		Merk, Germany	Study IV
Ethanol		Sigma-Aldrich	Study II-IV
Ethyl acetate		Sigma-Aldrich	Study II
Fetal bovine serum		Sigma-Aldrich	Study II-IV
Gelatin	Type B (Bovine skin)	Sigma-Aldrich	Study II
Genipin		Wako Chemicals	Study II
Glacial Acetic acid		Sigma-Aldrich	Study II

Hydroxyapatite	<200 nm particle size	Sigma-Aldrich	Study IV
Instant adhesive	Loctite 424	Henkel, Sweden	Study III,IV
Ketamine hydrochlor.	50 mg/ml	Trittau, Germany	Study III,IV
Poly(lactide-co-trimethylene carbonate)	Resomer LT 706 S (medical grade)	Evonik, Germany	Study III,IV
L-ascorbic acid 2-pho.	A8960-5G	Sigma-Aldrich	Study II-IV
Live/Dead assay kit	Kit for mammal. cells	Invitrogen, USA	Study IV
Low adherent plates	TC 48 well plate	Sarstedt, Germany	Study II-IV
Master mix	TaqMan Fast Universal	Applied Biosystems	Study III
MEM Alpha (α-MEM)		Gibco, UK	Study II-IV
PBS (Sterilized 1x)		Gibco, UK	Study II-IV
Penicillin-streptomycin	(PS)	HyClone, Austria	Study II-IV
PicoGreen	dsDNA assay kit	Invitrogen, USA	Study II-IV
Plastic embedding	Technovit® 9100	Kulzer, Germany	Study IV
P-nitrophenyl phosph.		Sigma-Aldrich	Study III,IV
Polycaprolactone	Mn: 80,000	Sigma-Aldrich	Study II
Polycaprolactone	Resomer C 212 (medical grade)	Evonik, Germany	Study III,IV
RNA extraction kit	Maxwell simplyRNA	Promega, USA	Study III
Sodium Hydroxide	(NaOH)	Sigma-Aldrich	Study II
Toluidine blue	1% solution, pH 10	J.T.Baker, UK	Study IV
Trypsin/EDTA		Lonza, USA	Study II-IV
Xylazine	Xyla-Ject	Adwia, Egypt	Study IV
Xylene		Sigma-Aldrich	Study IV
β-glycerol phosphate	BioUltra, for cell culture	Sigma-Aldrich	Study II-IV

Table 2: List of devices and equipment used in the thesis project

Device	Specifications	Manufacturer	Study
3D-Bioplotter	Manufacturer Series	EnvisionTEC, Germany	Study II-IV
Balance	TE 1245	Sartorius, Germany	Study II-IV
Cell counter (Auto.)	Countess	Invitrogen, USA	Study II-IV
Contact angle meas.	SL200A type, OCA	Dataphysics, Germany	Study II
Contact angle meas.	Goniometer Model 90	ramé-hart, USA	Study III,IV
Cut-off machine	Accutom-100	Struers, Denmark	Study IV
Drying oven		Termaks, Norway	Study II-IV
Fluorescence micro.	Eclipse Ti	Nikon, Japan	Study IV
Magnetic stirrer	RCT basic	IKA, Germany	Study II-IV
Mechanical testing	858 Mini Bionix II	MTS, USA	Study II-IV
Microplate reader	Varioskan™ LUX	Thermo Fisher, Finland	Study III,IV
Microplate reader	FLUOstar Optima	BMG Labtech, UK	Study II
Microscope camera	LEICA MC170 HD	Leica, Singapore	Study II-IV
Nanodrop	ND-1000 Spectro.	Nanodrop Tech, USA	Study III
qPCR System	StepOnePlus ™	Applied Biosystems	Study III,IV
SEM + EDX	Phenom XL Desktop	Thermo Fisher	Study III,IV
SEM	JSM-7400F	JEOL, Japan	Study II
Stereo microscope	LEICA M205 C	Leica, Germany	Study II-IV
Thermal cycler	SimpliAmp	Applied Biosystems	Study III
µCT	SkyScan 1172	Bruker, Belgium	Study II-IV

3.3. Systematic review and meta-analysis (Study I)

3.3.1. Systematic search strategy

To review the impact of materials used and the parameters required for 3D-printed templates intended for BTE, an initial database search was conducted in mid-September 2017. The search covered articles published in relevant peer-reviewed journals in PubMed/MEDLINE and the web of Science (ISI). All titles and keywords combining 3D-printing and bone regeneration in CBD were identified. Only research papers on resorbable/biodegradable polymers, ceramics and their blends/composites were included.

The database collection strategy was kept broad to avoid the exclusion of any relevant papers. After extensive follow-up and readings, more collective keywords were added and an updated "search key-words" list was prepared as follows: ((rapid prototyping OR 3D print* OR three-dimensional print* OR three-dimensional fabrication OR bioplotting OR additive manufactur*)) AND ((degradable OR biodegradable OR resorbable) AND / OR (template OR template OR membrane) NOT (titanium OR Ti)) AND ((bone) AND (regeneration OR augmentation OR repair OR reconstruction OR tissue engineering) AND (calvari* OR craniofacial OR cranial) AND (in vivo OR animal)).

The search was repeated on January 16th 2018, in order to include all relevant published or in-print papers up to the end of 2017, resulting in 52 papers. Further recently published relevant studies, dated in 2018 or later, were not included in the systematic review [99,148,149,150]. The inclusion of research papers was site-specific to CBD. On the other hand, all studies based on non-porous [151], or non-degradable (e.g. Ti, PEEK, etc.) biomaterials, or those with poorly-documented methodologies [37] were excluded, as well as experimental [133] or clinical [107] trials.

3.3.2. Data extraction and meta-analysis study

According to PRISMA guidelines for systematic research [152], the key information data were extracted from each included study, including the **p**opulation, **i**nterventions, **c**omparators, **o**utcomes, and **s**tudy design; abbreviated as PICOS. The type and number of animals used were denoted as "population" while the template composition and design/porosity were denoted as the "intervention" factors. The animal models were categorized according to species, while the time points of bone regeneration assessment were established as a proportional factor to understand the "outcome" results.

Additional inclusion criteria were considered to minimize data heterogenicity in the meta-analysis study, and a checklist was prepared (Table 3) to evaluate the relevance of the included studies to extract the required quantitative data. Finally, the effect size of new bone formation per each template group (type) was calculated per each time point for both rabbit and rat models.

The template porosity% and the mean NBA/TDA ± standard deviation (SD) were recorded from each study per each time point, where NBA represents the area of newly formed bone in histomorphometric analysis, and TDA represents the total defect area. After thorough reading of each included study, any uninformed numbers of these parameters were either digitally measured directly from the graphs (e.g. bar charts, box plots, etc.) [77] or calculated from the printing parameters (e.g. macro-porosity %) [153].

Table 3: Check lists of the studies included in the meta-analysis.

Main check list for studies included in the meta-analysis	**Additional check list to achieve homogenous data analysis**
3D-printed template (resorbable) Calvarial bone regeneration *In vivo* animal model Defined study parameters and number of animals (n)/group Histomorphometric quantification (from histological sections) Defined type of printed material(s)	Excluding printed membranes (GTR) Excluding printed particle templates Excluding added biological factors Excluding partial-thickness defects Excluding micro-computed tomography (µCT) histomorphometry

3.4. Polymer modifications and template printing (Studies II-IV)

All the polymers (as received or modified) were printed using a 3D-Bioplotter (melting-extrusion, pneumatic) with nozzle diameter = 0.4 mm. In addition, they all had a fixed inter-strand distance (0.3 mm) and were printed at 0/90° angles between layers.

3.4.1. Preparation of PCL/GL blends (Study II)

PCL pellets (6.125 g) were dissolved in a trisolvent mixture (10 ml); glacial acetic acid, ethyl acetate and water in 3:2:1 ratio, before being printed. PCL was mixed with GL in four ratios (2, 4, 8 and 16 (w/w)% GL) in the trisolvent mixture. For the 2% blend ratio (PC/GL2), 0.125 g of GL was dissolved in 10 mL of trisolvent mixture (45 °C, 2 h, stirring). PCL pellets (6 g) were then added, at continuous stirring (overnight) to achieve uniform blending. The other three blends (PCL/GL4, PCL/GL8 and PCL/GL16) were prepared by changing the percentage of GL added to the solution. To remove air bubbles from the formed gels, the blends were sonicated (1 h) then directly incubated at 37 °C (2 h) before being printed.

3.4.2. Printing of PCL/GL (Study II)

Direct non-melting-extrusion was applied to print PCL/GL, where the printed structures were set, based on solvent evaporation. The speed of the printing was set at ±30 mm/s, to print 4 layered sheets (~1.3 mm thickness). After printing, the templates were punched out (Ø = 8.5 mm), and dried before being immersed in genipin (1%) for crosslinking, then neutralized with NaOH solution (0.1 N), washed and finally lyophilized.

3.4.3. Printing of PCL and PLATMC (Study III)

Medical grade PCL and PLATMC were printed by melting-extrusion, as shown in Table 4. The physical and biological properties of relevance to their osteoconductive potential were evaluated in both 3D-printed polymers.

Table 4: The average printing parameters of PCL vs PLATMC

Polymer	Pressure	Temperature*	Printing speed	Printing time (total)	Feed /syringe
	(bar)	(°C)	(mm/sec)	(min)	(g)
PCL	8.4	110	1.6	360	3.5
PLATMC	8.0	195	2.0 - 5.0	85	3.0
*Polymers were pre-heated for 15 min, at 15-25 °C above the actual recorded temperature.					

3.4.4. Preparation of PLATMC/HA blends (Study IV)

A physical suspension method was used to blend PLATMC and HA at different ratios: 10, 30 and 50 (w/w)% HA [154], where dimethyl sulphoxane (DMSO) was used as a solvent (80 °C, 2 h, stirred). Dispersed HA in DMSO was sonicated (30 min.), before being added to PLATMC solution, under stirring (1 h); then the solution was drop-wise precipitated in distilled water (dH_2O) (Figure 9). PLATMC/HA beads were then washed (2h), dried, and lyophilized before yield calculations.

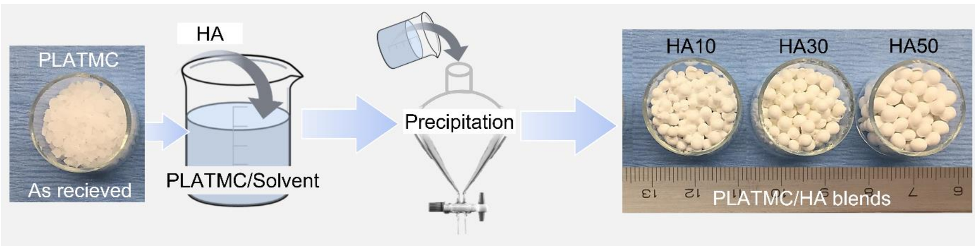

Figure 9: Schematic presentation of the preparation methods of PLATMC/HA blends.

3.4.5. Printing of PLATMC/HA blends (Study IV)

PLATMC/HA blends were printed with adjustable printing parameters as shown in Table 5. Templates were printed in sheets (30x30 mm) then punched out or cut to the required diameter. For the *in vitro* (cell seeding) studies, the 3rd and 4th layers were shifted and centered to fill the inter-distance between strands in the first 2 layers, in order to increase the seeding efficiency of the scaffolds as stated in Table 6.

Table 5: Average printing parameters of PLATMC/HA blends

Blend	Pressure	Temperature*	Printing speed	Printing time (total)	Feed /syringe
	(bar)	(°C)	(mm/sec)	(min)	(g)
HA10	8.0	200	4.5	85	2.7
HA30	8.0	205	2.5	105	3.1
HA50	8.0	210	2.5	70	3.1
*All blends were pre-heated for 15 minutes before printing at 15-25 °C above the actual recorded printing temperature.					

Table 6: Size and specifications of the 3D-printed templates (Studies III and IV)

	Layers number	Shifted layers	Thickness	Diameter (Ø)
			(mm)	(mm)
In vitro	4	Yes	1.3	8
Subcutaneous	13	No	4	4x5
Calvarial defect	6	No	2	9

3.4.6. Sterilization of templates before biological assessment

The templates used for biological characterization (*in vitro* and *in vivo*) were sterilized through immersion in ethanol (70%) plus sonication (10 min, twice). The ethanol was then aspirated in a biosafety cabinet, followed washing with PBS (twice), drying and exposure to UV (1 h). The templates were then packed in sterile bags and refrigerated (4 °C) for later use.

3.5. Template physical characterization (Study II-IV)

All the methods used to characterize the physical and biological properties of the printed templates are listed in Table 7, per each study.

Table 7: Summary of the main methods used in the experiments.

Methods			**PCL/GL blend**	**PCL vs PLATMC**	**PLATMC /HA blend**
			Study II	Study III	Study IV
Modification method		As received		×	
		Tri-solvent mixture	×		
		Drop- precipitation			×
Extrusion printing		Non-melting	×		
		Melting		×	×
Physical characterization		Wettability	×	×	
		Mass-loss (degrad.)		×	×
		Ca-release			×
		Mechanical	×	×	×
In vitro osteogenic differentiation	Seeded cells type	Rat-BMSCs	×		
		Human-BMSCs		×	×
	Viability and Prolifera-tion	Seeding efficiency		×	×
		AlamarBlue assay		×	
		DNA quantification	×	×	×
		Live/Dead staining			×
	Different-iation and ECM secretion	SEM	×	×	×
		Gene expression		×	
		ALP		×	×
		Alizarin red stain	×	×	×
In vivo assessment (rabbits)		Subcutaneous impl.		×	×
		CBD		×	×

3.5.1. Wettability test (Studies II - IV)

To determine their wettability, the water contact angle test was applied (at RT) to the blends, prepared either as flat discs or 3D-printed. Water (3 μL) was dropped onto the surface of each sample and the average contact angle was recorded (for triple measurements) at various positions on the surface.

3.5.2. Mass-loss (degradation) test (Study III, IV)

Printed samples from PCL, PLATMC and PLATMC/HA blends (Ø = 8 mm, n = 5) were precisely weighed precisely (W_o) then added in PBS (900 µL/sample) to sealed 48 well plates, then incubated (37 ºC, shaking at 100 RPM). The PBS was replaced by a fresh preparation every 5 days, up to 100 days. The mass change was recorded at 15, 30, 60 and 100 days, where the samples were washed, dried, frozen (overnight) and freeze-dried before being weighed (W_t). The Mass loss (%) was calculated according to the following equation [155], where W_o is the original weight of each template before immersion in PBS, and W_t is the dry weight recorded at each time point.

$$Mass\ loss\ (\%) = \frac{(W_o - W_t)}{W_o} \times 100$$

Tested samples at 1, 60 and 100 days were observed with SEM to determine signs of surface erosion and degradation. Samples were sputter coated (gold-platinum) and observed with SEM, by a secondary electron detector at 10 kV.

3.5.3. Calcium release monitoring (Study IV)

The Ca release from 3D-printed PLATMC/HA blends (n = 4), incubated in PBS (1 mL/sample, 37 ºC, shaking at 100 RPM) was recorded up to 100 days. PBS was aspirated at 1 h, then at 1, 2, 3, 4, 5, 7, 9, 15, 30, 50 and 80 days and replaced with freshly prepared PBS at each time point, while PLATMC samples were recorded as baseline. The Ca concentration in aspirated PBS was quantified by a calorimetric Ca assay kit compared to a standard Ca concentration [116], according to the manufacturer's recommendations, at absorbance = 575 nm. The released Ca (quantified values from the standard curve in µg) was then multiplied by the dilution factor and divided by the average weight of samples to calculate the amount of Ca released per unit mass template (µg/g).

3.5.4. Mechanical characterization (Studies II - IV)

Dumbbell-shaped samples (shaft dimensions = 17.5 × 4.5 × 1.5 mm L×W×H) were printed according to ASTM-D638 to test the mechanical properties of each group. The tensile stress, Young's modulus and elongation at failure were tested using a universal mechanical testing machine, at room temperature, and rate of tensile displacement at 3mm/sec.

3.6. *In vitro* osteogenic differentiation assessment (Studies II-IV)

3.6.1. Ethical approvals (Studies II - IV)

1. The rat-BMSCs used had previously been isolated at the Tissue Engineering Group lab., University of Bergen (UiB), with the approval of the Norwegian Animal Research Authority (local approval number 20146866) and kept frozen in liquid nitrogen (passage 2).

2. The human-BMSCs (hBMSCs) used were extracted from donated bone marrow aspirates (10 ml) from the anterior iliac crest of 8-14 years old patients, undergoing iliac crest surgery for cleft lip and palate repair at the Department of Plastic, Hand and Reconstructive Surgery, National Fire Damage Center, Bergen – Norway, and were obtained by informed parental consent. Ethical approval for this study was granted by the Regional Committee for Medical and Health Research Ethics (REK) in Norway (Ref. No. 2013/1248/REK sør-øst C). Human-BMSCs were isolated from bone marrow aspirates and characterized according to Samih et al. (2019), at the Tissue Engineering Group lab., UiB and kept frozen in liquid nitrogen (passage 2).

3.6.2. Rat-BMSCs seeding (Study II)

Frozen Lewis rat BMSCs were thawed in Minimum Essential Medium Alpha (α-MEM), supplemented with 1% (v/v) penicillin-streptomycin, and 10% (v/v) fetal bovine serum (FBS). The sterilized templates were prewetted (in 100 μL α-MEM/template) for at least 8 hours before being seeded with rat BMSC (passage 3).

The cells (at 85% confluence) were first trypsinized (Trypsin/EDTA) and counted using an automated cell counter. Subsequently, the cells were seeded onto PCL and

PCL/GL templates (1×10^5 cells/ scaffold) in 48-well plates (low adherent) and incubated (37 °C in 5% CO_2) for up to 21 days. Osteogenic medium (0.1 mM L-ascorbic acid 2-phosphate, 10 mM β-GP, and 100 nM dexamethasone) were added to the culture medium (after 24 h) and changed twice weekly. Accordingly, cell/template interactions were assessed at different time points, in terms of attachment, proliferation and differentiation as noted.

3.6.3. Human-BMSCs seeding (Studies III-V)

Frozen hBMSCs were treated and seeded the same as described earlier for the rat-BMSCs. The seeding efficiency of hBMSCs on printed PCL, PLATMC and PLATMC/HA was calculated 8-12 h after seeding. The seeded templates were transferred to another plate, and the remaining cells, attached and suspended cells per each well, were collected in 1.5 mL tubes, centrifuged, and resuspended in 100 µL α-MEM, and counted. The seeding efficiency was calculated using the following equation:

$$Seeding\ Efficiency\ (\%) = \frac{(\text{Seeded cells} - \text{Remaining cells})}{\text{Seeded cells}} \times 100$$

3.6.4. AlamarBlue (Study III)

In this test the cell viability and activity were assessed by using the reducing power of living cells to AlamarBlue reagent (resazurin-based), to quantitively measure viability. The reagent (30 uL) was directly added to the cells in culture medium (300 uL) according to the manufacturer's directions. The plates were incubated (protected from light), and control (background) samples were used containing culture media only. 100 µL (in duplicates) were then aspirated and added to 96 well plates to read "immediately" fluorescence (excitation/emission = 560/590 nm). The results were evaluated after subtracting the background fluorescence of the negative control samples.

3.6.5. Proliferation assay (DNA quantification) (Studies II – IV)

DNA quantification was assessed using a PicoGreen assay kit in cell lysis solution (0.1% Trition X-100, 300 µL), frozen (at -80 °C) and thawed (twice). Thawed samples were cut into pieces, added to lysate solution, sonicated (10 min, on ice), vortexed (1200 RPM, 10 sec) then finally centrifuged for 1-2 min at 10,000 RPM. From the supernatant, 50 µL were aspirated and mixed with diluted dye (according to the manufacturer's protocol). The intensity of fluorescence was measured at excitation/emission = 485/520 nm, and the cellular dsDNA content was calculated against a standard curve of known concentrations of DNA (ug/mL).

3.6.6. Live/Dead staining assay (Study IV)

A stock solution of PBS containing Ethidium homodimer-1 (red, 2 µL/mL) and Calcein AM (green, 1 µL/ml) was prepared and vortexed. Seeded templates were washed (PBS) to remove remnant media and serum, before the stock solution (300 uL) was added to cover the seeded templates, and incubated (30 min, RT, shaking at 100 RPM). The cells were then viewed under a fluorescence microscope at excitation/emission; Calcein AM = 494/517 nm and Ethidium homodimer-1 = 528/617 nm. At least 10 images were recorded and stacked at 10 µm z-distance.

3.6.7. SEM (Studies II - IV)

To determine cell attachment and ECM deposition, seeded samples (at 3 and 14 days) were prepared for SEM. The samples were fixed in glutaraldehyde solution (2.5%, pH 7.2) for 30 min, then dehydrated through a graded series of ethanol solutions (70, 80, 95, and 100%) for 10 min/each. The specimens were then mounted on aluminum holders, sputter-coated (gold-platinum) and examined by SEM by secondary electron detector at voltage of 10 kV. The ECM surface was examined for the presence of Ca and P ions, identified by Energy Dispersive X-ray (EDX) (studies III and IV), at a working distance 5.5 mm.

3.6.8. Gene expression analysis (Study III)

The real-time quantitative polymerase chain reaction (qPCR) technique was used to analyze the osteogenic gene expression of extracted RNA from seeded cells (n = 5), using an RNA extraction kit. The amount of RNA was measured using Nanodrop, then cDNA was synthesized through reverse transcription polymerase chain reaction (RT-PCR) using cDNA reverse transcription kit and a thermal cycler. qPCR was completed using a master mix and qPCR system. Each sample was assessed in duplicate, relative to an endogenous control; glyceraldehyde-3-phosphate dehydrogenase (GAPDH) gene (Table 8). The difference in threshold cycle value (△Ct) was equal to Ct gene minus Ct GAPDH. The mRNA in each sample was calculated using the comparative △△Ct (△Ct gene - △Ct control). The data were analyzed by the $2^{-\Delta\Delta CT}$ method and relative transcript levels were presented as fold change (in Log scale) relative to the control group for each study.

Table 8: List of genes assessed in the thesis experimental work

Gene and code	Name	Role
GAPDH Hs02758991_g1	Glyceraldehyde-3-phosphate dehydrogenase	House-keeping gene
Runx-2 Hs01047973_m1	Runt-related transcription factor 2	Early osteogenic marker (for osteoblast differentiation)
ALPL Hs01029144_m1	ALP; Alkaline phosphatase, liver/bone/kidney	Early to intermediate osteogenic marker
COL1A2 Hs00164099_m1	COL1; Collagen, type I, alpha 2	Early to intermediate osteogenic marker
BMP-2 Hs00154192_m1	Bone morphogenetic protein-2	Early to intermediate osteogenic marker
SPP1 Hs00959010_m1	Osteopontin	Late osteogenic marker
BGLAP Hs01587814_g1	Osteocalcin; Bone gamma carboxyglutamate protein	Late osteogenic marker

3.6.9. ALP activity assessment (Studies III, IV)

ALP secretion from the seeded hBMSCs was assessed as one of the osteogenic ECM components. The ALP activity was measured from the cell lysate supernatant from the DNA quantification assay. P-nitrophenyl phosphate (pNPP) was added (1:1) to lysate solution and the absorbance was measured at 405 nm (at continuous intervals; 5, 10 and 15 min.). The represented figures were normalized to cell number, as determined by the proliferation assay.

3.6.10. Alizarin red staining (Studies II - IV)

The amount of calcified ECM in the seeded samples was assessed by Alizarin red staining (2% in dH_2O at pH = 4.2) at 21 days, to measure Ca deposition on the printed templates. The samples were fixed, washed and kept drying until enough stain was added to cover each sample. The samples were incubated (10 min.), washed (dH_2O, 5-6 times, overnight), followed by ethanol (70%) overnight and aspirated dry. The dried samples were imaged by a stereo microscope using a mounted microscope camera. For the quantification calculations, the dye was extracted by immersing in cetylpyridinium chloride (100 mM) solution, and incubated (overnight, shaking). The optical density (OD) of the extracted dye was measured (in duplicates) at 544 nm (absorbance), using a microplate reader. Samples from Studies III and IV were diluted (1:7) to obtain relevant absorbance readings.

3.7. *In vivo* host response and bone regeneration assessment

3.7.1. Ethical approvals

The *in vivo* studies, subcutaneous implantation and CBD, were conducted on New Zealand white (NZW) rabbits, at the Institute of Graduate Studies and Research (IGSR), Alexandria University – Egypt. The animal experiment protocol was reviewed and accepted by the Institutional Animal Care and Use Committee (IACUC) - Alexandria University, Approval no. AU14-191013-2-5.

3.7.2. Subcutaneous implantation (Study III)

Three NZW adult male rabbits (3-4 months old) were used in this study, where 3D-printed PCL and PLATMC templates were implanted subcutaneously into the dorsal area of each rabbit. The rabbits were anesthetized by Xylazine (10mg/kg, IM) and Ketamine (25mg/kg, IM) then the dorsal area was shaved to ensure 5-6 cm space between samples, before being disinfected with povidone iodine (Figure 10). The incision lines were made on both sides, around 3 cm away and parallel to the midline followed by subcutaneous dissection to form pouches to receive one of the pre-sterilized 3D-printed samples. The incision was then sutured and the position of each sample was marked with cutaneous sutures (Figure 10). Samples were retrieved at 8 weeks' post implantation.

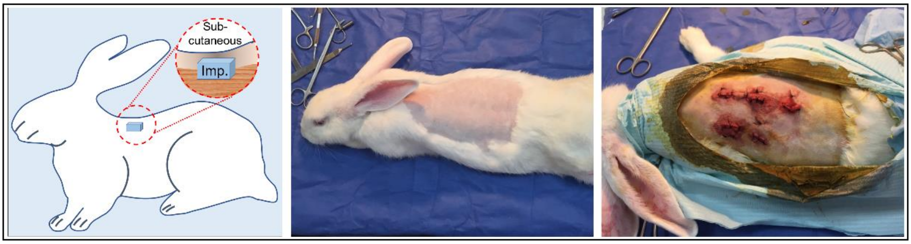

Figure 10: Surgical implantation of 3D-printed templates in subcutaneous pouches in NZW rabbit dorsum: (a) a schematic presentation of the subcutaneous implant position, (b) implant site preparation (shaved), and (c) the sutured pouches marking the sites of the implanted the 3D-printed templates.

3.7.3. Implantation in CBD model (Study III, IV)

To implement the CBD model, the rabbits were anesthetized and the surgical site (posteriorly from the coronal suture) was shaved with extended margins and wiped with Povidone-iodine. An incision line (3 - 4 cm long) was made on the crest of the sagittal suture and skin and periosteum were elevated. Two bone defects (Ø = 9 mm) were created (bilateral) by a trephine bur, on each rabbit calvarium, followed by the implantation of the prepared templates (2 mm thickness; 6 layers) of the exact defect diameter (Figure 11). In total, 24 skeletally-adult male NZW rabbits were used in this study, where one of five groups of 3D-printed templates; PCL, PLATMC and PLATMC/HA (10, 30 and 50) was implanted in each defect (in random order), in addition to an empty defect group (n = 8).

The surgical wound was closed in layers; the subcutaneous layer was closed with vicryl (3/0) resorbable sutures and the skin layer was closed with silk (3/0) sutures. To prevent further site contamination, topical antibiotic (Gentamicin) was applied to cover the surgical site. Immediately after the surgery, a pain killer (diclofenac sodium, 5 mg/kg, IM) was administrated daily (for the first 3 days after surgery). The silk sutures were removed after 1 week. The rabbits were euthanized after 4 and 8 weeks (n = 4 /time point/group). Collected bone samples were fixed, dehydrated, and processed for μCT and histological analysis.

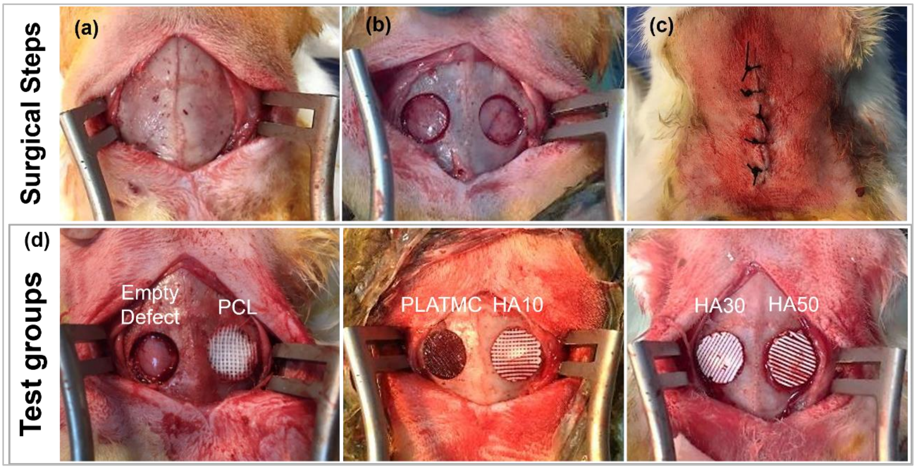

Figure 11: Surgical steps in implantation of 3D-printed templates in CBD in rabbits. (a-c) photographs of the surgical incision, the trephined defects (Ø = 9 mm) and closure of surgical wound, respectively. (d) photographs of the experimental groups (6 groups) included in the *in vivo* study.

3.7.4. Micro-computed tomography characterization

The amount of calcified bone formation within the implanted templates was analyzed by µCT. This was followed by sectioning of samples and staining for histological examination and histomorphometric (quantitative) analysis.

3.7.5. Histological processing

3.7.5.1. Processing of non-decalcified samples

Non-decalcified bone samples collected from CBD were processed for plastic embedding and histomorphometric analysis. After fixation and dehydration steps, the samples were pre-infiltrated in 3 series steps according to the plastic embedding protocol. The final embedding step was done using the polymerization mixture (well-stirred, at freezing temperature and vacuum). Polymerization was completed in approximately 24 h. Each sample was then trimmed and clamped on a high-precision cutting machine and five serial sections (around 60 µm thickness and 560 µm apart) were cut at the coronal third of the bone defect (glued onto plexiglass slides), followed by grinding and polishing of the cut surface up to 40 µm thickness. The sections were then stained with Toluidine blue (1%) and Acid Fuchsin (2%) before being scanned and the area of interest (AOI) was subjected to histomorphometric analysis.

3.7.5.2. Processing of decalcified samples

Subcutaneous implanted samples were directly processed for paraffin embedding. However, in the case of CBD samples, the plastic embedding of the un-cut half of each sample was then dissolved using xylene/chloroform solvent (1:1 for 3-5 h, shaking) followed by rehydration of the samples, decalcification in EDTA solution (10%, 4 weeks, changed twice/week), then rehydration and paraffin embedding. The samples were then sectioned (5 µm sections) and stained with Masson's Trichrome.

3.7.6. Histomorphometric analysis

Images for AOI of non-decalcified histology slides were analyzed using NIS-Elements Software (Nikon, Japan). In general, the total region of interest (ROI) was marked, from both edges of the template/defect, then the template area was calculated. The available defect area (ADA) was calculated as follows: ADA = Total ROI – template area. The sum of NBA within the defect was measured and the total regenerated bone was calculated as NBA/ADA (%). The mean of the middle three sections in each sample was calculated, and the mean of each group (n = 4) was presented.

3.8. Data presentation and statistical analysis

For Studies I and II, STATA software (Ver. 15.1; StataCorp LLC, TX, USA) was used for statistical calculations. In Studies III and IV, Prism software (GraphPad software, San Diego, CA, USA) was used for the statistical analysis and to draw the required graphs. Except for the meta-analysis study, all the results were expressed as group average ± standard deviations. For multiple group comparison, two-way analysis of variance (ANOVA) was applied. However, for comparisons of only two groups (Study III) one-way ANOVA was used to detect significant differences. The null hypothesis was rejected at p-value < 0.05, and Tukey's post hoc adjustment was used in all data comparisons, except for PCR data, due to higher data variances, Bonferroni correction adjustment was used.

4. Summary results and discussion

4.1. Literature review and meta-analysis outcomes (Study I)

Only the data on rabbits and rats, with adequate histomorphometry data, were suitable for meta-analysis [126]. Only the results on rabbits are considered and discussed here. Of the 18 rabbit model studies identified by the systematic review, nine studies were excluded because they did not meet the inclusion criteria for the meta-analysis, either due to use of 3D-printed templates as guided tissue regeneration (GTR) membranes [156,157], or due to the unavailability of some essential quantitative data [68,77,79,104,105,134,158]. The remaining nine studies considered in the meta-analysis are described in Table 9, and the forest plots of the effect size are described in Hassan et al. 2019 [126]. The effect size of the printed templates was calculated after sorting the used templates into three subgroups, according to the class of biomaterials: polymers (e.g. PCL, PDTEC, PLGA, PPF), ceramics (e.g. BCP, CHA, CSi, DCPD, HA, Mg, TCMP and β-TCP), and their blends (abbreviations are shown in Table 9).

Regarding the polymer-based templates, polymer and blend templates, the overall estimate of the effect size for the printed polymer templates was calculated as NBA/TDA and showed a homogenous effect size at 8 weeks (NBA/TDA = 8.51 ±7.5), while the printed polymer templates with additional porosity showed a homogenous effect size at both 8 weeks (5.65 ±1.57) and 16 weeks (9.99 ±9.77) (Figure 12). In contrast, the blended 3D-printed templates showed a homogenous effect size at 8 weeks (21.39 ±7.79). It was consistently reported that the blended templates have a higher effect than polymer templates. Hence, the purpose of the experimental work phase was to prepare functionalized (blended) polymers (e.g. with GL or HA) which would produce more efficient 3D-printed BTE templates.

Table 9: List of studies included in the meta-analysis of the 3D-printed templates in CBD in rabbits.

Study	Template	Porosity	Additional Features	n	Defect Ø	Follow-up
		(%)	(%)		(mm)	(week)
Simon et al. 2003	PLGA(50)/β-TCP PDTEC	80-87 50 to 90	Macro-channels /Grid structure	6	8	8, 16
Roy et al. 2003	PLGA(50)/ β-TCP PLGA(95)/ β-TCP	80-87	Macro-channels	12	8	8
Roy et al. 2003	HA	45	Macro-channels	6	8	8
Alge et al 2012	PPF/DCPD	37	added MSCs	6	10	6
Shim et al. 2012	PCL/PLGA PCL/PLGA/β-TCP	60	--	6	8	4, 8
Dadseta et al. 2015	PPF/TCMP PPF/CHA PPF/BCP	60 Coats	Added BMP-2	4	15	6
Sun et al 2016	CSi, CSi/Mg6 CSi/Mg10 CSi/Mg14	62	--	8	8	6, 12
Shao et al. 2017	TCP CSi/Mg10 CSi/Mg10/β-TCP	60.1 52.1 57.8	--	6	8	4, 8, 12
Shao et al. 2017	CSi CSi/Mg6	± 59 ± 53	Double Pore Size	6	8	4, 8, 12
BCP, biphasic calcium phosphate; **BMP-2**, bone morphogenetic protein-2; **CHA**, carbonated hydroxyapatite; **CSi**, calcium silicate (Wollastonite); **DCPD**, dicalcium phosphate dihydrate; **HA**, hydroxyapatite; **Mg**, magnesium; **MSCs**, mesenchymal stem cells; **n**, number of defects/group/time point; **Ø**, bone defect diameter; **PCL**, polycaprolactone; **PDTEC**, poly(DTE carbonate); **PLGA**, poly(D,L-lactide-co-glycolide); **PPF**, poly(propylene fumarate); **TCMP**, magnesium substituted β-tricalcium phosphate; **β-TCP**, β-tricalcium phosphate.						

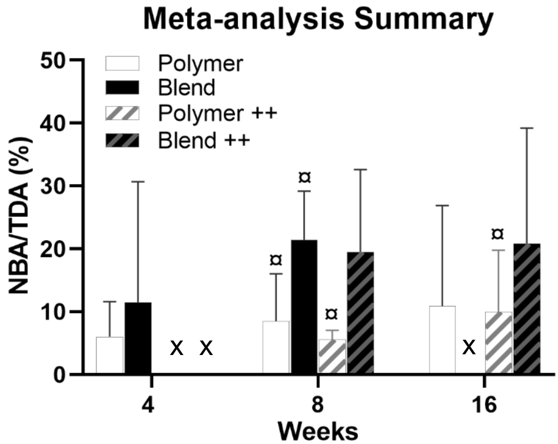

Figure 12 : Summary of the mean effect size (ES), and standard deviation of the meta-analyzed studies, for all the included 3D-printed polymer-base (polymer or blend) templates used in CBD in rabbits at 4, 8 and 16 weeks, measured as NBA/TDA. ++ indicates that the printed templates have additional porosity features, while ¤ indicates that the obtained data showed homogeneity, with I-square < 50%. (X) represents unavailable data.

4.2. PCL/GL blends showed enhanced osteoconductivity but compromised strength (Study II)

The aim of this study was to boost the osteoconductivity of PCL, by blending it with a biologically active natural polymer (e.g. GL), in the form of 3D-printed templates. The wettability of PCL gradually improved with increasing GL contents, where the contact angle decreased constantly from PCL (80°) to GL 16% (49°). However, with the inclusion of more GL within PCL, the tensile stress deteriorated. Pristine PCL showed high average tensile stress (6.25 MPa) while the average tensile stess of the PCL/GL blends was 4.60, 4.16, 3.33 and 1.33 MPa, at GL 2, 4, 8 and 16% respectively (Study 2). This decrease in the tensile stress of PCL/GL blends was probably related to the different solubilities of both polymers in the trisolvent mixture, with a tendency for GL to agglomerate into small spheroids, although being homogenously distributed across the printed templates.

On the other hand, the seeded rat-BMSCs showed varying cell-material interactions in their attachment and ECM production, at 3 and 14 days, respectively (Figure 13a and b). Cell attachment was found to increase with increasing GL percentage in the printed templates at 3 days. In addition, higher cell numbers were observed with ECM production over the template surface, especially in GL4, up to 16%, at 14 days. DNA quantification revealed increased proliferation rates, from 7 to 14 days, of the attached rat-BMSC, at GL4, up to 16% templates (Figure 13c). These results were in accordance with the reported markable cell (fibroblast) growth and proliferation on PCL/GL nanofibers sheets [159].

At 21 days, the Alizarin red stain, used to characterize calcified ECM production by the seeded cells on printed PCL/GL blends, revealed a linear quantitative increase in the detected calcification (color intensity), directly proportional to the increase in GL contents (Figure 13d-e). This could be related to the previously observed better cell attachment and proliferation directly proportional to GL content % in each template group. However, the compromised mechanical properties of PCL/GL blends, specially at high GL%, interfered with the lower limits of template manipulation and thus no further application was attempted *in vivo*. Therefore, the investigation now focused on the replacement of PCL with another polymer/copolymer, which could provide better mechanical and biological properties.

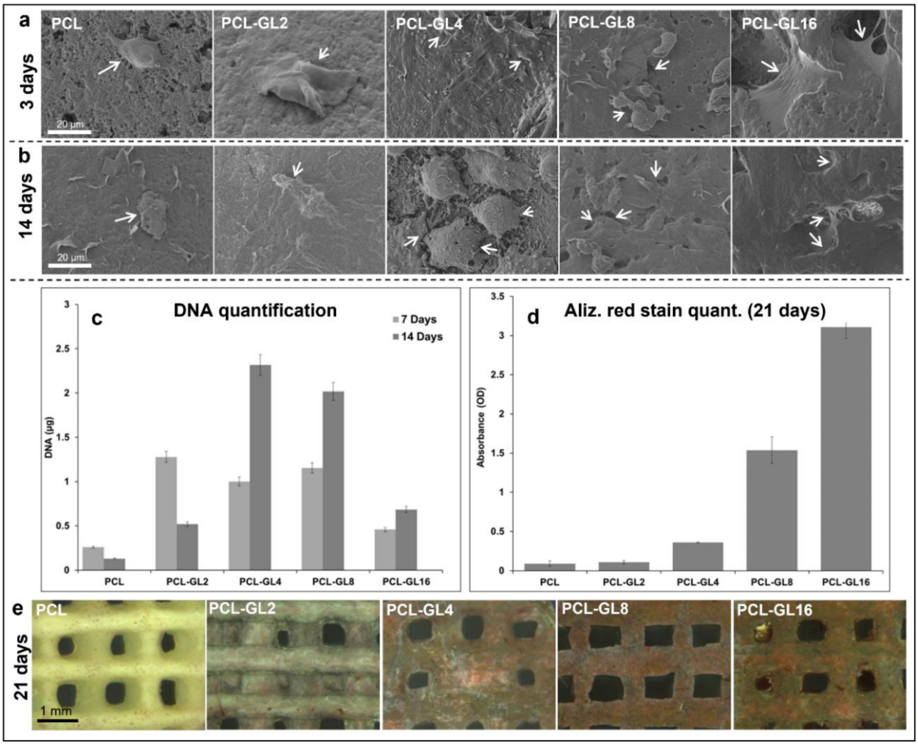

Figure 13: Figure caption next page.

Figure 13: Biological characterization of PCL/GL seeded with rat-BMSCs. SEM at high magnification at 3 (a) and 14 (b) days, showing the cellular attachments (white arrows). (c) proliferation of cells on the templates evaluated by DNA quantification (7 d and 14 d), while (d) and (e) represent the Alizarin red staining quantification (absorbance) and stained templates micrographs at 21 days, respectively.

4.3. PLATMC showed high strength, degradation and osteoconduction (Study III)

The wettability of PLATMC was significantly higher than PCL (Figure 14a) with a lower contact angle for both 3D-printed and cast sheet forms (Figure 14b and c). In addition, printed PLATMC revealed a 4-fold higher Young's modulus and 2-fold higher tensile stress than PCL (Figure 14d-f). On the other hand, at 100 days *in vitro*, PLATMC showed obvious signs of degradation: including both bulk and surface erosion degradation (Figure 15a), with significant mass-loss (6.21% ±3.39) (Figure 15b), compared to PCL (0.28% ±0.25). This property favors the use of PLATMC for BTE templates.

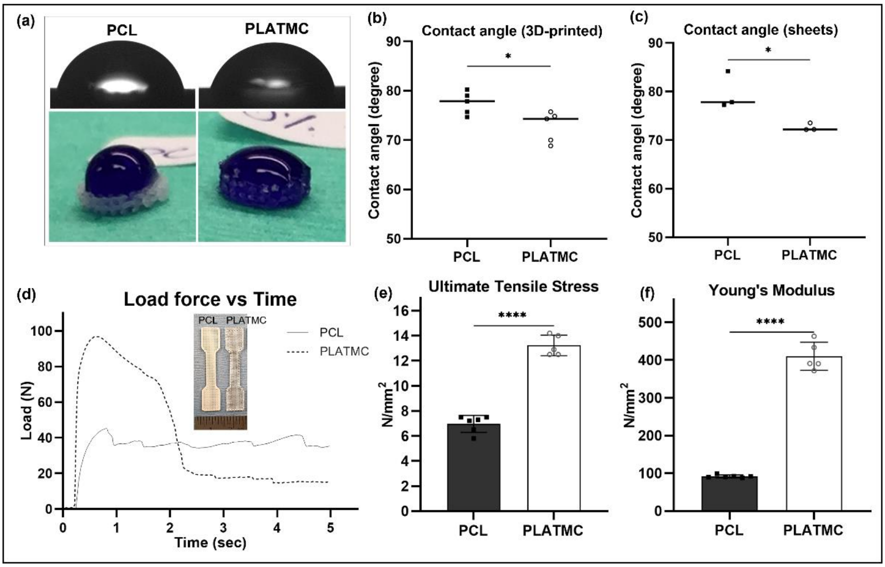

Figure 14: The wettability and tensile properties of 3D-printed PCL and PLATMC polymers. (a) represents a micrograph of contact angle measurements (top) and photographs for the wettability of both 3D-printed polymers shown by colored dH_2O (bottom), while (b) and (c) represents the measured contact angle of both polymers in 3D-printed and casted (sheet) forms. The tensile properties are shown as (d) the load force vs time curves, (e) Young's modulus, and (f) the calculated ultimate tensile stress (n = 5).

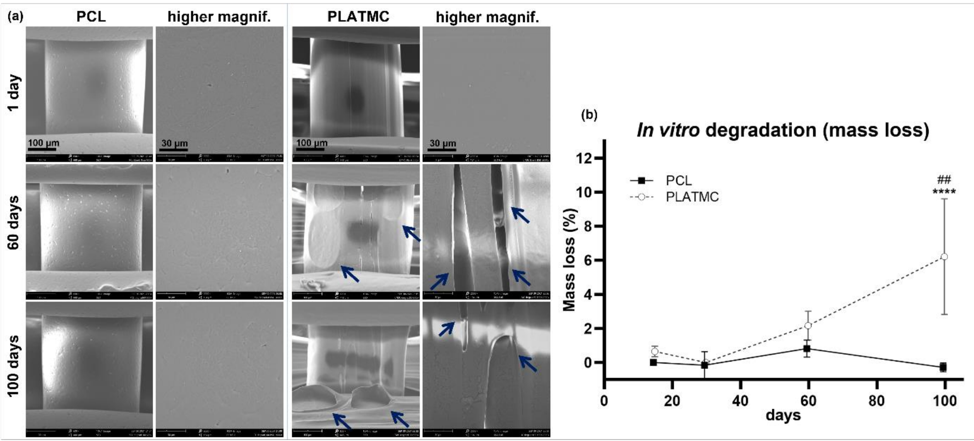

Figure 15: Summary of the characterized *in vitro* degradation of 3D-printed PCL versus PLATMC including: (a) SEM of the printed templates after 60 and 100 days, with signs of degradation of PLATMC marked with arrows, and (b) line-graph for the mass loss quantification; up to 100 days in PBS at 37 ºC. Statistical significance between each time point and the previous time point in the same group is marked with the hash symbol (#), while significance between the groups is marked with asterisks (*) at $p < 0.05$; **** $p < 0.0001$.

In vitro, when seeded with hBMSCs, in osteogenic medium up to 28 days, no significant difference in initial seeding efficiency, or cell proliferation (quantified DNA) was observed between PCL and PLATMC (Figure 16a). Slightly higher continuous proliferation of the seeded cells could be observed on PLATMC templates at 21 days. AlamarBlue assay disclosed significant cellular activity on PLATMC at 7 and 21 days, while at 14 days, SEM disclosed much higher ECM secretion on PLATMC (Figure 16b-c).

The attached cells on PLATMC (14 days) showed complete surface adhesion and the secretion of huge amounts of granular ECMVs (containing Ca and P to initiate biomineralization), agglomerated in globular accretions, covering the whole surface. While on PCL few crystallites (rod-like shaped and contains more Ca and P content) were seen around the attached cells, with minimal detection of agglomerated ECMVs on surface (Figure 16).

At the gene level, as shown in Figure 17, the PLATMC group expressed the same osteogenic markers as PCL at all time points; early (RUNX2), intermediate (BMP-2), and late (osteopontin and osteocalcin). However, compared to PCL, at 7 days, the expression of COL1 and ALP by PLATMC group was minimal. Two further observations in PLATMC group gene expression should be noted. The first was that at 7 days, expression of BMP-2 was slightly higher in PLATMC than PCL. The second observation of note was the significant increase in osteocalcin expression by PLATMC, at 21 days, compared with expression at 7 days.

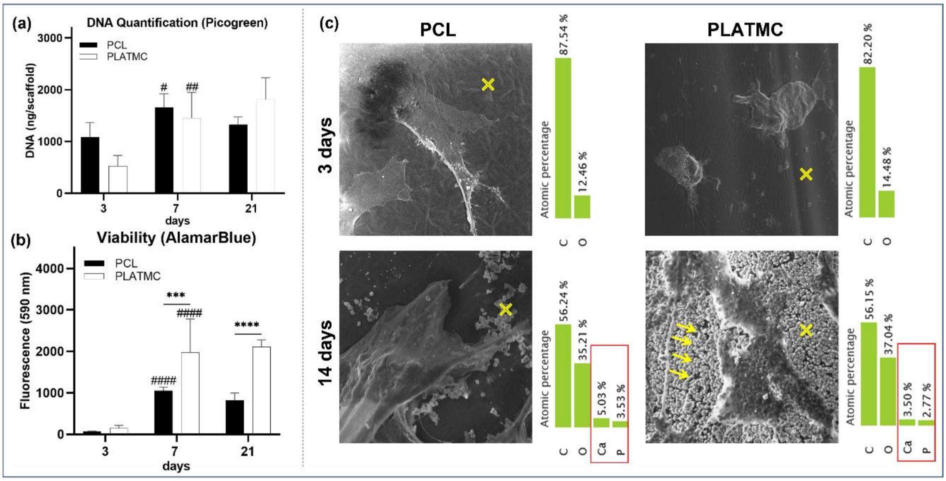

Figure 16: Bar charts representing the proliferation (a) and cellular activity (b) of hBMSCs seeded onto 3D-printed PCL and PLATMC at 3, 7 and 21 days. (c) SEM micrographs of hBMSCs seeded onto 3D-printed PCL and PLATMC at 3 and 14 days with corresponding EDX analysis to point marked with yellow (X). Note the submicron-sized ECMVs secreted in huge amounts at 14 days on the surface of PLATMC, marked with yellow arrows, with Ca and P contents. Statistical significance between each time point and the previous time point in the same group is marked with a hash (#), while significance between the groups is marked with asterisks (*) at p <0.05; *** p >0.0002, **** p <0.0001.

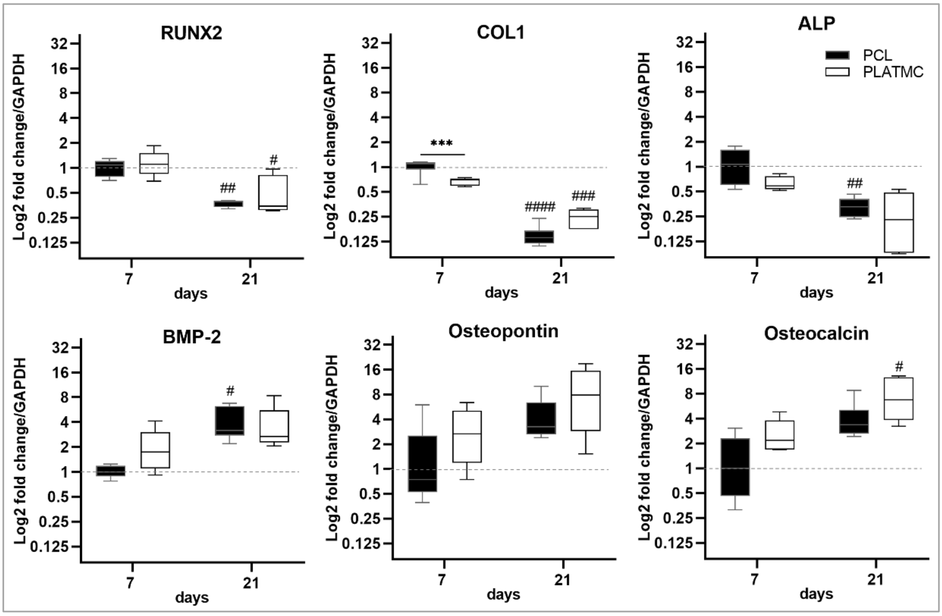

Figure 17: Box plots representing the gene expression of osteogenic markers at 7 and 21 days. Note the expression of PLATMC to the same markers was as high as for PCL, except for less expression of COL1 and ALP at 7 days. Statistical significance between each time point and the previous time point in the same group is marked with a hash (#), while significance between the groups is marked with asterisks (*) at $p < 0.05$.

On the other hand, in the PLATMC group, the characterized activity of secreted ALP was significantly less than for PCL at 7 and 21 days (Figure 18a), confirming the observations about ALP at the gene expression level. On the other hand, the biomineralization assay, shown by Alizarin red staining (Figure 18b-c), indicated that both groups exhibited equal amounts of mineralized ECM at 21 days. However, from 21 to 28 days, the PLATMC group showed significantly higher (active) biomineralization, whereas no corresponding increase in biomineralization was detected in the PCL group.

In vivo, the host response in the subcutaneous implantation model differed between the groups. At the PLATMC interface, the surrounding tissue interaction indicated a highly cellular, loose connective tissue interface, while a dense fibrous tissue interface was observed with PCL (Figure 19). Such defined physical and biological findings supported PLATMC as a promising BTE template candidate. This directed the thesis investigations toward the development of blended PLATMC templates with a bioceramic phase (e.g. HA), which could further enhance the osteoconductivity of PLATMC-based templates for biomaterials-based BTE.

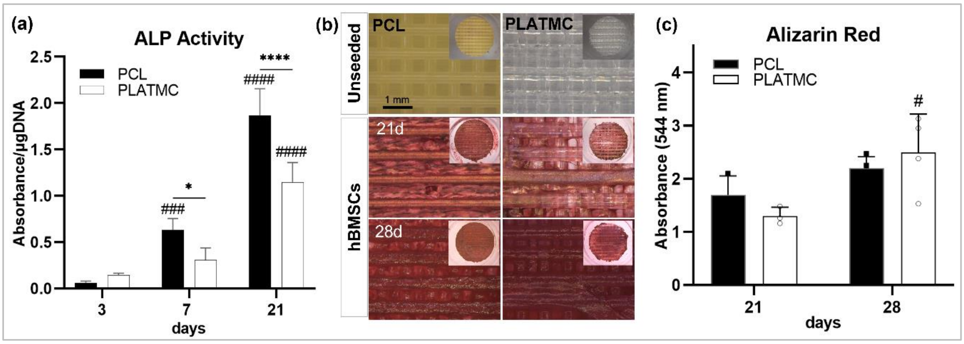

Figure 18: ALP activity and mineralized ECM secretion (*in vitro*), by seeded hBMSCs on PCL and PLATMC represented as: (a) column chart of ALP activity at 3, 7 and 21 days; (b) micrographs of Alizarin red stained 3D-printed templates at 21 and 28 days (scale bar = 1 mm), compared with unseeded templates (as blank), with inset pictures for the overall stained templates; (c) column chart presenting Alizarin red staining quantification (OD), absorbance at 544 nm.

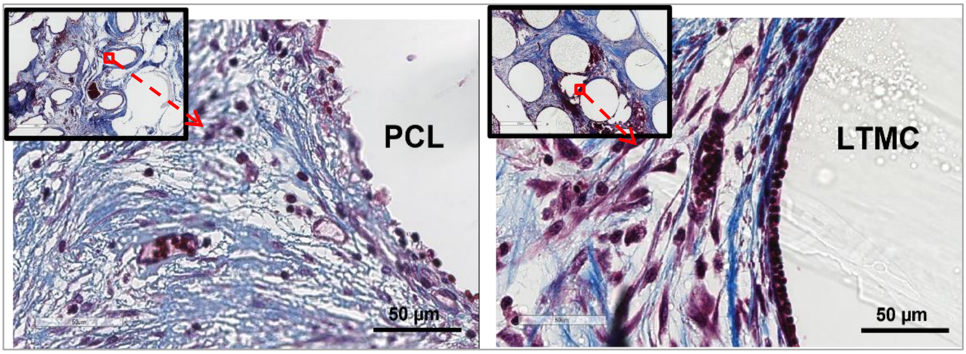

Figure 19: Representative histological micrographs for host response of the subcutaneous implanted 3D-printed PCL and PLATMC templates (8 weeks), stained with Massons' trichrome stain. The high magnification on each side focuses on the material/tissue interface of each group, while the inset figures are the 4x magnification of each group.

4.4. HA blends altered PLATMC physical and osteoconductive advantages (Study IV)

After the successful preparation of PLATMC/HA blends at 10, 30, and 50% (w/w)% HA, direct comparisons were made of these three blends, with PLATMC as the control (Figure 20a). With respect to mechanical properties, the addition of any percent of HA significantly reduced the ultimate tensile stress of PLATMC, while HA50 showed the least tensile stress (Figure 20b).

The *in vitro* degradation findings were obvious in SEM, where surface cracks were found in HA50 at 60 days and wide areas of surface erosion were found at 100 days (Figure 20c), while scarce degradation was noted in HA10 up to 100 days. The observed results were in accordance with the quantitative weight loss measurements (Figure 20d), where a distinctly high weight loss was directly proportional to the HA percentage in each group, with weight loss in HA50 reaching up to 6.68% ±1.65.

The Ca release from PLATMC/HA blends, detected *in vitro,* showed an instantly elevated Ca release from HA30 and HA50 up to 2 days, around 290 µg/g template and 406 µg/g template, respectively, with an obvious higher immediate release from HA50 (at 1 hour). This was followed by a steady Ca release phase from both groups up to 80 days, while much less Ca could be detected at 100 days (Figure 20e). On the other hand, minor amounts of Ca were released from HA10 up to 30 days, around 27 µg/g template, followed by relatively higher amounts up to 100 days, around 92 µg/g template.

Not many differences were noted *in vitro* among PLATMC and PLATMC/HA blends, in terms of hBMSCs seeding efficiency or proliferation. However, significant variances in later cell attachment and ECM deposition were observed. In general, ECM production was slightly higher in HA10 than in PLATMC and lowest in HA50. Live/dead stain at 7 days disclosed no obvious differences among the groups. Nevertheless, live/dead stain (Figure 21a) and SEM (Figure 21b) at 14 days confirmed that there were fewer cells attached on HA30 and much fewer on HA50.

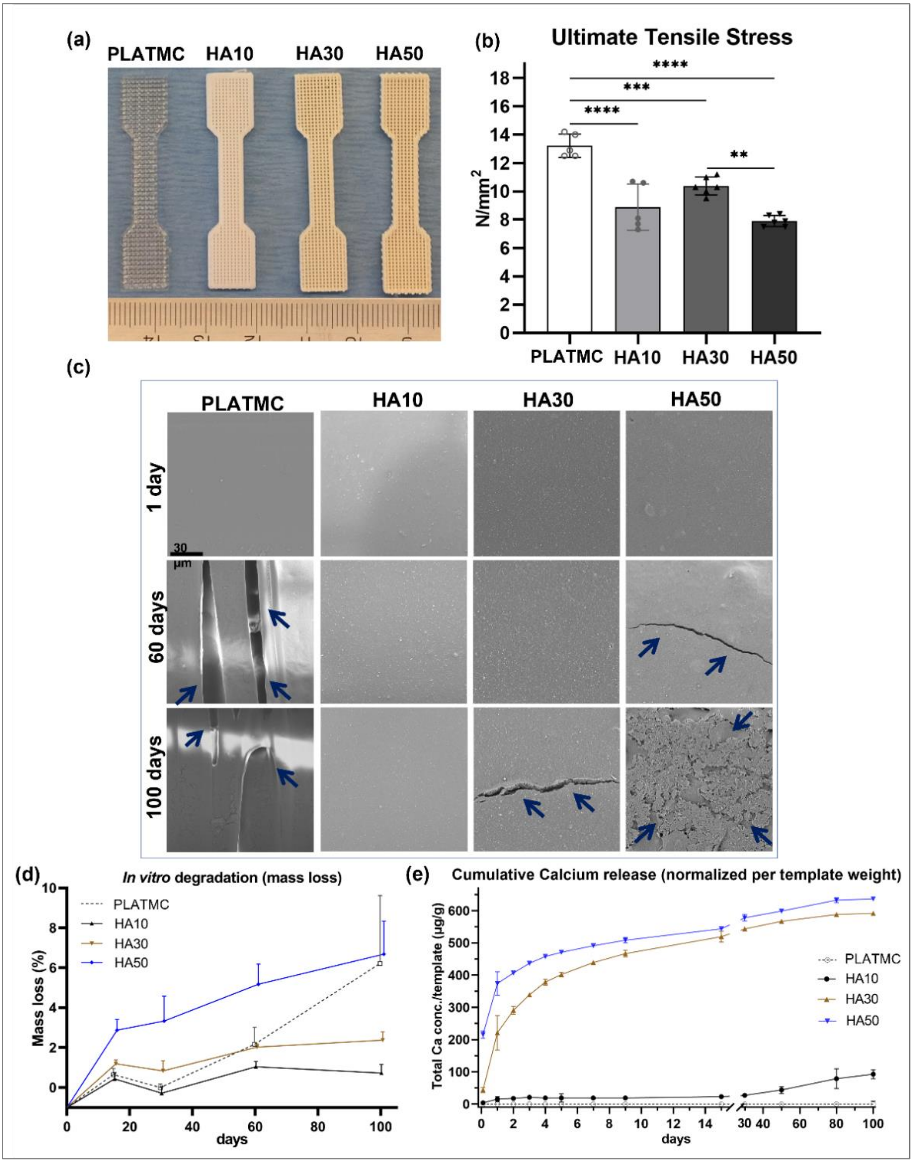

Figure 20: Summary of the characterized physical properties of PLATMC/HA blends, with PLATMC as the control. (a) 3D-printed templates in dumbbell-shape for tensile mechanical characterization according to ASTM-D638; (b) column chart of ultimate tensile stress; (c-e) degradation profile and calcium release up to 100 days in PBS at 37 ºC, (c) SEM micrographs with signs of degradation indicated with blue arrows, (d) mass loss quantification, and (e) cumulative calcium release.

At higher magnification, SEM showed greater variation of HA30 and HA50 compared with PLATMC and HA10, with minimal globular ECMVs on HA30 and no ECMVs on HA50. In contrast, HA10 showed a higher density of calcified ECM than PLATMC, with denser structural matrix production (Figure 21c).

On the other hand, with respect to cell proliferation (quantified DNA), no obvious differences were found among the groups in the at any time point. All the groups showed a doubling of quantified DNA at 7 days compared to 3 days, but no further cell proliferation was observed in any of the groups up to 21 days (Figure 22a).

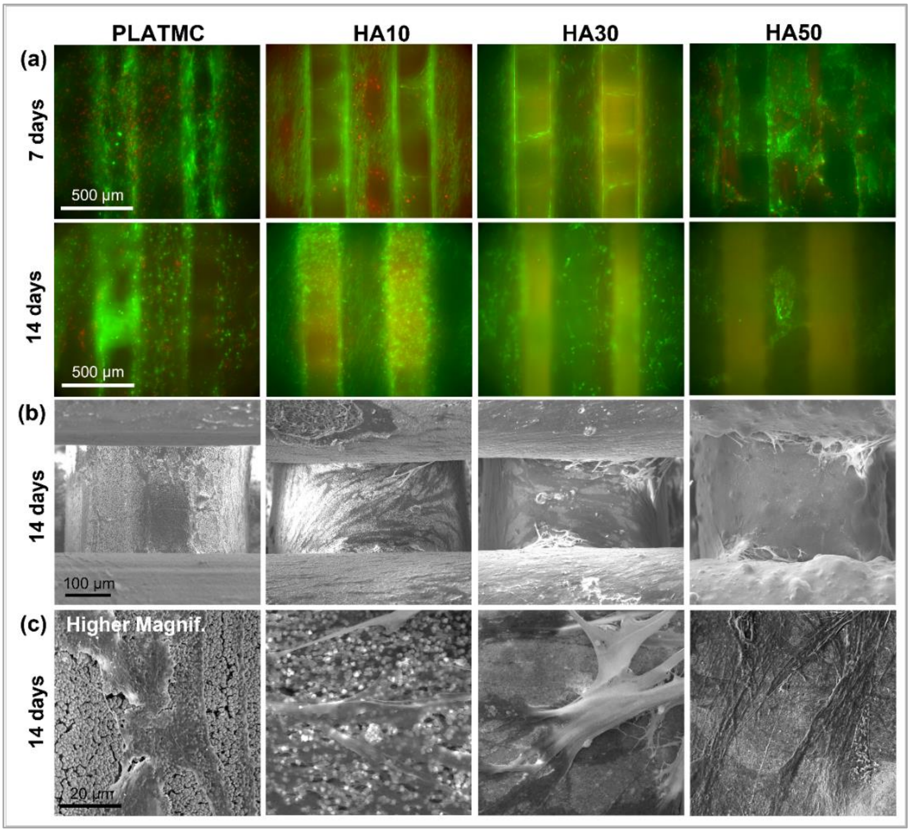

Figure 21: Micrographs of the viability and ECM production of seeded hBMSCs on 3D-printed PLATMC/HA blends. (a) live/dead fluorescence staining at 7 and 14 days; (b) SEM at 14 days showing the cellular attachment and ECM production, while higher magnifications are presented at (c).

The same applies to ALP activity, at 3 and 7 days, where no difference could be seen among the groups. However, at 21 days, ALP activity was significantly higher (2 - 3 times) in all groups compared to 7 days, while HA10 and HA30 were the highest, significantly higher than PLATMC at 21 days (Figure 22b). This was in accordance with the biomineralization assay observations at 21 days, where HA10 disclosed the highest accomplished biomineralization (Figure 22c). However, at 28 days, an obvious boost in biomineralization was seen in pristine PLATMC, while HA30 and HA50 were statistically the lowest.

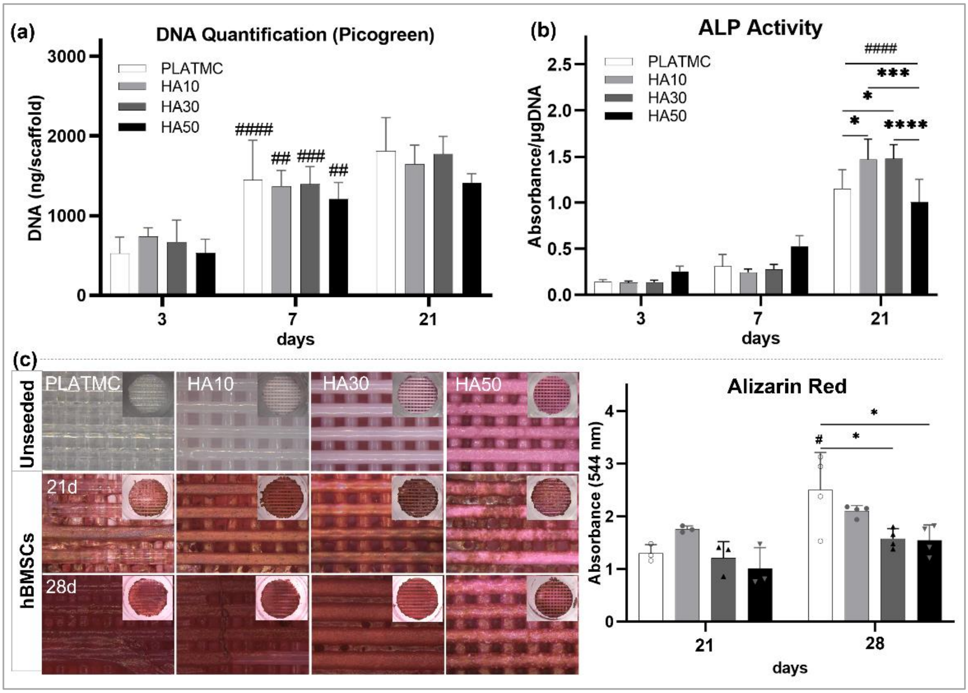

Figure 22: Summary of the proliferation and ECM production results, represented as: (a) column chart of DNA quantification, (b) ALP activity, and (c) Micrographs of Alizarin red stained 3D-printed PLATMC/HA templates seeded with hBMSCs at 21 and 28 days (scale bar = 1 mm), compared with unseeded templates (as blank), with inset pictures for the overall stained templates, in addition to a column chart presenting their quantification (OD), absorbance at 544 nm.

4.5. 3D-printed PLATMC revealed high osteoconduction in the CBD model (Study III and IV)

After the implantation of 3D-printed PCL, PLATMC, and PLATM/HA blends (HA10, HA30 and HA50) templates in the CBD model, the µCT showed some differences among the groups after 4 and 8 weeks (Figure 23). However, it was difficult to interpret the HA30 and HA50 templates, because their radiographic densities closely matched that of the surrounding bone. Thus, no quantitative data were calculated from the µCT results. However, the bone growth towards the defect center obviously followed the scaffold strands from all around the defect margins, with the best rate observed on PLATMC templates.

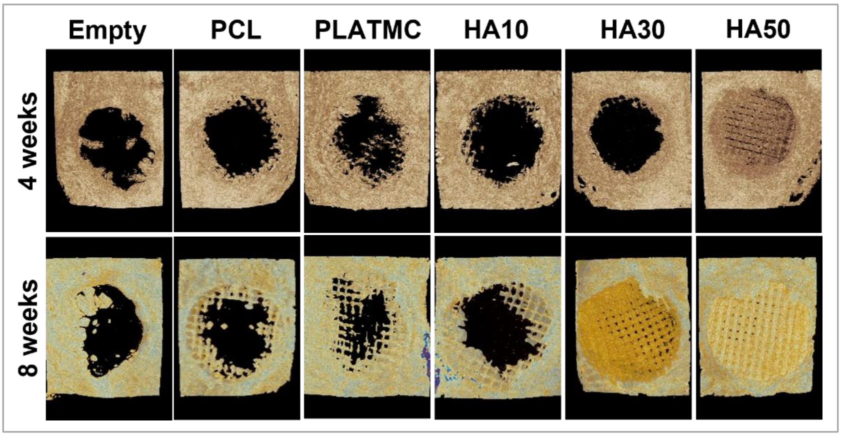

Figure 23: Reconstructed µCT pictures of the implanted templates in rabbits CBD.

The quantitative histomorphometric analysis, calculated from non-decalcified sections (Figure 24a), revealed that among all the groups, PLATMC exhibited the greatest amount of bone formation at 4 and 8 weeks (Figure 24b). At 4 weeks, the NBA/ADA of the PLATMC group was higher than the empty defect (statistically significant), and obviously higher than the PCL, HA30 and HA50 groups. The same trend was obvious at 8 weeks, where less NBA was detected in groups with higher HA content: thus, HA50 showed significantly less NBA than the PLATMC group. It should also be noted that, in general, less NBA was quantified at 8 weeks than at 4 weeks, in all the template-supported defects, except for the PLATMC group.

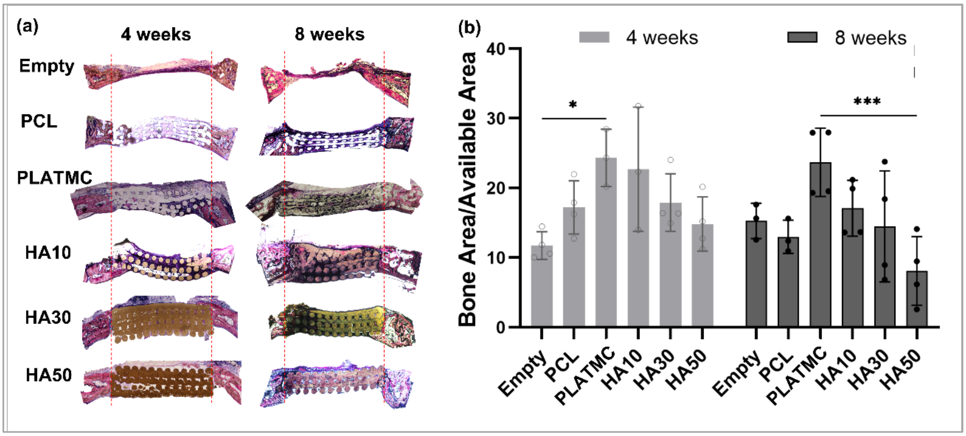

Figure 24: Representative non-decalcified histological sections of CBDs including all the test groups at 4 and 8 weeks stained with Toluidine blue and Acid fuchsin (a), while (b) is a bar chart of the histomorphometric analysis of new bone area per total available area (NBA/ADA).

Histologically, the empty defects (negative controls) showed marginal bone remodeling as a mean of healing the created defect. The remodeled bone creeping into the empty defects was very small in quantity and always accompanied by thinning of the original bone margins surrounding the defect. This confirmed the need for a well-designed porous template to support the regeneration process within the defect, as well as to support the bone defect margins and to prevent its collapse.

In direct comparison of PCL and PLATMC, it was obvious that some bone was growing within PCL templates at 4 weeks (Figure 25), but most spaces were filled with dense fibrous tissues lying between the newly formed bone and the PCL strands: i.e., distance osteogenesis. In contrast, on the PLATMC strands, a significantly higher amount of bone was observed passing through the PLATMC strands, obviously in close contact and noticeable osteoconduction onto PLATMC surface: i.e., contact osteogenesis.

In the PLATMC/HA blend groups, HA10 templates revealed the same contact osteogenesis as PLATMC templates (Figure 25), with spots of active bone formation integrated onto the surface of the HA10 strands. However, rare bone contact was observed on the HA30 and HA50 templates: in most cases only fibrous connective tissue was attached to their surfaces, i.e., distance osteogenesis. (Figure 25). At 8 weeks no significant changes were seen either in the quantity of the formed bone or in its contact with the template surface (Figure 26).

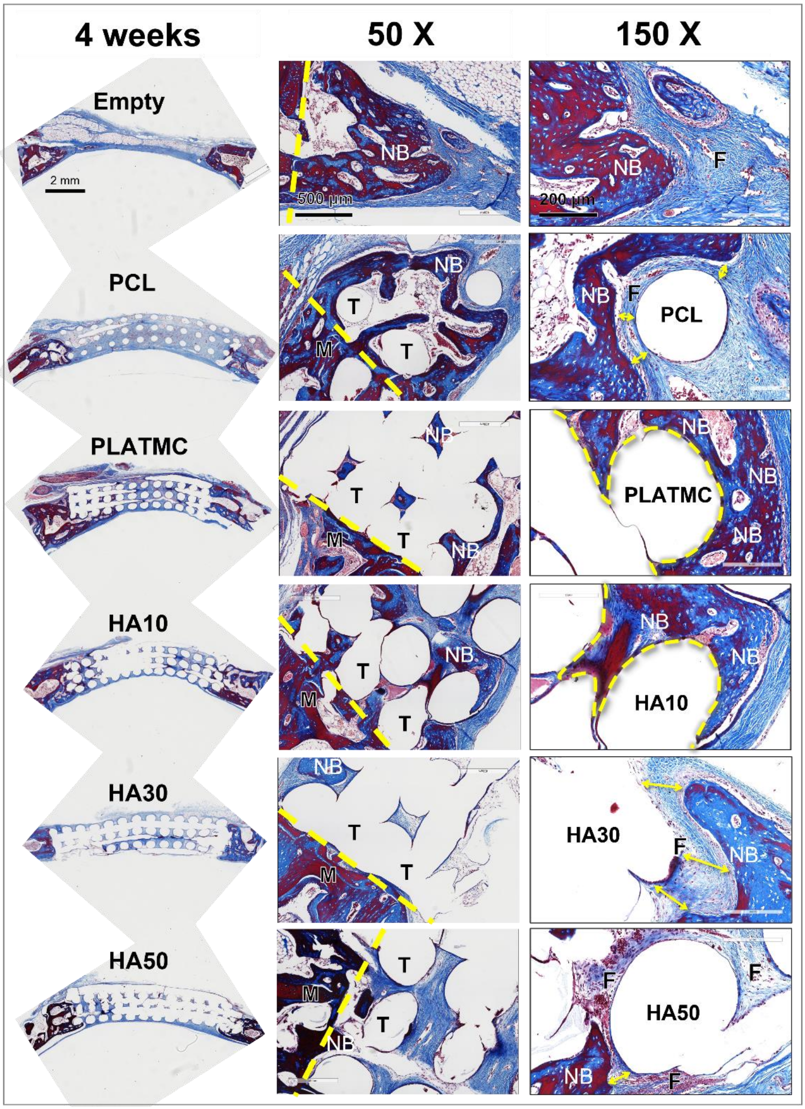

Figure 25: Representative decalcified histological micrographs of the CBDs (with the implanted 3D-printed templates) at 4 weeks and two higher magnifications of the bone ingrowth, 50x and 150x, stained with Masson's trichrome. At 50x: (YELLOW dotted line) denotes the interface between (M) and (T); (M) represents the original margin surrounding the defect; (T) represents the implanted templated; (NB) represents the new bone area. At 150x: curved (YELLOW dotted line) indicates the characterized NB contact line to T at higher magnifications (at PLATMC and HA10); (YELLOW double arrow) indicates the characterized gap between NB and T (at PCL, HA30 and HA50); (F) indicates fibrous connective tissue interface.

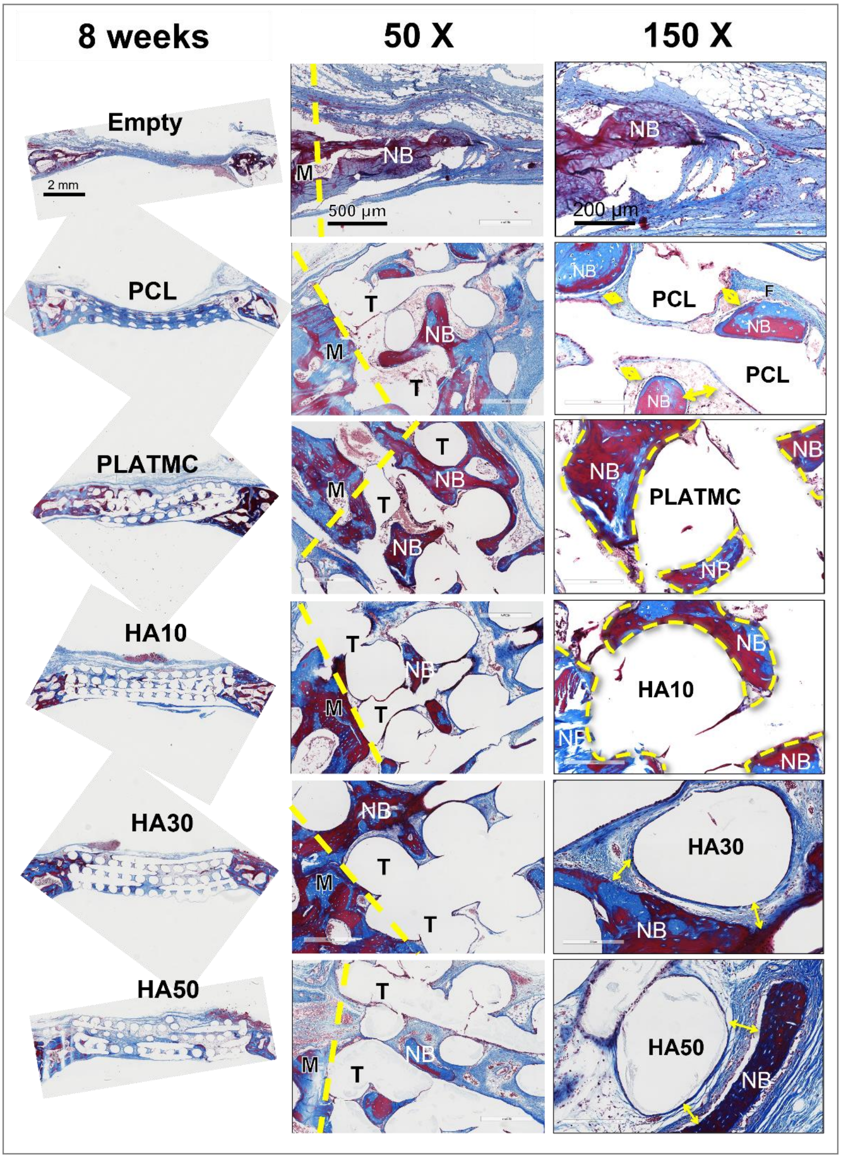

Figure 26: Representative decalcified histological micrographs of the CBDs (with the implanted 3D-printed templates) at 8 weeks and two higher magnifications of the bone ingrowth, 50x and 150x, stained with Masson's trichrome. At 50x: (YELLOW dotted line) denotes the interface between (M) and (T); (M) represents the original margin surrounding the defect; (T) represents the implanted templated; (NB) represents the new bone area. At 150x: curved (YELLOW dotted line) indicates the characterized NB contact line to T at higher magnifications (at PLATMC and HA10); (YELLOW double arrow) indicates the characterized gap between NB and T (at PCL, HA30 and HA50); (F) indicates fibrous connective tissue interface.

4.6. Discussion (Study III and IV)

4.6.1. *In vitro* biological results and related physical properties

Despite its bioinertness and poor degradability, PCL is among the most widely used polymers and the easiest to print at steady and repeatable parameters, especially in templates related to bone [160]. On the other hand, PLATMC was chosen based on recent reports, although in soft tissue applications, about its promising physical and biological properties [161,162]. Thus, a direct comparison was carried out between 3D-printed PLATMC and PCL, both in medical grade forms. PLATMC outperformed PCL with respect to the physical characteristics needed for BTE. PLATMC showed significantly higher wettability, tensile stress, and degradability. The tensile mechanical properties of PLATMC were within the previously reported ranges [155] and the same applied to the reported bulk degradation of PLATMC, attributed to leaching of water-soluble oligomers and low molecular-weight (Mn) species. In addition, the high variation noted for bulk degradation in the PLATMC group could be related to the changes in Mn while printing [161].

When seeded with hBMSCs in osteogenic medium, PCL exhibited normal cell attachment, proliferation, early osteogenic differentiation, noted by Runx2 expression, and expression of ECM essential components, COL1 and ALP at 7 days. In addition, SEM examination at 14 days revealed few growing CaP crystallites surrounding the cellular ECM, but no abundant globular accretions were observed on PCL surface. However, at 21 days, an overall reduction in cellular activity was detected by AlamarBlue assay, and limited biomineralization capacity was disclosed by Alizarin red staining. According to the reviewed literature, the osteogenic pathway associated with PCL was found to act through a Smad-dependent BMP signaling [163], which enhances cell differentiation and ALP activity but usually downregulates self-renewal of the preosteoblast as the differentiation potential increases [164].

In contrast, PLATMC showed steady cell proliferation, with the AlamarBlue assay showing marked cellular activity, up to 21 days. In addition, SEM examination revealed that abundance of agglomerated ECMVs, covering the entire PLATMC surface, are secreted by the differentiated hBMSCs. The secreted ECMVs, usually about 200 nm in diameter, are defined as membrane-invested globular structures which concentrates Ca and P ions, released by budding from the surface of active osteoblasts: these structures then aggregate, forming larger mineralized globular accretions, around 1µm in diameter [8,165]. These ECMVs and globular accretions are the key structures typically deposited by osteoblasts on osteoconductive implanted/substrate materials before the deposition of the overlying mineralizing collagen matrix [9,13].

It was not unexpected that normal expression of RUNX2 and BMP-2 was observed at PLATMC in the differentiated hBMSCs. However, on the other side, less COL1 and ALP were genetically expressed at 7 days and markedly less ALP activity was noted than for PCL at 7 and 21 days. Thus, there was an imbalance in the secretion of ECM components required for normal biomineralization at PLATMC: ECMVs/globular accretions at one side, and COL1 and ALP. This was observed as an overall limited biomineralization as high as the PCL group at 21 days. However, unlike PCL, continuous biomineralization activity was observed for PLATMC at 28 days, with a marked increase in quantity compared with that recorded at 21 days.

The mechanism of this delayed, but more powerful, osteoconductivity of PLATMC is assumed to be due to different osteogenic pathway action, which did not interfere with early osteogenic commitment of the osteogenic progenitor cells, but in addition, promoted osteoprogenitor proliferation (self-renewal). The TGF-β signaling pathway was found to promote the early osteoblastic lineage commitment of BMSCs, through the selective MAPKs and Smad2/3 pathways [5]. Moreover, this TGF- β signaling could result in inhibition of ALP activity and biomineralization by promoting proliferation through MAP3K-dependent pathways [166], as typically seen in the current results for seeded PLATMC templates. On the other hand, this MAPK/ERK signaling pathway was reported to stimulate hBMSCs to much higher osteogenic differentiation activity, tested at coated templates with natural-derived ECM [6], or osteogenic growth peptide [167].

On the other hand, the hypothesized enhancement of osteoconductivity through bulk modification with HA blends was successful, only at low percentage of HA inclusion

(HA10). The mild Ca released from HA10, around 27 µg/g template for the first 30 days, was enough to produce abundant calcified collagen matrix as early as 14 days, together with higher ALP activity than PLATMC, at 21 days. This in turn was seen as higher amount of biomineralized matrix detected on HA10 than PLATMC by Alizarin red at 21 days, but only a slight increase was disclosed at 28 days.

However, HA10 exhibited significantly less ultimate tensile stress and reduced degradation. This absence of degradation signs in HA10, although present in pristine PLATMC may indicate that HA, at this reduced ratio, act as a space filler, which reduces water sorption of PLATMC/HA blends, leading to the reduction of bulk degradation [155], which is considered as a limitation for BTE applications [126].

On the other hand, the inclusion of higher percentages of HA (HA30 and HA50), was accompanied by considerable degradation, but led to much higher Ca release, about 500 – 600 µg/g template for the first 30 days. Minor differences were noticed in DNA quantification (proliferation assay) among PLATMC and HA blends. However, less percentage of viable cells attached on HA30 template surface, were disclosed at 14 days by live/dead stain, and much less on HA50. While SEM revealed much less mineralized ECM on HA30 and almost no ECM on HA50. This in turn was reflected in Alizarin red staining as reduced mineralized ECM, on HA30 and HA50, compared to PLATMC and HA10, at 21 days. Moreover, at 28 days, HA30 and HA50 exhibited significantly reduced biomineralization compared with PLATMC.

These results disclosed by HA10 are in accordance with a recent study, where photo-crosslinked HA blends, containing 20 and 40 (w/w) % HA, with PTMC were found to be significantly osteoconductive, compared to control pristine PTMC resin. However, up to 30 days *in vitro*, the cumulated Ca release from HA20 and HA40 blends did not exceed 15 and 35 µg/template, respectively [116], due to scarce degradation rate of photo-crosslinked templates: about hundred fold less than non-crosslinked templates. However, on the other hand, the inhibited osteoconduction disclosed by the tested HA30 and HA50 templates in the current work could be due to the inflammatory response activated by the increased extracellular Ca concentrations [168], which are released early. The use of HA-based templates with high ionic fluctuations (high rate of released Ca) disclosed reduced cell adhesion, decreased proliferation and higher apoptosis of the seeded cells [169,170]. On the other hand, reduced osteoblast cell proliferation, lower osteoblastic gene expression and impeded ECM secretion were observed *in vitro* at nano HA particle concentrations higher than 25 µg/ml [171].

4.6.2. *In vivo* results based on *in vitro* outcomes

The host tissue responses to 3D-printed PCL and PLATMC templates in the subcutaneous model were closely related to their *in vitro* outcomes. No ectopic bone formation was observed in this subcutaneous model, due to the absence of osteogenic cues required for osteogenic lineage differentiation. On PCL templates, a dense fibrous connective tissue interface formed, corresponding to the normal foreign body reaction to implanted PCL, as reported in previous studies [172]. PLATMC templates had a loose connective tissue interface, with high cellular infiltration, and much less fibrous-related foreign body reaction. In a recent study of 3D-printed PLATMC and human platelet lysate hydrogels (HPLG) constructs, implanted subcutaneously into nude mice, ectopic mineralization was reported on cell-free constructs after 4 and 8 weeks [173]. However, no organized bone-like tissue or entrapped cells were observed.

When implanted in CBD models, the osteoconductive capacity of PCL and PLATMC were correlated closely with the *in vitro* results: compared to PCL, PLATMC exhibited higher osteoconduction and new bone ingrowth. In addition, obvious contact osteogenesis was observed on the surface of PLATMC, dominating almost all surfaces of new bone ingrowth at 4 and 8 weeks. In contrast, PCL exhibited a typical distance osteogenesis, with fibrous connective tissue interface against the new bone ingrowth. This could be in accordance with the recent reports characterizing PCL with abundant surronding fibrous tissue when implanted in bone defects [174]. Besides, the bone growing in the empty defects was comparable to previous studies in rats and rabbits, where the empty defects showed hypo-mineralized, remodeled bone margins creeping within the created critical size defects [21,175].

The observed contact osteogenesis on 3D-printed PLATMC has not previously been shown with any synthetic polymer used for BTR, or even for blended polymers with osteoconductive bioceramics [71,176]. These interesting findings could be related to the observed *in vitro* results, including stimulation of surrounding cells to attach, proliferate and secrete ECMVs directly onto the PLATMC surface, in the presence of needed osteogenic medium. Such defined physical and biological findings support the role of PLATMC as a BTE template, combining both biodegradation and osteoconductivity.

The *in vitro* outcomes of the HA blends, on the other hand, were highly linked to their *in vivo* results of the CBD model. HA10 showed new bone ingrowth and contact osteogenesis comparable with that of PLATMC, while HA30 and HA50 disclosed distance osteogenesis, with fibrous connective tissue interface and less bone ingrowth, comparable with PCL. The variation of bone ingrowth and osteoconduction by HA-based templates *in vivo* has been reported previously [62]. This was, however, assumed to be related to pore architecture advantages in the foamed templates compared to the 3D-printed templates, but no Ca release studies were conducted.

Thus, the results of the study confirm that only at mild rates of released Ca, osteoconduction and biomineralization are promoted *in vitro* and *in vivo*. In addition, the secreted mineralized ECM characterized *in vitro*, including the globular accretions and the mineralized structural matrix, are quite conclusive for the osteoconductivity of biomaterials and should be observed carefully as early as 14 days, up to 28 days.

Concluding remarks

From the implemented studies in the thesis project, it is concluded that:

- 3D-printing is promising to fabricate BTE templates, combining the optimal pore dimensions needed and mechanical strength, in addition to the ability to fabricate complex structures.

- Selection of osteoconductive biomaterials (i.e. polymers or polymer-based blends) with optimal pore size and biodegradation rate is crucial to fabricate effective BTE templates.

- Compared to PCL, modified PCL/GL templates boosted osteoconduction, but compromised the mechanical properties, which inhibited its application *in vivo*.

- PLATMC has physical and mechanical advantages, together with high osteoconductive potential.

- PLATMC has exclusive osteoconductive properties *in vitro*, and potent contact osteogenesis *in vivo* that qualify it to be used as next-generation 3D-printed BTE templates.

- At different ratios, HA could be blended with synthetic polymers, by drop precipitation method, and easily fabricated as 3D-printed templates.

- Addition of HA in sub-micron size, reduced the ultimate tensile stress of PLATMC, and altered its degradation profile and osteoconductivity.

- Low concentrations of Ca (mild Ca release rates) promoted osteoconduction, while higher concentrations of Ca release reduced osteoconduction.

Future perspectives

- The surface chemistry and surface charge of 3D-printed PLATMC need to be studied to determine the possible mechanisms of the following:

    1. Early cellular attachment and proliferation (*in vitro*).
    2. Signaling pathways for the osteogenic differentiation and secretion of globular accretions over the whole surface of templates (*in vitro*).
    3. Inhibition of ALP and COL1 expression and secretion at early time points (*in vitro*).

- The *in vivo* biodegradation profile of PLATMC needs to be characterized in bone defects, over longer time points (6, 12 and 18 months).

- The application of PLATMC in load-bearing (long bone) defects needs to be studied, in order to confirm its contact osteogenesis behaviour at different sites.

Acknowledgements

All praise to **Allah**, the creator of the heavens and the earth, alone with no partners, that gave me the blessings to have this work accomplished, gave me of all what I requested and even beyond what I asked him. Thank you, my **Parents,** and my **Wife** for your long standing with me in my life, words cannot express my gratitude to you.

I would like to express my deep gratitude to all of those who supported me to have this opportunity, making this PhD thesis, and passing all these challenges across the road to reach the goal. I would like to thank the **University of Bergen** for their generous hosting and funding to my PhD work. The thanks are extended to the **Faculty of Medicine** and the **Department of Clinical Dentistry**, for the inspiring working environment.

Indeed, my first gratitude to a person is to my main supervisor, Professor **Kamal Mustafa**, not only for his support, guidance, trust, and patience, but also for being too kind and generous like a father. All my co-supervisors are to be acknowledged, I was lucky enough to gain from their knowledge and experience. This goes to the late **Harald Gjengedal,** I wished you was present to see me finally defending my thesis and to be glad about me as you were always. Thanks **Mohamad Yassin** and **Salwa Suliman** for always being around, generously helping me and sharing your wide knowledge.

Ahmad Rashad, many thanks to you as a best friend, finding me the opportunity to come to Bergen, and giving me the sincere advice all the time. The appreciation is extended to the whole Tissue Engineering Group, **Siren Hammer Østvold** the group's mother and the endless smile, **Ying Xue, Kaia Berstad and Hisham Abdalla** the beating heart for the group and also **Odd Johan Lundberg** for his technical support to my work.

I would like to thank also all my elder fellow group members and co-authors **Samih Mohamed-Ahmed, Tarig Osman, Cecilie Gjerde, Niyaz Al-sharabi, Siddharth Shanbhag and Espen Helgeland** for their help and guidance. The newer group members and PhD candidates are also to be acknowledged, **Elisabeth Carlström, Hassan Ali, Neha Rana, Jannika Korkeamäki, Shuntaro Yamad, Mariann Haavik, Francesco Torelli, Masoumeh Jahani, Theo Luciani, Eylem Baysal, Natalia Arango and Nora Marek,** for their co-operation and best wishes. A special thank to my colleague, group member and roommate **Øyvind Goksøyr,** for the unlimited hours we shared knowledge and hope, and for helping with the Norewegian abstract.

I really want to thank the earlier and current leaders of the Department of Clinical Dentistry that I met, **Anne Åstrøm**, **Bodil Lund** and **Asgeir Bårdsen** together with the administration head **Signe Solberg** and all the administration and economic department for their endless efforts to keep the pace and the good working environment for the whole department. Thank you **Stein Atle Lie** for letting me enjoy statistics.

I am also grateful to the collaborators and co-authors, especially **Prof. Sherif Kandil** and **Ahmed Maher,** Alexandria University - Egypt, and **Dr. Azarudeen Suliman Raja,** Coimbatore Institute of Technology - India, and all the other funding sources that supported the work done within the PhD project: the **Research Council of Norway, Trond Mohn Research Foundation** and **Olav Thon foundation.**

More deep thanks go to the fellows and students that will read this thesis in the future and find something good to know and share.

References

1. Allori, A. C., Sailon, A. M. & Warren, S. M. Biological basis of bone formation, remodeling, and repair-part II: extracellular matrix. *Tissue Eng Part B Rev* **14**, 275–283 (2008).

2. Hayrapetyan, A., Jansen, J. A. & van den Beucken, J. J. Signaling Pathways Involved in Osteogenesis and Their Application for Bone Regenerative Medicine. *Tissue Eng. Part B Rev.* **21**, 75–87 (2015).

3. Wu, M., Chen, G. & Li, Y.-P. TGF-β and BMP signaling in osteoblast, skeletal development, and bone formation, homeostasis and disease. *Bone Res.* **4**, 16009 (2016).

4. Zou, M.-L. *et al.* The Smad Dependent TGF-β and BMP Signaling Pathway in Bone Remodeling and Therapies. *Front. Mol. Biosci.* **8**, 1–11 (2021).

5. Chen, G., Deng, C. & Li, Y. P. TGF-β and BMP signaling in osteoblast differentiation and bone formation. *Int. J. Biol. Sci.* **8**, 272–288 (2012).

6. Kang, Y., Kim, S., Bishop, J., Khademhosseini, A. & Yang, Y. The osteogenic differentiation of human bone marrow MSCs on HUVEC-derived ECM and β-TCP scaffold. *Biomaterials* **33**, 6998–7007 (2012).

7. Liu, T. M. & Lee, E. H. Transcriptional Regulatory Cascades in Runx2-Dependent Bone Development. *Tissue Eng. Part B Rev.* **19**, 254–263 (2013).

8. Kawasaki, K., Buchanan, A. V. & Weiss, K. M. Biomineralization in humans: Making the hard choices in life. *Annu. Rev. Genet.* **43**, 119–142 (2009).

9. Davies, J. E., Mendes, V. C., Ko, J. C. H. & Ajami, E. Topographic scale-range synergy at the functional bone/implant interface. *Biomaterials* **35**, 25–35 (2014).

10. Davies, J. E., Chernecky, R., Lowenberg, B. & Shiga, A. Deposition and resorption of calcified matrix in vitro by rat marrow cells. *Cells Mater.* **1**, 3–15 (1991).

11. Davies, J. E. In vitro modeling of the bone/implant interface. *Anat. Rec.* **245**, 426–445 (1996).

12. Davies, J. E. Mechanisms of endosseous integration. *Int. J. Prosthodont.* **11**, 391–401 (1998).

13. Lowenberg, B., Chernecky, R., Shiga, A. & Davies, J. Mineralized Matrix Production by Osteoblasts on Solid Titanium In Vitro. *Cells Mater.* **1**, 177–187 (1991).

14. Lee, K. *et al.* Bone regeneration via novel macroporous CPC scaffolds in critical-

sized cranial defects in rats. *Dent. Mater.* **30**, e199–e207 (2014).

15. Szpalski, C., Wetterau, M., Barr, J. & Warren, S. M. Bone Tissue Engineering: Current Strategies and Techniques—Part I: Scaffolds. *Tissue Eng. Part B Rev.* **18**, 246–257 (2012).

16. Allori, A. C., Sailon, A. M. & Warren, S. M. Biological basis of bone formation, remodeling, and repair-part I: biochemical signaling molecules. *Tissue Eng Part B Rev* **14**, 259–273 (2008).

17. Allori, A. C., Sailon, A. M., Pan, J. H. & Warren, S. M. Biological basis of bone formation, remodeling, and repair-part III: biomechanical forces. *Tissue Eng Part B Rev* **14**, 285–293 (2008).

18. Hallman, M. & Thor, A. Bone substitutes and growth factors as an alternative/complement to autogenous bone for grafting in implant dentistry. *Periodontol 2000* **47**, 172–192 (2008).

19. Schoekler, B. & Trummer, M. Prediction parameters of bone flap resorption following cranioplasty with autologous bone. *Clin. Neurol. Neurosurg.* **120**, 64–67 (2014).

20. Wang, W. & Yeung, K. W. K. Bone grafts and biomaterials substitutes for bone defect repair: A review. *Bioact. Mater.* **2**, 224–247 (2017).

21. Teotia, A. K. *et al.* Improved Bone Regeneration in Rabbit Bone Defects Using 3D Printed Composite Scaffolds Functionalized with Osteoinductive Factors. *ACS Appl. Mater. Interfaces* **12**, 48340–48356 (2020).

22. Thien, A., King, N. K. K., Ang, B. T., Wang, E. & Ng, I. Comparison of Polyetheretherketone and Titanium Cranioplasty after Decompressive Craniectomy. *World Neurosurg.* **83**, 176–180 (2015).

23. Ilizarov, G. A. & Ledyaev, V. I. The replacement of long tubular bone defects by lengthening distraction osteotomy of one of the fragments. 1969. *Clin. Orthop. Relat. Res.* 7–10 (1992).

24. Ai-Aql, Z. S., Alagl, A. S., Graves, D. T., Gerstenfeld, L. C. & Einhorn, T. A. Molecular mechanisms controlling bone formation during fracture healing and distraction osteogenesis. *J Dent Res* **87**, 107–118 (2008).

25. Langer, R. & Vacanti, J. P. Tissue Engineering. *Science (80-.).* **260**, 920–926 (1993).

26. Williams, D. F. *The Williams Dictionary of Biomaterials*. (Liverpool University Press, 1999). doi:10.5949/UPO9781846314438.

27. Williams, D. F. The Biomaterials Conundrum in Tissue Engineering. *Tissue Eng. Part A* **20**, 1129–1131 (2014).

28. Shang, F. *et al.* Advancing application of mesenchymal stem cell-based bone tissue regeneration. *Bioact. Mater.* **6**, 666–683 (2021).

29. Mohamed-Ahmed, S. *et al.* Comparison of bone regenerative capacity of donor-matched human adipose–derived and bone marrow mesenchymal stem cells. *Cell Tissue Res.* **383**, 1061–1075 (2021).

30. Cecilie Gudveig, G. *et al.* Autologous Porcine Bone Marrow Mesenchymal Cells for Reconstruction of a Resorbed Alveolar Bone: A Preclinical Model in Mini-Pigs. *Int. J. Stem cell Res. Ther.* **4**, (2017).

31. Gjerde, C. *et al.* Cell therapy induced regeneration of severely atrophied mandibular bone in a clinical trial. *Stem Cell Res. Ther.* **9**, 1–15 (2018).

32. Kuchler, U. *et al.* Bone-conditioned medium modulates the osteoconductive properties of collagen membranes in a rat calvaria defect model. *Clin. Oral Implants Res.* **29**, 381–388 (2018).

33. Shanbhag, S. *et al.* Cell therapy for orofacial bone regeneration: A systematic review and meta-analysis. *J. Clin. Periodontol.* **46**, 162–182 (2019).

34. Sanz, M. *et al.* Biomaterials and regenerative technologies used in bone regeneration in the craniomaxillofacial region: Consensus report of group 2 of the 15th European Workshop on Periodontology on Bone Regeneration. *J. Clin. Periodontol.* **46**, 82–91 (2019).

35. Yassin, M. A. *et al.* Cell seeding density is a critical determinant for copolymer scaffolds-induced bone regeneration. *J. Biomed. Mater. Res. Part A* **103**, 3649–3658 (2015).

36. Rojewski, M. T. *et al.* Translation of a standardized manufacturing protocol for mesenchymal stromal cells: A systematic comparison of validation and manufacturing data. *Cytotherapy* **21**, 468–482 (2019).

37. Ricci, J. L., Clark, E. A., Murriky, A. & Smay, J. E. Three-Dimensional Printing of Bone Repair and Replacement Materials. *J. Craniofac. Surg.* **23**, 304–308 (2012).

38. Hutmacher, D. W. & Cool, S. Concepts of scaffold-based tissue engineering - The rationale to use solid free-form fabrication techniques. *J. Cell. Mol. Med.* **11**, 654–669 (2007).

39. Mehta, M., Schmidt-Bleek, K., Duda, G. N. & Mooney, D. J. Biomaterial delivery of morphogens to mimic the natural healing cascade in bone. *Adv. Drug Deliv. Rev.* **64**, 1257–1276 (2012).

40. Lee, K., Silva, E. A. & Mooney, D. J. Growth factor delivery-based tissue engineering: General approaches and a review of recent developments. *J. R. Soc. Interface* **8**, 153–170 (2011).

41. Urist, M. R. Bone : Formation by Autoinduction. *Adv. Sci.* **150**, 893–899 (1965).

42. Urist, M. R. & Strates, B. S. Bone Morphogenetic Protein. *J. Dent. Res.* **50**, 1392–1406 (1971).

43. Katagiri, T. & Watabe, T. Bone Morphogenetic Proteins. *Cold Spring Harb. Perspect. Biol.* **8**, a021899 (2016).

44. Li, R. H. & Wozney, J. M. Delivering on the promise of bone morphogenetic proteins. *Trends Biotechnol.* **19**, 255–265 (2001).

45. Bergman, K. *et al.* Injectable cell-free template for bone-tissue formation. *J. Biomed. Mater. Res. - Part A* **91**, 1111–1118 (2009).

46. Dadsetan, M. *et al.* Effect of calcium phosphate coating and rhBMP-2 on bone regeneration in rabbit calvaria using poly(propylene fumarate) scaffolds. *Acta Biomater.* **18**, 9–20 (2015).

47. Suliman, S. *et al.* Release and bioactivity of bone morphogenetic protein-2 are affected by scaffold binding techniques in vitro and in vivo. *J. Control. Release* **197**, 148–157 (2015).

48. Martínez-Sanz, E. *et al.* Minimally invasive mandibular bone augmentation using injectable hydrogels. *J. Tissue Eng. Regen. Med.* **6**, s15–s23 (2012).

49. Neovius, E., Lemberger, M., Docherty, A. C. & Hilborn, J. Alveolar bone healing accompanied by severe swelling in cleft children treated with bone morphogenetic protein-2 delivered by hydrogel *. *Br. J. Plast. Surg.* **66**, 37–42 (2013).

50. Vavken, J., Mameghani, A., Vavken, P. & Schaeren, S. Complications and cancer rates in spine fusion with recombinant human bone morphogenetic protein-2 (rhBMP-2). *Eur. Spine J.* **25**, 3979–3989 (2016).

51. James, A. W. *et al.* A Review of the Clinical Side Effects of Bone Morphogenetic Protein-2. *Tissue Eng. Part B Rev.* **22**, 284–297 (2016).

52. Williams, D. F. On the nature of biomaterials. *Biomaterials* **30**, 5897–5909 (2009).

53. Hutmacher, D. W. Scaffolds in tissue engineering bone and cartilage. in *The Biomaterials: Silver Jubilee Compendium* vol. 21 175–189 (Elsevier, 2000).

54. Simon, J. L. *et al.* Engineered cellular response to scaffold architecture in a rabbit trephine defect. *J. Biomed. Mater. Res.* **66A**, 275–282 (2003).

55. Zhao, S. *et al.* Three-dimensional printed strontium-containing mesoporous bioactive glass scaffolds for repairing rat critical-sized calvarial defects. *Acta Biomater.* **12**, 270–280 (2015).

56. Li, J. *et al.* Investigation of angiogenesis in bioactive 3-dimensional poly(D,L-lactide-co-glycolide)/nano-hydroxyapatite scaffolds by in vivo multiphoton microscopy in murine calvarial critical bone defect. *Acta Biomater.* **42**, 389–399 (2016).

57. Barradas, A., Yuan, H., van Blitterswijk, C. & Habibovic, P. Osteoinductive biomaterials: current knowledge of properties, experimental models and biological mechanisms. *Eur. Cells Mater.* **21**, 407–429 (2011).

58. Wu, S., Liu, X., Yeung, K. W. K., Liu, C. & Yang, X. Biomimetic porous scaffolds for bone tissue engineering. *Mater. Sci. Eng. R Reports* **80**, 1–36 (2014).

59. Jensen, J. *et al.* Surface-modified functionalized polycaprolactone scaffolds for bone repair: In vitro and in vivo experiments. *J. Biomed. Mater. Res. Part A* **102**, 2993–3003 (2014).

60. Ripamonti, U., Richter, P. W. & Thomas, M. E. Self-Inducing Shape Memory Geometric Cues Embedded within Smart Hydroxyapatite-Based Biomimetic Matrices. *Plast. Reconstr. Surg.* **120**, 1796–1807 (2007).

61. Barba, A. *et al.* Osteoinduction by Foamed and 3D-Printed Calcium Phosphate Scaffolds: Effect of Nanostructure and Pore Architecture. *ACS Appl. Mater. Interfaces* **9**, 41722–41736 (2017).

62. Barba, A. *et al.* Osteogenesis by foamed and 3D-printed nanostructured calcium phosphate scaffolds: Effect of pore architecture. *Acta Biomater.* **79**, 135–147 (2018).

63. Vidal, L. *et al.* Regeneration of segmental defects in metatarsus of sheep with vascularized and customized 3D-printed calcium phosphate scaffolds. *Sci. Rep.* **10**, 7068 (2020).

64. Xiao, W., Zaeem, M. A., Bal, B. S. & Rahaman, M. N. Creation of bioactive glass (13–93) scaffolds for structural bone repair using a combined finite element modeling and rapid prototyping approach. *Mater. Sci. Eng. C* **68**, 651–662 (2016).

65. Murphy, C. M., Haugh, M. G. & O'Brien, F. J. The effect of mean pore size on cell attachment, proliferation and migration in collagen–glycosaminoglycan scaffolds for bone tissue engineering. *Biomaterials* **31**, 461–466 (2010).

66. Shao, H. *et al.* Bone regeneration in 3D printing bioactive ceramic scaffolds with improved tissue/material interface pore architecture in thin-wall bone defect. *Biofabrication* **9**, 025003 (2017).

67. Chang, B. *et al.* Influence of pore size of porous titanium fabricated by vacuum diffusion bonding of titanium meshes on cell penetration and bone ingrowth.

Acta Biomater. **33**, 311–321 (2016).

68. Simon, J. L. *et al.* In vivo bone response to 3D periodic hydroxyapatite scaffolds assembled by direct ink writing. *J. Biomed. Mater. Res. Part A* **83A**, 747–758 (2007).

69. Roy, T. D. *et al.* Performance of degradable composite bone repair products made via three-dimensional fabrication techniques. *J. Biomed. Mater. Res.* **66A**, 283–291 (2003).

70. Roy, T. D. *et al.* Performance of hydroxyapatite bone repair scaffolds created via three-dimensional fabrication techniques. *J. Biomed. Mater. Res.* **67A**, 1228–1237 (2003).

71. Shim, J.-H. *et al.* Stimulation of healing within a rabbit calvarial defect by a PCL/PLGA scaffold blended with TCP using solid freeform fabrication technology. *J. Mater. Sci. Mater. Med.* **23**, 2993–3002 (2012).

72. Kwon, D. Y. *et al.* Bone regeneration by means of a three-dimensional printed scaffold in a rat cranial defect. *J. Tissue Eng. Regen. Med.* **12**, 516–528 (2018).

73. Lim, J., Lee, J., Yun, H.-S., Shin, H.-I. & Park, E. K. Comparison of bone regeneration rate in flat and long bone defects: Calvarial and tibial bone. *Tissue Eng. Regen. Med.* **10**, 336–340 (2013).

74. Haberstroh, K. *et al.* Bone repair by cell-seeded 3D-bioplotted composite scaffolds made of collagen treated tricalciumphosphate or tricalciumphosphate-chitosan-collagen hydrogel or PLGA in ovine critical-sized calvarial defects. *J. Biomed. Mater. Res. - Part B Appl. Biomater.* **93**, 520–530 (2010).

75. Qi, X. *et al.* Three dimensional printing of calcium sulfate and mesoporous bioactive glass scaffolds for improving bone regeneration in vitro and in vivo. *Sci. Rep.* **7**, 42556 (2017).

76. Seol, Y.-J. *et al.* Improvement of Bone Regeneration Capability of Ceramic Scaffolds by Accelerated Release of Their Calcium Ions. *Tissue Eng. Part A* **20**, 2840–2849 (2014).

77. Kim, J. A., Lim, J., Naren, R., Yun, H. suk & Park, E. K. Effect of the biodegradation rate controlled by pore structures in magnesium phosphate ceramic scaffolds on bone tissue regeneration in vivo. *Acta Biomater.* **44**, 155–167 (2016).

78. Davies, J. E. Understanding peri-implant endosseous healing. *J. Dent. Educ.* **67**, 932–949 (2003).

79. Tamimi, F. *et al.* Osseointegration of dental implants in 3D-printed synthetic onlay grafts customized according to bone metabolic activity in recipient site. *Biomaterials* **35**, 5436–5445 (2014).

80. Williams, D. The Inert-Bioactivity Conundrum. in *Bio-Implant Interface* (eds. Ellingsen, J. E. & Lyngstadaas, S. P.) (CRC Press, 2003). doi:10.1201/9780203491430.ch23.

81. Hench, L. L. Bioactive materials: the potential for tissue regeneration. *J Biomed Mater Res* **41**, 511–518 (1998).

82. Jones, J. R. *et al.* Extracellular matrix formation and mineralization on a phosphate-free porous bioactive glass scaffold using primary human osteoblast (HOB) cells. *Biomaterials* **28**, 1653–1663 (2007).

83. Friedenstein, A. Y. Induction of bone tissue by transitional epithelium. *Clin Orthop Relat Res* **59**, 21–37 (1968).

84. Hassan, M. N., Mahmoud, M. M., El-Fattah, A. A. & Kandil, S. Microwave-assisted preparation of Nano-hydroxyapatite for bone substitutes. *Ceram. Int.* **42**, 3725–3744 (2016).

85. Lyons, J. G., Plantz, M. A., Hsu, W. K., Hsu, E. L. & Minardi, S. Nanostructured Biomaterials for Bone Regeneration. *Front. Bioeng. Biotechnol.* **8**, 1–28 (2020).

86. Artzi, Z. *et al.* Biomaterial Resorption Rate and Healing Site Morphology of Inorganic Bovine Bone and ß-Tricalcium Phosphate in the Canine : A 24-month Longitudinal Histologic Study and Morphometric Analysis. *Int J Oral Maxillofac Implant.* **19**, 357–368 (2004).

87. Kim, Y. S., Smoak, M. M., Melchiorri, A. J. & Mikos, A. G. An Overview of the Tissue Engineering Market in the United States from 2011 to 2018. *Tissue Eng. Part A* **25**, 1–8 (2019).

88. Jung, K., Corrigan, N., Wong, E. H. H. & Boyer, C. Bioactive Synthetic Polymers. *Adv. Mater.* **34**, 2105063 (2022).

89. Park, N. H. *et al.* Addressing Drug Resistance in Cancer with Macromolecular Chemotherapeutic Agents. *J. Am. Chem. Soc.* **140**, 4244–4252 (2018).

90. Takahashi, H., Caputo, G. A. & Kuroda, K. Amphiphilic polymer therapeutics: an alternative platform in the fight against antibiotic resistant bacteria. *Biomater. Sci.* **9**, 2758–2767 (2021).

91. Schaefer, S. *et al.* Rational Design of an Antifungal Polyacrylamide Library with Reduced Host-Cell Toxicity. *ACS Appl. Mater. Interfaces* **13**, 27430–27444 (2021).

92. Zelikin, A. N. & Stellacci, F. Broad-Spectrum Antiviral Agents Based on Multivalent Inhibitors of Viral Infectivity. *Adv. Healthc. Mater.* **10**, 2001433 (2021).

93. Neuhaus, O., Farina, C., Wekerle, H. & Hohlfeld, R. Mechanisms of action of

glatiramer acetate in multiple sclerosis. *Neurology* **56**, 702–708 (2001).

94. Vishwakarma, A. *et al.* Engineering Immunomodulatory Biomaterials To Tune the Inflammatory Response. *Trends Biotechnol.* **34**, 470–482 (2016).

95. Luangphakdy, V. *et al.* Evaluation of osteoconductive scaffolds in the canine femoral multi-defect model. *Tissue Eng. Part A* **19**, 634–48 (2013).

96. Feliciano, A. J., van Blitterswijk, C., Moroni, L. & Baker, M. B. Realizing tissue integration with supramolecular hydrogels. *Acta Biomater.* **124**, 1–14 (2021).

97. Pati, F. *et al.* Ornamenting 3D printed scaffolds with cell-laid extracellular matrix for bone tissue regeneration. *Biomaterials* **37**, 230–241 (2015).

98. Hung, B. P. *et al.* Three-Dimensional Printing of Bone Extracellular Matrix for Craniofacial Regeneration. *ACS Biomater. Sci. Eng.* **2**, 1806–1816 (2016).

99. Kim, J.-Y. *et al.* Synergistic Effects of Beta Tri-Calcium Phosphate and Porcine-Derived Decellularized Bone Extracellular Matrix in 3D-Printed Polycaprolactone Scaffold on Bone Regeneration. *Macromol. Biosci.* **18**, 1800025 (2018).

100. Nair, L. S. & Laurencin, C. T. Biodegradable polymers as biomaterials. *Prog. Polym. Sci.* **32**, 762–798 (2007).

101. Swetha, M. *et al.* Biocomposites containing natural polymers and hydroxyapatite for bone tissue engineering. *Int. J. Biol. Macromol.* **47**, 1–4 (2010).

102. Solorio, L., Zwolinski, C., Lund, A. W., Farrell, M. J. & Stegemann, J. P. Gelatin microspheres crosslinked with genipin for local delivery of growth factors. *J. Tissue Eng. Regen. Med.* **4**, 514–523 (2010).

103. KarbalaeiMahdi, A. *et al.* Neural differentiation of human induced pluripotent stem cells on polycaprolactone/gelatin bi-electrospun nanofibers. *Mater. Sci. Eng. C* **78**, 1195–1202 (2017).

104. Schantz, J.-T. *et al.* Repair of Calvarial Defects with Customised Tissue-Engineered Bone Grafts II. Evaluation of Cellular Efficiency and Efficacy in Vivo. *Tissue Eng.* **9**, 127–139 (2003).

105. Yeo, A., Wong, W. J. & Teoh, S. H. Surface modification of PCL-TCP scaffolds in rabbit calvaria defects: Evaluation of scaffold degradation profile, biomechanical properties and bone healing patterns. *J. Biomed. Mater. Res. - Part A* **93**, 1358–1367 (2010).

106. Schantz, J.-T. *et al.* Cranioplasty after Trephination using a Novel Biodegradable Burr Hole Cover: Technical Case Report. *Oper. Neurosurg.* **58**, E176 (2006).

107. Probst, F. A., Hutmacher, D. W., Müller, D. F., Machens, H.-G. & Schantz, J.-

T. Rekonstruktion der Kalvaria durch ein präfabriziertes bioaktives Implantat. *Handchirurgie · Mikrochirurgie · Plast. Chir.* **42**, 369–373 (2010).

108. Sharifi, S. & Grijpma, D. W. Resilient Amorphous Networks Prepared by Photo-Crosslinking High-Molecular-Weight D,L-Lactide and Trimethylene Carbonate Macromers: Mechanical Properties and Shape-Memory Behavior. *Macromol. Biosci.* **12**, 1423–1435 (2012).

109. Nafea, E. H., El-Massik, M. a, El-Khordagui, L. K., Marei, M. K. & Khalafallah, N. M. Alendronate PLGA microspheres with high loading efficiency for dental applications. *J. Microencapsul.* **24**, 525–538 (2007).

110. Savioli Lopes, M., Jardini, A. L. & Maciel Filho, R. Poly (lactic acid) production for tissue engineering applications. *Procedia Eng.* **42**, 1402–1413 (2012).

111. Fukushima, K. Poly(trimethylene carbonate)-based polymers engineered for biodegradable functional biomaterials. *Biomater. Sci.* **4**, 9–24 (2016).

112. Artham, T. & Doble, M. Biodegradation of Aliphatic and Aromatic Polycarbonates. *Macromol. Biosci.* **8**, 14–24 (2008).

113. Pêgo, A. P. *et al.* In vivo behavior of poly(1,3-trimethylene carbonate) and copolymers of 1,3-trimethylene carbonate with D,L-lactide or ε-caprolactone: Degradation and tissue response. *J. Biomed. Mater. Res. - Part A* **67**, 1044–1054 (2003).

114. Zhang, Z., Kuijer, R., Bulstra, S. K., Grijpma, D. W. & Feijen, J. The in vivo and in vitro degradation behavior of poly(trimethylene carbonate). *Biomaterials* **27**, 1741–1748 (2006).

115. Zeng, N., van Leeuwen, A. C., Grijpma, D. W., Bos, R. R. M. & Kuijer, R. Poly(trimethylene carbonate)-based composite materials for reconstruction of critical-sized cranial bone defects in sheep. *J. Cranio-Maxillofacial Surg.* **45**, 338–346 (2017).

116. Guillaume, O. *et al.* Surface-enrichment with hydroxyapatite nanoparticles in stereolithography-fabricated composite polymer scaffolds promotes bone repair. *Acta Biomater.* **54**, 386–398 (2017).

117. Dienel, K. E. G., van Bochove, B. & Seppälä, J. V. Additive Manufacturing of Bioactive Poly(trimethylene carbonate)/β-Tricalcium Phosphate Composites for Bone Regeneration. *Biomacromolecules* **21**, 366–375 (2020).

118. Pêgo, A. P., Poot, A. A., Grijpma, D. W. & Feijen, J. Biodegradable elastomeric scaffolds for soft tissue engineering. *J. Control. Release* **87**, 69–79 (2003).

119. Pêgo, A. P., Poot, A. A., Grijpma, D. W. & Feijen, J. Physical properties of high molecular weight 1,3-trimethylene carbonate and D,L-lactide copolymers. *J. Mater. Sci. Mater. Med.* **14**, 767–773 (2003).

120. Pêgo, A. P., Poot, A. A., Grijpma, D. W. & Feijen, J. In vitro degradation of trimethylene carbonate based (Co)polymers. *Macromol. Biosci.* **2**, 411–419 (2002).

121. Messias, A. D., Martins, K. F., Motta, A. C. & Duek, E. A. de R. Synthesis, Characterization, and Osteoblastic Cell Culture of Poly(L-co-D,L-lactide-co-trimethylene carbonate) Scaffolds. *Int. J. Biomater.* **2014**, 1–7 (2014).

122. Yamada, S., Yassin, M. A., Schwarz, T., Hansmann, J. & Mustafa, K. Induction of osteogenic differentiation of bone marrow stromal cells on 3D polyester-based scaffolds solely by subphysiological fluidic stimulation in a laminar flow bioreactor. *J. Tissue Eng.* **12**, 1–12 (2021).

123. Shanbhag, S. *et al.* Bone regeneration in rat calvarial defects using dissociated or spheroid mesenchymal stromal cells in scaffold-hydrogel constructs. *Stem Cell Res. Ther.* **12**, 575 (2021).

124. Louvrier, A. *et al.* How useful is 3D printing in maxillofacial surgery? *J. Stomatol. Oral Maxillofac. Surg.* **118**, 206–212 (2017).

125. De La Peña, A., De La Peña-Brambila, J., Pérez-De La Torre, J., Ochoa, M. & Gallardo, G. J. Low-cost customized cranioplasty using a 3D digital printing model: a case report. *3D Print. Med.* **4**, 4 (2018).

126. Hassan, M. N. *et al.* The bone regeneration capacity of 3D-printed templates in calvarial defect models: A systematic review and meta-analysis. *Acta Biomater.* **91**, 1–23 (2019).

127. Henkel, J. *et al.* Bone Regeneration Based on Tissue Engineering Conceptions — A 21st Century Perspective. *Bone Res.* **1**, 216–248 (2013).

128. Hesuani, Y. D. *et al.* Design and Implementation of Novel Multifunctional 3D Bioprinter. *3D Print. Addit. Manuf.* **3**, 64–68 (2016).

129. Duty, C. *et al.* What makes a material printable? A viscoelastic model for extrusion-based 3D printing of polymers. *J. Manuf. Process.* **35**, 526–537 (2018).

130. Tang, D. *et al.* Biofabrication of bone tissue: Approaches, challenges and translation for bone regeneration. *Biomaterials* **83**, 363–382 (2016).

131. Dávila, J. L. *et al.* Fabrication of PCL/β-TCP scaffolds by 3D mini-screw extrusion printing. *J. Appl. Polym. Sci.* **133**, 43031 (2016).

132. Jain, S., Fuoco, T., Yassin, M. A., Mustafa, K. & Finne-Wistrand, A. Printability and Critical Insight into Polymer Properties during Direct-Extrusion Based 3D Printing of Medical Grade Polylactide and Copolyesters. *Biomacromolecules* **21**, 388–396 (2020).

133. Jakus, A. E. *et al.* Hyperelastic "bone": A highly versatile, growth factor–free, osteoregenerative, scalable, and surgically friendly biomaterial. *Sci. Transl. Med.* **8**, 358ra127 (2016).

134. Heo, E. Y. *et al.* Novel 3D printed alginate–BFP1 hybrid scaffolds for enhanced bone regeneration. *J. Ind. Eng. Chem.* **45**, 61–67 (2017).

135. Hong, J. M. *et al.* Enhancement of bone regeneration through facile surface functionalization of solid freeform fabrication-based three-dimensional scaffolds using mussel adhesive proteins. *Acta Biomater.* **8**, 2578–2586 (2012).

136. Lee, J.-Y., Choi, B., Wu, B. & Lee, M. Customized biomimetic scaffolds created by indirect three-dimensional printing for tissue engineering. *Biofabrication* **5**, 045003 (2013).

137. Kwon, D. Y. *et al.* A computer-designed scaffold for bone regeneration within cranial defect using human dental pulp stem cells. *Sci. Rep.* **5**, 12721 (2015).

138. Lee, J. W. *et al.* Bone regeneration using a microstereolithography-produced customized poly(propylene fumarate)/diethyl fumarate photopolymer 3D scaffold incorporating BMP-2 loaded PLGA microspheres. *Biomaterials* **32**, 744–752 (2011).

139. Wang, Z. *et al.* Analysis of factors influencing bone ingrowth into three-dimensional printed porous metal scaffolds: A review. *J. Alloys Compd.* **717**, 271–285 (2017).

140. Black, C. *et al.* Characterisation and evaluation of the regenerative capacity of Stro-4+ enriched bone marrow mesenchymal stromal cells using bovine extracellular matrix hydrogel and a novel biocompatible melt electro-written medical-grade polycaprolactone scaffold. *Biomaterials* **247**, 119998 (2020).

141. Sparks, D. S. *et al.* A preclinical large-animal model for the assessment of critical-size load-bearing bone defect reconstruction. *Nat. Protoc.* **15**, 877–924 (2020).

142. Rohner, D. *et al.* Individuell mit CAD-CAM-Technik hergestellte, bioresorbierbare dreidimensionale Polycaprolaktongerüste zur experimentellen Rekonstruktion von kraniofazialen Defekten beim Schwein. *Mund-, Kiefer- und Gesichtschirurgie* **6**, 162–167 (2002).

143. Rohner, D., Hutmacher, D. W., Cheng, T. K., Oberholzer, M. & Hammer, B. In Vivo Efficacy of Bone-Marrow-Coated Polycaprolactone Scaffolds for the Reconstruction of Orbital Defects in the Pig. *J. Biomed. Mater. Res. - Part B Appl. Biomater.* **66**, 574–580 (2003).

144. Hutmacher, D. W., Schantz, J. T., Lam, C. X. F., Tan, K. C. & Lim, T. C. State of the art and future directions of scaffold-based bone engineering from a

biomaterials perspective. *J. Tissue Eng. Regen. Med.* **1**, 245–260 (2007).

145. Berner, A. *et al.* Autologous vs. allogenic mesenchymal progenitor cells for the reconstruction of critical sized segmental tibial bone defects in aged sheep. *Acta Biomater.* **9**, 7874–7884 (2013).

146. Henkel, J. *et al.* Scaffold-guided bone regeneration in large volume tibial segmental defects. *Bone* **153**, 116163 (2021).

147. Kobbe, P. *et al.* Convergence of scaffold-guided bone regeneration and RIA bone grafting for the treatment of a critical-sized bone defect of the femoral shaft. *Eur. J. Med. Res.* **25**, 70 (2020).

148. Li, X. *et al.* Composite PLA/PEG/nHA/Dexamethasone Scaffold Prepared by 3D Printing for Bone Regeneration. *Macromol. Biosci.* **18**, 1800068 (2018).

149. Diomede, F. *et al.* Three-dimensional printed PLA scaffold and human gingival stem cell-derived extracellular vesicles: A new tool for bone defect repair. *Stem Cell Res. Ther.* **9**, 1–21 (2018).

150. Kim, B. S., Yang, S. S. & Kim, C. S. Incorporation of BMP-2 nanoparticles on the surface of a 3D-printed hydroxyapatite scaffold using an ε-polycaprolactone polymer emulsion coating method for bone tissue engineering. *Colloids Surfaces B Biointerfaces* **170**, 421–429 (2018).

151. Komlev, V. S. *et al.* 3D Printing of Octacalcium Phosphate Bone Substitutes. *Front. Bioeng. Biotechnol.* **3**, 1–7 (2015).

152. Liberati, A. *et al.* The PRISMA statement for reporting systematic reviews and meta-analyses of studies that evaluate healthcare interventions: explanation and elaboration. *BMJ* **339**, b2700 (2009).

153. Sun, T. *et al.* Loading of BMP-2-related peptide onto three-dimensional nano-hydroxyapatite scaffolds accelerates mineralization in critical-sized cranial bone defects. *J. Tissue Eng. Regen. Med.* **12**, 864–877 (2018).

154. Bruyas, A. *et al.* Systematic characterization of 3D-printed PCL/β-TCP scaffolds for biomedical devices and bone tissue engineering: Influence of composition and porosity. *J. Mater. Res.* **33**, 1948–1959 (2018).

155. Cork, J., Whittaker, A. K., Cooper-White, J. J. & Grøndahl, L. Tensile properties and in vitro degradation of P(TMC-co-LLA) elastomers. *J. Mater. Chem. B* **3**, 4406–4416 (2015).

156. Shim, J. *et al.* Porosity effect of 3D-printed polycaprolactone membranes on calvarial defect model for guided bone regeneration. *Biomed. Mater.* **13**, 015014 (2017).

157. Shim, J.-H. *et al.* Efficacy of rhBMP-2 loaded PCL/PLGA/ β -TCP guided bone

regeneration membrane fabricated by 3D printing technology for reconstruction of calvaria defects in rabbit. *Biomed. Mater.* **9**, 065006 (2014).

158. Tamimi, F. *et al.* Craniofacial vertical bone augmentation: A comparison between 3D printed monolithic monetite blocks and autologous onlay grafts in the rabbit. *Biomaterials* **30**, 6318–6326 (2009).

159. Chong, E. J. *et al.* Evaluation of electrospun PCL/gelatin nanofibrous scaffold for wound healing and layered dermal reconstitution. *Acta Biomater.* **3**, 321–330 (2007).

160. Turnbull, G. *et al.* 3D bioactive composite scaffolds for bone tissue engineering. *Bioact. Mater.* **3**, 278–314 (2018).

161. Jain, S. *et al.* Engineering 3D degradable, pliable scaffolds toward adipose tissue regeneration; optimized printability, simulations and surface modification. *J. Tissue Eng.* **11**, 1–17 (2020).

162. Jain, S. *et al.* Understanding of how the properties of medical grade lactide based copolymer scaffolds influence adipose tissue regeneration: Sterilization and a systematic in vitro assessment. *Mater. Sci. Eng. C* **124**, 112020 (2021).

163. Xue, R. *et al.* Polycaprolactone nanofiber scaffold enhances the osteogenic differentiation potency of various human tissue-derived mesenchymal stem cells. *Stem Cell Res. Ther.* **8**, 148 (2017).

164. Luu, H. H. *et al.* Distinct roles of bone morphogenetic proteins in osteogenic differentiation of mesenchymal stem cells. *J. Orthop. Res.* **25**, 665–677 (2007).

165. Querido, W. *et al.* Ultrastructural and mineral phase characterization of the bone-like matrix assembled in F-OST osteoblast cultures. *Calcif. Tissue Int.* **89**, 358–371 (2011).

166. Bosetti, M., Boccafoschi, F., Leigheb, M. & Cannas, M. F. Effect of different growth factors on human osteoblasts activities: A possible application in bone regeneration for tissue engineering. *Biomol. Eng.* **24**, 613–618 (2007).

167. Wang, Q. *et al.* Osteogenic growth peptide-loaded 3D-printed PCL scaffolds for the promotion of osteogenesis through the ERK pathway. *Mater. Des.* **193**, 108811 (2020).

168. Rossol, M. *et al.* Extracellular Ca2+ is a danger signal activating the NLRP3 inflammasome through G protein-coupled calcium sensing receptors. *Nat. Commun.* **3**, 1329 (2012).

169. Sadowska, J. M., Guillem-Marti, J., Montufar, E. B., Espanol, M. & Ginebra, M. P. Biomimetic versus sintered calcium phosphates: The in vitro behavior of osteoblasts and mesenchymal stem cells. *Tissue Eng. - Part A* **23**, 1297–1309 (2017).

170. Sadowska, J. M. *et al.* In vitro response of mesenchymal stem cells to biomimetic hydroxyapatite substrates: A new strategy to assess the effect of ion exchange. *Acta Biomater.* **76**, 319–332 (2018).

171. Zhao, R. *et al.* Selective effect of hydroxyapatite nanoparticles on osteoporotic and healthy bone formation correlates with intracellular calcium homeostasis regulation. *Acta Biomater.* **59**, 338–350 (2017).

172. Chung, L. *et al.* Interleukin 17 and senescent cells regulate the foreign body response to synthetic material implants in mice and humans. *Sci. Transl. Med.* **12**, (2020).

173. Shanbhag, S. *et al.* Ectopic Bone Tissue Engineering in Mice Using Human Gingiva or Bone Marrow-Derived Stromal/Progenitor Cells in Scaffold-Hydrogel Constructs. *Front. Bioeng. Biotechnol.* **9**, 1–14 (2021).

174. Rai, B. *et al.* Differences between in vitro viability and differentiation and in vivo bone-forming efficacy of human mesenchymal stem cells cultured on PCL-TCP scaffolds. *Biomaterials* **31**, 7960–7970 (2010).

175. Chen, S. *et al.* Biomaterials with structural hierarchy and controlled 3D nanotopography guide endogenous bone regeneration. *Sci. Adv.* **7**, 1–15 (2021).

176. Paris, M. *et al.* Scaffold curvature-mediated novel biomineralization process originates a continuous soft tissue-to-bone interface. *Acta Biomater.* **60**, 64–80 (2017).

Original scientific reports (studies)

I

<u>Study I</u>

M. N. Hassan, M. A. Yassin, S. Suliman, S. A. Lie, H. Gjengedal, and K. Mustafa. “The bone regeneration capacity of 3D-printed templates in calvarial defect models: A systematic review and meta-analysis” Acta Biomaterialia, vol. 91, pp. 1–23, Jun. 2019.

Journal Impact Factor (2022) = 10.6

Acta Biomaterialia 91 (2019) 1–23

Contents lists available at ScienceDirect

Acta Biomaterialia

journal homepage: www.elsevier.com/locate/actabiomat

Review article

The bone regeneration capacity of 3D-printed templates in calvarial defect models: A systematic review and meta-analysis

Mohamad Nageeb Hassan *, Mohammed Ahmed Yassin, Salwa Suliman, Stein Atle Lie, Harald Gjengedal, Kamal Mustafa *

Tissue Engineering Group, Department of Clinical Dentistry, Faculty of Medicine, University of Bergen, Årstadveien 19, 5009 Bergen, Norway

ARTICLE INFO

Article history:
Received 4 January 2019
Received in revised form 3 April 2019
Accepted 4 April 2019
Available online 11 April 2019

Keywords:
3D printing
Degradable template
Bone regeneration
Calvarial bone defect

ABSTRACT

3D-printed templates are being used for bone tissue regeneration (BTR) as temporary guides. In the current review, we analyze the factors considered in producing potentially bioresorbable/degradable 3D-printed templates and their influence on BTR in calvarial bone defect (CBD) animal models. In addition, a meta-analysis was done to compare the achieved BTR for each type of template material (polymer, ceramic or composites). Database collection was completed by January 2018, and the inclusion criteria were all titles and keywords combining 3D printing and BTR in CBD models. Clinical trials and poorly-documented *in vivo* studies were excluded from this study. A total of 45 relevant studies were finally included and reviewed, and an additional check list was followed before inclusion in the meta-analysis, where material type, porosity %, and the regenerated bone area were collected and analyzed statistically.

Overall, the capacity of the printed templates to support BTR was found to depend in large part on the amount of available space (porosity %) provided by the printed templates. Printed ceramic and composite templates showed the best BTR capacity, and the optimum printed template structure was found to have total porosity >50% with a pore diameter between 300 and 400 μm. Additional features and engineered macro-channels within the printed templates increased BTR capacity at long time points (12 weeks). Although the size of bone defects in rabbits was larger than in rats, BTR was greater in rabbits (almost double) at all time points and for all materials used.

Statement of Significance

In the present study, we reviewed the factors considered in producing degradable 3D-printed templates and their influence on bone tissue regeneration (BTR) in calvarial bone defects through the last 15 years. A meta-analysis was applied on the collected data to quantify and analyze BTR related to each type of template material.

The concluded data states the importance of 3D-printed templates for BTR and indicates the ideal design required for an effective clinical translation. The evidence-based guidelines for the best BTR capacity endorse the use of printed composite and ceramic templates with total porosity >50%, pore diameter between 300 and 400 μm, and added engineered macro-channels within the printed templates.

Contents

* Corresponding authors.
E-mail addresses: nageeb.hassan@uib.no (M.N. Hassan), mohammed.yassin@uib.no (M.A. Yassin), salwa.suliman@uib.no (S. Suliman), stein.lie@uib.no (S.A. Lie), harald.gjengedal@uib.no (H. Gjengedal), kamal.mustafa@uib.no (K. Mustafa).

https://doi.org/10.1016/j.actbio.2019.04.017
1742-7061/

1. Introduction

Quarter a century ago, the classical foundations of "tissue engineering" were described in 1993 by Langer and Vacanti [1] to provide some solutions to tissue repair and regeneration, in parallel with the first patent on additive manufacturing [2]. Both fields are still expanding and more achievements are expected. Tissue engineering was introduced as an alternative approach to replacing loss and failure of organs since there was a significant shortage in donors [3] and difficulties in overcoming host immune responses leading to graft failure [4].

Bone is a highly dynamic tissue that plays different roles in human physiology, in addition to its major role in the mechanical support and protection of body organs [5,6]. It is one of the most frequently replaced tissues due to loss from osteoporosis, trauma and as a result of cancer resections [7]. To restore large osseous defects is a great challenge, particularly in load-bearing areas (e.g. jaws and limbs), yet around one million procedures occur each year in Europe and the worldwide market is currently estimated at € 5 billion [8]. The use of autogenous bone grafts is the current gold standard treatment but it has various limitations, including donor site morbidity and lack of availability [9].

The process of bone tissue regeneration (BTR) is dynamic and depends on the interplay between potential osteogenic cells, mechanical and structural properties of the surrounding extracellular matrix (ECM) and a microenvironment containing ions and growth factors [10]. Use of appropriate biomaterial scaffolds or templates is crucial for restoring, maintaining and improving the BTR process with a spatiotemporal accuracy [11,12]. Various preparation methods have been used to fabricate such templates including salt-leaching, solvent-casting, phase separation, gas-foaming, freeze-drying, and, most recently, 3D printing [13].

3D printing, a promising emerging technology facing the current global socio-economic health risks [14], is designed to organize the required porous properties of the template into an appropriate structure using computer-enabled printers. A 3D printer provides layer-by-layer fabrication of physical structures by selectively adding materials/inks from a feed print head, according to a programmed digital plan/model [15]. Uses of 3D printing technology varies from customizing dental guides in orthognathic surgeries, to stents to guide for reconstructions surgeries [16,17], or even prosthetic parts in cranioplasty [18,19] using "solid" non-degradable biomaterials.

As a promising strategy, 3D printing has attracted interest due to its facile preparation process [20] which might replace complicated processes currently used for preparing tissue templates. In addition, it can produce a highly porous structure with superior interconnectivity [21], and fabricate custom templates with specific or complex anatomic shapes [22] in a fast and reproducible way [23] (see Fig. 1).

The biomaterials used in printing degradable templates for *in vivo* use should be biocompatible in addition to being printable. The digital model should also consider various biomechanical and biological guidelines to facilitate proper implantation, tissue integration and healing. Various biodegradable, printed polymeric, ceramic and composite [24] templates has been prepared as prototypes for BTR [25] and implanted *in vivo* in different skeletal sites. However, some studies have shown distinct alterations between the hypothesized strategy design based on the *in vitro* outcomes and further implemented *in vivo* experiments [26,27].

Degradable biomaterials used in medicine began with polymeric biomaterials in 1969, when the US Food and Drug Administration (FDA) approved of polyglycolide (PGA) as a synthetic suture, followed by polylactide (PLA) and their co-polymers (PLGA) at different ratios [28]. Some of these polymeric templates were further used in calvarial bone defects (CBD) combined with osteogenic cells [29] or functionalized with bioactive molecules [30] to achieve BTR.

By the mid-1980s, another generation of biomaterials, in the form of bioactive materials, reached clinical use in a variety of orthopedic and dental applications. A bioactive material is one that elicits a specific biological response at the interface of the material, which results in the formation of a biological bond between tissues and the implanted material [31]. These include various composi-

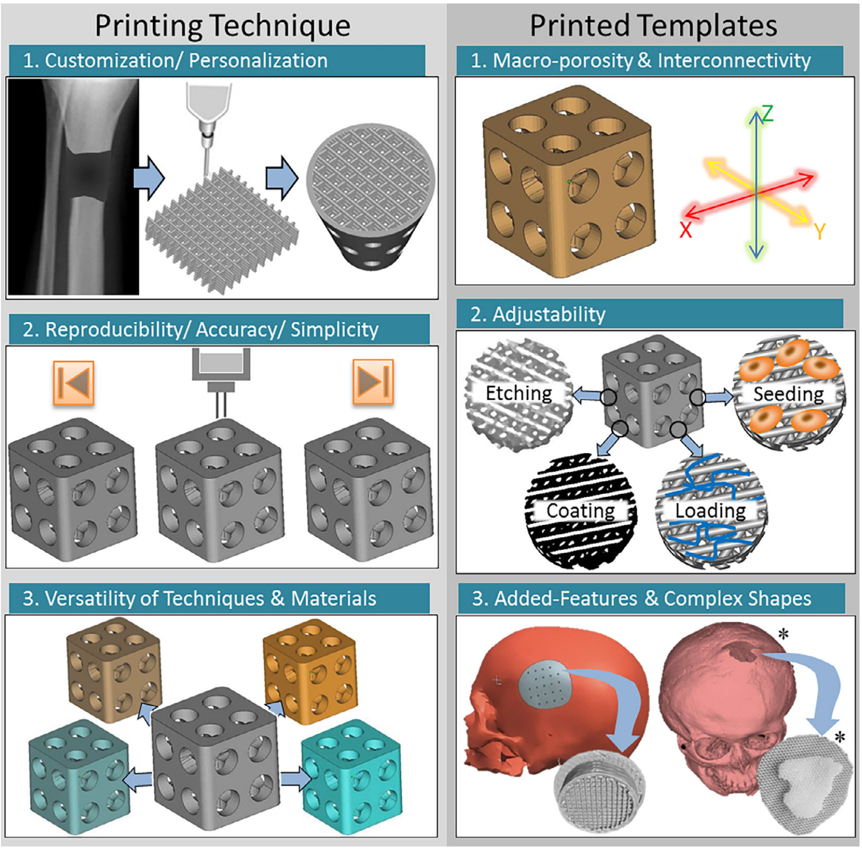

Fig. 1. A schematic presentation for the advantages of 3D printing techniques and the printed templates for BTR. The astrisk (*) labeled part – [41] (reproduced with permission from Thieme Gruppe).

tions of bioactive glasses (BG), and calcium phosphate (CaP)-based ceramics (e.g. hydroxyapatite (HA), β-tricalcium phosphate (TCP), biphasic calcium phosphates (BCP)) [32] that have been routinely used as porous implants, powders, and coatings on metallic prostheses to provide bioactive fixation with bone [33] and also used in CBD [7,34]. Thus CaP-based biomaterials are well known to be bioactive in BTR when used alone or in the form of composites with other polymers in order to gain better physical and processing properties.

In the literature, CBD are the most commonly used reproducible *in vivo* models for evaluating biological and host responses towards implanted 3D-printed templates. The main advantage of selecting CBD models to study BTR is the lack of mechanical stresses (i.e. are non-load bearing [35] that simplifies our understanding of the outcomes. We are intending here to understand the translational approaches, gaps and concepts of the degradable printed templates used for *in vivo* BTR in CBD through a systematic review and meta-analysis, before moving into clinical trials.

The aim of this study was to systematically review available literature to answer the question: what is the effect of using 3D-printed templates on BTR in terms of the newly regenerated bone area per total defect area (NBA/TDA) in CBD induced in experimental animal studies. In addition, a meta-analysis was done for the collected data to correlate the outcome NBA/TDA with each type of template's material (polymer, ceramic or composites), after excluding other factors affecting this process, e.g. the cells or growth factors used.

2. Materials and methods

2.1. Systematic search strategy

An initial database collection was done from the mid of September 2017 for all relevant peer-reviewed journal publications written in English, based in PubMed/MEDLINE and the Web of Science (ISI). Abstracts translated into English from French, German and Chinese in the scope of the current review were also considered. In addition, all the relevant articles found in the references and relevant review articles were checked and added as other sources. The systematic search was repeated on 16 January 2018, to include all research papers published in print or online through the end of 2017. Relevant studies from 2017 that were published online after 16 January 2018 were not included in the systematic review [36–39]

2.1.1. Data inclusion criteria

Inclusion criteria were all titles and keywords combining 3D printing and BTR in CBD *in vivo* (Table 1). Only research papers including resorbable/biodegradable polymers, ceramics and their

Table 1
Search Strategy for PubMed/MEDLINE on 16 September 2017 and 16 January 2018.

Search subject	Keywords	papers in MEDLINE	
		Mid Sep. 2017	Mid Jan. 2018
#1 Material category	((degradable OR biodegradable OR resorbable) AND/OR (template OR scaffold OR membrane) NOT (titanium OR Ti))	1,463,636	1,483,442
#2 Method of fabrication and design	((rapid prototyping OR 3D print* OR three-dimensional print* OR three-dimensional fabrication OR bioplotting OR additive manufactur*))	8428	9240
#3 Tissue and site	((bone) AND (regeneration OR augmentation OR repair OR reconstruction OR tissue engineering) AND (calvari* OR craniofacial OR cranial) AND (*in vivo* OR animal))	9245	9475
#4 Combination Search #2 and #3	((rapid prototyping OR 3D print* OR three-dimensional print* OR three-dimensional fabrication OR bioplotting OR additive manufactur*)) AND ((bone) AND (regeneration OR augmentation OR repair OR reconstruction OR tissue engineering) AND (calvari* OR craniofacial OR cranial) AND (*in vivo* OR animal))	83	94
#5 combination of all search key words	((rapid prototyping OR 3D print* OR three-dimensional print* OR three-dimensional fabrication OR bioplotting OR additive manufactur*)) AND ((degradable OR biodegradable OR resorbable) AND/OR (template OR template OR membrane) NOT (titanium OR Ti)) AND ((bone) AND (regeneration OR augmentation OR repair OR reconstruction OR tissue engineering) AND (calvari* OR craniofacial OR cranial) AND (*in vivo* OR animal))	44	52

composites were included. The database collection strategy was kept broad to avoid the exclusion of any relevant papers. The selection of key words and manual screening of the titles and abstracts was performed by two of the authors (M.N.H. and M.A.Y.). Variations among the findings between them were determined and categorized by direct discussions, to include only the papers consistent with the combined key words within the aim of the study.

2.1.2. Data exclusion criteria

All studies based on non-degradable biomaterials (e.g. titanium, PEEK) were excluded from the keyword searching stage. In addition, all *in vivo* studies on 3D-printed templates for craniofacial BTR with poorly-documented methodologies (e.g. did not mention the number of animals used) [40] were excluded, as well as all experimental [13] or clinical [41] trials. Our inclusion was site-specific to CBD, hence, BTR applications in prosthetic surgeries, mandibular [42] and midface reconstructions [43,44] were excluded. In addition, studies with printed templates without interconnected porosities were also excluded [45].

2.2. Data extraction

Key information data such as population, interventions, comparators, outcomes, and study design (PICOS), were extracted from each included study according to PRISMA guidelines [46]. In addition to the printing technique, the template composition, design and porosity were set as the "intervention" factors. Nevertheless, data about the type and number of the animals used as "population" as well as the defect size and duration of BTR assessment were established as proportional factors for each animal model to understand the "outcome" results.

2.3. Quality assessment and risk of bias

The methodological quality of the included animal studies were analyzed according to SYRCLE's risk of bias tool for animal studies [47]. The answer on the included main 10 questions (tools) should be either with "yes" that indicated low risk of bias, or "no" that indicated high risk of bias. For unclear items an answer with "unclear" was assigned.

2.4. Meta-analysis

Additional inclusion criteria were monitored and a checklist was prepared (Table 2) to assess the relevance of the included *in vivo* studies in the meta-analysis study and to minimize data heterogenicity. The quantitative measure of BTR for each template (effect size) was calculated and collected for each template group (type) per each time point for both rabbit and rat models.

The template porosity % and mean NBA/TDA ± standard deviation (SD) for each time point were copied from each included study. In the studies where such data were plotted only in graphs (e.g. bar charts), these data were digitally measured directly from the graphs using ImageJ software (NIH – USA). In addition, in a few studies where the data were plotted in box and whiskers graphs [35], the mean ± SD were re-calculated from the given quartiles' data. In other studies where the exact porosity of the template was not recorded within the text, we have calculated the macro-porosity from the printing parameters (strand width and distance between strands) as either stated in their methodologies or measured from the supplied photo of the template [48].

3. Results

3.1. Systematic search outcomes

From an initial pool of 65 relevant search-titles collected from Pubmed and Web of Science, only 26 studies were included after their title and abstract screening applying the inclusion/extrusion criteria check list. After full text analysis, a further 2 studies were excluded because the *in vivo* defect was not site-specific to CBD. The assessment of references included from the initial pool of

Table 2
Check lists of the included studies in meta-analysis.

Main Check List for included studies in Meta-analysis	Additional Check List to achieve homogenous data analysis
✓ 3D-printed template (resorbable)	✓ Excluding printed membranes (GTR)
✓ Calvarial bone regeneration	✓ Excluding printed particles templates
✓ *In vivo* animal model	✓ Excluding added biological factors
✓ Defined study parameters and number of animal (n)/group	✓ Excluding partial-thickness defects
✓ Histomorphometric quantification (from histological sections)	✓ Excluding micro-computed tomography (μCT) histomorphometry
✓ Defined the type of printed material(s)	

relevant studies plus other sources lead to the inclusion of an additional 21 studies, thus giving a total of 45 studies in the systematic review (Fig. 2).

It was noticed that in the first 10 years following initial publications about 3D-printed templates in CBD *in vivo* (2003–2012), only 14 articles were published for a mean of 1.2 articles per year. These studies were initiated by groups in USA and Singapore [49–51]. Within the past five years (2013–2017) the field was rapidly growing with a total of 31 published articles dominated by research groups in South Korea and China (Fig. 3). Within the included studies, printed templates were used in CBD of 6 different animal models: rats (19 studies), rabbits (18 studies), mice (4 studies), sheeps (2 studies), and pigs and goats (1 study/each).

The vast majority of studies were in rodents, exploring the effect of a wide variety of printed biomaterials with different combinations and ratios (Table 3). Almost half of the included studies were found to combine printed templates with cells, growth factors, or both, while the most common methods to assess BTR were either histology or micro-computed tomography (μCT) or both.

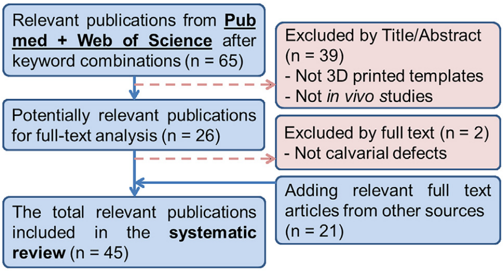

Fig. 2. Flowchart for the study screening and selection process and reasons for inclusion/exclusion. n = number of publications.

3.2. Printed calcium phosphates in CBD

Printed HA (particle size around 40 μm) templates were used in early attempts of using printed templates in CBD (8 mm Ø) without added cells or growth factors [50]. The added features (macro-pore size and axial channels) were found to improve the ability of printed HA templates to promote BTR compared with HA templates without axial channels.

When printed HA templates with smaller particle size (2 μm) were applied in CBD (11 mm Ø) in rabbits, a trend towards increased BTR and less soft tissue ingrowth was noticed within the template's smaller macro-pore channels (around 250 μm Ø) [52]. The use of macro-pore channels (250–750 μm Ø) with dimensions matching the ingrowing trabecular bone (100–250 μm Ø) was effective in conducting new bone across these "osteoconductive" templates in a rapid way across significant distances up to 16 weeks [52].

On the other hand, HA/TCP templates degraded faster than HA and demonstrated greater capacity for BTR (50% vs 30% NBA/TDA, respectively), in Sprague Dawley (Sp.Daw.) rats [53]. However, both printed templates showed significantly more BTR than the "commercialized" conventional porous HA (less than 10% NBA/TDA).

3.3. The enrichment of printed polymers and their composites

The first application of 3D-printed templates in CBD was by a research group based in the USA, who published three parallel studies in 2003 [49,50,54], using Ink-Jet 3D powder printing technology (TheriForm™ process). The bare templates were applied in CBD (8 mm Ø) of New Zealand White (NZW) rabbits without adding cells or growth factors. One study used the printed HA templates [50], while the other two studies used printed PLGA composite templates loaded with TCP (20%), implanted for at least 8 weeks and evaluated using histology and histomorphometry [49,54].

When compared to printed poly(DTE carbonate) (PDTEC) templates, the PLGA/TCP templates demonstrated their effect on the

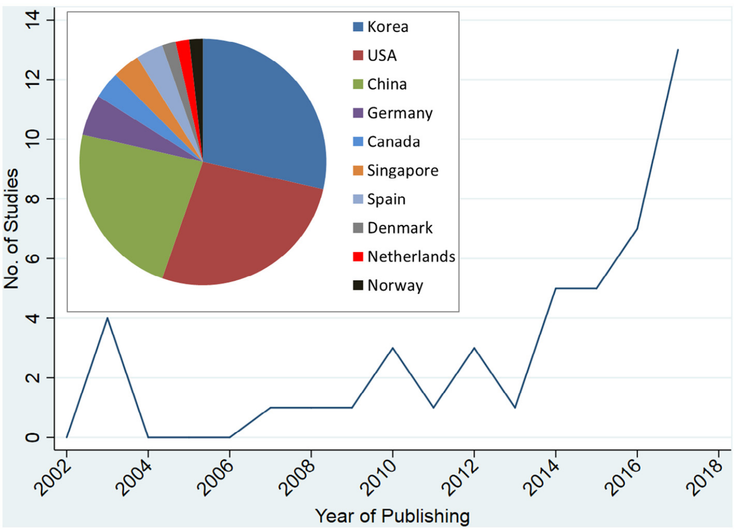

Fig. 3. Line chart representing the number of the published studies included in the systematic review sorted by the year of publishing. Inset graph for a pie chart represents the country affiliations of all the co-authors.

Table 3
All the potentially degradable printed templates used for calvarial bone regeneration *in vivo* (total = 45 study).

Author	Model	Template materials	Printing Technique	Used Cells/GF	Evaluation Method	Main Results
Simon et al. (2003) [54]	NZW (male, 3–4 kg)	PLGA/TCP *(20%) PDTEC	Ink-jet 3D powder Printing Technology (TheriForm™ process)	No	Radiographic, histology, histomorph.	Controlling the template architecture (pore geometry) affects the time and pattern of bone ingrowth
Roy et al. (2003) [49]	NZW (male, 3–4 kg)	PLGA/TCP *(20%) **(38–125 μm)	Ink-jet 3D powder Printing Technology (TheriForm™ process)	No	Florescence labeling, histology, histomorph.	Templates with macroscopic channels and gradient porosity had higher percentages of new bone area than without channels
Roy et al. (2003) [50]	NZW (male, 3–4 kg)	HA **(~40 μm)	Ink-jet 3D powder Printing Technology (TheriForm™ process)	No	Florescence labeling, histology, histomorph.	Template geometry; macropore size and axial channels; improve the ability of ceramic templates to promote bone healing
Schantz et al. (2003) [51]	NZW	PCL	FDM (FDM 3D Modeler system)	C-OB and MPCs	X-ray, μCT, histology, mechanical	The cell-seeded constructs revealed about 60% more calcification area than the unseeded templates or unrepaired defects
Simon et al. (2007) [52]	NZW (3.5–4 kg)	HA **(~2 μm)	direct-write process (JL2000, Sandia National Laboratories, Albuquerque, NM)	No	μCT, histology, SEM	There was a trend toward increased bone tissue and least soft tissue ingrowth within smaller macro-pore channels
Yu et al. (2008) [93]	Goats (15–18 kg; 1 year)	PLGA/TCP *(30%)	Low-temperature extrusion-molding (TissForm™, Dep. of Mech. Eng. Tsinghua University, China)	BMP-2	X-ray, CT scans, histology, mechanical	PLGA/TCP templates loaded with BMP-2 showed modest biodegradation and excellent osteogenesis
Tamimi et al. (2009) [82]	NZW (3.5–4 kg)	Monetite/TCP	3D-powder printing system (Z-Corporation, USA) using the TCP powder	No	Histology, histomorph, SEM	The bone height gained with monetite blocks was comparable to that with autologous bone. (vertical bone augmentation)
Kim et al. (2010) [59]	Sp.Daw. (240–260 g)	PCL/PLGA/TCP	Multihead deposition system (MHDS)	OB HUVECs	μCT, histology, immunohist.	Using OB and HUVECs seeded on printed templates produce more bone regeneration than either of them alone
Haberstroh et al. (2010) [98]	Merino sheeps (female, 72 ± 14 kg)	PLGA, TCP/Col, TCP/Col/Chit (hydrogel)	3D-bioplotting technology	OLB OLP	Histomorph.	The hydrogels had the best new bone formation and biodegradation, however, their stiffness are not applicable
Yeo et al. (2010) [57]	NZW	PCL/TCP *(20%)	FDM (3D Modeler RP system from Stratasys Inc, Eden Prairie, MN)	No	μCT, mechanical, histology	Templates with increased surface roughness displayed better new bone formation and mechanical properties
Lee et al. (2011) [61]	Wistar rats (male, 350–400 g, 12 w)	PPF/DEF/PLGA	Microstereolithography (MSTL)	BMP-2	μCT, histology and histomorph.	Printed templates showed significant increase in bone formation than traditional templates. BMP-2 promote more bone formation
Alge et al. (2012) [94]	NZW (male, ~ 4 kg)	PPF/DCPD	Benchtop rapid prototyping machine, T66 (Solidscape, Merrimack, NH)	MSCs	μCT, histology and histomorph.	Bone was able to grow into the template pores from the surrounding bone tissue, but MSCs did not show a significant positive effect
Shim et al. (2012) [58]	NZW (male, ~ 3.5 kg)	PCL/PLGA/TCP *(20%)	MHDS	No	μCT, histology and histomorph.	PCL/PLGAtemplate combined with TCP enhanced the compressive mechanical strength
Hong et al. (2012) [21]	Wistar rats (male, 350–400 g, 12 w)	PCL/PLGA	MHDS	MAPs/hADSCs	μCT, CB-CT and histology	Loading hADSCs in addition to MAP coating of 3D templates significantly enhanced bone regeneration capacity
Lee et al. (2013) [62]	Wistar rats (male, 350–400 g, 12 w)	PPF	MSTL	hADSCs/BMP-2	μCT, histology and histomorph.	Adding hADSCs to BMP on printed templates significantly improved bone reconstruction quality (synergetic effect)
Shim et al. (2014) [79]	NZW (~3.4 kg)	PCL/PLGA/TCP	MHDS	BMP-2	Histology, histomorph.	New bone was formed for the non-loaded membranes, but the sustained release of BMP significantly promoted bone formation
Jensen et al. (2014) [26]	Landrace Pigs (female, 8 mo)	PCL + nanoporous PCL	FDM (Fabrication, Bio-Scaffolder, SysEng GmbH, Germany)	AuMNCs/BMP-2	μCT, histology, histomorph.	Blocking of the printed template macro-pores (even by adding nanostructured-pores) showed negative effect on bone formation
Seol et al. (2014) [53]	Sp.Daw. (male, 12 w)	HA HA/TCP **(100 nm)	projection-based MSTL	No	μCT, histology	Printed HA/TCP templates had greater capacity for bone regeneration than HA alone. Also, rough surface increased calcium release

Zhao et al. (2014) [66]	Sp.Daw. (male, 12 w)	PVA/BG PHBHHx/BG *(75–87.5%) **(<50 μm)	3D-Bioplotter (EnvisionTEC, Germany)	No	μCT, histology, histomorph.	BG/PHBHHx composite templates had better mechanical properties and good osteogenic capability
Tamimi et al. (2014) [81]	NZW (3.5–4 kg)	Monetite/TCP	3D-powder printing system (Z-Corporation, USA) using the TCP powder	No	CT, CB-CT, histology, histomorph.	Adding interconnected channels and grooves to 3D printed templates results in more pronounced bone growth inside
Wang et al. (2015) [95]	C57BL/6J mice	Alg/HA	Pneumatic bioprinting System	Atsttrin	X-ray, histology, histomorph.	The anti-inflammatory properties and structure of 3D-printed Atsttrin-Alg/HA templates promote bone defect repair
Kwon et al. (2015) [23]	Sp.Daw. (320–350 g; 8 w)	PLGC	3D plotter (ProtekKorea; Daejeon, Korea)	hDPSCs/OF	Fluorescence imaging, μCT, histology, histomorph.	PLGC template with hDPSCs/OF resulted in the highest neo-bone formation. Also, *in vivo* degradation of PLGC templates was independent to cells
Zhao et al. (2015) [67]	Sp.Daw. (male, 12 w)	St-BG	3D-Bioplotter (EnvisionTEC, Germany)	No	Microfil perfusion, μCT, histology, histomorph.	Strontium-containing BG provided superior osteoconductive activity, stimulation to new blood vessel and degradation
Pati et al. (2015) [60]	Sp.Daw. (7 w)	PCL/PLGA/TCP **(~100 nm)	MHDS	D-ECM (coating)	μCT, histology	Adding D-ECM to printed templates generates an off-the-shelf bone graft substitutes with increased osteoconductive capacity
Dadsetan et al. (2015) [65]	NZW (females)	PPF/TCMP PPF/CHA PPF/BCP	Stereolithography (3D Systems, Valencia, CA)	BMP-2	μCT histology, histomorph., mechanical	CHA coated templates were the best and BMP-2 dose had a major effect on bone regeneration within the templates
Hung et al. (2016) [64]	Murine model	DCB/PCL	A custom hot-melt pressure extruder	hADSCs	CT, histology	Printing of hybrid templates (DCB:PCL) could fabricate complex geometries and showed greater bone regeneration than PCL
Sun et al. (2016) [70]	NZW (2.8 ± 0.2 kg)	Csi-Mg	3D ceramic ink writing equipment	No	μCT, histology, histomorph., mechanical	CSi-Mg enhanced new bone regeneration in addition to possessing excellent strength and reasonable degradability
Zhang et al. (2016) [76]	Sp.Daw. (300–350 g; 8 w)	PLA/HA *(15%)	mini-deposition system (MDS, located in Shanghai 3D printing center)	No	μCT, histology, histomorph.	Printed PLA/HA templates have normal inflammation reaction, good osteogenic and degradation activity as the conventional templates
Xiao et al. (2016) [100]	Sp.Daw. (350 ± 50 g; 3 mo)	BG **(~1 μm)	Robocasting Extrusion (RoboCAD 3.0; 3D Inks, LLC, OK, USA)	No	Histology, histomorph.	Templates with porosity gradient showed double flexural strength than the grid-like templates but same *in vivo* new bone formation
Kim J-et al. (2016) [35]	NZW (male, 12–15 w)	MgP	paste extruding deposition	No	μCT, histology and histomorph.	MgP completely degradable at 4 w and pore architecture formed by the template struts greatly influence bone formation
Li et al. (2016) [86]	BALB/c mice (male, 7 w)	PLGA/HA	3D low-temperature paste printer (Tissue Form II, China)	PDGFB-expressing LVvec	μCT, histology, Multi-photon microscopy	The released Lentiviral vectors and expressed PDGFB, facilitated angiogenesis and enhanced new bone regeneration
Pei et al. (2016) [68]	Sp.Daw. (12 w, 250–300 g)	C3S/BG cement	3D-Bioplotter (EnvisionTEC, Germany)	No	Fluorescent labeling, μCT, histology, histomorph.	C3S/BG templates significantly improved the osteogenic capacity compared to the pure C3S templates
Li et al. (2017) [96]	Sp.Daw. (male, 200 ± 20 g)	PCL	3D-Bioplotter (EnvisionTEC, Germany)	PRP	μCT, histology, histomorph.	Freeze-dried PRP-PCL templates showed better orthotopic bone formation than bare PCL or traditional PRP-PCL templates
Sun et al. (2017) [48]	Sp.Daw. (male, 7–8 w)	HA	Microsyringe extrusion free-forming system (MAM Micro-Droplet Jetting; Shanghai Fochif Mechatronics, China)	BMP-2/P28 peptide	μCT, histology histomorph.	Loading printed HA templates (sintered at 1000 °C) with P28 or BMP-2 promoted the repair of bone defects
Ishack et al. (2017) [97]	C57BL/6; A2A knockout mice	HA/TCP *(15:85)	3D direct-write microprinter gantry robot system (Aerotech Pittsburgh, PA)	BMP-2/DIPY	μCT, histology, histomorph.	Adding BMP-2 or dipyridamole significantly enhance bone regeneration
Hwang et al. (2017) [63]	Sp.Daw. (250–300 g; male)	PCL/PLGA/TCP *(20%)	Extrusion-based 3D printing	No	Histology, histomorph.	3D micro-blocks showed better ability to maintain bone defects and to support barrier membranes than powder bone grafts

(continued on next page)

Table 3 (*continued*)

Author	Model	Template materials	Printing Technique	Used Cells/GF	Evaluation Method	Main Results
Shao et al. (2017) [72]	NZW (2.7 ± 0.4 kg, male)	CSi/Mg/TCP	Robocasting extrusion (home-made equipment)	No	μCT, histology, histomorph., biomechanic.	CSi/Mg/TCP templates have significant synergetic effect on osteoconductivity than CSi or TCP templates alone
Shao et al. (2017) [71]	NZW (2.8 ± 0.5 kg, male)	CSi/Mg	Robocasting extrusion (home-made equipment)	No	μCT, histology, histomorph.	Templates with double layer pore morphology showed more significant osteoconductivity than single layer pore morphology at 8 and 12 w
Heo et al. (2017) [20]	NZW (2.7–3.4 kg)	Alg	3D printer developed by the Korea Institute of Machinery & Materials (KIMM)	BFP1	μCT	BFP1-conjugated hybrid Alg templates showed dose dependent, good bone regeneration effect at longer time intervals (12 w)
Qi et al. (2017) [69]	Sp.Daw. (250–300 g; male)	PCL/CSH/BG	3D-Bioplotter (EnvisionTEC, Germany)	No	μCT, histology, histomorph.	PCL/CSH/BG templates significantly enhanced new bone formation with the increase of BG % in templates
Cho et al. (2017)[83]	Sp.Daw.	PCL	Local installed dispenser (RPR-LM40, DCT Co., Korea)	No	μCT, histology, immunohist.	The highly interconnected porous SLUP templates promoted more bone regeneration than printed templates
Shim et al. (2017) [80]	NZW (male, 3.3–3.5 kg, 12–13 w)	PCL	MHDS	No	μCT, histology, histomorph.	Better new bone formation achieved with decreasing the pore size and porosity % of the printed membranes
Kwon et al. (2018) [84]	Sp.Daw. (320–350 g; 8 w)	PLA/TCP *(10–30%)	3D bioprinter (ProtekKorea; Daejeon, Korea)	MG-63	Fluorescence imaging, μCT, histology, histomorph.	Printed templates effectively support new bone formation. MG-63 cells showed significantly more new bone formation
Bekisz et al. (2018) [77]	Dorset/Finn sheep (~62 kg)	TCP/Col	Robocasting extrusion (RoboCAD 4.3, 3D Inks LLC, OK, USA)	DIPY (coat)	Histology, histomorph.	Osteogenesis was higher in DIPY-coated templates compared to controls
Kim et al. (2018) [78]	Sp.Daw. (male, 10 w)	MgP	Paste extrusion deposition (3D printing system manufactured in-house)	Indene compound	μCT, histology, histomorph, immunohist.	Indene loaded templates showed significant dose dependent enhancement to bone regeneration *in vivo*

Alg, alginate; AuMNCs, autologous mononuclear cells; BCP, biphasic calcium phosphate; BFP1, Bone formation peptide-1; BG, bioactive silicate glass; BMP-2, bone morphogenetic protein-2; C3S, tricalcium silicate; C-OB, calvarial osteoblasts; CHA, carbonated hydroxyapatite; Chit, chitosan; Col, collagen; CSH, calcium sulfate hydrate; CSi, calcium silicate (Wollastonite); D-ECM, decellularized cell-laid extra cellular matrix; DCB, decellularized bone matrix; DCPD, dicalcium phosphate dihydrate; DEF, diethyl fumerate; DIPY, dipyridamole; FDM, fused deposition modeling; HA, hydroxyapatite; hADSCs, human adipose tissue-derived stem cells; hDPSCs, human dental pulp stem cells; HUVECs, human umbilical vein endothelial cells; LVvec, lentiviral vectors; MAPs, recombinant mussel adhesive proteins; MG-63, human osteoblastoma cell line; Mg, magnesium; MgP, magnesium phosphate; mo, months; Monetite, dicalcium phosphate anhydrous; MPCs, mesenchymal progenitor cells; MSCs, mesenchymal stem cells; NZW, New Zealand white rabbit; OB, osteoblasts; OF, osteogenic factors; OLB; osteoblast-like cells from bone, OLP; Osteoblast-like cells from periosteum, PCL, polycaprolactone; PDGFB, platelet-derived growth factor-B; PDTEC, poly(DTE carbonate); PHBHHx, Poly(3-hydroxybutyrate-co-3-hydroxyhexanoate); PGA, poly(glycolide); PLA, Poly-L-lactide; PLGA, poly(D,L-lactide-co-glycolide); PLGC, PLA-co-PGA-co-PCL; PPF, poly(propylene fumarate); PRP, platelet-rich plasma; PVA, poly(vinyl alcohol); Sp.Daw, Sprague–Dawley rats; SLUP, salt-leaching using powder; St-BG, strontium-containing BG; TCMP, magnesium substituted β-tricalcium phosphate; TCP, β-tricalcium phosphate; w, weeks.

* Percent of the ceramic phase.

** Particle size of the ceramic phase.

time and pattern of bone ingrowth in relation to their architecture and pore geometry [54]. On the other hand, adding macroscopic channels and a porosity gradient to PLGA/TCP templates revealed much higher BTR than templates without channels [49].

Printed polycaprolactone (PCL) templates in CBD were introduced by another research group, at the national university of Singapore, in 2003 [51]. Before applying them *in vivo*, they were fully characterized for osteogenesis-inducing ability in a 3D culture system [55]. The PCL templates (70% porosity) were fabricated through fused-deposition modeling (FDM) and applied in large CBD (15 mm Ø) in NZW rabbits, for follow up intervals up to 3 months. The templates seeded with calvarial osteoblasts (OB) and mesenchymal progenitor cells, showed about 60% more calcification areas than both the unseeded template group and the empty CBD (negative controls) [51].

Later, the parameters necessary to process medical-grade PCL and its composites (PCL/HA, PCL/TCP) through FDM, were evaluated, patented, and approved for clinical use by FDA [44] based on 2 successful clinical trials [41,56]. Furthermore, the treatment of PCL based templates with NaOH increased their surface roughness and displayed better mechanical integration properties and better BTR in CBD [57].

Another substantial research work was coauthored by multidisciplinary research coordinated by a group at Pohang University of Science and Technology (POSTECH) – South Korea. This group printed various biomaterials, applied in the CBD (8 mm Ø) of NZW rabbits [58], Sp.Daw. rats [53,59,60] and Wistar rats [21,61,62]. In their primary endeavors, they used printed PCL/PLGA/TCP seeded with OB and human umbilical vein endothelial cells (HUVEC) in rat CBD [59]. After seeding each cell type alone on printed templates, they showed significant increase in BTR over unseeded templates, with significantly more activity for OB-seeded templates. However, significantly greater BTR was observed when combining both cell types on printed templates. On the other hand, when they applied printed poly(propylene fumarate) (PPF) based templates with/without bone morphogenetic protein-2 (BMP-2) in rats CBD, it was evident that BMP-2 loaded PPF templates significantly promoted BTR compared with unloaded printed templates at both the early (4 week) and later (11 week) time points [61]. Further, by adding pre-osteoblasts differentiated from adipose tissue-derived stem cells (ADSC) on PPF templates, an increased synergetic effect on BMP-loaded templates was seen [62].

Two main challenges were highlighted in their work [61]; the first was the poor degradation rate of PPF template that was problematic for BTR. The second problem was about the importance of developing a mechanism by which 3D-printed templates could attract stem cells from blood through surface treatment of the templates. They next focused on developing relatively fast degrading printed PCL/PLGA templates coated with adhesive proteins in order to promote the entrapment of stem cells and ADSC [21]. However, no significantly enhanced BTR was achieved using the advantage of better degradation, compared to the previously used poorly degradable PPF with the same parameters.

In general, BTR was found to increase significantly with composites than polymers at both the early (4 week) and late (8 week) time points [58]. In addition, the incorporation of TCP to the printed (PCL/PLGA) templates was found to enhance its compressive mechanical strength. Moreover, when PCL/PLGA/TCP functionalized with mineralized and decellularized ECM were used in the same defect model (8 week), BTR showed around 50% NBA/TDA [60]. However, using PCL/PLGA/TCP templates without functionalization yielded only 30% NBA/TDA [60]. Thus, functionalized templates were considered to be printable off-the-shelf bone graft substitutes/templates with increased osteoconductive capacity.

On the contrary, when mixed/filled with collagen, the printed PCL/PLGA/TCP in the form of micro-blocks (particle-like, to fill CBD) failed to show either satisfactory BTR or any significant difference in BTR from conventional BCP particles group for up to 8 weeks in rat CBD [63]. However, it should be noted that this study lacked the 3D support required by the printed templates for BTR.

Printed decellularized bone matrix (DCB) particles in the form of hybrid templates with PCL were also studied in mice CBD. They showed improved biological properties and surface roughness relative to pure PCL [64]. Although being significantly more bioactive than pure PCL templates *in vitro* and *in vivo*, only fractional BTR was found with the hybrid templates. More recently, a significant synergetic effect was shown for the printed PCL/TCP/DCB in rabbit CBD after 6 and 12 weeks follow-up [37].

Other successful trials used calcium phosphates (e.g. BCP, Mg-substituted tricalcium phosphate (TCMP), and carbonated HA (CHA)) coatings on the surface of printed PPF in order to enhance its biological properties [65]. The used printed templates (60% porosity) in oversized (15 mm Ø) CBD created in NZW rabbits, showed better BTR, with a superior action of CHA compared to TCP and BCP coatings.

3.4. Printed bioactive-glasses (BG) and silicate-based templates in CBD

Printed BG-based templates in CBD were first applied by the research group from Shanghai University – China, using a controlled degradability and architecture, osteoinductive and high compressive strength composite templates applied on the CBD (5 mm Ø) of Sp.Daw. rats [66–69]. A copolymer, polyhydroxybutyrate (PHB), was added to BG to print PHB/BG (1:3) that were tested for 8 weeks [66]. The histomorphometric data for NBA/TDA showed around 33.8% in case of PHB/BG, significantly higher than the regenerated bone with poly(vinly alcohol) (PVA)/BG (1:7) based templates (18.08%). This was attributed to the much less degradation rate of PVA-based templates. Nevertheless, the blank control group in this model did not exceed 5% NBA/TDA.

This was followed by further studies on the printing of modified forms of BG in the form of strontium (Sr)-containing [67], tricalcium silicate (C3S)-based [68] and calcium sulfate hydrate (CSH)-combined [69] BG templates. At the highest porosity % (70%) of printed Sr-BG, better osteoconductivity (36% NBA/TDA) was revealed, and additional stimulation of new blood vessel formation was demonstrated [67].

The relatively slow-degrading printed C3S/BG (7:3) templates at 70% porosity were found to have significantly improved osteogenic capacity, three times greater than the pure C3S. However, this did not exceed 30% NBA/TDA on histomorphometric analysis at 8 weeks [68]. Combining BG with the rapidly resorbing CSH (printed with PCL at different ratios) was found to be successful in BTR in CBD, with a direct proportion between NBA/TDA and the increase of BG ratio [69]. With the increase of BG ratio, BTR increased from 5% (at 0% BG) to around 30% (at 60% BG) at 8 weeks. However, it was still obvious from the histological micrographs that PCL/CSH/BG struts were un-resorbed up to 8 weeks, which would have resulted in insufficient room for BTR to grow at the highest bioactive ratios.

Another group of studies was done using printed calcium silicate (CSi) doped with magnesium (Mg) for BTR of CBD (8 mm Ø) in NZW rabbits [70–72]. This doping led to promoted mechanical and degradation properties for the developed CSi-Mg templates, while preserving its osteoactivity. This was proved through the histomorphometric data up to 12 weeks, where increasing the doping percentage led to significantly increased BTR up to 22% compared to pure CSi, that showed only 14% NBA/TDA [70]. On the other hand, with larger (double) pore size, significant BTR was observed at 8 and 12 weeks [71], although some mismatching in the histomorphometric quantitative outcomes of the single layer CSi templates was observed between both studies at 12 weeks [70,71].

Due to the favorable degradation rate of TCP, which is a clinically available product, further work was done through the addition of TCP within the printed CSi-Mg, which showed a synergetic effect on osteoconductivity (35% NBA/TDA, after 12 weeks) compared with each of these templates alone [72]. This suggests a role for the release of bioactive ions (in this case, of Ca^{+2}, Mg^{+2} and SiO_3^{+2}) together with the desired biodegradation rate to enhance BTR.

In addition to being tested in CBD, printed CSi-Mg templates were also tested in load-bearing sites in NZW rabbits i.e. in distal femur defect repair [73] and mandibular bone defects [74]. Among the other CSi and TCP templates used, CSi-Mg showed optimal pH values while degradation and the highest compressive strength before and after soaking in simulated body fluid. In addition, CSi-Mg showed the highest BTR% at both sites among the other tested biomaterials [73,74].

3.5. Quality assessment and risk of bias

The size of bone defects was critical factor in successful BTR [35], and the variability of surgical techniques was noticed among animal models used. It is known that CBD are non-healing when their diameters (Ø) are equal to or >4 mm in mice [64,75], 5 mm in rats [69,76], 8 mm in rabbits [72], and 22 mm in sheep [77]. In addition, it is inferred that animal models have influence on BTR outcomes, as some studies showed that at early time points in rats (e.g. 4 week) BTR was not prominent in histomorphometric analysis in negative control defects and in defects with printed templates implanted [78].

Among the differences in surgical techniques that might have influenced the implanted template outcomes, some studies that used 3D printed templates in CBD also used additional conventional membrane structures over the defect sites in order to prevent soft tissue ingrowth while healing [57,63]. On the other hand, others were isolating the implant site from the effect of any pericranium self-renewal capacity [61]. Few studies applied fixation to hold printed templates in place, using different methods to secure immobilization for better healing [51,79,80]. Finally, most of the studies were based on local (institutional/university-based) approvals of animal care committees, which may have differed.

The frequency distribution percent of the risk of bias assessment for each question of the SYRCLE risk of bias tool is shown in Figs. 4 and 5 for all the included studies in rabbits and rats, respectively. Within the analyzed studies for both animal models, there were low risks for selection bias, represented by the first 3 questions. However, a high risk of performance bias was detected because of the non-applied blinded care givers/investigators (question 5) and high risk of detection bias represented by the low extent of random selection of study models, and the unblended approach for outcome assessors (questions 6 and 7, respectively).

3.6. Meta-analysis

The meta-analysis performed in the current study was divided by animal model in order to avoid any bias in results related to variations among species. We found that the data liable for meta-analysis were only valid for rabbits and rats (Tables 4 and 5, respectively), while the number of animal studies to be compared in mice and large animals (Tables 6 and 7, respectively) were insufficient to extract reliable data. Therefore, we only included the histomorphometric data recorded from histological sections as NBA/TDA that should be more reliable. Differences could be detected in the same studies reporting both histological NBA/TDA and μCT (BV/TV) results [26,69], while in other studies only marginal differences were detected [66,70–72].

Accordingly, only 19 of the 37 studies included in the systematic review in rabbits and rats were consistent with the check list prepared for the inclusion criteria for the meta-analysis study and the exclusion was decided as follows. In the rabbit model, 18 studies were considered in the systematic review from which only

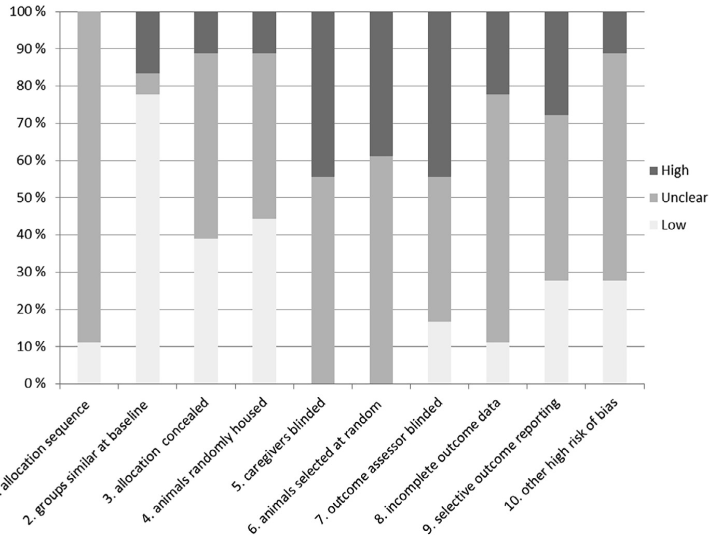

Fig. 4. The frequency distribution (%) of the risk of bias assessment for each question according to the SYRCLE's risk of bias tool in the included studies that used rabbit models. All items were judged as "yes", "unclear" or "no"; where yes = low risk of bias, unclear = unclear, and no = high risk of bias.

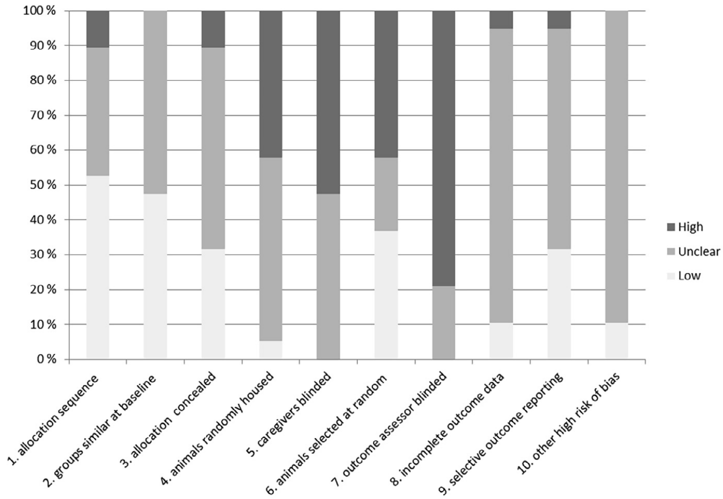

Fig. 5. The frequency distribution (%) of the risk of bias assessment for each question according to the SYRCLE's risk of bias tool in the included studies that used rats. All items were judged as "yes", "unclear" or "no"; where yes = low risk of bias, unclear = unclear, and no = high risk of bias.

Table 4
Showing the studies used printed templates in calvarial bone defects in rabbits.

Study	Template	Porosity (%)	Additional Features (%)	n	Defect Ø (mm)	Follow up (week)	Cells/GF	Included in Meta-analysis
Simon et al. (2003) [54]	PLGA(50)/TCP PDTEC	80–87 50 to 90	Macro-channels/Grid structure	6	8	8, 16	–	Yes
Roy et al. (2003) [49]	PLGA(50)/TCP PLGA(95)/TCP	80–87	Macro-channels	12	8	8	–	Yes
Roy et al. (2003) [50]	HA	45	Macro-channels	6	8	8	–	Yes
Schantz et al. (2003) [51]	PCL	70	–	10	15	12	C-OB/MPCs	No
Simon et al. (2007) [52]	HA	56–70	–	8	11	8, 16	–	No
Tamimi et al. (2009) [82]	Monetite/TCP	44	–	8	10	8	–	No
Yeo et al. (2010) [57]	PCL/TCP (20%)	75		3	6	2, 4, 8, 12, 24	–	No
Alge et al. (2012) [94]	PPF/DCPD	37	–	6	10	6	MSCs	Yes
Shim et al. (2012) [58]	PCL/PLGA PCL/PLGA/TCP	60	–	6	8	4, 8	–	Yes
Shim et al. (2014) [79]	PCL/PLGA/TCP	50	*Membranes	6	10	4, 8	BMP-2	No
Tamimi et al. (2014) [81]	Monetite/TCP	44	C-Groove/interconnected channels	16	10	8	–	No
Dadseta et al. (2015) [65]	PPF/TCMP PPF/CHA PPF/BCP	60	*TCMP, CHA, BCP coatings	4	15	6	BMP-2	Yes
Sun et al. (2016) [70]	CSi, CSi/Mg6 CSi/Mg10 CSi/Mg14	62	–	8	8	6, 12	–	Yes
Kim et al. (2016) [35]	MgP	37.8	8.52 or 17.53 (porosity %)	5	4, 6	4, 8	–	
Shao et al. (2017) [71]	TCP CSi/Mg10 CSi/Mg10/TCP	60.1 52.1 57.8	–	6	8	4, 8, 12	–	Yes
Shao et al. (2017) [72]	CSi CSi/Mg6	±59 ± 53	Double Pore Size	6	8	4, 8, 12	–	Yes
Heo et al. (2017) [20]	Alg	~50	–	6	8	6, 12	BFP1	No
Shim et al. (2017) [80]	PCL	305,070	*Membranes	8	6	4	–	No

Alg, alginate; BCP, biphasic calcium phosphate; BFP1, Bone formation peptide-1; BMP-2, bone morphogenetic protein-2; C-OB, calvarial osteoblasts; CHA, carbonated hydroxyapatite; CSi, calcium silicate (Wollastonite); DCPD, dicalcium phosphate dihydrate; HA, hydroxyapatite; Mg, magnesium; MgP, magnesium phosphate; Monetite, dicalcium phosphate anhydrous; MPCs, mesenchymal progenitor cells; MSCs, mesenchymal stem cells; n, number of defects/group/time point; Ø, bone defect diameter; PCL, polycaprolactone; PDTEC, poly(DTE carbonate); PLGA, poly(D,L-lactide-co-glycolide); PPF, poly(propylene fumarate); TCMP, magnesium substituted β-tricalcium phosphate; TCP, β-tricalcium phosphate.

9 studies were excluded for the meta-analysis as follows, Schantz et al. [51], Yeo et al. [57], Heo et al. [20] and Simon et al. [52] calculated histomorphometric data from μCT in terms of bone volume/total volume (not NBA/TDA), while Shim et al. [79,80] have used 3D-printed templates as guided tissue regeneration (GTR) membranes. The studies of Tamimi et al. calculated only the height

Table 5
Showing the studies used 3D printed templates in calvarial bone defects in rats.

Study	Template	Porosity (%)	Additional Porosity (%)	n	Defect Ø (mm)	Follow up (week)	Cells/GF	Included in Meta-analysis
Kim et al. (2010) [59]	PCL/PLGA/TCP	66.7	–	4	8	8, 12	OB/HUVECs	No
Lee et al. (2011) [61]	PPF/DEF/PLGA	>70	–	5	8	4, 11	BMP-2	Yes
Hong et al. (2012) [21]	PCL/PLGA	66.7	–	5	8	8	MAPs/hADSCs	No
Lee et al. (2013) [62]	PPF	>70	–	4	8	11	hADSCs/BMP-2	No
Seol et al. (2014) [53]	HA HA/TCP	50	6.02 3.47	5	8	16	–	Yes
Zhao et al. (2014) [66]	PVA/BG PHBHHx/BG	70	–	6	5	8	–	Yes
Kwon et al. (2015) [23]	PLGC	40	–	5	6	4, 8, 12	hDPSCs/OF	Yes
Zhao et al. (2015) [67]	St-BG	70	–	6	5	8	–	Yes
Pati et al. (2015) [60]	PCL/PLGA/TCP (~100 nm)	66	–	??	8	8	D-ECM (coat)	No
Zhang et al. (2016) [76]	PLA/HA (85:15)	60	–	8	5	4, 8	–	No
Xiao et al. (2016) [100]	BG	33–43	Porosity gradient	7	4.6	12	–	Yes
Pei et al. (2016) [68]	C3S/BG cement	70	–	10	5	8	–	No
Li et al. (2017) [96]	PCL	60	–	8	5	2, 4, 8, 12	PRP (coat)	Yes
Sun et al. (2017) [48]	HA	50	35	4	5	6, 12	BMP-2/P28 peptide	Yes
Hwang et al. (2017) [63]	PCL/PLGA/TCP	32	*Particle templates	8	8	2, 8	–	No
Qi et al. (2017) [69]	PCL/CSH/BG	46.6	21	6	5	8	–	Yes
Cho et al. (2017) [83]	PCL	57.2	–	6	8	4, 8	–	No
Kwon et al. (2018) [84]	PLA PLA/TCP (10–30%)	25	–	5	5	4, 8, 12	MG-63	No
Kim et al. (2018) [78]	MgP	46.6	–	6	5	4, 8	Indene compound	Yes

BG, bioactive silicate glass; BMP-2, bone morphogenetic protein-2; C3S, tricalcium silicate; CSH, calcium sulfate hydrate; D-ECM, decellularized cell-laid extra cellular matrix; DEF, diethyl fumerate; HA, hydroxyapatite; hADSCs, human adipose tissue-derived stem cells; hDPSCs, human dental pulp stem cells; HUVECs, human umbilical vein endothelial cells; MAPs, recombinant mussel adhesive proteins; MgP, magnesium phosphate; MG-63, human osteoblastoma cell line; n, number of defects/group/time point; OB, osteoblasts; OF, osteogenic factors; Ø, bone defect diameter; PCL, polycaprolactone; PHBHHx, Poly(3-hydroxybutyrate-co-3-hydroxyhexanoate); PGA, poly(glycolide); PLA, Poly-L-lactide; PLGA, Poly(D,L-lactide-co-glycolide); PLGC, PLA-co-PGA-co-PCL; PPF, poly(propylene fumarate); PRP, platelet-rich plasma; PVA, poly(vinyl alcohol); SLUP, salt-leaching using powder; St-BG, strontium-containing BG; TCP, β-tricalcium phosphate.

Table 6
Showing the studies used 3D printed templates in calvarial bone defects in mice.

Study	Template	Porosity (%)	Mouse type	n	Defect Ø (mm)	Follow up (week)	Cells/GF
Wang et al. (2015) [95]	Alg/HA	80	C57BL/6J mice	5	7 × 5	1, 8, 16	Atsttrin
Hung et al. (2016) [64]	DCB/PCL	60	Murine model	4	4	6, 12	hADSCs
Li et al. (2016) [86]	PLGA/HA	~50	BALB/c mice	6	4	8	PDGFB-expressing LVvec
Ishack et al. (2017) [97]	HA/TCP	55	C57BL/6; A2A knockout mice	5	3	2, 4, 8	BMP-2/DIPY

Alg, alginate; BMP-2, bone morphogenetic protein-2; DCB, decellularized bone matrix; DIPY, dipyridamole; HA, hydroxyapatite; hADSCs, human adipose tissue-derived stem cells; LVvec, lentiviral vectors; n, number of defects/group/time point; Ø, bone defect diameter; PCL, polycaprolactone; PDGFB, platelet-derived growth factor-B; PLGA, poly(D,L-lactide-co-glycolide); TCP, β-tricalcium phosphate.

Table 7
Showing the studies used 3D printed templates in calvarial bone defects in large animals.

Study	Template	Porosity (%)	Animal type	n	Defect Ø (mm)	Follow up (week)	Cells/GF
Yu et al. (2008) [93]	PLGA/TCP	40–90	Goats	3	15	12, 24	BMP-2
Haberstroh et al. (2010) [98]	PLGA, TCP/Col, TCP/Col/Chit (hydrogel)	~50	Merino sheeps	3	20 × 20	14	OLB OLP
Jensen et al. (2014) [26]	PCL	~80	Landrace Pigs	8	10	8, 12	AuMNCs/BMP-2
Bekisz et al. (2018) [77]	TCP/Col	43	Dorset/Finn sheep	5	11	3, 6	DIPY (coat)

AuMNCs, autologous mononuclear cells; BMP-2, bone morphogenetic protein-2; Chit, chitosan; Col, collagen; DIPY, dipyridamole; n, number of defects/group/time point; OLB; Osteoblast-like cells from bone, OLP; Osteoblast-like cells from periosteum, Ø, bone defect diameter; PCL, polycaprolactone; PLGA, poly(D,L-lactide-co-glycolide); TCP, β-tricalcium phosphate.

of BTR in partial calvarial defects [81,82], while Kim et al. [35] did not report the number of used rabbits either for each group or for the whole experiment. Thus, the remaining 9 studies in the rabbit models were considered in the meta-analysis.

In the rat model, only 10 studies were included in the meta-analysis, while the other 9 studies were excluded as follows: Kim et al. [59], Zhang et al. [76], Hong et al. [21], Cho et al. [83] and Kwon et al. [84] calculated histomorphometric data from μCT in terms of bone volume. The study of Lee et al. [62] was excluded because it only calculated the area of collagen-I after immunohistochemistry, and the represented data lack any standard deviation. The study of Hwang et al. [63] was excluded because the printed templates were used in the form of particles (micro-blocks), while Pati et al. [60] and Pei et al. [68] did not show a reliable number of animals used for each group. The data were considered heterogeneous at I-squared >50% [85].

3.6.1. The role of printed templates for BTR in rabbits

For the printed ceramic templates without additional porosity, their overall estimate of effect size was homogenous at 4, 6, and 8 weeks, and heterogeneous at 12 weeks. Within the homogenous data shown, BTR showed continuous increase with time (Fig. 6a). On the other hand, the printed ceramic templates with additional porosity revealed homogenous effect size only at 4 and 12 weeks (Fig. 6b).

The printed composite templates without additional porosity showed homogenous effect size at 6 and 8 weeks (Fig. 7a), while no homogenous data were shown for the printed composite templates with additional porosity (Fig. 7b). In contrast, the printed polymer templates without additional porosity showed homogenous effect size only at 8 weeks (Fig. 8a), while the printed polymer templates with additional porosity showed homogenous effect size at both 8 and 16 weeks (Fig. 8b).

Within the homogeneous data, the highest BTR for printed templates without additional porosity were observed for composite templates (8 week, 21.39 ± 7.79) and ceramic templates (12 week, 24.33 ± 5.33). The additional porosity was found to have higher BTR only when compared to printed ceramic templates at long-term follow up (12 week), otherwise there was no observed advantage for additional porosity on BTR in this animal model for the same biomaterial type and time points. On the other hand, the least BTR was observed for polymer templates even with additional porosity at 8 weeks (5.65 ± 1.56) and 16 weeks (9.99 ± 9.78).

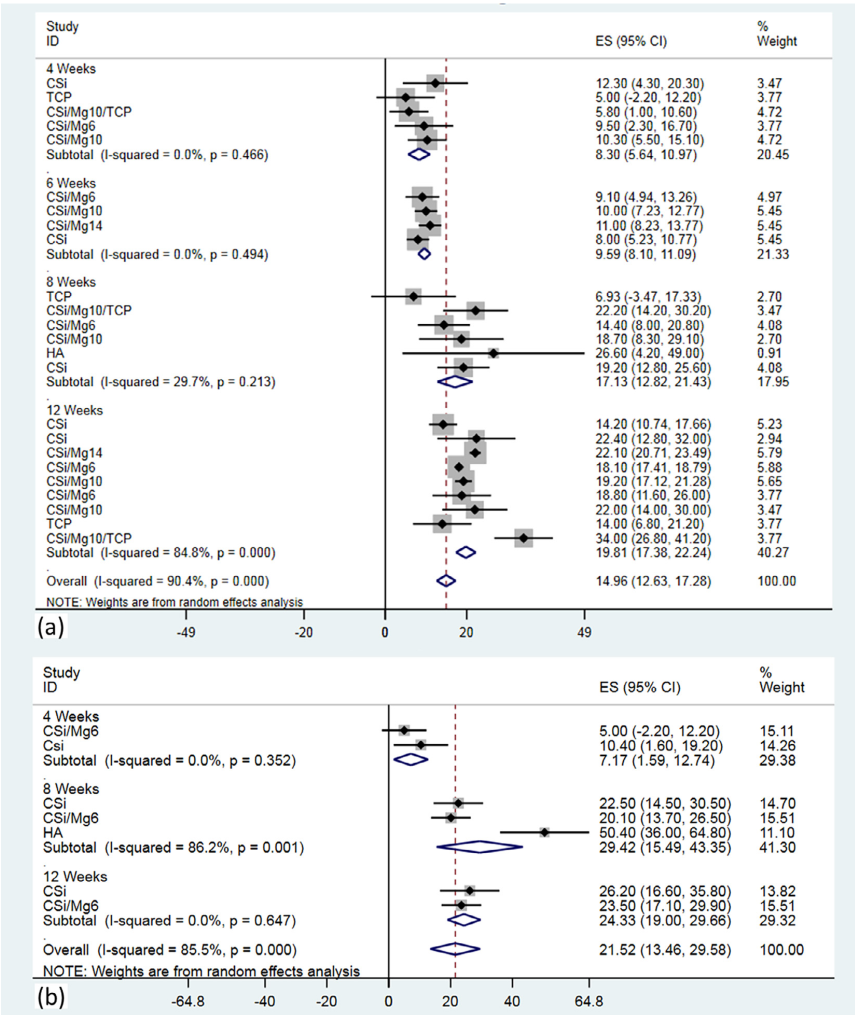

Fig. 6. Forest plots of the effect size (ES) for all the included printed ceramic templates used in rabbits, measured in NBA/TDA. (a) Represents the printed ceramic templates used without any additional porosity. (b) Represents the printed ceramic templates used with additional porosity. For each template/time point, the relative weight of the individual experiments, and 95% confidence intervals (CI) are displayed as grey squares and whiskers, respectively. The unfilled blue diamond indicates the overall estimate and its 95% CI for each time point. (For interpretation of the references to colour in this figure legend, the reader is referred to the web version of this article.)

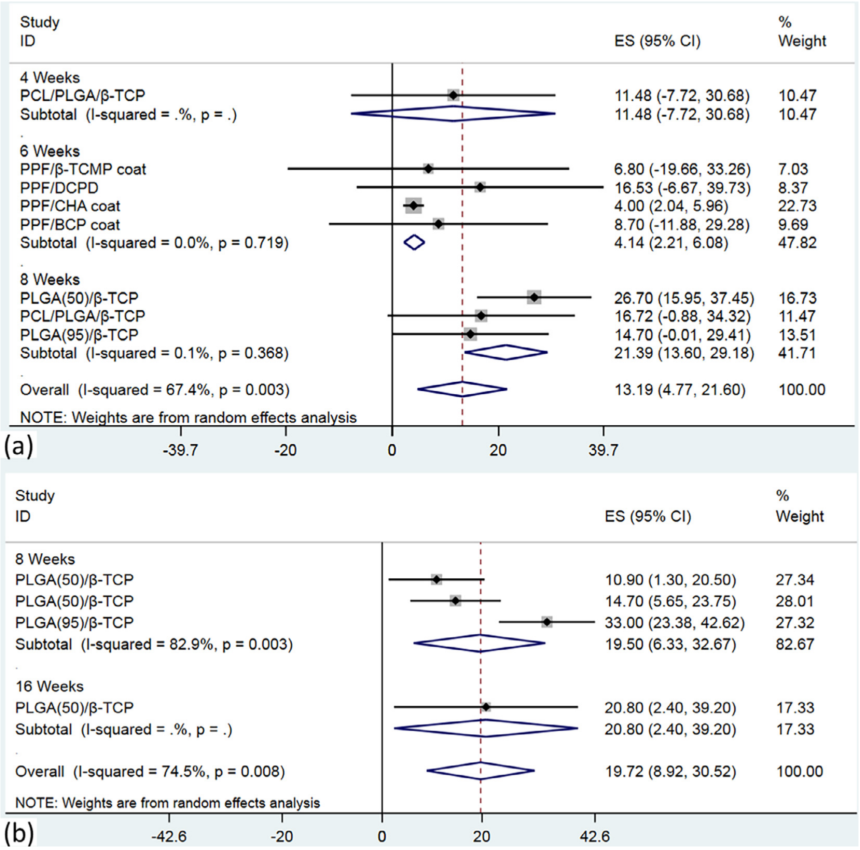

Fig. 7. Forest plots of the effect size (ES) for all the included printed composite templates used in rabbits, measured in NBA/TDA. (a) Represents the printed composite templates used without any additional porosity. (b) Represents the printed composite templates used with additional porosity. For each template/time point, the relative weight of the individual experiments, and 95% confidence intervals (CI) are displayed as grey squares and whiskers, respectively. The unfilled blue diamond indicates the overall estimate and its 95% CI for each time point. (For interpretation of the references to colour in this figure legend, the reader is referred to the web version of this article.)

3.6.2. The role of printed templates for BTR in rats

In rats, the printed ceramic templates without additional porosity showed high homogeneity at 8 weeks (Fig. 9a), while the printed ceramic templates with additional porosity revealed homogenous effect size only at 12 weeks (Fig. 9b). However, for the printed composite templates the only shown homogeneous data were for composite templates without additional porosity at 8 weeks (Fig. 10), while no homogeneous data were found for any of the printed polymer templates (Fig. 11).

Within the homogeneous data, both printed ceramic and composite templates without additional porosity showed comparable BTR at 8 weeks, 8.33 ± 7.68 and 9.0 ± 10.14, respectively. However, the ceramic templates with additional porosity revealed the highest BTR at 12 weeks (11.16 ± 9.56) and 16 weeks (14.54 ± 7.99). Nevertheless, no comparable results were noticed within the collected data in order to estimate the exact effect of the additional porosity. The models of CBD were very convenient for the current study, due to their accessibility surgical techniques and the abundance in literature. However, in all comparable time points and template type and structure, BTR outcome in rats was shown to be less than half BTR in rabbits.

4. Discussion

Improving the osteo-conductivity/bioactivity of the printed templates was found to take a step towards BTR, but did not achieve complete regeneration alone [67–69]. In most cases, 3D-printed templates showed more significant BTR than conventional porous templates fabricated from the same material as shown in ceramics [53] and polymers [61]. This could be due to the fact that printed templates are more efficiently providing the 3D interconnectivity needed to promote BTR [61] (Fig. 12), in addition to other physical and biological inherent biomaterials properties that are discussed below.

4.1. The role of template structure and porosity percentage (The primary space)

Besides the biological conductivity or bioactivity of the template, it is important to provide/maintain a space for angiogenesis and tissue ingrowth for good BTR approach [54,67,86]. Furthermore, the presence of macro-channels in the used templates showed more definite BTR than templates without channels in

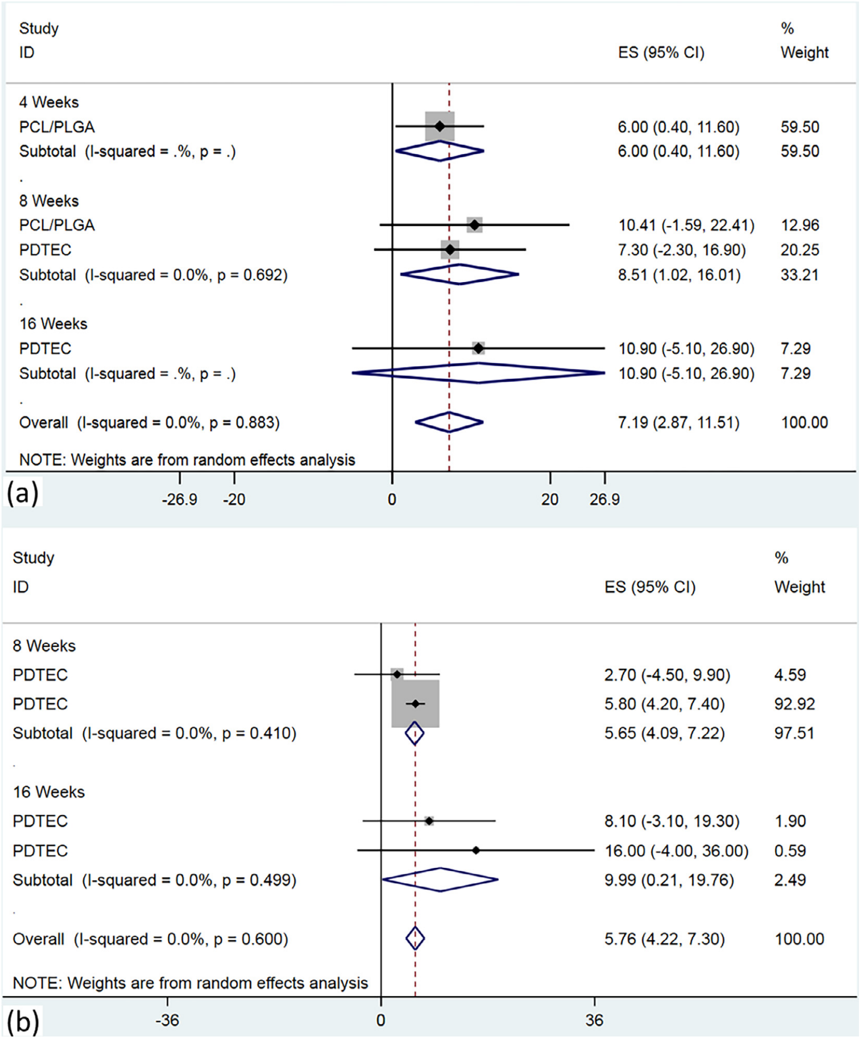

Fig. 8. Forest plots of the effect size (ES) for all the included printed polymeric templates used in rabbits, measured in NBA/TDA. (a) Represents the printed polymeric templates used without any additional porosity. (b) Represents the printed polymeric templates used with additional porosity. For each template/time point, the relative weight of the individual experiments, and 95% confidence intervals (CI) are displayed as grey squares and whiskers, respectively. The unfilled blue diamond indicates the overall estimate and its 95% CI for each time point. (For interpretation of the references to colour in this figure legend, the reader is referred to the web version of this article.)

various studies done in printed ceramics [50,52,81] and their composites [49,54]. This space can be achieved by considering a proper pore size (300–400 μm) as macro-pores forming the maximum allowed porosity % (>50%) for the printed template without jeopardizing the mechanical withstanding of the printed structure [87].

Jensen et al. demonstrated that any kind of interfering the available space within printed templates by closing the printed macropores, even with adding nano-porous structures, lead to a significant delay of BTR [26]. They performed a comparative study on pigs' CBD (non-penetrating defects) where the unmodified PCL showed good osteoconductivity and osseointegration after both 8 and 12 weeks compared to the nano-structured porous PCL templates. This hindered BTR was observed even if mononuclear cells or BMP-2 were added to such porous-obstructed templates. Others developed a porosity gradient design based on finite element modeling to improve the flexural strength of 3D-printed BG. The porosity gradient BG templates possessed double the flexural strength compared to the grid-like templates, but achieved the same BTR (19% NBE/TDE) when implanted in rat CBD for up to 12 weeks [100].

A recently developed highly porous PCL template, fabricated with the salt-leaching using powder (SLUP) method, promoted more BTR than printed PCL (which had less general porosity) in their study among 3 different template structures fabricated from PCL [83]. The pore size range showed to play a role in the effect difference between SLUP (50–300 μm) versus conventional salt leached templates (100–180 μm), although having a slight difference in general porosity showing 74.0 and 70.8% respectively. Therefore,

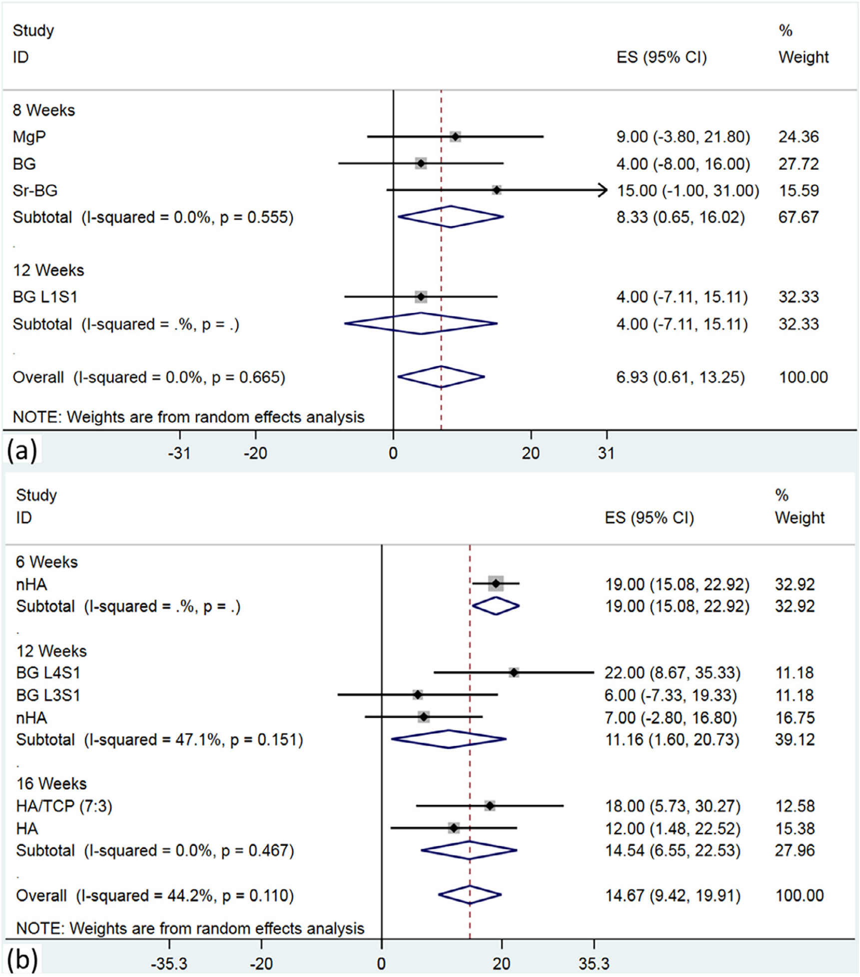

Fig. 9. Forest plots of the effect size (ES) for all the included printed ceramic templates used in rats, measured in NBA/TDA. (a) Represents the printed ceramic templates used without any additional porosity. (b) Represents the printed ceramic templates used with additional porosity. For each template/time point, the relative weight of the individual experiments, and 95% confidence intervals (CI) are displayed as grey squares and whiskers, respectively. The unfilled blue diamond indicates the overall estimate and its 95% CI for each time point. (For interpretation of the references to colour in this figure legend, the reader is referred to the web version of this article.)

this pore size range difference lead to an increased percent (almost double) of BTR in SLUP than conventional salt leached templates when tested in CBD (8 mm Ø) in rats for up to 8 weeks.

As previously mentioned, the printing of macro-pore channels within osteoconductive templates showed increased *in vivo* BTR [49,50] and less soft tissue ingrowth. The macro-porous structure should dimensionally accommodate the ingrowing trabecular bone (100–250 μm Ø) [52]. These growing trabeculae were found to form a coating layer creeping on the template struts and then thicken to fill the available space [52].

Previous studies determined the optimal pore size for *in vitro* osteogenic differentiation to be between 300 and 500 μm, while being ≥600 μm for *in vivo* bone ingrowth in porous Titanium (Ti) scaffolds [88]. However, others recommend more specific macro-pore diameter to be optimum, estimated *in vitro* to be >300 μm Ø [89] and *in vivo* to be from 320 to 400 μm [52,71,90]. Beyond this limit (around 500 μm) printed PLA/HA templates significantly failed to exceed the BTR observed at conventional porous TCP template with the same porosity percentage (60%) in CBD in rats [76] (Fig. 13).

As a translational approach, it is also important not to ignore the need for additional micro-porosity and surface roughness on the printed struts in order to enhance protein adsorption, and cellular attachment and function [52,91]. In addition, the rate of template degradation should consider the space needed during the initial healing time for the organized and unrestricted inclusion of BTR set-up. This healing period may differs across species and across the implantation sites even within the same animal model [92].

4.2. The role of template degradability (The secondary space)

It is crucial to use tunable, degradable templates, in which *in vivo* degradation will not be influenced by the presence or

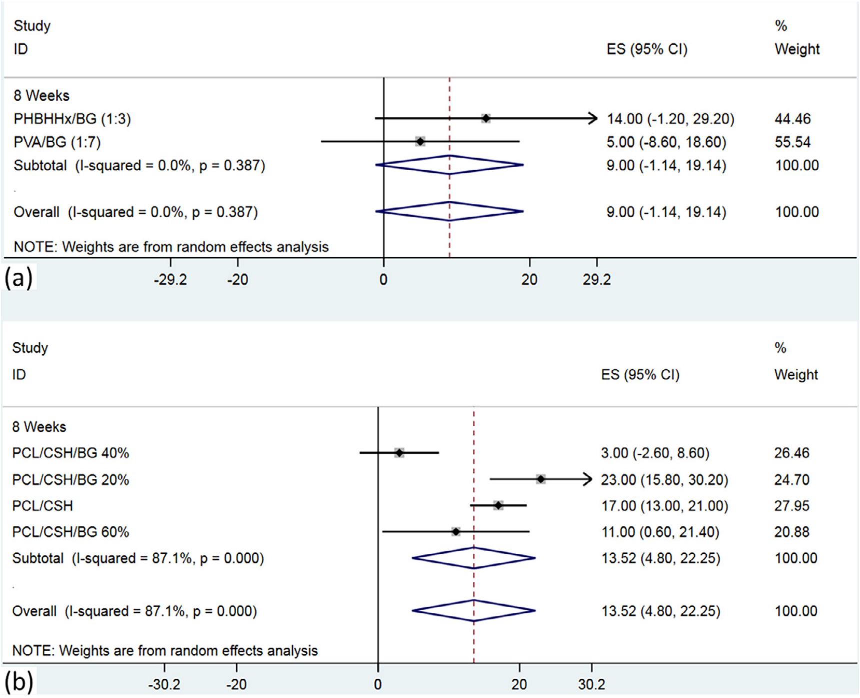

Fig. 10. Forest plots of the effect size (ES) for all the included printed composite templates used in rats, measured in NBA/TDA. (a) Represents the printed composite templates used without any additional porosity. (b) Represents the printed composite templates used with additional porosity. For each template/time point, the relative weight of the individual experiments, and 95% confidence intervals (CI) are displayed as grey squares and whiskers, respectively. The unfilled blue diamond indicates the overall estimate and its 95% CI for each time point. (For interpretation of the references to colour in this figure legend, the reader is referred to the web version of this article.)

absence of loaded cells [23] or growth factors [93]. This degradation rate, even for the same material used, should match the changes in BTR of different sites in the body [92]. This is due to the fact that the growth of NBA is limited to both, the available space given (primary space) and the secondary space regulated by the degradation rate of the used template [58,84].

As previously mentioned, with the increase of BG ratio, BTR increased relative to the increase of *in vivo* degradation of the printed template [69]. On the other hand, when compared to conventional commercially available porous templates, the majority of 3D-printed templates showed superior degradation and BTR [53]. This could be related to the fact that the printed higher interconnected porosity also promoted more rapid biodegradation and enhanced BTR and remodelling activities [35].

The degrading printed HA/TCP provided this secondary space, showing greater BTR than the printed HA templates with lower degradation rate [53]. On the other hand, in the slowly degraded printed PPF-reinforced CaP templates, the loaded mesenchymal stem cells (MSCs) did not promote more BTR than unloaded templates. This could be related to the lack of any secondary space for loaded MSCs to play their supposed role [94]. More recently, Kim et al. (2017) explored the effect of the biodegradation rate of the fast degrading printed magnesium phosphate (MgP) templates with/without additional micro-porosity for BTR [35]. MgP templates showed complete degradation in 4 weeks, where the added micro-pore architecture within the template struts resulted in better BTR.

4.3. The role of added biological factors for BTR

Various biological factors, e.g. anti-inflammatory protein (Atsttrin) [95], freeze-dried platelet-rich plasma (FD-PRP) [96], and platelet-derived growth factor-BB (PDGFB) [86], were loaded on printed templates for BTR in CBD. Most of these factors showed better BTR than comparable unloaded templates. However, the added value created did not significantly improve the BTR % in these CBDs [86,95], and their mechanism of action were not explained [96]. On the other hand, BMP-2 and MSCs were successfully loaded on the printed templates with significant improvement in BTR.

4.3.1. The added value of BMP-2 and comparable agents

BMP-2 has a major influence on BTR when loaded on printed templates at both short term (4–8 weeks) and longer (12–24 weeks) periods [39,61]. In addition, it was characterized by a dose dependent action that is directly proportional to the amount of BTR [65]. However, this is applicable only when there are enough allowed space/porosity by the applied templates for BTR [26].

Yu et al. (2008), reported the first large animal trial in CBD (15 mm Ø) in goats up to 24 w. They used highly porous PLGA/TCP templates loaded with BMP-2 that showed reasonable biodegradation and excellent osteogenesis compared to unloaded templates [93]. More recently, BMP-2 was further compared to other “healing agents” that could be loaded on printed templates for *in vivo* BTR [48,97]. The effect of a new peptide (P28) loaded

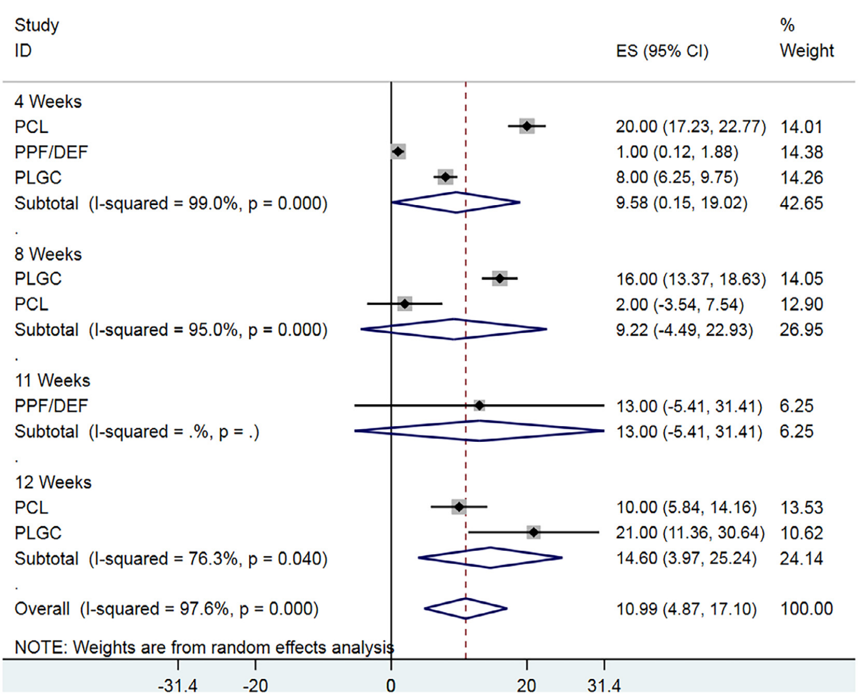

Fig. 11. Forest plot of the effect size (ES) for all the included printed polymer templates used in rats, measured in NBA/TDA, showing the printed polymer templates used without any additional porosity for each template/time point, the relative weight of the individual experiments, and 95% confidence intervals (CI) are displayed as grey squares and whiskers, respectively. The unfilled blue diamond indicates the overall estimate and its 95% CI for each time point. (For interpretation of the references to colour in this figure legend, the reader is referred to the web version of this article.)

on highly porous nHA templates for BTR in rat CBD was found to have the same effect created by BMP-2 (around 42% NBA/TDA) at 12 weeks [48]. Both showed double the BTR showed by solely nHA (around 20%).

Similarly, dipyridamole (DIPY) loaded on printed HA/TCP was found to have the same significant result on BTR as BMP-2 (both around 45%), by increasing the surrounding local adenosine levels. This was higher than BTR achieved in bare printed HA/TCP, which showed around 30% at 8 weeks after implantation in CBD in C57B6 and adenosine A2A receptor knockout (A2AKO) mice [97]. In addition, their follow-up short term study (up to 6 weeks) in small CBD in sheeps, using printed TCP/collagen, revealed that BTR was higher in DIPY loaded templates compared to controls [77]. In this study, μCT results were not supplied, but two remarkable notes could be highlighted; first, almost no template degradation took place for this period. Second, the histomorphometric analysis showed 30% BTR (at only 6 weeks) using these "capped" templates loaded with DIPY in a large animal model. This noticeable BTR was observed within the full thickness of the templates at 6 weeks in case of loaded and unloaded templates as a result of the capping strategy that prevent soft tissue invasion on the expense of BTR [79].

Others introduced bone formation peptides (e.g. BFP-1) loaded on printed alginate templates in rabbit CBD [20], which showed dose dependency and better BTR at longer follow-up intervals (up to 12 w). Indene compounds (KR-34893) loaded on printed MgP templates have been shown to be also dose dependent with significant BTR (up to 32% NBA/TDA) at 8 weeks [78]. Nevertheless, both studies showed fluctuating amounts of BTR related to the dose of both healing agents at shorter follow-up time points.

4.3.2. Cell-loaded templates for calvarial BTR

Loading printed templates with pre-differentiated cells showed significant *in vivo* BTR compared to unloaded templates [51]. In addition, other studies showed that adding stem cells, e.g. human dental pulp stem cells (hDPSCs) [23] or pre-differentiated cells [62] to printed templates loaded with other growth factors had a synergetic effect on BTR. However, this effect is still controlled to some extent by the template nature, such as bioactivity, interconnectivity and biodegradation. For example, printed PLA-co-PGA-co-PCL (PLGC) templates loaded with hDPSCs and osteogenic factors (OF) showed significantly more BTR than unloaded templates [23]. However, the lack of biological osteoconductivity, biodegradation and proper porosity % could have been limiting factors in the achievement of reasonable BTR.

When using a degrading osteoconductive template (printed PLA/TCP) loaded with osteoblastoma cells (MG-63), in the same animal model [84], a satisfactory matching BTR rate was noticed. The biodegradation and osteoconductivity of unloaded templates lead to about 25% BTR, while for MG-63 cells loaded templates BTR was increased to 45%.

4.4. Printed templates in non-penetrating CBDs

Another group of studies aimed for vertical BTR using printed templates, where non-penetrating (partial thickness) CBD were

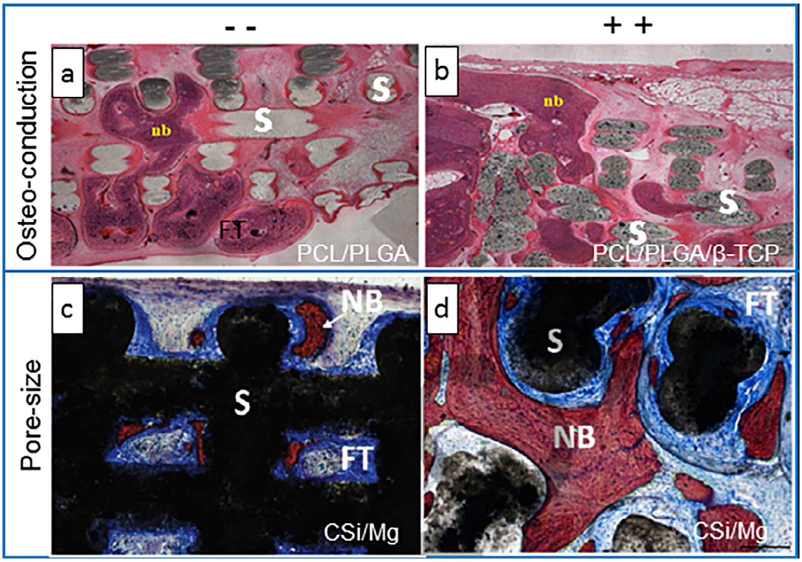

Fig. 12. Histological findings of studies that used 3D-printed templates in rabbits' CBD after 8 weeks; (a and b) shows an increased BTR in (b) than (a) when added the osteoconductive "TCP". (c and d) shows an increased BTR in (d) than (c) when increasing the pore diameter (>300 µm). nb, new bone; S, printed template; FT, fibrous tissue. (a and b) H&E stain (×50) – [58] (reproduced with permission from Springer Nature), while (c and d) Van Gieson's stain (×100) – [71] (reproduced with permisson from IOP Publishing).

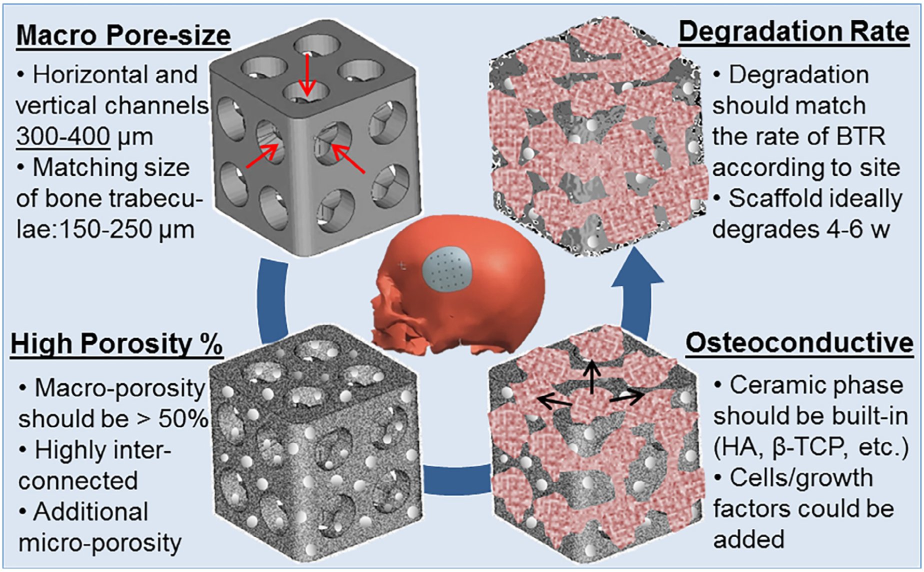

Fig. 13. Schematic presentation for the main features to safely upgrade 3D-printed templates for BTR into translational trials.

implemented *in vivo*. When using printed Monetite/TCP onlays, with 44% porosity in NZW rabbits, the bone height gained was comparable to that with autologous bone after 8 weeks [82]. In addition, their further investigations revealed that adding 3D interconnected channels and grooves to the printed templates gave more pronounced BTR and integration inside the printed onlays [81]. The regenerated bone within these onlays was further loaded with Ti implants that revealed normal osseointegration.

Others also applied printed onlays on square (20 × 20 mm) partial-thickness CBD (non-penetrating) defects in Merino sheep but not for the primary aim of vertical BTR [98]. They used various hydrogel-based (TCP/collage/chitosan) and polymer-based (PLGA) templates, for 14 weeks follow-up. Their results revealed that hydrogels had the best BTR related to their good biodegradation rate unlike the case of PLGA templates that degrades less. The role of the added osteoblast-like cells was obvious in increasing the amount of new bone formation in hydrogel and TCP base templates, but the hydrogel stiffness was not found applicable for practical surgical use.

4.5. Guided BTR with printed membranes

Recently, printed membranes were successfully used to support conventional templates for BTR with more reliable mechanical properties than conventional membranes [99]. The POSTECH research group have also tested printed membranes for guided bone regeneration (GBR) techniques in the CBD of NZW rabbits [79,80].

The sustained release of BMP-2 from printed membranes was found significant for GBR, although a fair amount of new bone was formed for the non-loaded composite (PCL/PLGA/TCP) barrier membranes. However, the more interesting observation was that these membranes were sufficient to promote complete BTR of CBD within 8 weeks [79]. This suggests the way to consider templates as a support for BTR, and to prevent external factors from jeopardizing healing.

Despite what was assumed in the case of printed templates, augmented bone formation was achieved with the printed membranes by decreasing their pore size and porosity % to properly do their function as GBR barriers/membranes [80] (Fig. 14a). Therefore, it would be convenient and extremely useful to use 3D printing in the fabrication of prospective templates with extra features (e.g. combined bone template with GBR membrane in one structure) for certain BTR applications [77,41] (Fig. 14d and g).

4.6. The outlook for BTR

As an aid in BTR, 3D-printing is essential in customizing the needed templates; their general design and sub-structures. In addition, the physical and biological properties of the printed biomaterials and their relative degradation are challenges that should be calculated and considered for each individual application. The interconnected macro-porosity created by 3D printing is crucial to bone formation and ingrowth within the struts of the template [88]. Adding micro-porosity within the printed struts should enhance template degradation and BTR [35], while filling the gaps

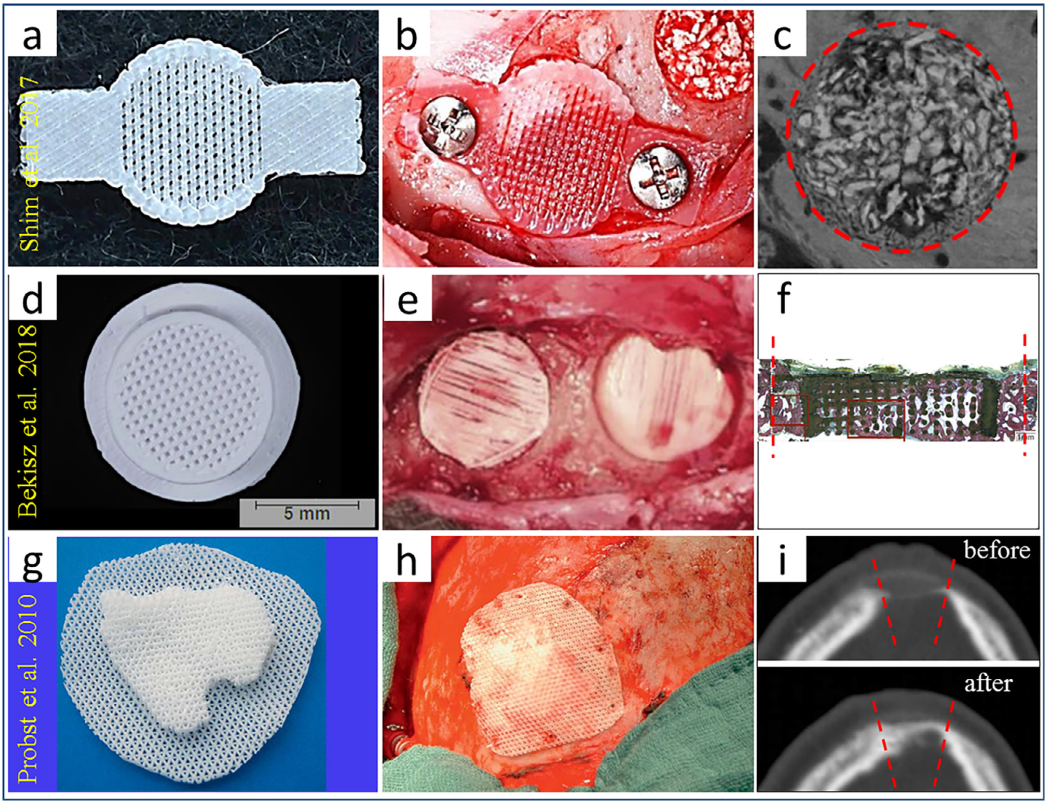

Fig. 14. Macroscopic photographs and findings with minor modifications from previous studies that used 3D printed templates with extra features for BTR in different calvarial models. (a) PCL, (d) TCP/Col coated with DIPY, and (g) PCL/TCP– printed templates. (b, e, and h) are showing the surgical implantation of the templates and their fixation in rabbits (b), sheep (e), and human (h) calvarial defects, respectively. The BTR out-come of the implanted printed structures is shown respectively in (c, f and i). (c) is μCT after 4 weeks, (f) is histology after 6 weeks, and (I) are coronal-CT scans to the defect before (upper), and 6 months after implantation (lower). A red dashed line is used to mark the original defect borders. (a, b and c) – [80] are reproduced with permission from IOP Publishing, (d, e and f) – [77] are reproduced with permission from Elsevier, and (g, h and i) – [41] are reproduced with permission from Thieme Gruppe. (For interpretation of the references to colour in this figure legend, the reader is referred to the web version of this article.)

between the printed macro-porosity will hinder osteoconduction [26].

In the current study, it was obvious that BTR outcomes with printed templates differs according to the biomaterials used, additional features/porosity, added osteogenic factors and also according to the animal model used. Thus, the printed structures were found to frequently enhance the performance of less osteoconductive templates and allowed for reasonable BTR, compared to the more osteogenic conventional scaffolds [54]. However, printed porosity should be added to other factors, e.g. template degradation rate, in order to allow for and complement with the regeneration process. Meanwhile, adding other external biological agents, osteogenic growth factors and cells should further support BTR [12]. These osteogenic factors are dose dependent, and should also be chosen according to the site and size of the bone defect in order to allow for the best performance [20,65,78].

4.7. Limitations of the current study

1. For the scoring purposes of NBA/TDA, very few studies considered scoring the BTR as a combined formation of mineralized bone matrix and supporting marrow-like area [35], which would be more realistic, but is technically demanding. This might lead to uncertain BTR quantification, although more precise than quantifications based on μCT.
2. The surgical technique for placing the templates inside CBD varied in method of fixation, if any, and repositioning [57,60,76] versus removal of the overlying periosteum [48,58].

4.8. Conclusion

3D-printed templates are successful and reliable in BTR, meanwhile, they require the biological conductivity, degradation and biocompatibility of their materials. The capacity of 3D-printed templates for BTR depends on readily controlled design factors, e.g. high porosity % with maximum interconnectivity, in addition to having an optimum macro-pore size (300–400 μm) to fit the growing bone trabeculae. Furthermore, they can be loaded with BMP-2 and other bone formation proteins for a dose dependent action, and can be customized in size for the site of BTR in order to allow for the best performance.

Acknowledgements

The Authors would like to acknowledge the University of Bergen for supporting this work. This work was partially funded by the Research Council of Norway through the BEHANDLING project (Grant no. 273551) and Bergen Research Foundation, Norway (BFS2018TMT10).

Disclosure

The authors have no conflict of interest to disclose.

References

[1] R. Langer, J.P. Vacanti, Tissue engineering, Science 260 (1993) 920–926.
[2] E.M. Sachs, J.S. Haggerty, M.J. Cima, P.A. Williams, Patent: three-dimensional printing techniques, US5204055A, 1993. https://patents.google.com/patent/US5204055A/en.
[3] C. Mandrycky, Z. Wang, K. Kim, D.-H. Kim, 3D bioprinting for engineering complex tissues, Biotechnol. Adv. 34 (2016) 422–434, https://doi.org/10.1016/j.biotechadv.2015.12.011.
[4] J.R. Jones, L.L. Hench, Factors affecting the structure and properties of bioactive foam scaffolds for tissue engineering, J. Biomed. Mater. Res. B. Appl. Biomater. 68 (2004) 36–44, https://doi.org/10.1002/jbm.b.10071.
[5] A.C. Allori, A.M. Sailon, S.M. Warren, Biological basis of bone formation, remodeling, and repair-part I: biochemical signaling molecules, Tissue Eng. Part B Rev. 14 (2008) 259–273, https://doi.org/10.1089/ten.teb.2008.0082.
[6] A.C. Allori, A.M. Sailon, J.H. Pan, S.M. Warren, Biological basis of bone formation, remodeling, and repair-part III: biomechanical forces, Tissue Eng. Part B Rev. 14 (2008) 285–293, https://doi.org/10.1089/ten.teb.2008.0084.
[7] K. Lee, M.D. Weir, E. Lippens, M. Mehta, P. Wang, G.N. Duda, W.S. Kim, D.J. Mooney, H.H.K. Xu, Bone regeneration via novel macroporous CPC scaffolds in critical-sized cranial defects in rats, Dent. Mater. 30 (2014) e199–e207, https://doi.org/10.1016/j.dental.2014.03.008.
[8] Periodic Report 2 – REBORNE (Regenerating Bone defects using New biomedical Engineering approaches), (2016) 1–2. https://cordis.europa.eu/project/rcn/92715/reporting/en.
[9] M. Hallman, A. Thor, Bone substitutes and growth factors as an alternative/complement to autogenous bone for grafting in implant dentistry, Periodontology 2000 (47) (2008) 172–192.
[10] C. Szpalski, M. Wetterau, J. Barr, S.M. Warren, Bone tissue engineering: current strategies and techniques—Part I: scaffolds, Tissue Eng. Part B Rev. 18 (2012) 246–257, https://doi.org/10.1089/ten.teb.2011.0427.
[11] M. Nageeb, S.R. Nouh, K. Bergman, N.B. Nagy, D. Khamis, M. Kisiel, T. Engstrand, J. Hilborn, M.K. Marei, Bone engineering by biomimetic injectable hydrogel, Mol. Cryst. Liq. Cryst. 555 (2012) 177–188, https://doi.org/10.1080/15421406.2012.635530.
[12] D.F. Williams, The biomaterials conundrum in tissue engineering, Tissue Eng. Part A 20 (2014) 1129–1131, https://doi.org/10.1089/ten.tea.2013.0769.
[13] A.E. Jakus, A.L. Rutz, S.W. Jordan, A. Kannan, S.M. Mitchell, C. Yun, K.D. Koube, S.C. Yoo, H.E. Whiteley, C.-P. Richter, R.D. Galiano, W.K. Hsu, S.R. Stock, E.L. Hsu, R.N. Shah, Hyperelastic "bone": a highly versatile, growth factor–free, osteoregenerative, scalable, and surgically friendly biomaterial 358ra127 LP-358ra127, Sci. Transl. Med. 8 (2016), https://doi.org/10.1126/scitranslmed.aaf7704.
[14] World Economic Forum, The Global Risks Report 2017 12th ed., 2017. doi:10.1017/CBO9781107415324.004.
[15] Y.D. Hesuani, F.D.A.S. Pereira, V. Parfenov, E. Koudan, A. Mitryashkin, N. Replyanski, V. Kasyanov, A. Knyazeva, E. Bulanova, V. Mironov, Design and implementation of novel multifunctional 3D bioprinter, 3D Print Addit. Manuf. 3 (2016) 64–68, https://doi.org/10.1089/3dp.2015.0040.
[16] A. Louvrier, P. Marty, E. Weber, E. Euvrard, B. Chatelain, A. Barrabé, C. Meyer, How useful is 3D printing in maxillo-facial surgery?, J Stomatol. Oral Maxillofac. Surg. (2017), https://doi.org/10.1016/j.jormas.2017.07.002.
[17] E. Farré-Guasch, J. Wolff, M.N. Helder, E.A.J.M. Schulten, T. Forouzanfar, J. Klein-Nulend, Application of additive manufacturing in oral and maxillofacial surgery, J. Oral Maxillofac. Surg. 73 (2015) 2408–2418, https://doi.org/10.1016/j.joms.2015.04.019.
[18] J.A. Morales-gómez, E. Garcia-estrada, J.E. Leos-bortoni, M. Delgado-brito, L.E. Flores-huerta, A.A.D. La Cruz-arriaga, L.J. Torres-díaz, Á.R.M. De León, Cranioplasty with a low-cost customized polymethylmethacrylate implant using a desktop 3D printer, J. Neurosurg. (2018) 1–7, https://doi.org/10.3171/2017.12.JNS172574.
[19] A. De La Peña, J. De La Peña-Brambila, J. Pérez-De La Torre, M. Ochoa, G.J. Gallardo, Low-cost customized cranioplasty using a 3D digital printing model: a case report, 3D Print Med. 4 (2018) 4, https://doi.org/10.1186/s41205-018-0026-7.
[20] E.Y. Heo, N.R. Ko, M.S. Bae, S.J. Lee, B.J. Choi, J.H. Kim, H.K. Kim, S.A. Park, I.K. Kwon, Novel 3D printed alginate–BFP1 hybrid scaffolds for enhanced bone regeneration, J. Ind. Eng. Chem. 45 (2017) 61–67, https://doi.org/10.1016/j.jiec.2016.09.003.
[21] J.M. Hong, B.J. Kim, J.H. Shim, K.S. Kang, K.J. Kim, J.W. Rhie, H.J. Cha, D.W. Cho, Enhancement of bone regeneration through facile surface functionalization of solid freeform fabrication-based three-dimensional scaffolds using mussel adhesive proteins, Acta Biomater. 8 (2012) 2578–2586, https://doi.org/10.1016/j.actbio.2012.03.041.
[22] J.-Y. Lee, B. Choi, B. Wu, M. Lee, Customized biomimetic scaffolds created by indirect three-dimensional printing for tissue engineering, Biofabrication. 5 (2013), https://doi.org/10.1088/1758-5082/5/4/045003 045003.
[23] D.Y. Kwon, J.S. Kwon, S.H. Park, J.H. Park, S.H. Jang, X.Y. Yin, J.-H. Yun, J.H. Kim, B.H. Min, J.H. Lee, W.-D. Kim, M.S. Kim, A computer-designed scaffold for bone regeneration within cranial defect using human dental pulp stem cells, Sci. Rep. 5 (2015) 12721, https://doi.org/10.1038/srep12721.
[24] V. Luangphakdy, E. Walker, K. Shinohara, H. Pan, T. Hefferan, T.W. Bauer, L. Stockdale, S. Saini, M. Dadsetan, M.B. Runge, A. Vasanji, L. Griffith, M. Yaszemski, G.F. Muschler, Evaluation of osteoconductive scaffolds in the canine femoral multi-defect model, Tissue Eng. Part A 19 (2013) 634–648, https://doi.org/10.1089/ten.TEA.2012.0289.
[25] H. Seitz, W. Rieder, S. Irsen, B. Leukers, C. Tille, Three-dimensional printing of porous ceramic scaffolds for bone tissue engineering, J. Biomed. Mater. Res. -Part B Appl. Biomater. 74 (2005) 782–788, https://doi.org/10.1002/jbm.b.30291.
[26] J. Jensen, J.H.D. Rölfing, D.Q. Svend Le, A.A. Kristiansen, J.V. Nygaard, L.B. Hokland, M. Bendtsen, M. Kassem, H. Lysdahl, C.E. Bünger, Surface-modified functionalized polycaprolactone scaffolds for bone repair: In vitro and in vivo experiments, J. Biomed. Mater. Res. Part A 102 (2014) 2993–3003, https://doi.org/10.1002/jbm.a.34970.
[27] B. Rai, J.L. Lin, Z.X.H. Lim, R.E. Guldberg, D.W. Hutmacher, S.M. Cool, Differences between in vitro viability and differentiation and in vivo bone-forming efficacy of human mesenchymal stem cells cultured on PCL-TCP

scaffolds, Biomaterials 31 (2010) 7960–7970, https://doi.org/10.1016/j.biomaterials.2010.07.001.
[28] L.S. Nair, C.T. Laurencin, Biodegradable polymers as biomaterials, Prog. Polym. Sci. 32 (2007) 762–798, https://doi.org/10.1016/j.progpolymsci.2007.05.017.
[29] M.A. Yassin, K.N. Leknes, T.O. Pedersen, Z. Xing, Y. Sun, S.A. Lie, A. Finne-Wistrand, K. Mustafa, Cell seeding density is a critical determinant for copolymer scaffolds-induced bone regeneration, J. Biomed. Mater. Res. Part A 103 (2015) 3649–3658, https://doi.org/10.1002/jbm.a.35505.
[30] M.A. Yassin, K. Mustafa, Z. Xing, Y. Sun, K.E. Fasmer, T. Waag, A. Krueger, D. Steinmüller-Nethl, A. Finne-Wistrand, K.N. Leknes, A copolymer scaffold functionalized with nanodiamond particles enhances osteogenic metabolic activity and bone regeneration, Macromol. Biosci. 17 (2017) 1–11, https://doi.org/10.1002/mabi.201600427.
[31] L.L. Hench, Bioactive materials: the potential for tissue regeneration, J Biomed Mater Res. 41 (1998) 511–518, https://doi.org/10.1002/(SICI)1097-4636(19980915)41:4<511::AID-JBM1>3.0.CO;2-F [pii].
[32] M.N. Hassan, M.M. Mahmoud, A.A. El-Fattah, S. Kandil, Microwave-assisted preparation of nano-hydroxyapatite for bone substitutes, Ceram. Int. 42 (2016) 3725–3744, https://doi.org/10.1016/j.ceramint.2015.11.044.
[33] Z. Artzi, M. Weinreb, N. Givol, M. Rohrer, C. Nemcovsky, H. Prasad, H. Tal, Biomaterial resorption rate and healing site morphology of inorganic bovine bone and ß-tricalcium phosphate in the canine: a 24-month longitudinal histologic study and morphometric analysis, Int. J. Oral Maxillofac Implant. 19 (2004) 357–368.
[34] R.M. El Backly, S.H. Zaky, B. Canciani, M.M. Saad, A.M. Eweida, F. Brun, G. Tromba, V.S. Komlev, M. Mastrogiacomo, M.K. Marei, R. Cancedda, Platelet rich plasma enhances osteoconductive properties of a hydroxyapatite-β-tricalcium phosphate scaffold (Skelite™) for late healing of critical size rabbit calvarial defects, J. Cranio-Maxillofacial Surg. 42 (2014) 1–10, https://doi.org/10.1016/j.jcms.2013.06.012.
[35] J.A. Kim, J. Lim, R. Naren, H. Suk Yun, E.K. Park, Effect of the biodegradation rate controlled by pore structures in magnesium phosphate ceramic scaffolds on bone tissue regeneration in vivo, Acta Biomater. 44 (2016) 155–167, https://doi.org/10.1016/j.actbio.2016.08.039.
[36] X. Li, Y. Wang, Z. Wang, Y. Qi, L. Li, P. Zhang, X. Chen, Y. Huang, Composite PLA/PEG/nHA/dexamethasone scaffold prepared by 3D printing for bone regeneration, Macromol. Biosci. 18 (2018) 1–11, https://doi.org/10.1002/mabi.201800068.
[37] J.Y. Kim, G. Ahn, C. Kim, J.S. Lee, I.G. Lee, S.H. An, W.S. Yun, S.Y. Kim, J.H. Shim, Synergistic effects of beta tri-calcium phosphate and porcine-derived decellularized bone extracellular matrix in 3D-printed polycaprolactone scaffold on bone regeneration, Macromol. Biosci. 18 (2018) 1–10, https://doi.org/10.1002/mabi.201800025.
[38] F. Diomede, A. Gugliandolo, P. Cardelli, I. Merciaro, V. Ettorre, T. Traini, R. Bedini, D. Scionti, A. Bramanti, A. Nanci, S. Caputi, A. Fontana, E. Mazzon, O. Trubiani, Three-dimensional printed PLA scaffold and human gingival stem cell-derived extracellular vesicles: a new tool for bone defect repair, Stem Cell Res. Ther. 9 (2018) 1–21, https://doi.org/10.1186/s13287-018-0850-0.
[39] B.S. Kim, S.S. Yang, C.S. Kim, Incorporation of BMP-2 nanoparticles on the surface of a 3D-printed hydroxyapatite scaffold using an ε-polycaprolactone polymer emulsion coating method for bone tissue engineering, Colloids Surf., B Biointerfaces 170 (2018) 421–429, https://doi.org/10.1016/j.colsurfb.2018.06.043.
[40] J.L. Ricci, E.A. Clark, A. Murriky, J.E. Smay, Three-dimensional printing of bone repair and replacement materials, J. Craniofac. Surg. 23 (2012) 304–308, https://doi.org/10.1097/SCS.0b013e318241dc6e.
[41] F.A. Probst, D.W. Hutmacher, D.F. Müller, H.-G. Machens, J.-T. Schantz, Rekonstruktion der Kalvaria durch ein präfabriziertes bioaktives Implantat,, Handchirurgie Mikrochirurgie Plast. Chir. 42 (2010) 369–373, https://doi.org/10.1055/s-0030-1248310.
[42] U. Meyer, J. Neunzehn, H.P. Wiesmann, Computer-Aided Approach for Customized Cell-Based Defect Reconstruction, in: 2012: pp. 27–43. doi:10.1007/978-1-61779-764-4_2.
[43] D. Rohner, D.W. Hutmacher, P. See, K.C. Tan, V. Yeow, S.Y. Tan, S.T. Lee, B. Hammer, Individuell mit CAD-CAM-Technik hergestellte, bioresorbierbare dreidimensionale Polycaprolaktongerüste zur experimentellen Rekonstruktion von kraniofazialen Defekten beim Schwein., Mund. Kiefer. Gesichtschir. 6 (2002) 162–167. doi:10.1007/s10006-002-0389-0.
[44] D.W. Hutmacher, S. Cool, Concepts of scaffold-based tissue engineering – the rationale to use solid free-form fabrication techniques, J. Cell. Mol. Med. 11 (2007) 654–669, https://doi.org/10.1111/j.1582-4934.2007.00078.x.
[45] V.S. Komlev, V.K. Popov, A.V. Mironov, A.Y. Fedotov, A.Y. Teterina, I.V. Smirnov, I.Y. Bozo, V.A. Rybko, R.V. Deev, 3D printing of octacalcium phosphate bone substitutes, Front. Bioeng. Biotechnol. 3 (2015) 1–7, https://doi.org/10.3389/fbioe.2015.00081.
[46] A. Liberati, D.G. Altman, J. Tetzlaff, C. Mulrow, P.C. Gøtzsche, J.P.A. Ioannidis, M. Clarke, P.J. Devereaux, J. Kleijnen, D. Moher, The PRISMA statement for reporting systematic reviews and meta-analyses of studies that evaluate healthcare interventions: explanation and elaboration, BMJ 339 (2009), https://doi.org/10.7326/0003-4819-151-4-200908180-00136 b2700.
[47] C.R. Hooijmans, M.M. Rovers, R.B.M. De Vries, M. Leenaars, M. Ritskes-hoitinga, M.W. Langendam, SYRCLE's risk of bias tool for animal studies, BMC Med. Res. Methodol. 14 (2014) 1–9, https://doi.org/10.1186/1471-2288-14-43.
[48] T. Sun, K. Zhou, M. Liu, X. Guo, Y. Qu, W. Cui, Z. Shao, X. Zhang, S. Xu, Loading of BMP-2-related peptide onto three-dimensional nano-hydroxyapatite scaffolds accelerates mineralization in critical-sized cranial bone defects, J. Tissue Eng. Regen. Med. (2017), https://doi.org/10.1002/term.2371.
[49] T.D. Roy, J.L. Simon, J.L. Ricci, E.D. Rekow, V.P. Thompson, J.R. Parsons, Performance of degradable composite bone repair products made via three-dimensional fabrication techniques, J. Biomed. Mater. Res. 66A (2003) 283–291, https://doi.org/10.1002/jbm.a.10582.
[50] T.D. Roy, J.L. Simon, J.L. Ricci, E.D. Rekow, V.P. Thompson, J.R. Parsons, Performance of hydroxyapatite bone repair scaffolds created via three-dimensional fabrication techniques, J. Biomed. Mater. Res. 67A (2003) 1228–1237, https://doi.org/10.1002/jbm.a.20034.
[51] J.-T. Schantz, D.W. Hutmacher, C.X.F. Lam, M. Brinkmann, K.M. Wong, T.C. Lim, N. Chou, R.E. Guldberg, S.H. Teoh, Repair of calvarial defects with customised tissue-engineered bone grafts II. Evaluation of cellular efficiency and efficacy in vivo, Tissue Eng. 9 (2003) 127–139, https://doi.org/10.1089/10763270360697030.
[52] J.L. Simon, S. Michna, J.A. Lewis, E.D. Rekow, V.P. Thompson, J.E. Smay, A. Yampolsky, J.R. Parsons, J.L. Ricci, In vivo bone response to 3D periodic hydroxyapatite scaffolds assembled by direct ink writing, J. Biomed. Mater. Res. Part A 83A (2007) 747–758, https://doi.org/10.1002/jbm.a.31329.
[53] Y.-J. Seol, J.Y. Park, J.W. Jung, J. Jang, R. Girdhari, S.W. Kim, D.-W. Cho, Improvement of bone regeneration capability of ceramic scaffolds by accelerated release of their calcium ions, Tissue Eng. Part A 20 (2014) 2840–2849, https://doi.org/10.1089/ten.TEA.2012.0726.
[54] J.L. Simon, T.D. Roy, J.R. Parsons, E.D. Rekow, V.P. Thompson, J. Kemnitzer, J.L. Ricci, Engineered cellular response to scaffold architecture in a rabbit trephine defect, J. Biomed. Mater. Res. 66A (2003) 275–282, https://doi.org/10.1002/jbm.a.10569.
[55] J.-T. Schantz, S.H. Teoh, T.C. Lim, M. Endres, C.X.F. Lam, D.W. Hutmacher, Repair of calvarial defects with customized tissue-engineered bone grafts I. Evaluation of osteogenesis in a three-dimensional culture system, Tissue Eng. 9 (2003) 113–126, https://doi.org/10.1089/10763270360697021.
[56] J.T. Schantz, T.C. Lim, C. Ning, H.T. Swee, C.T. Kim, C.W. Shih, D.W. Hutmacher, Cranioplasty after trephination using a novel biodegradable burr hole cover: technical case report, Neurosurgery 58 (2006) 1–4, https://doi.org/10.1227/01.NEU.0000193533.54580.3F.
[57] A. Yeo, W.J. Wong, S.H. Teoh, Surface modification of PCL-TCP scaffolds in rabbit calvaria defects: evaluation of scaffold degradation profile, biomechanical properties and bone healing patterns, J. Biomed. Mater. Res. A 93 (2010) 1358–1367, https://doi.org/10.1002/jbm.a.32633.
[58] J.-H. Shim, T.-S. Moon, M.-J. Yun, Y.-C. Jeon, C.-M. Jeong, D.-W. Cho, J.-B. Huh, Stimulation of healing within a rabbit calvarial defect by a PCL/PLGA scaffold blended with TCP using solid freeform fabrication technology, J. Mater. Sci. Mater. Med. 23 (2012) 2993–3002, https://doi.org/10.1007/s10856-012-4761-9.
[59] J.Y. Kim, G.-Z. Jin, I.S. Park, J.-N. Kim, S.Y. Chun, E.K. Park, S.-Y. Kim, J. Yoo, S.-H. Kim, J.-W. Rhie, D.-W. Cho, Evaluation of solid free-form fabrication-based scaffolds seeded with osteoblasts and human umbilical vein endothelial cells for use in vivo osteogenesis, Tissue Eng. Part A 16 (2010) 2229–2236, https://doi.org/10.1089/ten.tea.2009.0644.
[60] F. Pati, T.H. Song, G. Rijal, J. Jang, S.W. Kim, D.W. Cho, Ornamenting 3D printed scaffolds with cell-laid extracellular matrix for bone tissue regeneration, Biomaterials 37 (2015) 230–241, https://doi.org/10.1016/j.biomaterials.2014.10.012.
[61] J.W. Lee, K.S. Kang, S.H. Lee, J.Y. Kim, B.K. Lee, D.W. Cho, Bone regeneration using a microstereolithography-produced customized poly(propylene fumarate)/diethyl fumarate photopolymer 3D scaffold incorporating BMP-2 loaded PLGA microspheres, Biomaterials 32 (2011) 744–752, https://doi.org/10.1016/j.biomaterials.2010.09.035.
[62] J.W. Lee, K.J. Kim, K.S. Kang, S. Chen, J.W. Rhie, D.W. Cho, Development of a bone reconstruction technique using a solid free-form fabrication (SFF)-based drug releasing scaffold and adipose-derived stem cells, J. Biomed. Mater. Res. A 101 (2013) 1865–1875, https://doi.org/10.1002/jbm.a.34485.
[63] K.S. Hwang, J.W. Choi, J.H. Kim, H.Y. Chung, S. Jin, J.H. Shim, W.S. Yun, C.M. Jeong, J.B. Huh, Comparative efficacies of collagen-based 3D printed PCL/PLGA/β-TCP composite block bone grafts and biphasic calcium phosphate bone substitute for bone regeneration, Materials (Basel) 10 (2017), https://doi.org/10.3390/ma10040421.
[64] B.P. Hung, B.A. Naved, E.L. Nyberg, M. Dias, C.A. Holmes, J.H. Elisseeff, A.H. Dorafshar, W.L. Grayson, Three-dimensional printing of bone extracellular matrix for craniofacial regeneration, ACS Biomater. Sci. Eng. 2 (2016) 1806–1816, https://doi.org/10.1021/acsbiomaterials.6b00101.
[65] M. Dadsetan, T. Guda, M.B. Runge, D. Mijares, R.Z. LeGeros, J.P. LeGeros, D.T. Silliman, L. Lu, J.C. Wenke, P.R. Brown Baer, M.J. Yaszemski, Effect of calcium phosphate coating and rhBMP-2 on bone regeneration in rabbit calvaria using poly(propylene fumarate) scaffolds, Acta Biomater. 18 (2015) 9–20, https://doi.org/10.1016/j.actbio.2014.12.024.
[66] S. Zhao, M. Zhu, J. Zhang, Y. Zhang, Z. Liu, Y. Zhu, C. Zhang, Three dimensionally printed mesoporous bioactive glass and poly(3-hydroxybutyrate-co-3-hydroxyhexanoate) composite scaffolds for bone regeneration, J. Mater. Chem. B 2 (2014) 6106, https://doi.org/10.1039/C4TB00838C.
[67] S. Zhao, J. Zhang, M. Zhu, Y. Zhang, Z. Liu, C. Tao, Y. Zhu, C. Zhang, Three-dimensional printed strontium-containing mesoporous bioactive glass scaffolds for repairing rat critical-sized calvarial defects, Acta Biomater. 12 (2015) 270–280, https://doi.org/10.1016/j.actbio.2014.10.015.

[68] P. Pei, X. Qi, X. Du, M. Zhu, S. Zhao, Y. Zhu, Three-dimensional printing of tricalcium silicate/mesoporous bioactive glass cement scaffolds for bone regeneration, J. Mater. Chem. B 4 (2016) 7452–7463, https://doi.org/10.1039/C6TB02055K.
[69] X. Qi, P. Pei, M. Zhu, X. Du, C. Xin, S. Zhao, X. Li, Y. Zhu, Three dimensional printing of calcium sulfate and mesoporous bioactive glass scaffolds for improving bone regeneration in vitro and in vivo, Sci. Rep. 7 (2017) 42556, https://doi.org/10.1038/srep42556.
[70] M. Sun, A. Liu, H. Shao, X. Yang, C. Ma, S. Yan, Y. Liu, Y. He, Z. Gou, Systematical evaluation of mechanically strong 3D printed diluted magnesium doping wollastonite scaffolds on osteogenic capacity in rabbit calvarial defects, Sci. Rep. 6 (2016) 34029, https://doi.org/10.1038/srep34029.
[71] H. Shao, X. Ke, A. Liu, M. Sun, Y. He, X. Yang, J. Fu, Y. Liu, L. Zhang, G. Yang, S. Xu, Z. Gou, Bone regeneration in 3D printing bioactive ceramic scaffolds with improved tissue/material interface pore architecture in thin-wall bone defect, Biofabrication 9 (2017), https://doi.org/10.1088/1758-5090/aa663c 025003.
[72] H. Shao, A. Liu, X. Ke, M. Sun, Y. He, X. Yang, J. Fu, L. Zhang, G. Yang, Y. Liu, S. Xu, Z. Gou, 3D robocasting magnesium-doped wollastonite/TCP bioceramic scaffolds with improved bone regeneration capacity in critical sized calvarial defects, J. Mater. Chem. B 5 (2017) 2941–2951, https://doi.org/10.1039/C7TB00217C.
[73] A. Liu, M. Sun, H. Shao, X. Yang, C. Ma, D. He, Q. Gao, Y. Liu, S. Yan, S. Xu, Y. He, J. Fu, Z. Gou, The outstanding mechanical response and bone regeneration capacity of robocast dilute magnesium-doped wollastonite scaffolds in critical size bone defects, J. Mater. Chem. B 4 (2016) 3945–3958, https://doi.org/10.1039/c6tb00449k.
[74] H. Shao, M. Sun, F. Zhang, A. Liu, Y. He, J. Fu, X. Yang, H. Wang, Z. Gou, Custom repair of mandibular bone defects with 3D printed bioceramic scaffolds, J. Dent. Res. 97 (2018) 68–76, https://doi.org/10.1177/0022034517734846.
[75] D.M. Gupta, M.D. Kwan, B.J. Slater, D.C. Wan, M.T. Longaker, Applications of an athymic nude mouse model of nonhealing critical-sized calvarial defects. TL – 19, J. Craniofac. Surg. 19 VN-r (2008) 192–197, https://doi.org/10.1097/scs.0b013e31815c93b7.
[76] H. Zhang, X. Mao, Z. Du, W. Jiang, X. Han, D. Zhao, D. Han, Q. Li, Three dimensional printed macroporous polylactic acid/hydroxyapatite composite scaffolds for promoting bone formation in a critical-size rat calvarial defect model, Sci. Technol. Adv. Mater. 17 (2016) 136–148, https://doi.org/10.1080/14686996.2016.1145532.
[77] J.M. Bekisz, R.L. Flores, L. Witek, C.D. Lopez, C.M. Runyan, A. Torroni, B.N. Cronstein, P.G. Coelho, Dipyridamole enhances osteogenesis of three-dimensionally printed bioactive ceramic scaffolds in calvarial defects, J. Cranio-Maxillofacial Surg. 46 (2018) 237–244, https://doi.org/10.1016/j.jcms.2017.11.011.
[78] J.A. Kim, H.-S. Yun, Y.-A. Choi, J.-E. Kim, S.-Y. Choi, T.-G. Kwon, Y.K. Kim, T.-Y. Kwon, M.A. Bae, N.J. Kim, Y.C. Bae, H.-I. Shin, E.K. Park, Magnesium phosphate ceramics incorporating a novel indene compound promote osteoblast differentiation in vitro and bone regeneration in vivo, Biomaterials 157 (2018) 51–61, https://doi.org/10.1016/j.biomaterials.2017.11.032.
[79] J.-H. Shim, M.-C. Yoon, C.-M. Jeong, J. Jang, S.-I. Jeong, D.-W. Cho, J.-B. Huh, Efficacy of rhBMP-2 loaded PCL/PLGA/β-TCP guided bone regeneration membrane fabricated by 3D printing technology for reconstruction of calvaria defects in rabbit, Biomed. Mater. 9 (2014), https://doi.org/10.1088/1748-6041/9/6/065006 065006.
[80] J. Shim, J. Jeong, J. Won, J.-H. Bae, G. Ahn, H. Jeon, W.-S. Yun, E.-B. Bae, J.-W. Choi, S.-H. Lee, C.-M. Jeong, H.Y. Chung, J.-B. Huh, Porosity effect of 3D-printed polycaprolactone membranes on calvarial defect model for guided bone regeneration, Biomed. Mater. 13 (2017), https://doi.org/10.1088/1748-605X/aa9bbc 015014.
[81] F. Tamimi, J. Torres, K. Al-Abedalla, E. Lopez-Cabarcos, M.H. Alkhraisat, D.C. Bassett, U. Gbureck, J.E. Barralet, Osseointegration of dental implants in 3D-printed synthetic onlay grafts customized according to bone metabolic activity in recipient site, Biomaterials 35 (2014) 5436–5445, https://doi.org/10.1016/j.biomaterials.2014.03.050.
[82] F. Tamimi, J. Torres, U. Gbureck, E. Lopez-Cabarcos, D.C. Bassett, M.H. Alkhraisat, J.E. Barralet, Craniofacial vertical bone augmentation: a comparison between 3D printed monolithic monetite blocks and autologous onlay grafts in the rabbit, Biomaterials 30 (2009) 6318–6326, https://doi.org/10.1016/j.biomaterials.2009.07.049.
[83] Y.S. Cho, M.W. Hong, M. Quan, S.-Y. Kim, S.-H. Lee, S.-J. Lee, Y.Y. Kim, Y.-S. Cho, Assessments for bone regeneration using the polycaprolactone SLUP (salt-leaching using powder) scaffold, J. Biomed. Mater. Res. A 105 (2017) 3432–3444, https://doi.org/10.1002/jbm.a.36196.
[84] D.Y. Kwon, J.H. Park, S.H. Jang, J.Y. Park, J.W. Jang, B.H. Min, W.-D. Kim, H.B. Lee, J. Lee, M.S. Kim, Bone regeneration by means of a three-dimensional printed scaffold in a rat cranial defect, J. Tissue Eng. Regen. Med. 12 (2018) 516–528, https://doi.org/10.1002/term.2532.
[85] C.R. Hooijmans, J. IntHout, M. Ritskes-Hoitinga, M.M. Rovers, Meta-analyses of animal studies: An introduction of a valuable instrument to further improve healthcare, ILAR J. 55 (2014) 418–426, https://doi.org/10.1093/ilar/ilu042.
[86] J. Li, Q. Xu, B. Teng, C. Yu, J. Li, L. Song, Y. Xiao Lai, J. Zhang, W. Zheng, P.G. Ren, Investigation of angiogenesis in bioactive 3-dimensional poly(D,L-lactide-co-glycolide)/nano-hydroxyapatite scaffolds by in vivo multiphoton microscopy in murine calvarial critical bone defect, Acta Biomater. 42 (2016) 389–399, https://doi.org/10.1016/j.actbio.2016.06.024.
[87] S. Wu, X. Liu, K.W.K. Yeung, C. Liu, X. Yang, Biomimetic porous scaffolds for bone tissue engineering, Mater. Sci. Eng. R Reports 80 (2014) 1–36, https://doi.org/10.1016/j.mser.2014.04.001.
[88] Z. Wang, C. Wang, C. Li, Y. Qin, L. Zhong, B. Chen, Z. Li, H. Liu, F. Chang, J. Wang, Analysis of factors influencing bone ingrowth into three-dimensional printed porous metal scaffolds: a review, J. Alloys Compd. 717 (2017) 271–285, https://doi.org/10.1016/j.jallcom.2017.05.079.
[89] C.M. Murphy, M.G. Haugh, F.J. O'Brien, The effect of mean pore size on cell attachment, proliferation and migration in collagen–glycosaminoglycan scaffolds for bone tissue engineering, Biomaterials 31 (2010) 461–466, https://doi.org/10.1016/j.biomaterials.2009.09.063.
[90] B. Chang, W. Song, T. Han, J. Yan, F. Li, L. Zhao, H. Kou, Y. Zhang, Influence of pore size of porous titanium fabricated by vacuum diffusion bonding of titanium meshes on cell penetration and bone ingrowth, Acta Biomater. 33 (2016) 311–321, https://doi.org/10.1016/j.actbio.2016.01.022.
[91] Q.L. Loh, C. Choong, Three-dimensional scaffolds for tissue engineering applications: role of porosity and pore size, Tissue Eng. Part B Rev. 19 (2013) 485–502, https://doi.org/10.1089/ten.teb.2012.0437.
[92] J. Lim, J. Lee, H.S. Yun, H.I. Shin, E.K. Park, Comparison of bone regeneration rate in flat and long bone defects: calvarial and tibial bone, Tissue Eng. Regen. Med. 10 (2013) 336–340, https://doi.org/10.1007/s13770-013-1094-9.
[93] D. Yu, Q. Li, X. Mu, T. Chang, Z. Xiong, Bone regeneration of critical calvarial defect in goat model by PLGA/TCP/rhBMP-2 scaffolds prepared by low-temperature rapid-prototyping technology, Int. J. Oral Maxillofac. Surg. 37 (2008) 929–934, https://doi.org/10.1016/j.ijom.2008.07.012.
[94] D.L. Alge, J. Bennett, T. Treasure, S. Voytik-Harbin, W.S. Goebel, T.-M.G. Chu, Poly(propylene fumarate) reinforced dicalcium phosphate dihydrate cement composites for bone tissue engineering, J. Biomed. Mater. Res. A 100 (2012) 1792–1802, https://doi.org/10.1002/jbm.a.34130.
[95] Q. Wang, Q. Xia, Y. Wu, X. Zhang, F. Wen, X. Chen, S. Zhang, B.C. Heng, Y. He, H. W. Ouyang, 3D-printed atsttrin-incorporated alginate/hydroxyapatite scaffold promotes bone defect regeneration with TNF/TNFR signaling involvement, Adv. Healthc. Mater. 4 (2015) 1701–1708, https://doi.org/10.1002/adhm.201500211.
[96] J. Li, M. Chen, X. Wei, Y. Hao, J. Wang, Evaluation of 3D-printed polycaprolactone scaffolds coated with freeze-dried platelet-rich plasma for bone regeneration, Materials (Basel) 10 (2017), https://doi.org/10.3390/ma10070831.
[97] S. Ishack, A. Mediero, T. Wilder, J.L. Ricci, B.N. Cronstein, Bone regeneration in critical bone defects using three-dimensionally printed β-tricalcium phosphate/hydroxyapatite scaffolds is enhanced by coating scaffolds with either dipyridamole or BMP-2, J. Biomed. Mater. Res. Part B Appl. Biomater. 105 (2017) 366–375, https://doi.org/10.1002/jbm.b.33561.
[98] K. Haberstroh, K. Ritter, J. Kuschnierz, K.H. Bormann, C. Kaps, C. Carvalho, R. Mülhaupt, M. Sittinger, N.C. Gellrich, Bone repair by cell-seeded 3D-bioplotted composite scaffolds made of collagen treated tricalciumphosphate or tricalciumphosphate-chitosan-collagen hydrogel or PLGA in ovine critical-sized calvarial defects, J. Biomed. Mater. Res. Part B Appl. Biomater. 93 (2010) 520–530, https://doi.org/10.1002/jbm.b.31611.
[99] J.Y. Won, C.Y. Park, J.H. Bae, G. Ahn, C. Kim, D.H. Lim, D.W. Cho, W.S. Yun, J.H. Shim, J.B. Huh, Evaluation of 3D printed PCL/PLGA/β-TCP versus collagen membranes for guided bone regeneration in a beagle implant model, Biomed. Mater. 11 (2016), https://doi.org/10.1088/1748-6041/11/5/055013.
[100] W. Xiao, M.A. Zaeem, B.S. Bal, M.N. Rahaman, Creation of bioactive glass (13–93) scaffolds for structural bone repair using a combined finite element modeling and rapid prototyping approach, Mater. Sci. Eng. C 68 (2016) 651–662, https://doi.org/10.1016/j.msec.2016.06.011.

Study II

R. S. Azarudeen*, **M. N. Hassan**[1], M. A. Yassin, M. Thirumarimurugan, N. Muthukumarasamy, D. Velauthapillai, and K. Mustafa. "3D-printable polycaprolactone-gelatin blends characterized for *in vitro* osteogenic potency" Reactive and Functional Polymers, vol. 146, no. December 2019, p. 104445, Jan. 2020.

Journal Impact Factor (2022) = 4.9

II

[1] Shared contribution

Reactive and Functional Polymers 146 (2020) 104445

Contents lists available at ScienceDirect

Reactive and Functional Polymers

journal homepage: www.elsevier.com/locate/react

3D printable Polycaprolactone-gelatin blends characterized for *in vitro* osteogenic potency

Raja S. Azarudeen[a,b,*,1], Mohamad Nageeb Hassan[a,1], Mohammed Ahmed Yassin[a], M. Thirumarimurugan[b], N. Muthukumarasamy[c], Dhayalan Velauthapillai[d], Kamal Mustafa[a]

[a] Tissue Engineering Group, Department of Clinical Dentistry, Faculty of Medicine, University of Bergen, 5020 Bergen, Norway
[b] Department of Chemical Engineering, Coimbatore Institute of Technology, Coimbatore 641 014, Tamil Nadu, India
[c] Department of Physics, Coimbatore Institute of Technology, Coimbatore 641 014, Tamil Nadu, India
[d] Department of Computing, Mathematics and Physics, Western Norway University of Applied Sciences, Inndalsveien 28, 5063 Bergen, Norway

ARTICLE INFO

Keywords:
Polycaprolactone
Gelatin
3D printing
Bone regeneration
BMSC

ABSTRACT

Synthetic polycaprolactone (PCL) was modified with various concentrations of gelatin (GL) to enhance its physical properties and biological activity for bone regeneration. A novel trisolvent mixture has been used to mix PCL and GL that were fabricated as scaffolds using 3D plotting. The scaffolds were characterized for their mechanical properties, hydrophilicity and swelling ability. In addition, the structure and morphology of the printed scaffolds were analyzed by Fourier-Transform infrared spectroscopy (FTIR), X-ray diffraction (XRD), scanning electron microscopy (SEM) and microcomputed tomography (μCT). Attachment, proliferation and osteogenic differentiation of rat bone marrow stromal cells (BMSC) cultured on the printed scaffolds were evaluated within 21 days. Increasing GL content in the scaffolds led to an enhanced hydrophilic nature, better pore size distribution and interconnected micro-pores. This resulted in better cellular attachment, proliferation and osteogenic differentiation. Although the multiple reactive sites and biochemical compatibility provided by GL improved the scaffolds' osteogenic potency, the tensile strength and elasticity of the printed scaffolds are yet challenging with increasing GL contents.

1. Introduction

Tissue engineering approaches based on combining cells, degradable scaffolds and biological molecules that mimic natural healing have been tried in attempts to regenerate bone tissues [1,2]. Bone tissue engineering has the ability to provide an effective treatment compared to the current bone graft methods; because they have the potential to restore the fully damaged bone tissues. Various natural and synthetic biomaterials have been used to restore, maintain and improve the structure and function of bone. However, limiting factors are present in each biomaterial tested, either physical, chemical, biological or mechanical properties that affect their use [3]. As a result, blends and composite biomaterials have been designed for bone tissue engineering applications combining natural and/or synthetic polymers with or without bioceramics [4–6].

Polycaprolactone (PCL) is an FDA approved synthetic polymer that has been widely used in the field of bone regeneration due to its physical and mechanical properties, *e.g.* biocompatibility, low melting temperature, slow degradation rate, and high tensile strength [7,8]. However, poor cell attachment behavior was observed with pure PCL due to its hydrophobic nature [9]. Thus various PCL blends have been studied in attempts to improve its physical and biological properties for use in bone regeneration [10,11]. Gelatin (GL) is a natural polymer derived from the hydrolysis of collagen, produced at low cost and having good cellular attachment properties due to hydrophilicity and through integrin mediation. However, GL is characterized by thermal sensitivity, fast biodegradation and poor mechanical strength that limit its application as the sole component in bone scaffolds. Thus, studies have evaluated a mixture of GL with other polymers [12] and bioceramics [13] attempting to increase their biocompatibility and biologically active bone scaffolds while retaining stable thermal and mechanical behavior.

3D printing and additive manufacturing have recently been used to fabricate complex structures and matrices with an interconnected pore structure and high mechanical strength [14]. In addition, it is improving the design, structure and fabrication of scaffolds compared to previously produced by conventional solvent-casting, gas foaming, and electrospinning techniques [15,16]. PCL possesses suitable mechanical

* Corresponding author at: Department of Chemical Engineering, Coimbatore Institute of Technology, Coimbatore 641 014, Tamil Nadu, India.
E-mail address: azarudeen.r@cit.edu.in (R.S. Azarudeen).

[1] The authors have equally contributed to this article and are both first authors.

https://doi.org/10.1016/j.reactfunctpolym.2019.104445
Received 11 October 2019; Received in revised form 4 December 2019; Accepted 4 December 2019
Available online 05 December 2019
1381-5148/

property and biocompatibility. However, it has several drawbacks like hydrophobicity and slow degradation rate. Similarly, gelatin has good hydrophilicity and fast degradation rate; but it cannot be used as base material to construct scaffold due to lesser mechanical property.

Gelatin was previously coated on electrospun PCL fibers through layer-by-layer self-assembly process. The incorporation of gelatin was found to promote the nucleation and growth of calcium phosphate followed by better cell attachment and proliferation on the top of the used scaffolds [17]. On the other hand, gelatin was added through electrospinning on spun PCL matrices using two separate solvents; bi-electrospun nanofibers showed enhanced support for pluripotent stem cells attachment, proliferation and differentiation towards neural cells [18].

Hence, this study aimed to achieve a 3D printable blend from PCL and GL with enhanced biological properties *i.e.* better cellular attachment and osteogenic differentiation. A novel trisolvent approach was used to blend both the polymers at room temperature, in order to overcome their mismatched thermal behavior. This blend was used to fabricate 3D printed PCL-GL scaffolds at different ratio (up to 16% GL), that were chemically crosslinked using genipin. The prepared scaffolds were characterized for their physical, spectral and mechanical properties. In addition, rat bone marrow stromal cells (BMSC) were cultured on PCL-GL scaffolds in osteogenic media for 21 days to characterize their attachment, proliferation and osteogenic differentiation.

2. Materials and methods

2.1. Materials

Polycaprolactone pellets (M_n: 80,000), gelatin (type B from bovine skin), glacial acetic acid, ethyl acetate, and phosphate buffered saline (PBS) were obtained from Sigma Aldrich (Schnelldorf, Germany) and used without further purification. Genipin, the crosslinker was purchased from Wako Chemicals (Neuss, Germany). Double distilled and ultrapure water used throughout the experiments were prepared in our laboratory.

2.2. Fabrication of porous 3D PCL-GL composite scaffolds

Blends of GL with PCL were prepared in four ratios (2, 4, 8 and 16 *w*/w % of GL in PCL) by dissolving in a trisolvent mixture (acetic acid: ethylacetate: water in 3:2:1 ratio). For the 2% blend ratio (PCL-GL2), 125 mg of GL was dissolved in 10 mL of a trisolvent mixture at 45 °C with constant shaking at 600 rpm for 2 h. Next PCL pellets (6 g) were added to the above solution and shaking was continued overnight to attain uniform blending followed by sonication for 1 h to remove air bubbles before printing. Similarly, three other blends were prepared by changing the percent of GL added to the solution; 4% GL (PCL-GL4), 8% GL (PCL-GL8) and 16% GL (PCL-GL16) were compared with the control group of PCL dissolved in trisolvent without GL.

Each group was incubated at 37 °C for 2 h before being printed using a 3D-Bioplotter® (Manufacturer Series, EnvisionTEC, Gladbeck, Germany). Grid structure scaffolds (30 × 30 × 1.5 mm, L × W × H; 4 layered) were printed (0/90°) with strut size 0.4 mm and distance of 0.5 mm between the strands at 24 °C and around 2.5 bar. The speed of the printing was set at 30 mm/s and pre- and post-flow were adjusted to 0.15 s after several trials to optimized flow. After printing, the scaffolds were punched out (Ø = 8.5 mm), dried overnight at room temperature and then immersed in 1% genipin at 20 °C for 48 h for efficient GL crosslinking. After that the scaffolds were neutralized with 0.1 N NaOH solution and washed thrice with double distilled water at room temperature to remove the residual acidic solvent and lyophilized for 24 h.

2.3. Characterization of the scaffolds

2.3.1. Spectral and crystallographic characterization

The chemical interactions and linkages between GL and PCL in the scaffolds were confirmed by FTIR spectroscopy performed using the ATR-FTIR instrument (Nicolet iS 50, ThermoFisher Scientific, Cambridge, MA, USA) controlled by OMNIC 9.3 research software. The scanning range was 4000 to 400 cm^{-1} with a resolution of 2 cm^{-1}. The amorphous and crystalline nature of the fabricated scaffolds was examined through X-ray diffraction patterns observed with an X-ray diffractometer (D8 Advance ECO, Bruker, Billerica, MA, USA) with 1 kW X-ray source and SSD 160 detector to confirm the incorporation of the GL to PCL and the morphological changes occurred in the scaffolds.

2.3.2. Scanning electron microscopy (SEM)

The surface morphology of the scaffolds was viewed using a scanning electron microscope (SEM) (JSM-7400F, JEOL, Tokyo, Japan). The bare scaffolds were dried and then sputter coated with gold-platinum. In addition, the printed scaffolds seeded with cells were studied after being fixed in 2.5% glutaraldehyde (at 3 and 14 days) before being dried, coated and scanned at low voltage (4 kV) to assess cell adhesion and proliferation.

2.3.3. Microcomputed tomography (μCT)

Microcomputed tomography (μCT) was employed to determine the porosity and porous interconnectivity of the printed scaffolds. The printed scaffolds were punched in to cylindrical shapes (Ø = 5 mm) before being scanned (without filters) using the SkyScan 1172 μCT imaging system (SkyScanVR v.1.5.23, Kontich, Belgium) with 10 μm resolution, 40 kV voltage and 250 mA current. A cone beam reconstruction algorithm was adopted to reconstruct the raw images of the scaffold to serial coronal oriented tomograms at a threshold level of 40/255.

2.3.4. Hydrophilicity and water uptake

The water contact angle for the prepared blends (made in to flat discs) was measured to determine the hydrophilicity of the blended groups at room temperature (SL200A type Dataphysics OCA 15, Filderstadt, Germany). Water (3 μL) was dropped on the surface of each prepared sample and the contact angle was recorded. An average value was obtained for triple measurements at various positions of the surface of the scaffold.

The swelling behavior of the scaffolds was determined using the gravimetric method. A known weight of the scaffolds was soaked in 50 mL of double distilled water and subjected to constant shaking at 37 °C. At intervals of 1 h the scaffolds were taken out of the glass bottle and dried gently with filter paper to remove the excess residual water adsorbed on the surface of the scaffolds. It was assumed that the equilibrium had been reached after 48 h. The swelling index (hydrophilic nature) of the scaffolds at time t was determined as follows, where W_t is the weight of swollen scaffolds at time t and W_d is the weight of the dry scaffold.

$$\textit{Swelling index}\,(\%) = \frac{(W_t - W_d)}{W_d} \times 100$$

2.3.5. Mechanical characterization

Dumbbell-shaped samples were printed to test the mechanical properties of each group according to ASTM-D638 with shaft dimensions of 17.5 × 4.5 × 1.5 mm (L × W × H). The tensile strength, Young's modulus and elongation at break for the scaffolds ($n = 3$) were tested using a universal testing machine (MTS, 858 Mini Bionix II instrument, Eden Prairie, MN, USA).

2.4. In vitro biological evaluation

2.4.1. Cell isolation

BMSC were applied to the fabricated polymeric scaffolds. The cells were isolated from the femurs of donor Lewis rats, pooled and maintained as described previously [19]. Before experiments, the animals were housed in a uniform condition for at least a week time. Then the animals were euthanized by providing an overdose of carbon dioxide inhalation followed by removing the femurs, which were cleaned and washed 3× in Dulbecco's PBS (Gibco, life Technologies Limited, UK) supplemented with 3% penicillin-streptomycin solution (PS) (10,000 units/mL Penicillin / 10,000 μg/mL streptomycin, HyClone laboratories, Austria). The metaphyseal ends of the femurs were detached and the marrow cavity was flushed with minimum essential medium (α-MEM, gibco, life Technologies Limited, UK) supplemented with 1% (*v*/v) PS and (v/v) 15% fetal bovine serum (FBS, Sigma, Germany) in to a sterile Falcon tube. Then the cells were centrifuged and re-suspended in fresh α-MEM containing 15% FBS and cultured in T175 flasks for adherent cells (NUNC, A-S, Roskilde, Denmark) in a humidified incubator (5% CO_2, 37 °C). Next, the medium was changed daily with fresh α-MEM containing 1% PS and 15% FBS until 80% confluence was reached.

Approval for the study was received from the Norwegian Animal Research Authority and the study was performed according to the European Conventional for the Protection of Vertebrates used for Scientific Purposes (local approval number 20146866).

2.4.2. Cell seeding

Lewis rat BMSC was seeded on the printed scaffolds to investigate the potential of the developed scaffold to support their growth and differentiation in osteogenic medium at higher GL percentages. The prepared scaffolds were sterilized before cell seeding using ethyl alcohol (70% for 30 min.) under shaking (1000 RPM for 1 min.), followed by UV radiation (2 h) and washing with PBS (twice - 20 min). Afterwards, the sterilized scaffolds were prewetted overnight in α-MEM (100 μL/scaffold) containing PS (1% *v*/v).

At 85% confluency, the BMSC (passage 3) were trypsinized (Trypsin/EDTA, Lonza, USA) and counted using an automated cell counter (Countess, Invitrogen, ThermoFischer Scientific, CA, USA). Subsequently, the cells (86% viability) were seeded on the scaffolds in a density of (1×10^5 cells/scaffold) in low adherent plates (TC 96 well plate, Suspension; Sarstedt, Nümbrecht, Germany) and incubated at 37 °C in 5% CO_2 for up to 21 days. Osteogenic media (0.05 mM ascorbic acid, 10 mMb-glycerophosphate, and 100 nM dexamethasone) was added to the culture medium after 24 h and changed 2 × each week. Cell/scaffold interactions in terms of attachment, proliferation and differentiation were assessed at different time points as noted.

2.4.3. Cell attachment and proliferation

SEM was used to determine cell attachment and proliferation. After culture for 3 and 14 days, samples were prepared for SEM as follows. First, the medium was replaced with 2.5% glutaraldehyde in α-MEM without serum and fixed for 30 min at room temperature. Second, samples were fixed in 2.5% glutaraldehyde in 0.1 M sodium cacodylate pH 7.2 with 0.1 M sucrose for 30 min at room temperature. The samples were then treated with 1% osmium tetroxide in distilled water for 1 h, followed by dehydration through a graded series of ethanol solutions (70, 80, 95, and 100%), critical point-dried (using CO_2 as transitional fluid and the specimens mounted on aluminum holders), and sputter-coated with a 10 nm conducting layer of gold platinum. Finally, the samples were examined by SEM (Jeol JSM 7400F, Tokyo, Japan) using a voltage of 4 kV.

Live/dead assay (Invitrogen, Life Technologies, Carlbad, CA, USA) was used to determine the viability of the BMSC on the printed scaffolds at 21 days and imaged using a fluorescence microscope (Olympus, Tokyo, Japan). In addition, cell proliferation assay (Picogreen dsDNA quantification kit, Invitrogen) were done in triplicate at days 7 and 14. Lysate solution (with 0.1% TritonX) was added to cultured scaffolds, DNA was extracted from lysate solution by freeze-thaw cycles followed by vortexing, where the fluorescence intensity of the solution was measured to quantify the DNA content against a standard solution using a microplate reader (FLUOstar Optima, BMG LABTECH, Aylesbury, Bucks,UK) at 485 and 525 nm excitation and emission [20].

2.4.4. Cell differentiation

Osteogenic differentiation of the seeded cells was tested using Alizarin red S staining at day 21 to measure calcium deposition on the printed scaffolds. The scaffolds were imaged, then the dye were extracted using 100 mM cetylpyridinium chloride (300 μL/scaffold) incubated for 4 h at room temperature for quantification of staining. The optical density (absorbance) was measured for the extracted dye at 544 nm using a microplate reader (FLUOstar Optima, BMG LABTECH, Aylesbury, Bucks, UK).

2.4.5. Statistical analysis

Statistical analysis was calculated as group average with standard deviations and compared using one way analysis of variance (ANOVA) using STATA software (Ver. 15.1; StataCorp LLC, TX, USA). Tukey's *post hoc* test was used to evaluate differences between groups. A p value of < 0.05 was considered significant.

3. Results and discussion

3.1. Morphology, porosity and hydrophilicity

As GL content increased from 2 to 16%, the color of the scaffolds changed steadily from the white to dark blue due to the crosslinking of genipin, with the color intensity is directly related to the amount of GL (Fig. 1). In addition, SEM images clearly illustrate that PCL-GL scaffolds had a rough surface due to the incorporation of GL. The most rough surface morphology and highest porosity were clearly observed in PCL-GL8 and PCL-GL16 scaffolds.

The μCT analysis revealed some variations among the printed

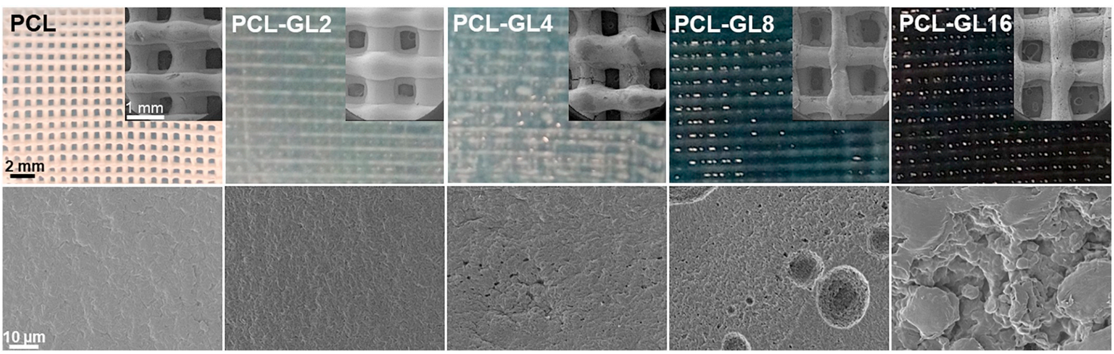

Fig. 1. Optical images and SEM micrographs of the printed scaffolds characterizing their surfaces.

Table 1
Pore properties of PCl-gelatin composite scaffolds from μ-computed tomography.

Sample	Pore volume (mm^3)	Open porosity (%)	Closed porosity (%)	Total porosity (%)	Fractal dimension	Surface area (mm^2)
PCL	3.81 ± 0.048	48.34 ± 0.371	0.98 ± 0.522	48.84 ± 0.163	2.43 ± 0.025	110.11 ± 0.94
PCL-GL2	3.19 ± 0.658	44.09 ± 0.307	1.30 ± 0.482	44.82 ± 0.431	2.41 ± 0.018	89.96 ± 0.54
PCL-GL4	5.09 ± 0.031	55.58 ± 0.749	0.99 ± 0.212	56.02 ± 0.547	2.68 ± 0.104	205.59 ± 0.29
PCL-GL8	5.04 ± 0.955	62.30 ± 0.634	0.43 ± 0.0923	62.47 ± 0.602	2.67 ± 0.022	243.63 ± 0.02
PCL-GL16	5.13 ± 0.484	68.62 ± 0.542	0.39 ± 0.544	68.75 ± 0.325	2.59 ± 0.033	292.23 ± 0.98

scaffolds regarding their surface area, open and closed porosity, total porosity and fractal dimensions (Table 1). Comparable surface topography and internal structure with highly interconnected pores for all the scaffolds were observed, while the total porosity (%) was found to increase with the increase of their GL content. The calculated mean pore size distribution (Fig. 2a) showed a wide range of porosity (10–400 μm) with 100% interconnectivity. Thus, the essential porosity range required for bone regeneration processes was observed for GL based scaffolds [21].

Various surface modifications have been introduced to enhance the physical and biological properties of PCL, including alkaline hydrolysis with sodium hydroxide (NaOH) [22], plasma treatments [23] and various coatings [24,25]. However, enhancing the bulk properties in addition to the surface physical properties should accommodate for sustainable biological performance.

The water uptake capacity of PCL-GL scaffolds was found to be higher, as expected than the PCL scaffolds (Fig. 2b). The significantly increased percentage of water uptake by the scaffolds corresponded to the GL content with respect to time. The crosslinking by genipin did not influence the hydrophilicity since it crosslinks only the amino groups presents in GL, leaving behind the hydrophilic carboxylic groups [26]. GL should therefore enhance surface wettability, which should be supporting cellular adhesion and proliferation and the rate of biodegradation [27,28]. This was further verified by measuring the hydrophilicity of PCL and PCL-GL, which were found to improve with increasing GL contents, represented with the contact angle values (Fig. 2c). PCL prepared in the trisolvent mixture showed an average contact angle value equal to 80 ± 2°, which was better than previously reported values of PCL prepared in HFIP or chloroform:water mixture (118°) [29] and PCL prepared from trifluoroethanol solvent by electrospinning method (109°) [30]. In addition, the average contact angle of PCL-GL2 to PCL-GL16 decreased steadily, indicating better hydrophilicity with increasing GL content, and accordingly the amine and carboxyl functional groups.

3.2. Chemical, crystallographic and mechanical properties

The typical characteristic spectral bands for the fabricated scaffolds were observed through attenuated total reflectance-FTIR spectroscopy to assure the presence of GL in polycaprolactone after crosslinking with genipin. The spectra for all the scaffolds are presented in Fig. 3a and the observed wavenumber/bands/signals are clearly elucidated in Supplementary Table 1, and interpreted according to the earlier reported literature [31–37]. For PCL scaffold, the bands appeared at 2909.44 and 2824.42 cm^{-1} were assigned to symmetrical and asymmetrical $–CH_2$ stretching vibrations; while, 1715.72 cm^{-1}were assigned as stretching vibration of –C=O group of ester linkage,1323.45 cm^{-1} was attributed to C—O and C—C stretching vibrations. However, from the spectrum of PCL-GL4, the band observed at 1677 cm^{-1} is assigned to –C=O stretching vibration of amide I; 1507.22 cm^{-1} is assigned to in-plane bending vibration of –NH for amide II (coupling interaction between –NH and C—N stretch); 1239.44 cm^{-1} is attributed to –C-N stretching vibration of amide III (-NH deformation and C—N stretch); 1429 and 1376.34 cm^{-1} is assigned to asymmetrical and symmetrical bending vibrations of $–CH_2$ and CH_3. From these band observations, it is clearly suggested that the newly appearing vibrations for the GL-incorporated scaffolds were not observed for the PCL scaffolds, confirming the successful blending of GL into the PCL matrix. The slight variation in the relative intensity of FTIR spectra of the PCL-GL scaffolds compared to the GL spectrum is probably due to the reduction of GL free amino

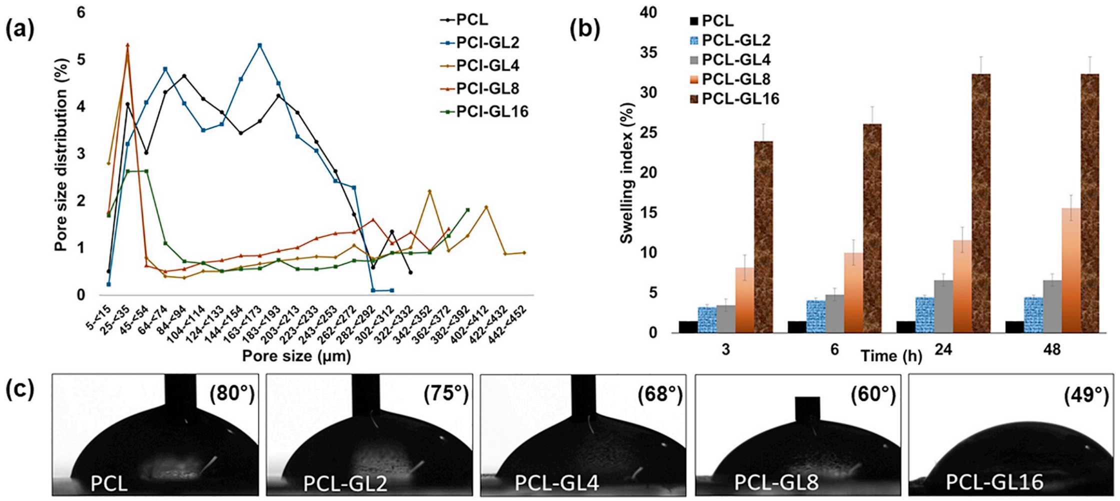

Fig. 2. The effect of increasing gelatin concentration on the physical properties of the prepared blends showing (a) pore size distribution; (b) swelling index; and (c) optical photographs for the contact angle measurements.

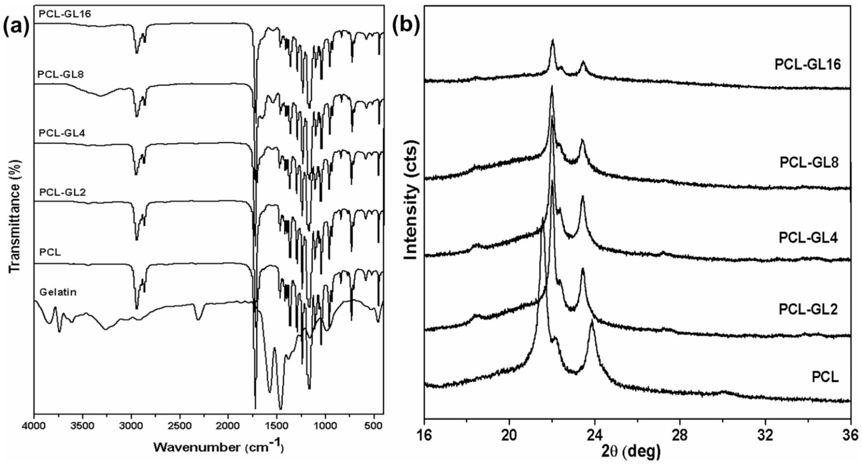

Fig. 3. The effect of increasing gelatin (%) on the spectral and crystallographic properties of the prepared blends using (a) FTIR, and (b) XRD.

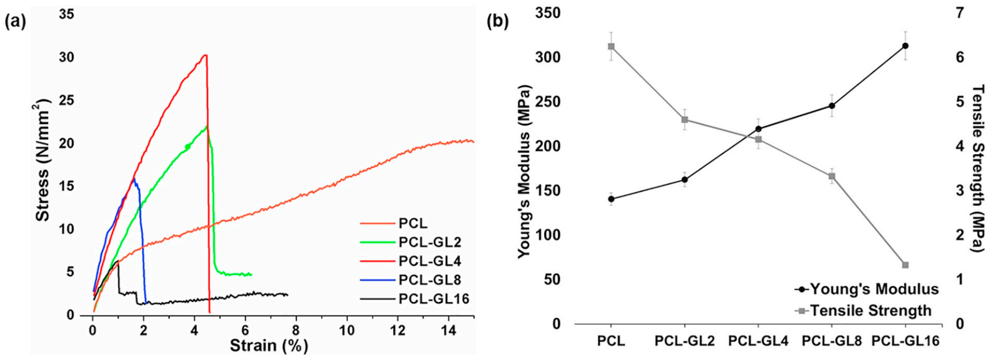

Fig. 4. Mechanical properties of the printed scaffolds. (a) Stress-Strain curve; (b) Young's modulus (MPa) *vs.* Tensile strength (MPa).

groups that react with genipin molecules. A nucleophilic attack between the primary amine of GL and the hetero group of the genipin followed by a nucleophilic substitution reaction between the ester group of genipin and the primary amine of gelatin are consistent with a minimal residual toxicity [38]. This reaction would permit the cells to recognize and bind with GL matrix and support their proliferation and differentiation.

The X-ray diffraction patterns observed for the PCL-GL 3D scaffolds are illustrated in Fig. 3b. There were two sharp peaks observed in all the patterns of scaffolds at around $2\theta = 21.7$ and $23.9°$. The intensity of these peaks were the result of the semi-crystalline nature of PCL, but they decreased for the PCL-GL8 and PCL-GL16 groups, suggesting a more amorphous structure possibly due to the gelatin molecules entanglement in to the PCL molecular chains [39].

The measured Young's modulus (stiffness) and tensile strength (Fig. 4) show PCL scaffolds possessed low stiffness (140.78 MPa) but high strength (6.25 MPa), whereas a trend towards decreased tensile strength and increased stiffness was observed for increased incorporation of GL in scaffolds (Supplementary Table 2). However, the observed decrease in tensile strength of GL incorporated scaffold is probably due to a tendency of GL towards agglomeration and the creation of pores due to its variant solubility in the trisolvent mixture, in addition to the increased amorphous tendency in scaffolds containing increased GL. It was noted that the mechanical properties may influence the cell attachment and proliferation. The effects are observed through the mechanotransductive pathways and also due to the other parameter like scaffold architecture. The PCL-GL scaffolds possess an adequate mechanical strength that manages to increase the percentage of the live cells, cell attachment and proliferation.

3.3. Biological activity and osteoconduction

BMSC attachments to the printed scaffolds as shown by SEM and viability results by live/dead analyses are shown in Fig. 5. Cell attachment and spreading on the scaffold at day 3 and day 14 showed spindle shaped cells with varying cell-cell interactions. Attachment was found to increase with increasing GL percent in the printed scaffolds at day 3. In addition, the density of cells increased at day 14, with spreading over the scaffolds' surface and towards the inner pores in PCL-GL4 up to the PCL-GL16 group. This was also confirmed by live/dead fluorescent images at day 21.

This active promotion of cellular attachment was even noticed through the promoted BMSC attachment and proliferation on tissue culture plates (low adherent plates), proportional to the increase of their GL content (Fig. 6a, PCL-GL4 up to the PCL-GL16 groups at day 7). In addition, only these three PCL-GL groups showed increased proliferation rates of BMSC on printed scaffolds from day 7 to 14 as measured by DNA quantification using the Picogreen assay (Fig. 6b).

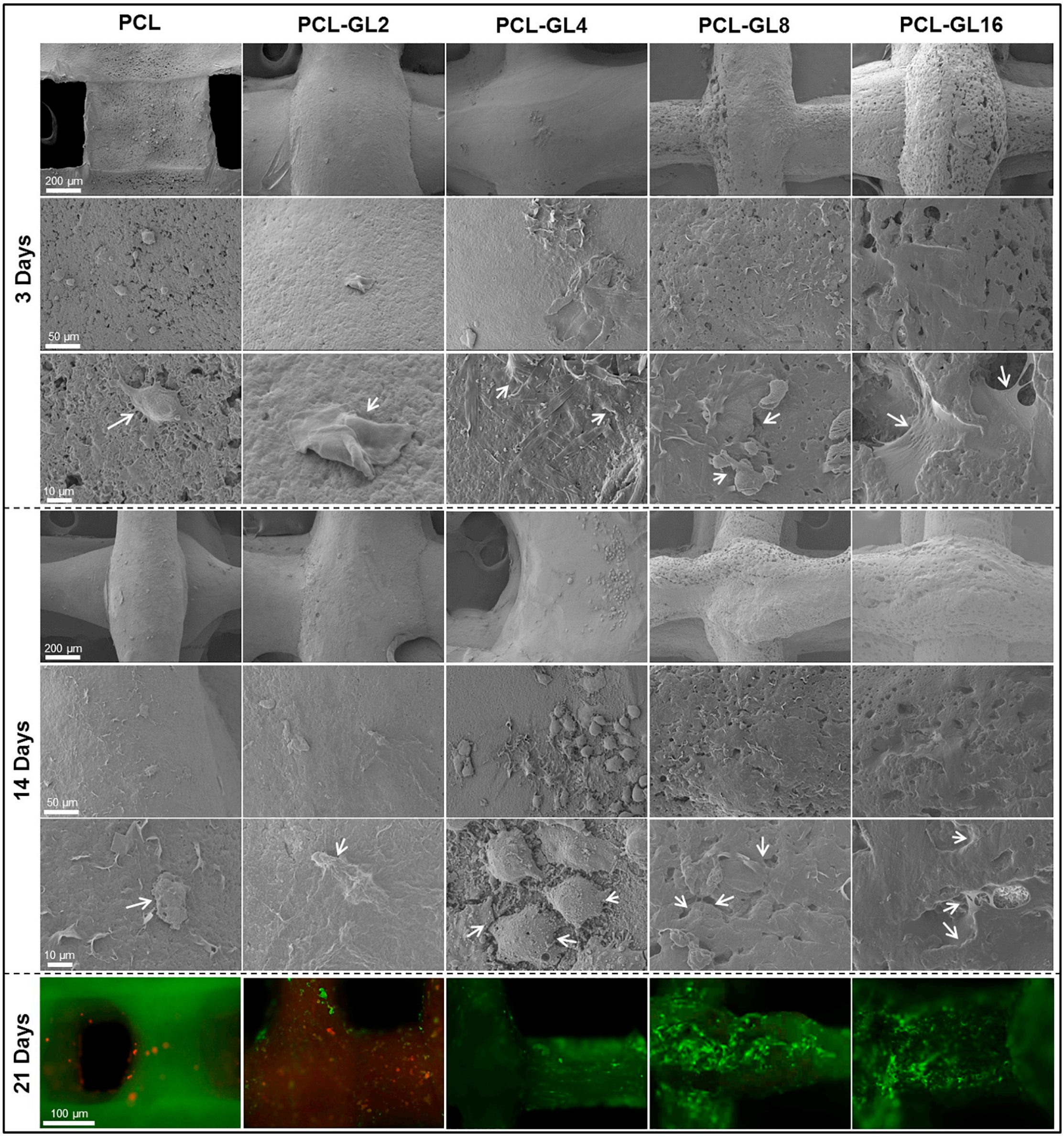

Fig. 5. SEM and fluorescence micrographs for the attached BMSC on the printed scaffolds. SEM are shown at different magnifications after 3 and 14 days. Last row is showing fluorescence micrographs for the live/dead cells after 21 days. Cellular attachments are pointed with white arrows.

The Alizarin red-S stain showed a linear increase in color intensity directly related to the increase of GL contents (Fig. 6c and d), resulting from BMSC osteogenic differentiation and calcium deposition on each scaffolds group at day 21. The live/dead analyses illustrated an increased percent of live cells attached in the PCL-GL8 and PCL-GL16 groups due to the presence of reactive sites and electrostatic attraction provided by GL [32,40]. Further, the Alizarin red-S stain results suggest that the incorporated GL molecules provided specific dose-dependent molecular cues in addition to physically promoting attachment to PCL *via* hydrophilicity and integrin interactions with the binding motifs [41]. These molecules have been reported to afford an optimized environment to promote cellular attachment and osteo-bioactivity [42]. The trisolvent mixture used here did not appear to interfere with biological activity, as no adverse reactions were noted with the seeded cells.

The outcomes in the current study demonstrate two interacting factors that are affected by increasing the content of GL in PCL scaffolds through the trisolvent method resulting in favorable physical and biological properties. The first interplaying factor is the more porous structure and surface area seen with increased GL incorporation. The

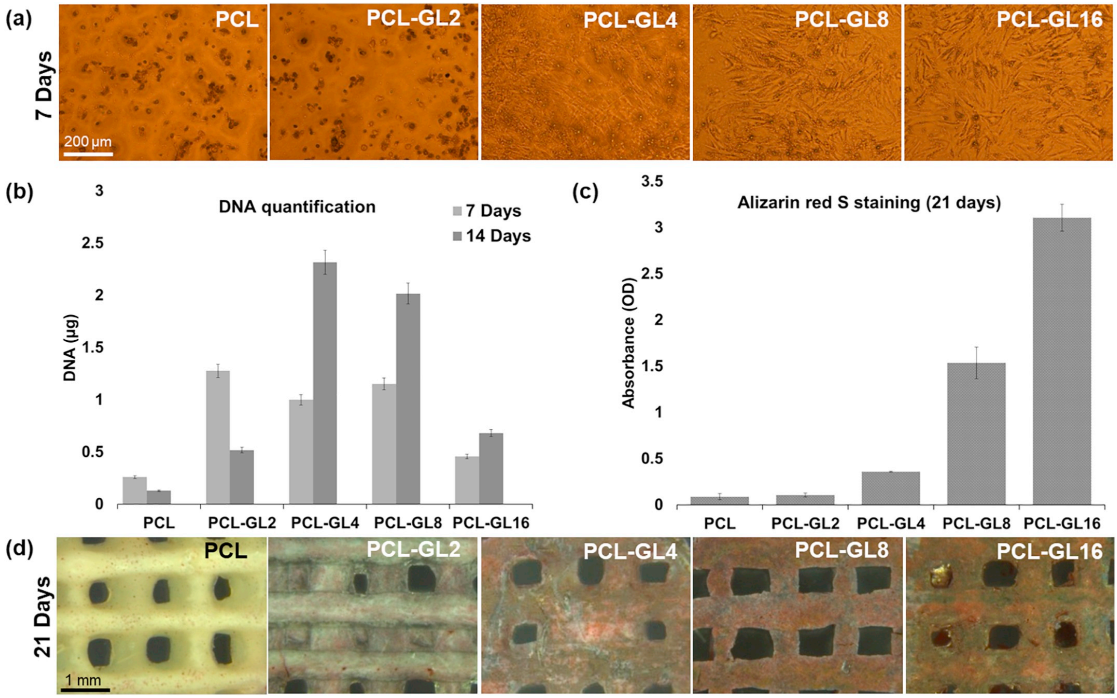

Fig. 6. Biological characterization of the printed scaffolds seeded with BMSC. (a) Microscopic images showing the effect of the scaffold extraction media on the attachment of BMSC on low adherent plates at 7 days, (b) Proliferation of cells on the scaffolds evaluated by DNA quantification (7 and 14 days). (c) Optical density (quantification) of the extracted Alizarin red stain from the scaffolds (21 days). (d) Micrographs for the alizarin red stained scaffolds after 21 days. (For interpretation of the references to color in this figure legend, the reader is referred to the web version of this article.)

addition of 2% GL was found to close the fractional porosity (> 250 µm) previously reported in the printed PCL scaffolds. However, with increasing GL content (4–16%), increased porosity is created (300–450 µm) that negatively affected the tensile strength with higher GL content, but created more favorable conditions for cells to attach, proliferate and differentiate. Nevertheless, this divergent porosity could have limited the complete retrieval of the attached cells and their DNA quantification at PCL-GL4 up to PCL-GL16 groups, that showed less quantified amount of cells than expected (Fig. 6b), especially at 7 days. While the second interplaying factor is the bio-chemical nature of GL to increase the surface and bulk hydrophilicity, integrin-mediated cell attachment and to promote cell proliferation on the printed scaffold and surrounding media (culture plates) by improving the signal transduction *via* integrin. Hence, the PCL-GL scaffold would mimic the nature structure of extracellular matrix that promotes osteoconduction.

4. Conclusion

In this study, PCL-GL was blended in a trisolvent mixture to construct 3D printed scaffolds that were characterized physically, mechanically, and biologically. Inclusion of GL modified the PCL scaffolds towards increased hydrophilicity, better pore size distribution and interconnectivity, and more reactive sites for cell attachment. In turn, this promoted cell proliferation and differentiation, illustrated by favorable BMSC interaction with PCL-GL scaffolds compared to the pristine PCL scaffolds. Overall, the combined characteristics and properties of 3D printing and PCL-GL provided a conducive architecture and environment for positive osteogenic potency.

Declaration of Competing Interest

The authors declare that they have no known competing financial interests or personal relationships that could have appeared to influence the work reported in this paper.

Acknowledgements

All the authors acknowledge the University of Bergen and Western Norway University of Applied Sciences (HVL). This work was funded by HVL Bergen, Norway through UTFORSK project (UTF-2016-LONG-TERM/10051). This work was also supported by the Western Norway Regional Health Authority (Helse Vest RHF) projects #502027 and #912048. This work was partially funded by the Research Council of Norway through the BEHANDLING project (Grant no. 273551) and Bergen Research Foundation, Norway (BFS2018TMT10). Raja S. Azarudeen sincerely conveys his thanks to HVL Bergen, UiB Bergen and CIT India for the financial aid, their constant support and encouragement.

Appendix A. Supplementary data

Supplementary data to this article can be found online at https://doi.org/10.1016/j.reactfunctpolym.2019.104445.

References

[1] L. Roseti, V. Parisi, M. Petretta, C. Cavallo, G. Desando, I. Bartolotti, B. Grigolo, Scaffolds for bone tissue engineering: state of the art and new perspectives, Mater. Sci. Eng. C 78 (2017) 1246–1262.

[2] S. Stratton, N.B. Shelke, K. Hoshino, S. Rudraiah, S.G. Kumbar, Bioactive polymeric scaffolds for tissue engineering, Biact. Mater. 1 (2) (2016) 93–108.
[3] R. Dorati, A. De Trizio, T. Modena, B. Conti, F. Benazzo, G. Gastaldi, I. Genta, Biodegradable scaffolds for bone regeneration combined with drug-delivery systems in osteomyelitis therapy, Pharmaceuticals (Basel) 10 (4) (2017) 96.
[4] M. Nageeb, S.R. Nouh, K. Bergman, N.B. Nagy, D. Khamis, M. Kisiel, T. Engstrand, J. Hilborn, M.K. Marei, Bone engineering by biomimetic injectable hydrogel, Mol. Cryst. Liq. Cryst. 555 (2012) 177–188.
[5] C. Szpalski, M. Wetterau, J. Barr, S.M. Warren, Bone tissue engineering: current strategies and techniques-part I: scaffolds, Tissue Eng. Part B Rev. 18 (2012) 246–257.
[6] Y. Kim, G. Kim, Collagen/alginate scaffolds comprising core (PCL)–shell (collagen/alginate) struts for hard tissue regeneration: fabrication, characterisation, and cellular activities, J. Mater. Chem. B 1 (2013) 3185–3194.
[7] S.Y. Heo, S.C. Ko, G.W. Oh, N. Kim, I.W. Choi, W.S. Park, W.K. Jung, Fabrication and characterization of the 3D-printed polycaprolactone/fish bone extract scaffolds for bone tissue regeneration, J. Biomed. Mater. Res. B Appl. Biomater 107 (6) (2019) 1937–1944.
[8] Z. Heydari, D. Mohebbi-Kalhori, M.S. Afarani, Engineered electrospun polycaprolactone (PCL)/octacalcium phosphate (OCP) scaffold for bone tissue engineering, Mater. Sci. C Mater. Biol. Appl. 81 (1) (2017) 127–132.
[9] M. Yang, X. Gao, Z. Shen, X. Shi, Z. Lin, Gelatin-assisted conglutination of aligned polycaprolactone nanofilms into a multilayered fibre-guiding scaffold for periodontal ligament regeneration, RSC Adv. 9 (2019) 507–518.
[10] B.P. Hung, B.A. Naved, E.L. Nyberg, M. Dias, C.A. Holmes, J.H. Elisseeff, A.H. Dorafshar, W.L. Grayson, Three-dimensional printing of bone extracellular matrix for craniofacial regeneration, ACS Biomater. Sci. Eng. 2 (2016) 1806–1816.
[11] J.Y. Won, C.Y. Park, J.H. Bae, G. Ahn, C. Kim, D.H. Lim, D.W. Cho, W.S. Yun, J.H. Shim, J.B. Huh, Evaluation of 3D printed PCL/PLGA/β-TCP versus collagen membranes for guided bone regeneration in a beagle implant model, Biomed. Mater. 11 (2016) 055013.
[12] N. Celikkin, S. Mastrogiacomo, J. Jaroszewics, X.F. Walboomers, W. Swieszkowski, Gelatin methacrylate scaffold for bone tissue engineering: the influence of polymer concentration, J. Biomed. Mater. Res. A 106 (1) (2018) 201–209.
[13] S. Rungsiyanont, N. Dhanesuan, S. Swasdison, S. Kasugai, Evaluation of biomimetic scaffold of gelatin-hydroxyapatite crosslink as a novel scaffold for tissue engineering: biocompatibility evaluation with human PDL fibroblasts, human mesenchymal stromal cells, and primary bone cells, J. Biomater. Appl. 27 (2012) 47–54.
[14] T.H. Kim, Y.P. Yun, Y.E. Park, S.H. Lee, W. Yong, J. Kundu, J.W. Jung, J.H. Shim, D.W. Cho, S.E. Kim, H.R. Song, In vitro and in vivo evaluation of bone formation using solid freeform fabrication-based bone morphogenic protein-2 releasing PCL/PLGA scaffolds, Biomed. Mater. 9 (2014) 25008.
[15] C. Wu, Y. Luo, G. Cuniberti, Y. Xiao, M. Gelinsky, Three-dimensional printing of hierarchical and tough mesoporous bioactive glass scaffolds with a controllable pore architecture, excellent mechanical strength and mineralization ability, Acta Biomater. 7 (2011) 2644–2650.
[16] A. Lode, K. Meissner, Y. Luo, F. Sonntag, S. Glorius, B. Nies, C. Vater, F. Despang, T. Hanke, M. Gelinsky, Fabrication of porous scaffolds by three-dimensional plotting of a pasty calcium phosphate bone cement under mild conditions, J. Tissue Eng. Regen. Med. 8 (2014) 682–693.
[17] X. Li, J. Xie, X. Yuan, Y. Xia, Coating electrospun poly(ε-caprolactone) fibers with gelatin and calcium phosphate and their use as biomimetic scaffolds for bone tissue engineering, Langmuir 24 (2008) 14145–14150.
[18] A. KarbalaeiMahdi, M. Shahrousvand, H.R. Javadi, M. Ghollasi, F. Nouroz, M. Kamali, A. Salimi, Mater. Sci. Eng. C 78 (2017) 1195–1202.
[19] M.A. Yassin, K.N. Leknes, T.O. Pedersen, Z. Xing, Y. Sun, S.A. Lie, A. Finne-Wistrand, K. Mustafa, Cell seeding density is a critical determinant for copolymer scaffolds induced bone regeneration, J. Biomed. Mater. Res. A 103A (2015) 3649–3658.
[20] S. Jain, S.R.K. Meka, K. Chatterjee, Curcumin eluting nanofibers augment osteogenesis toward phytochemical based bone tissue engineering, Biomed. Mater. 11 (2016) 055007.
[21] M.A. Yassin, K.N. Leknes, Y. Sun, S.A. Lie, A. Finne-Wistrand, K. Mustafa, Surfactant tuning of hydrophilicity of porous degradable copolymer scaffolds promotes cellular proliferation and enhances bone formation, J. Biomed. Mater. Res. A 104A (2016) 2049–2059.
[22] J. Jensen, J.H.D. Rolfing, D.Q. Le, A.A. Kristiansen, J.V. Nygaard, L.B. Hokland, M. Bendtsen, M. Kassem, H. Lysdahl, C.E. Bünger, Surface-modified functionalized polycaprolactone scaffolds for bone repair: in vitro and in vivo experiments, J. Biomed. Mater. Res. Part A. 102 (2014) 2993–3003.
[23] H. Jeon, H. Lee, G. Kim, A surface-modified poly(ε-caprolactone) scaffold comprising variable nanosized surface-roughness using a plasma treatment, Tissue Eng. C 20 (12) (2014) 951–963.
[24] C.H. Chen, M.Y. Lee, V.B.H. Shyu, Y.C. Chen, C.T. Chen, J.P. Chen, Surface modification of polycaprolactone scaffolds fabricated via selective laser sintering for cartilage tissue engineering, Mater. Sci. Eng. C 40 (2014) 389–397.
[25] A. Rashad, S. Mohamed-Ahmed, M. Ojansivu, K. Berstad, M.A. Yassin, T. Kivijärvi, E.B. Heggset, K. Syverud, K. Mustafa, Coating 3D printed polycaprolactone scaffolds with nanocellulose promotes growth and differentiation of mesenchymal stem cells, Biomacromolecules. 19 (11) (2018) 4307–4319.
[26] E.J. Chong, T.T. Phan, I.J. Lim, Y.Z. Zhang, B.H. Bay, S. Ramakrishna, C.T. Lim, Evaluation of electrospun PCL/gelatin nanofibrous scaffold for wound healing and layered dermal reconstitution, Acta Biomater. 3 (2007) 321–330.
[27] J. Lee, J.J. Yoo, A. Atala, S.J. Lee, Controlled heparin conjugation on electrospun poly(ε-caprolactone)/gelatin fibers for morphology-dependent protein delivery and enhanced cellular affinity, Acta Biomater. 8 (2012) 2549–2558.
[28] G. Yang, H. Lin, B.B. Rothrauff, S. Yu, R.S. Tuan, Multilayered polycaprolactone/gelatin fiber-hydrogel composite for tendon tissue engineering, Acta Biomater. 35 (2016) 68–76.
[29] M.P. Prabhakaran, J.R. Venugopal, T.T. Chyan, L.B. Hai, C.K. Chan, A.Y. Lim, S. Ramakrishna, Electrospun biocomposite nanofibrous scaffolds for neural tissue engineering, Tissue Eng. 14 (11) (2008) 1787–1797.
[30] Y. Zhang, H. Ouyang, C.T. Lim, S. Ramakrishna, Z.M. Huang, Electrospinning of gelatin fibers and gelatin/PCL composite fibrous scaffolds, J. Biomed. Mater. Res. B Appl. Biomater 72B (2005) 156–165.
[31] X. Jing, M.R. Salick, T. Cordie, H.Y. Mi, X.F. Peng, L.S. Turng, Electrospinning homogeneous nanofibrous poly(propylene carbonate)/gelatin composite scaffolds for tissue engineering, Ind. Eng. Chem. Res. 53 (2014) 9391–9400.
[32] S.R. Gomes, G. Rodrigues, G.G. Martins, M.A. Roberto, M. Mafra, C.M.R. Henriques, J.C. Silva, *In vitro* and *in vivo* evaluation of electrospun nanofibers of PCL, chitosan and gelatin: a comparative study, Mater. Sci. Eng. C 46 (2015) 348–358.
[33] M.P. Prabhakaran, J.R. Venugopal, S. Ramakrishna, Mesenchymal stem cell differentiation to neuronal cells on electrospun nanofibrous substrates for nerve tissue engineering, Biomaterials 30 (2009) 4996–5003.
[34] R.S. Azarudeen, M.A.R. Ahamed, R. Subha, A.R. Burkanudeen, Heavy and toxic metal ion removal by a novel polymeric ion-exchanger: synthesis, characterization, kinetics and equilibrium studies, J. Chem. Technol. Biotechnol. 90 (2015) 2170–2179.
[35] R.S. Azarudeen, M. Thirumarimurugan, K.P. Athmiya, R. Monisha, V. Prashanthini, Antibacterial chitosan–copolymer membranes for drug delivery: synthesis, characterization, drug release profile and kinetics, J. Chem. Technol. Biotechnol. 92 (2017) 1659–1666.
[36] M.A.R. Ahamed, R.S. Azarudeen, N.M. Kani, Antimicrobial applications of transition metal complexes of benzothiazole based terpolymer: synthesis, characterization, and effect on bacterial and fungal strains, Bioinorg. Chem. Appl. 2014 (2014) 76408516 pages.
[37] A.L. Daniel-da-Silva, A.M. Salgueiro, T. Trindade, Effects of Au nanoparticles on thermoresponsive genipin-crosslinked gelatin hydrogels, Gold Bull. 46 (2013) 25–33.
[38] L. Solorio, C. Zwolinski, A.W. Lund, M.J. Farrell, J.P. Stegemann, Gelatin microspheres crosslinked with genipin for local delivery of growth factors, J. Tissue Eng. Regen. Med. 4 (7) (2010) 514–523.
[39] R. Ke, W. Yi, S. Tao, Y. Wen, Z. Hongyu, Electrospun PCL/gelatin composite nanofiber structures for effective guided bone regeneration membranes, Mater. Sci. Eng. C 78 (2017) 324–332.
[40] Y. Huang, S. Onyeri, M. Siewe, A. Moshfeghian, S.V. Madihally, In vitro characterization of chitosan–gelatin scaffolds for tissue engineering, Biomaterials 26 (2005) 7616–7627.
[41] N. Davidenko, C.F. Schuster, D.V. Bax, R.W. Farndale, S. Hamaia, S.M. Best, R.E. Cameron, Evaluation of cell binding to collagen and gelatin: a study of the effect of 2D and 3D architecture and surface chemistry, J. Mater. Sci. Mater. Med. 27 (10) (2016) 148.
[42] M.A.A. Perez, V. Guarino, V. Cirillo, L. Ambrosio, *In vitro* mineralization and osteogenesis in poly(ε-caprolactone)/gelatin nanofibers, J. Biomed. Mater. Res. Part A 100A (2012) 3008–3019.

<u>Study III</u>

M. N. Hassan, M. A. Yassin, A. M. Eltawila, A. E. Aladawi, S. Mohamed-Ahmed, S. Suliman, S. Kandil, and K. Mustafa. "Contact Osteogenesis by Biodegradable 3D-printed Poly(lactide-co-trimethylene carbonate)". Biomaterials Research, Accepted (Sep. 2022).

Journal Impact Factor (2022) = 15.8

III

Contact Osteogenesis by Biodegradable 3D-printed Poly(lactide-co-trimethylene carbonate)

Mohamad Nageeb Hassan[1 *], Mohammed Ahmed Yassin[1], Ahmed Maher Eltawila[2,3], Ahmed Emad Aladawi[4], Samih Mohamed-Ahmed[1], Salwa Suliman[1], Sherif Kandil[2], and Kamal Mustafa[1 *]

[1] Centre for Translational Oral Research (TOR), Department of Clinical Dentistry, Faculty of Medicine, University of Bergen, Årstadveien 19, 5009 Bergen - Norway.

[2] Department of Materials Science, Institute of Graduate Studies and Research (IGSR), Alexandria University, El-Shatby, 21526 Alexandria - Egypt.

[3] Department of Dental Biomaterials, Faculty of Oral and Dental Medicine, Delta University for Science and Technology, Coastal International Road, 11152 Gamasa - Egypt.

[4] Department of Dental Biomaterials, Faculty of Dentistry, Alexandria University, El-Azarita, 21526 Alexandria - Egypt.

* Corresponding Authors:
Mohamad N. Hassan; e-mail: nageeb.hassan@uib.no; Tel:55586382
Kamal Mustafa; e-mail: kamal.mustafa@uib.no; Tel: 55586097

Abstract

Background: To support bone regeneration, 3D-printed templates function as temporary guides. The preferred materials are synthetic polymers, due to their ease of processing and biological inertness. Poly(lactide-co-trimethylene carbonate) (PLATMC) has good biological compatibility and currently used in soft tissue regeneration. The aim of this study was to evaluate the osteoconductivity of 3D-printed PLATMC templates for bone tissue engineering, in comparison with the widely used 3D-printed polycaprolactone (PCL) templates.

Methods: The printability and physical properties of 3D-printed templates were assessed, including wettability, tensile properties and the degradation profile. Human bone marrow-derived mesenchymal stem cells (hBMSCs) were used to evaluate osteoconductivity and extracellular matrix secretion *in vitro*. In addition, 3D-printed templates were implanted in subcutaneous and calvarial bone defect models in rabbits.

Results: Compared to PCL, PLATMC exhibited greater wettability, strength, degradation, and promoted osteogenic differentiation of hBMSCs, with superior osteoconductivity. However, the higher ALP activity disclosed by PCL group at 7 and 21 days did not dictate better osteoconductivity. This was confirmed *in vivo* in the calvarial defect model, where PCL disclosed distant osteogenesis, while PLATMC disclosed greater areas of new bone and obvious contact osteogenesis on surface.

Conclusions: This study shows for the first time the contact osteogenesis formed on a degradable synthetic co-polymer. 3D-printed PLATMC templates disclosed unique contact osteogenesis and significant higher amount of new bone regeneration, thus could be used to advantage in bone tissue engineering.

Keywords: 3D-printing; poly(lactide-co-trimethylene carbonate); polycaprolactone; printability; degradation; ALP activity; osteoconduction

1. Introduction

Extensive work has been introduced through bone tissue engineering (BTE) to replace the current treatment options for augmentation/replacement of lost bone tissues, circumventing the limitations associated with autogenous, allogenic, or xenogeneic grafts (1). In addition to the classical requirements of biocompatibility, tailored biodegradation rate, adequate mechanical properties, porosity, sterilizability and off-the-shelf availability, the ideal template for BTE should offer adequate osteoconductivity (2).

Osteoconduction is defined as the ability to support recruitment and migration of differentiating osteogenic cells to the implanted surface. The implanted surface should promote osteogenic cell activation and extracellular matrix (ECM) deposition to allow for the next healing phase known as new (*de novo*) bone formation directly on its surface (3). The combination of these two healing phases results in contact osteogenesis, at the light microscopic level, this appears as intimate bone contact to the implanted surface, commonly known as osseointegration (4).

At the ultrastructural level of contact osteogenesis, the collagen compartment of the bone is separated from the implanted surface by a continuous submicron-thick layer involving individual fused globules known as globular accretions, forming the cement line matrix (5,6). Approximately 1µm diameter, these globular accretions were first described by the group of John Davies, in the early 90's (7), as the primary event in mineralized ECM secretion by active (secretory) osteoblasts on implanted materials, before the deposition of overlying mineralizing collagen matrix (6). In contrast, bone could be formed in relation to implanted materials through distance osteogenesis, similar to physiologic appositional bone growth, that encroaches on the implant surface. Hence, the bioinert (non-osteoconductive) implant becomes surrounded by bone through distance osteogenesis, but always partially obscured by general fibrous connective tissue ECM (5).

The biologically-derived natural polymers are considered biologically active, with osteoconductive properties. However, they are characterized by suboptimal mechanical properties and questions have been raised about their tissue reactivity and purification complexity (8,9). In contrast, biodegradable synthetic polymers used in BTE tend to be bioinert and incapable of performing specific biological functions (10). They offer the advantage of mechanical strength, resilience, and ease of processing. However to date, there are no reports of synthetic polymers exhibiting inherent osteoconductivity which activates contact osteogenesis on the surface (11). Thus, many attempts were further applied to boost their physical properties and osteoconductivity, customized per application, including co-polymerization, blending, making composites and functionalized coatings (12).

Aliphatic polyesters are thermoplastic polymers with hydrolytically degradable aliphatic ester linkages, which have been extensively investigated in BTE applications. Among the most extensively studied are polylactide (PLA), polylactide-co-glycolide (PLGA) and polycaprolactone (PCL).

PCL is a semi-crystalline polymer that is highly processible due to its low melting point (55-60 ºC); it usually takes 24 to 36 months before full biodegradation. The first 3D-printed templates introduced for BTE in the calvarial bone defect (CBD) model were fabricated from PCL (13), with following successful clinical trials (14,15). Thus, 3D-printed medical-grade PCL templates were approved by FDA for clinical use (12).

In contrast, poly(trimethylene carbonate) (PTMC) are high molecular weight, amorphous polymers (aliphatic polycarbonates which contain a carbonate ester group in their main chain). They exhibit excellent flexibility and surface degradation profile, but poor mechanical strength, and have been investigated as potential implant materials for soft tissue regeneration (16,17). Co-polymer networks of PLA with PTMC, known as poly(lactide-co-trimethylene carbonate) (PLATMC), prepared with various PTMC content (mol %), showed higher toughness, flexibility and elongations at break (up to 800 %) (18,19). In addition, they were found to degrade through bulk hydrolysis autocatalyzed by the generated acidic end groups (20), and have been used to support soft tissue regeneration with excellent biocompatibility (21,22). PLATMC was recently used by our group for some BTE applications, and showed positive results within the limitations of the experiments (23,24).

Promising results have been reported for 3D-printed templates, which are reproducible, highly porous structures with superior interconnectivity (25). BTE is enhanced through these 3D-printed templates and bone ingrowth was revealed within the strands of the template (26). The aim of this study was to characterize the osteoconductivity of 3D-printed PLATMC, compared to the widely used PCL, as BTE templates. The degradation of PLATMC has been determined *in vitro*, by monitoring mass loss and surface erosion according to previously reported protocols (27,28). The osteoconductive potential of the printed templates was tested *in vitro* using human bone marrow-derived mesenchymal stem cells (hBMSC), where cell attachment, proliferation, osteogenic differentiation, and ECM secretion were assessed. This was then evaluated *in vivo*, where the subcutaneous and CBD models in rabbits were used to evaluate tissue response to the implanted templates and the amount of new bone formation, respectively.

2. Methods

2.1. Printing of PCL and PLATMC

Medical grade PCL (RESOMER C 212, Evonik - Germany) and PLATMC (Resomer LT 706 S, Evonik - Germany) were used as received and printed using a pneumatic melting-extrusion printer (3D-Bioplotter, Manufacturer Series, EnvisionTEC, Germany). The printing structure was designed to print strands with 0.4 mm diameter, strand interdistance of 0.35 mm, and 0/90^{o} angle between layers (Figure 1a).

2.2. Printability and yield calculations

The printability of both polymers was measured through their output shape fidelity. The ratio of the measured printed strand diameter (S) over the measured strand interdistance (d) was calculated and compared to the related ratios in their ideal design (Figure 1a). In addition, the printing-yield and density of the printed templates were calculated for each polymer, to allow comparison of their processing efficiency. The printing-yield was calculated according to the following equation:

$$Printing\_Yeild\ (\%) = \frac{W_{Print}}{W_{feed}} \times 100$$

where W_{print} is the total weight of printed templates/each printing-run and W_{feed} is the gross weight of the feed materials added to the printing cartridge for each specific printing-run. On the other hand, the weight of the printed groups was recorded to calculate their densities (g cm^{-3}) as follows: density = W_{print}/V_{print}, where W_{print} is the weight of printed templates in grams, while V_{print} is their calculated geometric volume.

2.3. Sterilization of printed templates for biological assessment

All printed templates used for biological characterization (*in vitro* and *in vivo*) were prewashed using sterilized 1x PBS plus sonication (5-10 min, twice) followed by immersion in ethanol (70%, 30 min, twice), then the ethanol was aspirated in a safety cabinet, followed by drying (ethanol full evaporation at room temperature (*RT*)). The templates were then exposed to UV light for 1 h and packed in sterile bags, before removal from the safety cabinet and storage until use.

2.4. Physical and mechanical testing of printed templates

2.4.1. Wettability

The water contact angle test was applied (at *RT*) on the prepared blends, either 3D-printed (n = 5) or cast into flat sheets (n = 3), to determine their hydrophilicity, using (Contact Angle

Goniometer Model 90, CA Edition, ramé-hart - USA). Water (3 µL) was dropped onto the surface of each sample and the average contact angle was recorded (for triple measurements) at various positions on the surface.

2.4.2. Tensile properties

Dumbbell-shaped samples (shaft dimensions = 17.5 × 4.5 × 1.5 mm) were printed according to ASTM-D638 to test the mechanical properties of each group. The tensile strength, Young's Modulus and elongation at break (n = 5) were tested using a universal tensile testing machine (MTS, 858 Mini Bionix II instrument, Eden Prairie, MN, USA), at room temperature, and rate of tensile displacement at 3 mm sec^{-1}.

2.4.3. Degradation (*In vitro*)

Printed PCL and PLATMC samples (Ø = 8 mm, n = 5) were weighed precisely (W_o) then put in PBS (900 µL/sample) in 48 well plates. The wells were coded, to guarantee later matching of their mass change (specific per each sample), sealed, and incubated (37 ºC, shaking 100 RPM). The PBS was replaced with a fresh preparation every 5 days, up to 100 days. The mass change was recorded at 15, 30, 60 and 100 days, where the samples were washed (dH_2O, 3 times) dried at (37 ºC, 4 h), frozen (overnight) and freeze-dried (48 h) before being weighed (W_t). The Mass loss (%) was calculated according to the following equation:

$$Mass\ loss\ (\%) = \frac{(W_o - W_t)}{W_o} \times 100$$

Where W_o is the original weight of each template before immersion in PBS, and W_t is the dry weight recorded at each time point. In addition, the surface morphology of the tested templates was recorded at three time points, after 1, 60 and 100 days of incubation, using scanning electron microscopy (SEM) (Phenom XL Desktop, Thermo Fisher). The templates were dried and then sputter coated with gold-platinum (around 50 Ångstrom thickness) and scanned by a secondary electron detector.

2.5. *In vitro* osteogenic characterization using hBMSCs

2.5.1. Cell seeding and efficiency calculations

After informed parental consent, donated bone marrow aspirates (10 mL) were obtained from the anterior iliac crest of 8-14 years-old patients, undergoing iliac crest surgery for cleft lip and palate repair at the Department of Plastic, Hand and Reconstructive Surgery, National Fire Damage Center, Bergen – Norway. Ethical approval for this study was granted by the Regional Committee for Medical and Health Research Ethics (REK) in Norway (Ref. No.

2013/1248/REK sør-øst C). The hBMSCs were isolated from bone marrow aspirates, characterized according to our protocols (29). The cells were kept frozen in liquid nitrogen (passage 2), then thawed in α-MEM, expanded, and seeded onto the printed templates. One day after seeding, osteogenic supplements (0.1 mM L-ascorbic acid 2-phosphate, 10 mM β-GP, and 100 nM dexamethasone) were added to the culture medium to provide the essential factors needed for osteogenic differentiation and matrix biomineralization. The culture medium with osteogenic supplements was changed twice weekly.

The seeding efficiency of hBMSCs on printed PCL and PLATMC ($2x10^5$ cell cm^{-2}) was calculated after seeding for 8-12 h, incubated at 37 °C and 5% CO_2. The seeded templates were then transferred to another plate, and the remaining cells, attached and suspended cells per each well, were collected (1.5 mL Eppendorf safe-lock tubes), centrifuged, resuspended in 100 µL α-MEM, stained (4% trypan blue) and counted. The seeding efficiency was calculated using the following equation:

$$Seeding\ Efficiency\ (\%) = \frac{(\text{Seeded cells} - \text{Remaining cells})}{\text{Seeded cells}} \times 100$$

2.5.2. Cytoskeleton immunofluorescence staining

Seeded samples were stained by immunofluorescence, after 3 h, 1 and 3 days. The samples were washed (PBS, twice), fixed (4% paraformaldehyde, 15 min), washed, permeabilized (0.1% Triton X, 10 min, at *RT*), then finally washed. A working solution was prepared, including fluorescent Phalloidin (red) (A12379, Invitrogen, USA), acting as an F-actin filament stain, and DAPI (4′, 6-diamidino-2-phenylindole) (blue), acting as a dsDNA stain. This working solution was added (40 min, shaking), then washed before the seeded samples were examined in a fluorescence microscope (Nikon Eclipse Ti, Tokyo, Japan).

2.5.3. Monitoring cell attachment and ECM deposition by SEM

At 3 and 14 days, seeded samples were prepared for SEM to observe cell attachment and ECM deposition, respectively. Samples were fixed in glutaraldehyde solution (2.5%, pH 7.2) for 30 min, then dehydrated through a graded series of ethanol solutions (70, 80, 95, and 100%) for 10 min/each. Dried samples were mounted on aluminum holders, sputter-coated with gold-platinum and examined by SEM using a voltage of 10 kV. The ECM contents were examined for the presence of Ca and P ions, identified by Energy Dispersive X-ray (EDX), at a working distance 5.5 mm.

2.5.4. Live/Dead staining assay

Seeded samples at 7 and 14 days were characterized for their cell viability, including intracellular esterase activity (green) and plasma membrane integrity using a LIVE/DEAD ® Viability/Cytotoxicity Kit for mammalian cells (Invitrogen). A stock solution of PBS containing Ethidium homodimer-1 (red, 2 µL mL^{-1}) and Calcein AM (green, 1 µL mL^{-1}) was prepared and vortexed. Seeded templates were washed (twice) by D-PBS (37 ºC, 15 min) to remove remnant media and serum. The working solution (300 µL) was then added directly to cells (ensuring that all cells were covered with solution), before incubation (30 min, *RT*, shaking 100 RPM). The cells were then observed under fluorescence microscope at excitation/emission; Calcein AM = 494/517 nm, and Ethidium homodimer-1 = 528/617 nm. At least 10 Images were captured and stacked at 10 µm z-distance.

2.5.5. Lactate dehydrogenase (LDH) assay

LDH enzyme activity secreted in the culture medium was determined after 3, 7 and 21 days indicating the presence of apoptosis or toxicity of cells, thus evaluating indirectly the viability of the seeded cells. A calorimetric assay, LDH Assay Kit (ab102526, abcam), was used according to manufacturer's protocol to measure the enzyme activity. To exclude the biological interference of FBS to the results, negative control samples (media including FBS, without cells) were set, and their absorbance optical density (OD) readings were subtracted from those of the test samples.

Only 10 µL from each sample (in duplicate, n = 4) was added to the reaction mix, and the output was measured immediately (within 5 min) at OD = 450 nm, on a multimode microplate reader (Varioskan™ LUX, VLBL00D0, Thermo fisher Scientific, Vantaa – Finland). LDH activity in the test samples was measured in a kinetic mode, every 3 min for a total of 30 min, protected from light. The results were calculated as $\Delta A = (A_2 - A_1)$, where A_1 is the OD at time 1 (T_1 = 15 min) and A_2 is the OD at time 2 (T_2 = 21 min). The calculated ΔA was related to a standard curve to reveal the amount of reduced reagent (Nicotinamide adenine dinucleotide (NAD) to NADH), in nmol) generated by LDH during the reaction time (ΔT) (min). The total LDH activity of each sample was calculated as follows:

$$LDH\ activity = \frac{\text{calculated NADH}}{\Delta \text{T x } V} \text{ (nmol min}^{-1}\text{ mL}^{-1}\text{)}$$

Where V is the original sample volume added to the reaction well (mL).

2.5.6. AlamarBlue assay

The metabolic activity of the cells was assessed by alamarBlue reagent (AlamarBlue HS, Invitrogen - Thermo Fisher Scientific, USA) (resazurin-based), that function as cell health indicator by using the reducing power of living cells to quantitatively measure viability. The reagent (30 μL) was added directly to cells in culture medium (300 μL) as directed by the manufacturer. The plates (n = 5) were incubated in a cell culture incubator (4 h, 37 °C) protected from direct light, and control (background) samples, containing culture media only, were used. From each well, 100 μL were aspirated (in duplicate) and added to 96 well plates to read immediate fluorescence (excitation at 560 nm, emission at 590 nm). The results were calculated by subtracting the background fluorescence from the fluorescence signal of the seeded templates.

2.5.7. Proliferation assay (DNA quantification)

DNA was quantified using a Quanti-iT PicoGreen® dsDNA assay kit (Invitrogen - Thermo Fisher Scientific, USA). At each timepoint, the seeded samples were stored in cell lysate solution (0.1% Triton X-100, 300 μL), frozen at -80 ºC then thawed twice. Thawed samples (n = 5) were cut into pieces, put into 1.5 mL tubes (Eppendorf) together with the lysate solution, sonicated (10 min on ice), vortexed (1200 RPM, 10 sec), then finally centrifuged for 1-2 min at 10,000 RPM. From the supernatant, 50 μL were aspirated and added to diluted Picogreen dye (in accordance with the manufacturer's protocol). The intensity of fluorescence was measured at excitation/emission = 485/520 nm, and the cellular dsDNA content was calculated against a standard curve of a known concentration of DNA (μg mL^{-1}), obtained by serial dilution.

2.5.8. Alkaline phosphatase (ALP) activity

The Alkaline phosphatase (ALP) activity was assessed as an indicator of osteogenic ECM secretion by the seeded cells. ALP was collected from cell lysate used in the DNA quantification assay (n = 5). *p*-Nitrophenyl phosphate (*p*NPP, Sigma) was added (1:1) to the thawed lysate solution to measure ALP expression. OD was measured at 405 nm at different time points (5, 10 and 15 min), and the results were normalized to cell number, determined by the proliferation assay.

2.5.9. Osteogenic gene expression analysis

The real-time quantitative polymerase chain reaction (RT-qPCR) technique was used to analyze the gene expression of seeded cells on different printed templates. RNA was extracted from samples at 7 and 21 days (n = 5) using a Maxwell® 16 LEV simplyRNA kit (Promega, Madison, WI, USA). The amount of RNA extracted was measured by spectrophotometry (Nanodrop ND-1000, Nanodrop Technologies, Wilmington, DE, USA). High-Capacity cDNA Reverse Transcription Kit (Applied Biosystems, Foster City, CA, USA), and SimpliAmp Thermal Cycler (Applied Biosystems) were used to synthesize cDNA. To detect the gene expression of the osteogenesis-related human genes, RT-qPCR was applied, using TaqMan Fast Universal PCR Master Mix (Applied Biosystems) and a StepOne™ RT-PCR System (Applied Biosystems). Each sample was assessed in duplicate, and the amplification efficiency of different genes (listed in Table S1) was determined relative to an endogenous control: glyceraldehyde-3-phosphate dehydrogenase (GAPDH) gene. The difference in threshold cycle value ($\triangle Ct$) was equal to Ct gene minus Ct GAPDH, while the mRNA in each sample was calculated using the comparative $\triangle\triangle Ct$ ($\triangle Ct$ gene - $\triangle Ct$ control) value method. Data were analyzed by the $2^{-\Delta\Delta CT}$ method and relative transcript levels of the PLATMC group were presented as fold change (in Log scale) relative to PCL.

2.5.10. Alizarin red staining

Assessment of osteogenic differentiation was based on ECM secretion and mineralization. The seeded samples were stained with Alizarin red (2% in dH_2O at pH = 4.2) to measure calcium deposition on the printed templates. Samples (21 and 28 days) were fixed, washed, and kept drying. Enough stain was then added to cover each sample. The samples were then incubated (10 min), washed (dH_2O, 5-6 times, overnight), followed by ethanol (70%) overnight, and then aspirated. The dried samples were examined by a stereo microscope (LEICA M205 C, Germany) with mounted microscope camera. The dye was extracted using cetylpyridinium chloride (100 mmol, 300 µL/sample, 4 h, *RT*) and quantified at OD = 544 nm using a microplate reader. After dye extraction, some samples were further monitored for any remaining attached mineralized matrix, by additional SEM qualitative analysis.

2.6. *In vivo* characterization in rabbit model

The *in vivo* study comprised subcutaneous implantation and CBD models in New Zealand white (NZW) rabbits and was conducted at the Institute of Graduate Studies and Research (IGSR), Alexandria University, Egypt. The animal experiment protocol was reviewed and accepted by the institutional animal care and use committee (IACUC) - Alexandria University, approval no. AU14-191013-2-5.

2.6.1. Subcutaneous implantation model surgery

Three adult male NZW rabbits (3-4 months old) were used in this study. 3D-printed PCL and PLATMC templates were implanted subcutaneously in the dorsal area in each rabbit (n = 3). The rabbits were anesthetized by Xylazine (10 mg kg^{-1}, IM) and Ketamine (25 mg kg^{-1}, IM). The dorsal area was widely shaved, to ensure a space of at least 5-6 cm between the samples. The area was then disinfected with povidone iodine. The incision lines were made on both sides of the dorsum, around 3 cm away from and parallel to the midline, followed by the subcutaneous dissection to form pouches to receive one of the pre-sterilized 3D-printed samples. The incision was then sutured and the position of each sample was also marked with cutaneous sutures. The samples were retrieved at 8 weeks post-implantation.

2.6.2. Calvarial defect model surgery

In total, eight skeletally-adult male NZW rabbits were used in this study. 3D-printed PCL and PLATMC templates were implanted in each defect (in random order). Using a trephine bur, two bone defects (Ø = 9 mm) were created bilaterally, on each rabbit calvarium, followed by the implantation of the prepared templates (2 mm thickness and 9 mm diameter). The surgical wound was closed in layers; the subcutaneous layer was closed with vicryl (3/0) resorbable sutures, while the skin layer was closed with silk (3/0) sutures. To prevent surgical site contamination, topical antibiotic (Gentamicin) was applied to cover the site.

Immediately after the surgery, a pain killer (diclofenac sodium, 5 mg kg^{-1}, IM) was administrated daily (first 3 days after surgery). The silk sutures were removed after 1 week. The rabbits were euthanized after 4 and 8 weeks (n = 4 /time point/group). Collected bone samples were fixed, dehydrated, and processed for μCT and histology analysis.

2.6.3. Data collection and analysis

The μCT analysis was used to determine the amount of calcified bone formation within the implanted templates. This was followed by sectioning of samples and staining for histological examination and histomorphometric (quantitative) analysis. After histological examination, the samples were analyzed using NIS-Elements Software (Nikon, Japan).

For histomorphometric analysis, the total region of interest (ROI) was marked, from both edges of the template/defect, then the template area was calculated. The available defect area (ADA) was calculated as follows: ADA = Total ROI – template area. The sum of new bone area (NBA) within the defect was measured and total regenerated bone was calculated as NBA/ADA (%). The mean of the middle three sections in each sample was calculated, and the mean of each group (n = 4) was presented. For bone contact calculations, the entire length of new growing bone in direct contact with the template surface (bone contact length) was traced, while the total borders of new growing bone within the implanted templates (total bone boarders) were calculated. The values measured were expressed as a percentage of the bone contact length per total bone borders.

2.7. Statistical methods and analysis

To carry out the statistical analysis, Prism software (GraphPad software, San Diego, CA, USA) was used and the results were expressed as group average ± standard deviations. For comparisons of mean values, t-test was applied. If the Levene's test for variances was significant, the welch test assuming non-equal variances was applied. For the analysis over time, we applied multiple t-test with Holm-Šídák adjustment for multiple comparisons. The null hypothesis was rejected at p-value < 0.05.

3. Results

3.1. Comparison of printability and process parameters of PLATMC and PCL

Compared to PCL, the melting-extrusion of PLATMC was challenging and showed relatively uneven printing rates during processing through the extrusion-based printer head used with pneumatic pressure through a syringe. This required high pre-heating and relatively high printing temperatures: above 220 °C and around 195 °C, respectively (Table S2). However, both maintained reproducible structures closely related to their ideal design (Figure 1a and b) and no intergroup differences were shown in the printability of PCL and PLATMC. On the other hand, there was no significant difference in printing-yield (gain) after the printing process (Figure 1c), but the printed PLATMC revealed higher density than PCL (Figure 1d).

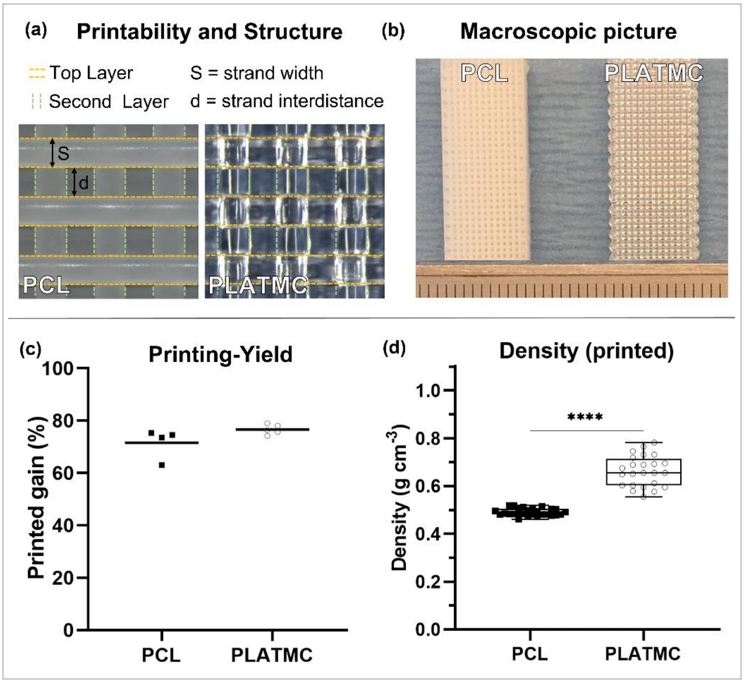

Figure 1: Printability of the 3D-printed PCL and PLATMC, and their calculated printing-yield and density of the printed templates. (a) microscopic pictures to the printed structures, marked with dashed lines to track the strands in the top two layers, on which the strand width (diameter) and strand interdistance were measured to determine the printability of each polymer. (b) macroscopic pictures for the printed structures, scale bar in mm. (c) graph for the mean printing-yield (n = 4), and (d) box plots for the density of the printed templates (n = 25). The statistical significance between the groups is marked with Asterisks (*), **** *p* <0.0001.

3.2. Physical advantages of PLATMC over PCL

The wettability of PLATMC was significantly higher than PCL, with lower contact angles on the 3D-printed as well as the cast sheets (Figure 2a - c). In addition, printed PLATMC revealed 4-fold higher Young's Modulus and 2-fold higher tensile strength than PCL (Figure 2d - f). On the other hand, PLATMC showed slightly increasing degradation *in vitro* up to 60 days, with significant mass-loss (6.21% ±3.39) recorded at 100 days (Figure 3a) and showed obvious signs of degradation, including both bulk and surface erosion degradation (Figure 3b). By comparison, PCL exhibited almost complete absence of degradation (0.28% ±0.25).

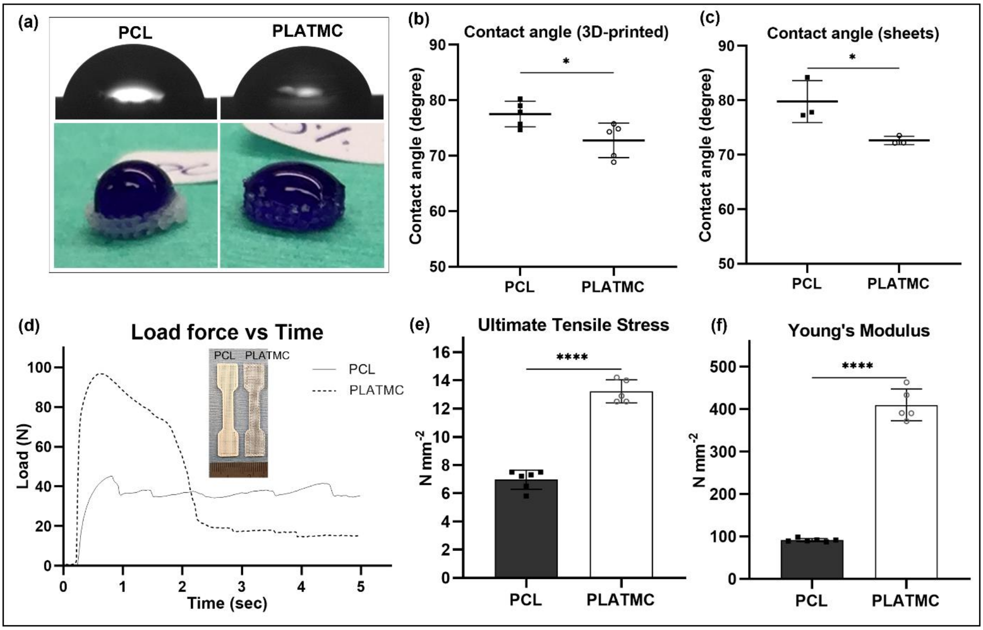

Figure 2: Physical characterization of the 3D-printed PCL and PLATMC, in terms of wettability and mechanical properties. (a) micrographs for contact angle measurement (top), and macroscopic images for the hydrophilic behavior using a drop of dye/water (bottom raw). (b) and (c) charts for the contact angle measurements of PLATMC versus PCL in 3D-printed (b) and casted sheet forms (c), respectively. (d) load force vs time curves, with inset photographs for the printed samples prepared according to ASTM-D638. (e) and (f) column charts of the mean ultimate tensile stress, and Young's modulus, respectively. Note the significant higher wettability and tensile strength of PLATMC. * p >0.0332, **** p <0.0001.

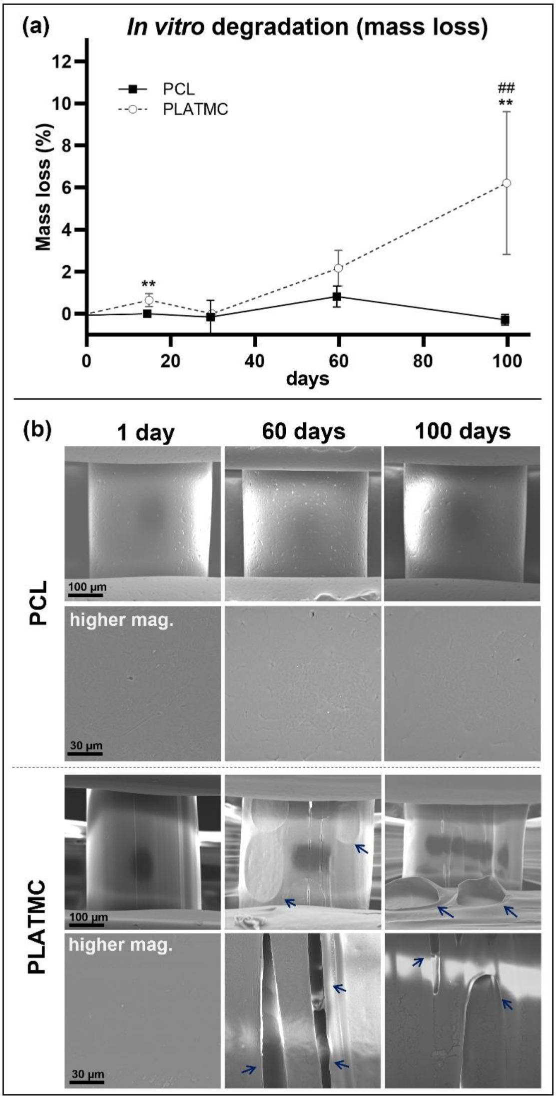

Figure 3: *In vitro* degradation of the 3D-printed PCL and PLATMC in PBS at 37 ºC monitored up to 100 days. (a) line-graph for the mass loss quantification. Note the significant higher degradation rate of PLATMC compared to the undetectable degradation of PCL, ~~**** p <0.0001~~, while significance between each time point and the previous time point in the same group is marked with hash symbol (#), **p >0.0021. (b) SEM micrographs for the printed templates at 1, 60 and 100 days, with signs of degradation marked with blue arrows.

3.3. Osteoconduction *in vitro* and abundant ECM secretion on the PLATMC surface

No significant differences in initial seeding efficiency were noticed between PLATMC and PCL (Figure S1). Moreover, there were no observed differences in the early attachment of hBMSCs at 3 h and 1 day (Figure 4a). However, at 3 days, the cells attached to PCL revealed higher proliferation and more spindle morphology, while stellate cellular morphology was observed on PLATMC, with noticeably enhanced F-actin polymerization, characterized by SEM and immunofluorescence, respectively (Figure 4). However, live/dead stain disclosed no intergroup differences in cell viability up to 14 days (Figure 4b).

The ECM secretion observed by SEM at 14 days on PLATMC was unique, with obvious abundant globular accretions of the cement line matrix, micron-size in diameter in the form of aggregated ECM vesicles (ECMVs), totally covering and adhering to the template surface (Figure 4c). Whereas PCL groups showed inadequate ECM secretion, with considerably fewer numbers of rod-like shaped crystallites (2-4 μm in length). EDX characterization of the secreted ECM confirmed the presence of Ca and P ions in both groups, whereas the crystallites produced on PCL surfaces, revealed higher total atomic percentages of Ca and P than those presented within the globular accretions on PLATMC surfaces (Figure 4c).

The presented continuous layer of globular accretions of the cement line matrix covering PLATMC surface at 14 days was further characterized by SEM qualitative analysis, and spots of overlying cells and secreted structural matrix were shown on the top of the globular matrix layer (Figure 5a). Furthermore, the samples characterized at 21 and 28 days after Alizarin red dye extraction (removal of mineralized matrix for quantification) revealed that globular accretions were totally adherent to PLATMC surfaces and were shown at the size of 1-2 μm in diameter/each. In addition, layers of remaining structural matrix were adherent on the top of the globular matrix (Figure 5b). On the other hand, no remaining matrix or adherent globular accretions were found on PCL surface after dye extraction at 21 and 28 days (Figure 5b).

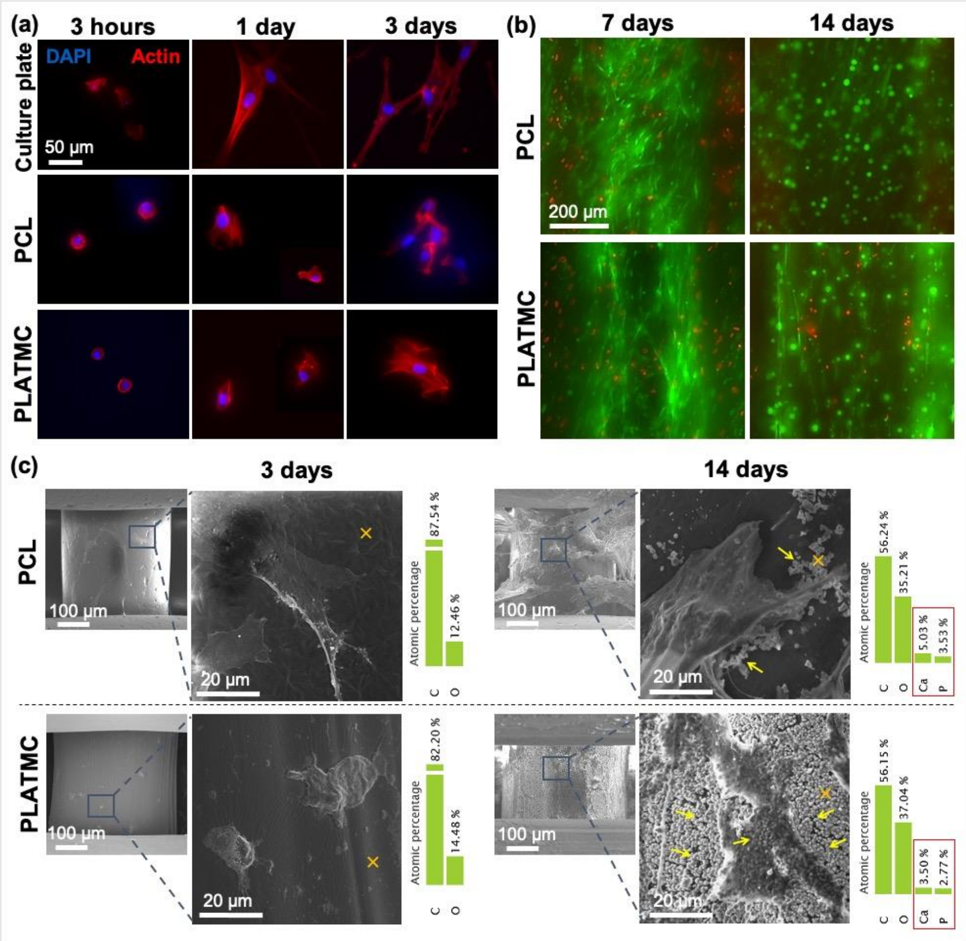

Figure 4: hBMSCs attachment, viability and ECM secretion on 3D-printed PCL and PLATMC: (a) microscopic images showing cytoskeleton immunofluorescence staining after 3 h, 1 day, and 3 days compared to culture plate surface (control); F-actin filaments stained by Phalloidin (red) and nuclei stained by DAPI (blue). (b) Live/dead stain for seeded cells after 7 and 14 days (z-stacked images). (c) SEM showing cell adhesion (3 days), and ECM deposition (14 days) and the corresponding EDX characterization to the substrate surface marked with (x). Note the abundant secretion of micron-sized globular accretions marked by YELLOW arrows on PLATMC compared to PCL (14 days), with their Ca and P contents characterized by EDX.

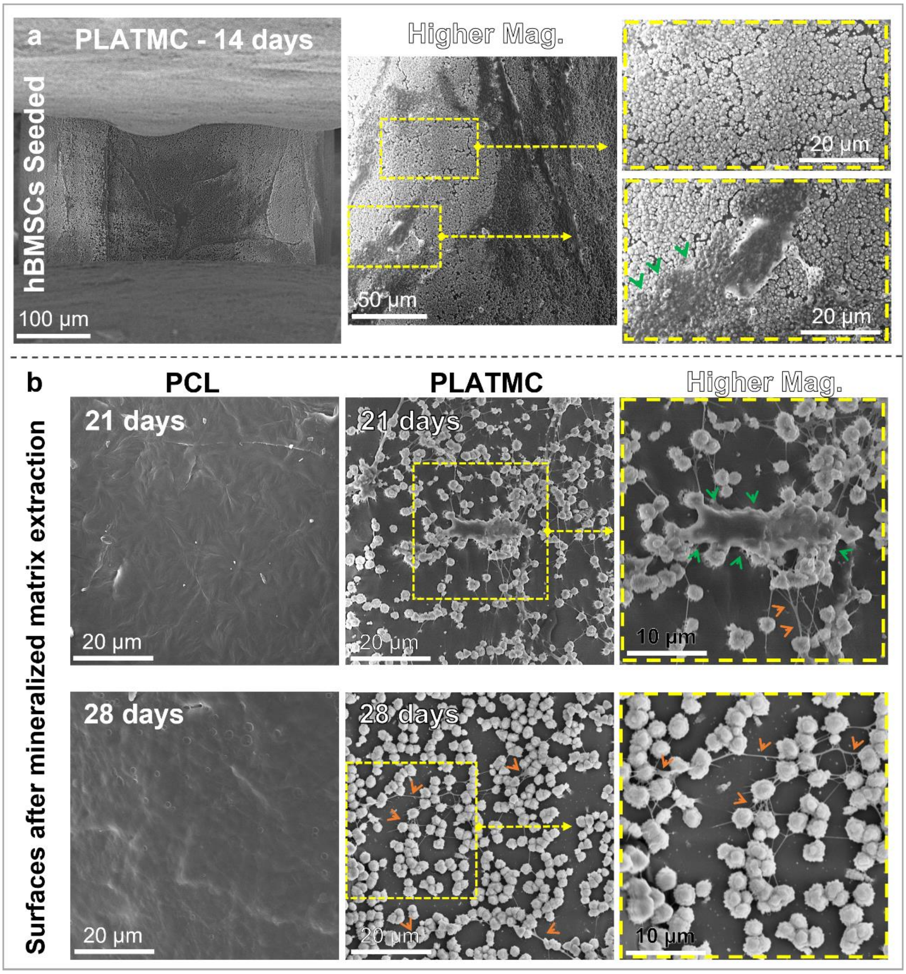

Figure 5: SEM micrographs analyzing the remarkable globular accretions of the cement line matrix, totally covering, and anchored to the surface of PLATMC templates. (a) General view of the globular layer secreted by seeded hBMSCs on the surface of 3D-printed PLATMC templates at 14 days. At higher magnifications, the surface is totally covered with globular (vesicular) layer in addition to layers of homogenous structural matrix on the top of the globular layer. (b) SEM micrographs of PCL and PLATMC samples, at 21 and 28 days after Alizarin red dye and mineralized ECM extraction, showing the persistent anchorage of globular accretions (1-2 µm diameter/each) to PLATMC surface, while no remaining matrix or cells were noticed on PCL. Not the cells/matrix anchored to the top of the globular accretions (Green arrowheads) and the connecting fibrillar collagen (ORANGE arrowheads).

The number of cells attached to the template surface detected through DNA quantification assay revealed earlier higher proliferation rate on PCL at 3 days. However, noticeable continuous proliferation was observed later only on PLATMC at 21 days (Figure 6a). Meanwhile, the lactate dehydrogenase (LDH) activity assay revealed no intergroup differences in apoptotic tendency (Figure 6b). On the other hand, the alamarBlue assay revealed significant metabolic activity of the seeded cells on PLATMC at all time points compared to PCL (Figure 6c).

PLATMC group underwent a significant increase in ALP activity as early as 3 days compared to PCL. However, it was of interest to note that PCL exhibited significant boost in ALP activity at 7 and 21 days (Figure 6d). This was also apparent at the gene level, where PCL group at 7 days revealed higher ALP expression together with statistically significant enhanced collagen type I (COL1) expression (Figure 7a). Instead, the other osteogenic markers were normally expressed by both groups; early markers (RUNX2 and BMP-2) at 7 days and late markers (Osteopontin and Osteocalcin) at 21 days (Figure 7a). In addition, Alizarin red staining at 21 days showed equivalent mineralization in both groups, while significant active mineralization continued only in PLATMC at 28 days (Figure 7b).

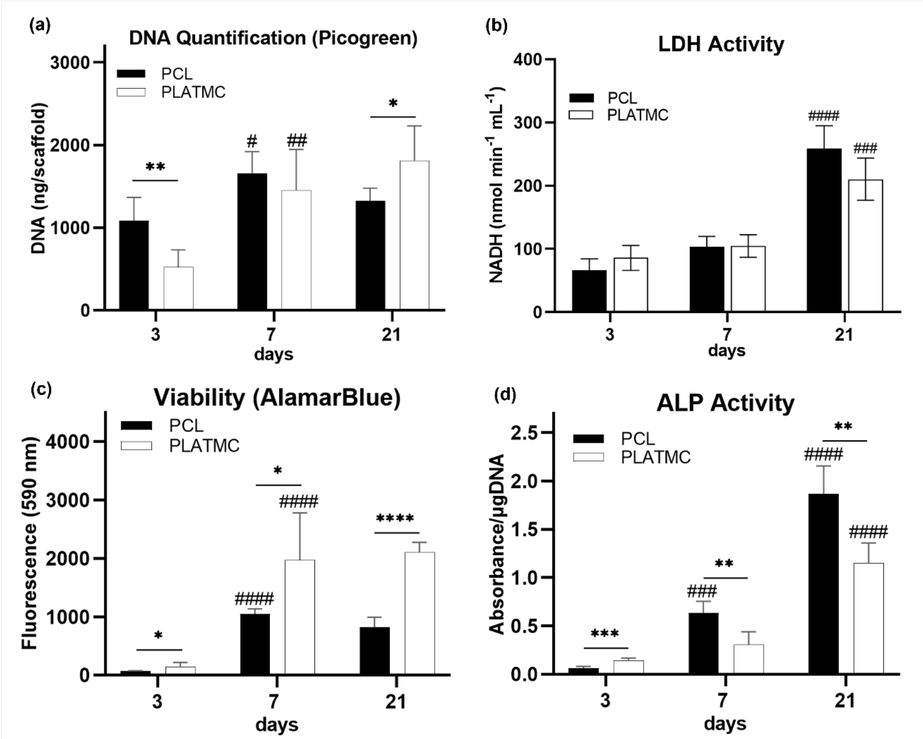

Figure 6: Quantitative analysis of cellular proliferation and activity of hBMSCs seeded on 3D-printed PCL and PLATMC at 3, 7 and 21 days, represented as column charts showing: (a) cell proliferation characterized by DNA quantification using Picogreen assay; (b) apoptotic tendency characterized by LDH activity assay; (c) cell metabolic activity characterized by alamarBlue assay; and (d) ALP activity. Note the higher proliferation rate and viability on PLATMC, while less ALP activity compared to PCL. Statistical significance between each time point and the previous time point in the same group is marked with hash symbol (#), while significance between the groups is marked with Asterisks (*) at p <0.05; * p >0.0332, ** p >0.0021, *** p >0.0002, **** p <0.0001.

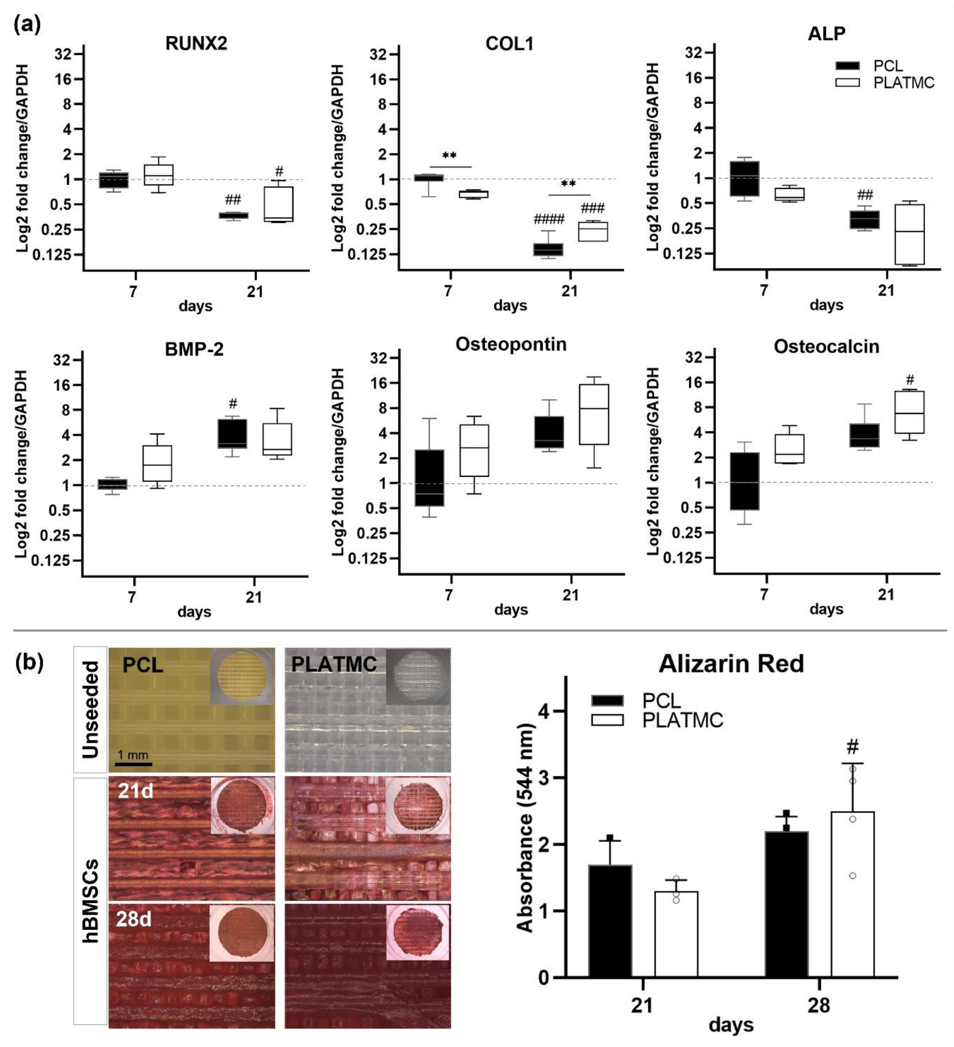

Figure 7: Osteogenic differentiation of hBMSCs seeded on 3D-printed PCL and PLATMC characterized by gene expression of osteogenic markers and Alizarin red staining. (a) box plots representing the gene expression of selected osteogenic markers at 7 and 21 days. (b) left-hand side shows micrographs of the mineralization stained by Alizarin red at 21 and 28 days, compared with unseeded templates (blank), while the inset pictures show the gross view. A column chart is plotted on the right-hand side representing the quantified optical density of the dissolved stain of each group subtracted from blanks (unseeded templates). Statistical significance between each time point and the previous time point in the same group is marked with hash symbol (#), while significance between the groups is marked with Asterisks (*) at p <0.05; * p >0.0332, ** p >0.0021, *** p >0.0002, **** p <0.0001.

3.4. PLATMC promotes new bone formation *in vivo* through contact osteogenesis

Within the implanted 3D-printed templates in the subcutaneous model (8 weeks), there were no signs of ectopic bone formation or mineralization in either group. The observed biomaterial/tissue interface at PLATMC indicated a highly cellular loose connective tissue interface, with few mononuclear inflammatory cells, and fewer macrophages (Figure 8a). On the other hand, PCL exhibited a much denser connective tissue interface, more abundant macrophages and thin-walled vascular invasion with large areas of bleeding, despite considerable variation from one area to another.

In the CBD, it was observed that the bone growth towards the defect center was clearly following the scaffold strands from around the defect margins. As seen in the μCT results (Figure 8b), the best rate of mineralized bone ingrowth occurred on PLATMC templates as early as 4 weeks (21.2 % ± 4.5), but less observed mineralized bone ingrowth at 8 weeks (15.2 % ± 3.3). Nevertheless, within the defect area at PCL templates, smaller amount of mineralized bone was quantified that revealed (16.4 % ± 0.8) and (11.9 % ± 1.3) at 4 and 8 weeks, respectively.

On the other hand, histological examination (Figure 9a) disclosed characteristic contact osteogenesis of *de novo* bone on PLATMC strands, at both 4 and 8 weeks, whereas on PCL strands a fibrous connective tissue interface was usually seen separating the growing new bone from PCL surface. Quantitative histomorphometric analysis of histological sections disclosed greater new bone area at PLATMC with (24.3 % ± 4.1) and (23.7 % ± 4.9), at 4 and 8 weeks, respectively, compared to PCL templates (16.1 % ± 5.2) and (11.4 % ± 3.6). A statistical intergroup significance was disclosed at 8 weeks (p = 0.0299) (Figure 9b). in addition, calculations of the bone contact (%) showed significance on PLATMC (85.3 % ± 3.6) and (75.9 % ± 10.6) which was 2.5 to 3 fold higher than PCL (26.6 % ± 1.4) and (20.6 % ± 3.5) at 4 and 8 weeks, respectively (Figure 9c). Thus, PLATMC exhibited noticeable contact osteogenesis while PCL revealed apparent distance osteogenesis, with minimum new bone contact.

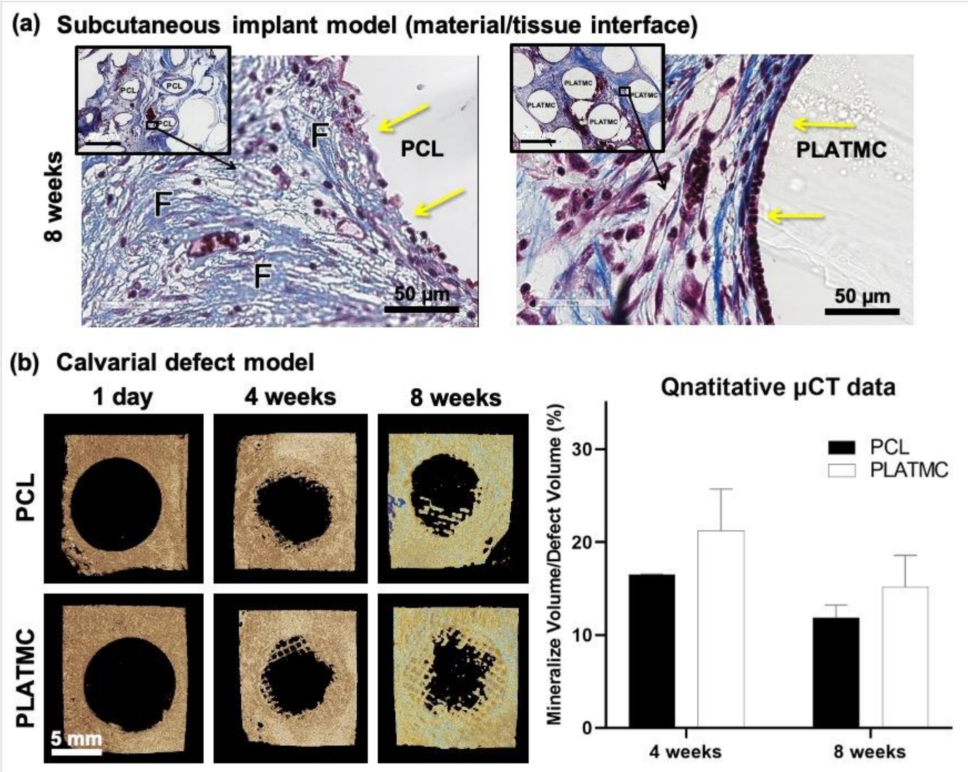

Figure 8: Summary of the outcomes from *in vivo* implantation of 3D-printed PCL and PLATMC templates (in rabbits); in subcutaneous model and in calvarial defect model. (a) representative histological micrographs of the subcutaneously implanted templates focusing on the material/tissue interface at 8 weeks as indicated by YELLOW arrows (scale bar = 50 µm), stained with Massons' trichrome, while the inset figures represent the overall view at lower magnification (scale bar = 500 µm); (**F**) represents fibrous connective tissues. (b) µCT reconstructed pictures of the calvarial defect model at 4 and 8 weeks, while a bar chart is plotted on the right-hand side representing their quantified mineralized volume/total defect volume (n = 4 /group/timepoint).

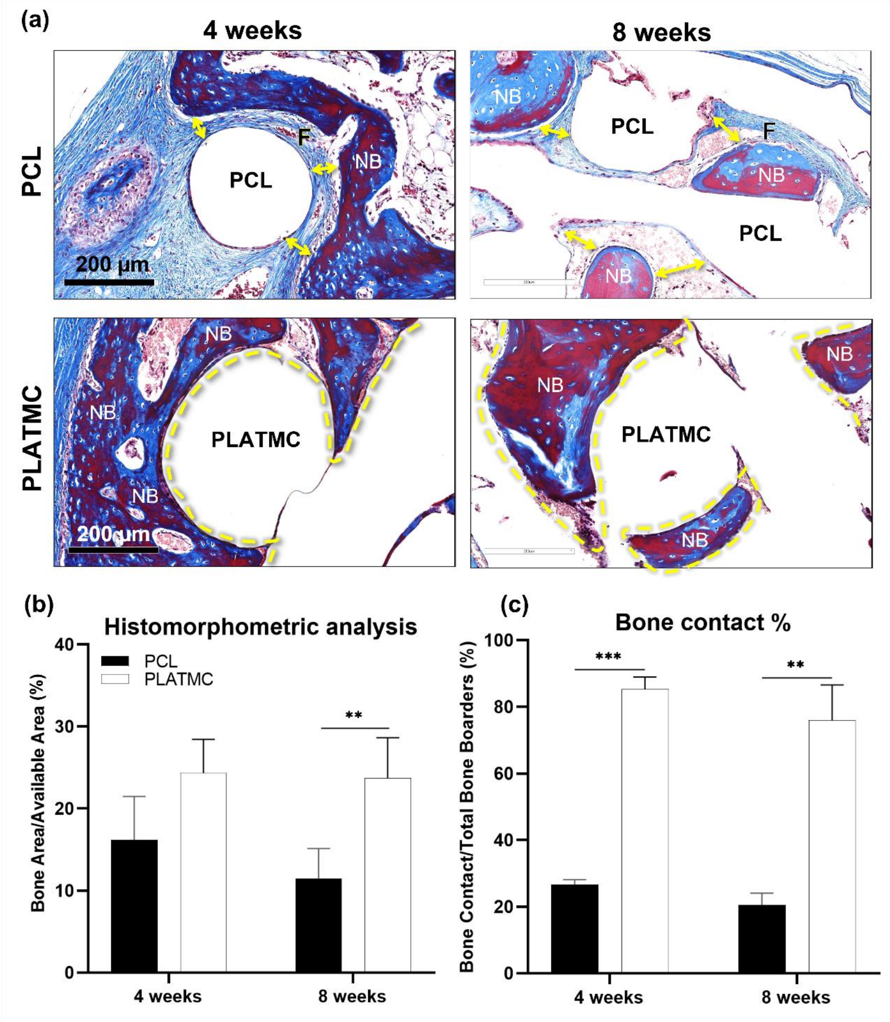

Figure 9: Summary of the histological outcomes of 3D-printed PCL and PLATMC templates implanted in the calvarial defect model (in rabbits). (a) histological micrographs (stained with Masson's trichrome) at 4 and 8 weeks (scale bar = 200 µm) showing the interface of new bone with template strands. Note the direct contact (contact osteogenesis) of the new formed bone on PLATMC. (b) and (c) represents the quantitative histomorphometric analysis and bone contact (%) calculation, respectively. (**F**) represents fibrous connective tissues; (**YELLOW dashed Line**) represents areas of contact osteogenesis (present only at PLATMC); (**NB**) represents areas of new bone; (**YELLOW double arrow**) represents the characterized gap (fibrous connective tissue) at material/tissue interface (present only at PCL).

4. Discussion

Particularly for polymer-based templates used for BTE, 3D-printing is a promising alternative to the methods previously used to fabricate 3D porous templates, while improving the mechanical resistance of the structure. For BTE, 3D-printing has showed satisfactory outcomes (26). It can reproducibly create customized templates with specific or complex anatomic shapes, with highly porous structure and superior interconnectivity (30). In the present study, PLATMC was selected for investigation because of recent reports of its favorable physical and biological properties in soft tissue applications (31,32). The study comprised extensive characterization, to test the osteoconductivity of PLATMC for potential BTE applications. Direct comparison was made with FDA approved, 3D-printed medical grade PCL (14,33).

Printability is defined as the capability of polymer to form and maintain reproducible 3D-templates using a defined printing technique. This affects the structure of the printed templates, in relation to their ideal design, and consequently affects their mechanical and biological properties (34,35). In the present study, the printability of both PCL and PLATMC was very close to their ideal design. However, PLATMC required little real-time adjustments in the printing temperature and speed while printing. This variation in parameters could be related to the recently reported significant loss of molecular weight of PLATMC during printing (31). The calculated tensile mechanical performance of PLATMC was close to the previously reported ranges (36) and markedly better than the tensile properties of PCL. The same applies to the reported bulk degradation of PLATMC, attributed to leaching out of water-soluble oligomers and low molecular-weight polymers (36).

The seeded cells on PCL showed earlier proliferation by fluorescence microscopic images and DNA quantification at 3 days. However, with regard to *in vitro* osteogenic differentiation, the seeded hBMSCs on PLATMC showed stellate-like morphology, with enhanced F-actin polymerization (3 days), and were normally differentiated and committed to the osteogenic lineage, as evidenced by ALP activity at 3 days and by the expression of RUNX2 and BMP-2 at 7 days (37,38). This was in addition to the steady proliferation rate, as shown by DNA quantification at 21 days on PLATMC, and noticeable higher metabolic activity revealed by alamarBlue assays at all time points.

The abundant globular matrix layer observed on PLATMC at 14, 21 and 28 days covering and adherent on its surface, was found to be a remarkable distinction from PCL. This justified the subsequent *in vitro* active mineralization, and *in vivo* contact osteogenesis seen with PLATMC. This was on agreement to the previously described studies that pointed to ECMVs and globular accretions as the key structure deposited by osteoblasts as a cement line matrix, interdigitating with osteoconductive implanted/substrate materials, above which the mineralizing collagen matrix can be seen (6,39).

In the reviewed literature, secreted ECMVs, usually about 200 nm in diameter, were defined as membrane-invested globular structures which concentrate calcium (Ca) and Phosphate (P) ions, released by budding from the surface of active osteoblasts (40). Moreover, ECMVs usually aggregate, with noncollagenous proteins including osteopontin, and increase in size, creating larger mineralized globular accretions, around 1μm in diameter (41). In consequence, mature osteoblasts should lay down COL1 (known as the structural matrix), together with ALP secretion, to initiate mineralization in alkaline environment (40,42).

Globular accretions were considered the dominant feature of the mineralizing nodules, before the deposition of bone-like matrix in osteoblast cultures (41), adipocyte-derived differentiated osteoblasts (43), and on other BTE substrates (44). This was also explored in the current study, after Alizarin red dye and matrix extraction from seeded PLATMC templates at 21 and 28 days, that disclosed how the globular cement line matrix was quite persistent and firmly anchored to PLATMC surface.

In contrast, the higher ALP activity at 7 and 21 days in addition to the higher expression of ALP and COL1 at 7 days led to the observation of mineralized crystallites on the surface of PCL as early as 14 days. The mineralized crystallites appeared as rod-like shaped structures, bigger than the globular accretions observed on PLATMC, and with higher Ca and P contents, indicating existing mineralization, i.e. CaP crystallization. However, these crystallites were scarce and accompanied by significantly limited cellular metabolic activity, as evidenced by alamarBlue assays at 7 and 21 days. This in turn revealed a reasonable amount of mineralization, detected by Alizarin red staining at 21 and 28 days.

Meanwhile, as expected, mineralization as high as seen on PCL was observed on PLATMC at 21 days, due to the earlier noticed reduction in ALP activity and COL1 expression on PLATMC at 7 days, compared to PCL. Nevertheless, unlike PCL later at 28 days, PLATMC group exhibited significantly continued active mineralization which led to boosted mineralization, detected by Alizarin red staining. This could be due to the markedly higher secretion of ALP and expression of osteopontin and osteocalcin at 21 days than that at 7 days.

In literature, PCL is reported to act through a Smad-dependent BMP pathway (45), which enhances cell differentiation and ALP activity, but usually downregulates self-renewal of the preosteoblast as the differentiation potential increases (46). It could be assumed from the data currently shown, that PLATMC induces a different pathway, the TGF-β signaling pathway, to promote the early osteoblastic lineage commitment of hBMSCs, through selective MAPKs and Smad2/3 pathways (47). TGF- β signaling was found to inhibit ALP activity and osteoblast mineralization to promote proliferation through a MAP3K-dependent pathway (48). In addition, when templates were coated with natural-derived ECM (49), or osteogenic growth peptide (50) a MAPK/ERK signaling pathway was reported to stimulate much higher osteogenic differentiation and activation of hBMSCs. However, this needs further investigation and confirmation for PLATMC.

Because of the absence of osteogenic cues required for osteogenic lineage differentiation, the subcutaneous implantation of 3D-printed templates of PCL and PLATMC did not result in ectopic bone formation. Instead, a dense fibrous connective tissue interface was typically seen with PCL, corresponding to the foreign body reaction to implanted PCL reported in previous studies (51). In contrast, much less fibrous-related foreign body reaction was observed in the host response to PLATMC, but rather a loose connective tissue interface with high cellular infiltration was shown. On the other hand, a recent study by our group reported ectopic mineralization on cell-free constructs of 3D-printed PLATMC and human platelet lysate hydrogels (HPLG), when implanted subcutaneously in nude mice after 4 and 8 weeks (52). Although HPLG has some advantages, no organized bone-like tissue or entrapped cells were observed.

In the CBD model, where the environment is rich in osteogenic signals, a potent osteoconduction and greater amount of new bone ingrowth were observed on PLATMC. The quantified new bone detected by μCT showed advantage for PLATMC compared to PCL, with no statistically significant intergroup differences. However, on histological examination, marked amount of new bone ingrowth was observed on PLATMC at 8 weeks and definite contact osteogenesis of the new formed bone to PLATMC surface was observed at both 4 and 8 weeks.

In the current study, the active mineralized matrix production and contact osteogenesis on PLATMC surface were presented only *in vitro* and in the calvarial defect model, where osteogenic supplements and signals are presented. Hence, this is typically presented by osteoconductive surfaces but no osteoinductive properties were shown, as demonstrated by the subcutaneous implantation model. It should be noted that the contact osteogenesis observed on 3D-printed PLATMC has not been reported previously for any synthetic polymer used for BTR, or even for blended polymers with osteoconductive bioceramics (53,54). These interesting findings could be related to the observed *in vitro* results, including stimulation of surrounding cells to attach, proliferate and secrete globular cement line matrix directly onto the PLATMC surface, only in osteogenic supplement medium. Such defined physical and biological findings favor the application of PLATMC as a BTE template which combines both biodegradation and osteoconductivity.

5. Conclusion

Compared to PCL, PLATMC templates exhibited markedly superior wettability, mechanical and degradation properties. The study disclosed biological advantages favoring the application of 3D-printed PLATMC templates for bone tissue engineering.

The seeded cells exhibited initial faster proliferation as early as 3 days on PCL, while on PLATMC they exhibited earlier osteogenic differentiation and higher metabolic activity. Abundant secretion of globular accretions of the cement line matrix was shown totally covering the PLATMC surface as early as 14 days and disclosed as active mineralization process *in vitro* up to 28 days of culture. This was also reflected *in vivo* as early as 4 weeks, when new bone ingrowth was observed with evident contact osteogenesis. As a synthetic co-polymer, PLATMC was unique in its ability to activate osteoconduction and contact osteogenesis on its surface.

List of abbreviations

ALP: Alkaline phosphatase; BTE: bone tissue engineering; CBD: calvarial bone defect; COL1: Collagen type I; ECM: extracellular matrix; ECMVs: Extracellular matrix vesicles; EDX: Energy Dispersive X-ray; hBMSCs: human bone marrow-derived mesenchymal stem cells; LDH: Lactate dehydrogenase; OD: optical density; PCL: polycaprolactone; PLATMC: Poly(lactide-co-trimethylene carbonate); PTMC: Poly(trimethylene carbonate); ROI: Region of interest; SEM: Scanning electron microscopy.

Declarations:

Ethics approval

The animal experiment was prior reviewed and approved from the institutional animal care and use committee (IACUC) - Alexandria University, approval no. AU14-191013-2-5.

Consent for publication

Not applicable.

Availability of data and materials

Not applicable.

Competing interests

The authors declare no financial or commercial conflicts of interest.

Funding

This project was funded by University of Bergen, Norway. This work was partially funded by the Research Council of Norway through the BEHANDLING project (Grant no. 273551), Trond Mohn Research Foundation, Norway (BFS2018TMT10) and Olav Thon foundation.

Author's contributions

MNH, MAY, AME, AEA, SMA, SS, SK and KM were responsible for the overall design of the study, and composition of the manuscript. MNH fabricated the 3D-printed substrates. MNH, MAY and AME generated the primary data. MNH and MAY conducted data analysis. MNH, AME and AEA performed the in vivo study. All authors read and approved the final manuscript.

Acknowledgements

The authors would like to thank Dr. Ahmad Rashad for his recommendations and comments throughout this study. The authors would like to thank Dr. Tarig Al-Hadi Osman for his valuable comments on the biomaterial/tissue interface section, and Dr. Wessam A. Ahmed for his assistance in the *in vivo* studies. We also thank Prof. Stein Atle Lie for his assistance in the statistical methods.

References

1. Wang W, Yeung KWK. Bone grafts and biomaterials substitutes for bone defect repair: A review. Bioact Mater [Internet]. 2017;2(4):224–47. Available from: https://doi.org/10.1016/j.bioactmat.2017.05.007
2. Carrel J-P, Wiskott A, Moussa M, Rieder P, Scherrer S, Durual S. A 3D printed TCP/HA structure as a new osteoconductive scaffold for vertical bone augmentation. Clin Oral Implants Res [Internet]. 2016 Jan;27(1):55–62. Available from: http://www.ncbi.nlm.nih.gov/pubmed/25350936
3. Davies JE. Understanding peri-implant endosseous healing. J Dent Educ [Internet]. 2003 Aug;67(8):932–49. Available from: http://www.ncbi.nlm.nih.gov/pubmed/12959168
4. Tamimi F, Torres J, Al-Abedalla K, Lopez-Cabarcos E, Alkhraisat MH, Bassett DC, et al. Osseointegration of dental implants in 3D-printed synthetic onlay grafts customized according to bone metabolic activity in recipient site. Biomaterials [Internet]. 2014;35(21):5436–45. Available from: http://dx.doi.org/10.1016/j.biomaterials.2014.03.050

5. Davies JE. Mechanisms of endosseous integration. Int J Prosthodont [Internet]. 1998;11(5):391–401. Available from: http://www.ncbi.nlm.nih.gov/pubmed/9922731
6. Davies JE. Bone bonding at natural and biomaterial surfaces. Biomaterials. 2007;28(34):5058–67.
7. Lowenberg B, Chernecky R, Shiga A, Davies J. Mineralized Matrix Production by Osteoblasts on Solid Titanium In Vitro. Cells Mater. 1991;1(2):177–87.
8. Turnbull G, Clarke J, Picard F, Riches P, Jia L, Han F, et al. 3D bioactive composite scaffolds for bone tissue engineering. Bioact Mater [Internet]. 2018 Sep;3(3):278–314. Available from: https://linkinghub.elsevier.com/retrieve/pii/S2452199X17300397
9. Swetha M, Sahithi K, Moorthi A, Srinivasan N, Ramasamy K, Selvamurugan N. Biocomposites containing natural polymers and hydroxyapatite for bone tissue engineering. Int J Biol Macromol [Internet]. 2010 Jul 1 [cited 2012 Jul 24];47(1):1–4. Available from: http://www.ncbi.nlm.nih.gov/pubmed/20361991
10. Jung K, Corrigan N, Wong EHH, Boyer C. Bioactive Synthetic Polymers. Adv Mater [Internet]. 2022 Jan 5;34(2):2105063. Available from: https://onlinelibrary.wiley.com/doi/10.1002/adma.202105063
11. Vishwakarma A, Bhise NS, Evangelista MB, Rouwkema J, Dokmeci MR, Ghaemmaghami AM, et al. Engineering Immunomodulatory Biomaterials To Tune the Inflammatory Response. Trends Biotechnol [Internet]. 2016 Jun;34(6):470–82. Available from: http://dx.doi.org/10.1016/j.tibtech.2016.03.009
12. Hutmacher DW, Cool S. Concepts of scaffold-based tissue engineering - The rationale to use solid free-form fabrication techniques. J Cell Mol Med. 2007;11(4):654–69.
13. Schantz J-T, Hutmacher DW, Lam CXF, Brinkmann M, Wong KM, Lim TC, et al. Repair of Calvarial Defects with Customised Tissue-Engineered Bone Grafts II. Evaluation of Cellular Efficiency and Efficacy in Vivo. Tissue Eng [Internet]. 2003 Aug 30;9(supplement 1):127–39. Available from: http://www.liebertonline.com/doi/abs/10.1089/10763270360697030
14. Schantz J-T, Lim T-C, Ning C, Teoh SH, Tan KC, Wang SC, et al. Cranioplasty after Trephination using a Novel Biodegradable Burr Hole Cover: Technical Case Report. Oper Neurosurg [Internet]. 2006 Feb;58(SUPPL. 1):E176. Available from: https://academic.oup.com/ons/article-lookup/doi/10.1227/01.NEU.0000193533.54580.3F
15. Probst FA, Hutmacher DW, Müller DF, Machens H-G, Schantz J-T. Rekonstruktion der Kalvaria durch ein präfabriziertes bioaktives Implantat. Handchirurgie · Mikrochirurgie

· Plast Chir [Internet]. 2010 Dec 10;42(06):369–73. Available from: http://www.thieme-connect.de/DOI/DOI?10.1055/s-0030-1248310
16. Fukushima K. Poly(trimethylene carbonate)-based polymers engineered for biodegradable functional biomaterials. Biomater Sci [Internet]. 2016;4(1):9–24. Available from: http://xlink.rsc.org/?DOI=C5BM00123D
17. Artham T, Doble M. Biodegradation of Aliphatic and Aromatic Polycarbonates. Macromol Biosci [Internet]. 2008 Jan 9;8(1):14–24. Available from: https://onlinelibrary.wiley.com/doi/10.1002/mabi.200700106
18. Pêgo AP, Poot AA, Grijpma DW, Feijen J. Physical properties of high molecular weight 1,3-trimethylene carbonate and D,L-lactide copolymers. J Mater Sci Mater Med. 2003;14(9):767–73.
19. Peterson GI, Dobrynin A V., Becker ML. Biodegradable Shape Memory Polymers in Medicine. Adv Healthc Mater. 2017;6(21).
20. Pêgo AP, Poot AA, Grijpma DW, Feijen J. In vitro degradation of trimethylene carbonate based (Co)polymers. Macromol Biosci. 2002;2(9):411–9.
21. Pêgo AP, Poot AA, Grijpma DW, Feijen J. Biodegradable elastomeric scaffolds for soft tissue engineering. J Control Release. 2003;87(1–3):69–79.
22. Tosoratti E, Fisch P, Taylor S, Laurent-Applegate LA, Zenobi-Wong M. 3D-Printed Reinforcement Scaffolds with Targeted Biodegradation Properties for the Tissue Engineering of Articular Cartilage. Adv Healthc Mater [Internet]. 2021 Dec 18;10(23):2101094. Available from: https://onlinelibrary.wiley.com/doi/10.1002/adhm.202101094
23. Yamada S, Yassin MA, Schwarz T, Hansmann J, Mustafa K. Induction of osteogenic differentiation of bone marrow stromal cells on 3D polyester-based scaffolds solely by subphysiological fluidic stimulation in a laminar flow bioreactor. J Tissue Eng [Internet]. 2021 Jan 24;12:1–12. Available from: http://journals.sagepub.com/doi/10.1177/20417314211019375
24. Shanbhag S, Suliman S, Mohamed-Ahmed S, Kampleitner C, Hassan MN, Heimel P, et al. Bone regeneration in rat calvarial defects using dissociated or spheroid mesenchymal stromal cells in scaffold-hydrogel constructs. Stem Cell Res Ther [Internet]. 2021 Dec 14;12(1):575. Available from: https://doi.org/10.1186/s13287-021-02642-w
25. Kwon DY, Kwon JS, Park SH, Park JH, Jang SH, Yin XY, et al. A computer-designed scaffold for bone regeneration within cranial defect using human dental pulp stem cells. Sci Rep [Internet]. 2015 Oct 3;5(1):12721. Available from:

http://www.nature.com/articles/srep12721

26. Hassan MN, Yassin MA, Suliman S, Lie SA, Gjengedal H, Mustafa K. The bone regeneration capacity of 3D-printed templates in calvarial defect models: A systematic review and meta-analysis. Acta Biomater [Internet]. 2019 Jun;91:1–23. Available from: https://linkinghub.elsevier.com/retrieve/pii/S174270611930251X

27. Li WJ, Cooper JA, Mauck RL, Tuan RS. Fabrication and characterization of six electrospun poly(α-hydroxy ester)-based fibrous scaffolds for tissue engineering applications. Acta Biomater. 2006;2(4):377–85.

28. Yeo A, Rai B, Sju E, Cheong JJ, Teoh SH. The degradation profile of novel, bioresorbable PCL–TCP scaffolds: Anin vitro andin vivo study. J Biomed Mater Res Part A [Internet]. 2008 Jan [cited 2017 Mar 28];84A(1):208–18. Available from: http://doi.wiley.com/10.1002/jbm.a.31454

29. Mohamed-Ahmed S, Fristad I, Lie SA, Suliman S, Mustafa K, Vindenes H, et al. Adipose-derived and bone marrow mesenchymal stem cells: a donor-matched comparison. Stem Cell Res Ther [Internet]. 2018 Dec 19;9(1):168. Available from: https://stemcellres.biomedcentral.com/articles/10.1186/s13287-018-0914-1

30. Do AV, Khorsand B, Geary SM, Salem AK. 3D Printing of Scaffolds for Tissue Regeneration Applications. Adv Healthc Mater. 2015;4(12):1742–62.

31. Jain S, Yassin MA, Fuoco T, Liu H, Mohamed-Ahmed S, Mustafa K, et al. Engineering 3D degradable, pliable scaffolds toward adipose tissue regeneration; optimized printability, simulations and surface modification. J Tissue Eng [Internet]. 2020 Jan 16;11:1–17. Available from: http://journals.sagepub.com/doi/10.1177/2041731420954316

32. Jain S, Yassin MA, Fuoco T, Mohamed-Ahmed S, Vindenes H, Mustafa K, et al. Understanding of how the properties of medical grade lactide based copolymer scaffolds influence adipose tissue regeneration: Sterilization and a systematic in vitro assessment. Mater Sci Eng C [Internet]. 2021 May;124(December 2020):112020. Available from: https://doi.org/10.1016/j.msec.2021.112020

33. Schantz J-T, Teoh SH, Lim TC, Endres M, Lam CXF, Hutmacher DW. Repair of Calvarial Defects with Customized Tissue-Engineered Bone Grafts I. Evaluation of Osteogenesis in a Three-Dimensional Culture System. Tissue Eng [Internet]. 2003 Aug 30;9(supplement 1):113–26. Available from: http://www.liebertonline.com/doi/abs/10.1089/10763270360697021

34. Zimmerling A, Yazdanpanah Z, Cooper DML, Johnston JD, Chen X. 3D printing

PCL/nHA bone scaffolds: exploring the influence of material synthesis techniques. Biomater Res [Internet]. 2021 Dec 26;25(1):3. Available from: https://biomaterialsres.biomedcentral.com/articles/10.1186/s40824-021-00204-y

35. Naghieh S, Chen X. Printability–A key issue in extrusion-based bioprinting. J Pharm Anal [Internet]. 2021 Oct;11(5):564–79. Available from: https://doi.org/10.1016/j.jpha.2021.02.001

36. Cork J, Whittaker AK, Cooper-White JJ, Grøndahl L. Tensile properties and in vitro degradation of P(TMC-co-LLA) elastomers. J Mater Chem B. 2015;3(21):4406–16.

37. Liu TM, Lee EH. Transcriptional Regulatory Cascades in Runx2-Dependent Bone Development. Tissue Eng Part B Rev [Internet]. 2013 Jun;19(3):254–63. Available from: https://www.liebertpub.com/doi/10.1089/ten.teb.2012.0527

38. Katagiri T, Watabe T. Bone Morphogenetic Proteins. Cold Spring Harb Perspect Biol [Internet]. 2016 Jun 1;8(6):a021899. Available from: http://cshperspectives.cshlp.org/lookup/doi/10.1101/cshperspect.a021899

39. Rau J V, Cesaro SN, Ferro D, Barinov SM, Fadeeva I V. FTIR study of carbonate loss from carbonated apatites in the wide temperature range. J Biomed Mater Res - Part B Appl Biomater [Internet]. 2004;71(2):441–7. Available from: http://www.scopus.com/inward/record.url?eid=2-s2.0-7744226122&partnerID=40&md5=5ac1ad7464b576ab9a5f3cb4c98abe20

40. Kawasaki K, Buchanan A V., Weiss KM. Biomineralization in humans: Making the hard choices in life. Annu Rev Genet. 2009;43:119–42.

41. Querido W, Abraçado LG, Rossi AL, Campos APC, Rossi AM, San Gil RAS, et al. Ultrastructural and mineral phase characterization of the bone-like matrix assembled in F-OST osteoblast cultures. Calcif Tissue Int. 2011;89(5):358–71.

42. Cölfen H. Biomineralization: A crystal-clear view. Nat Mater [Internet]. 2010 Dec [cited 2012 Mar 7];9(12):960–1. Available from: http://www.ncbi.nlm.nih.gov/pubmed/21102512

43. Kishimoto N, Momota Y, Hashimoto Y, Ando K, Omasa T, Kotani J. Dedifferentiated fat cells differentiate into osteoblasts in titanium fiber mesh. Cytotechnology. 2013;65(1):15–22.

44. Lee YJ, Lee JH, Cho HJ, Kim HK, Yoon TR, Shin H. Electrospun fibers immobilized with bone forming peptide-1 derived from BMP7 for guided bone regeneration. Biomaterials [Internet]. 2013;34(21):5059–69. Available from: http://dx.doi.org/10.1016/j.biomaterials.2013.03.051

45. Xue R, Qian Y, Li L, Yao G, Yang L, Sun Y. Polycaprolactone nanofiber scaffold enhances the osteogenic differentiation potency of various human tissue-derived mesenchymal stem cells. Stem Cell Res Ther [Internet]. 2017 Dec 24;8(1):148. Available from: http://stemcellres.biomedcentral.com/articles/10.1186/s13287-017-0588-0
46. Luu HH, Song W-X, Luo X, Manning D, Luo J, Deng Z-L, et al. Distinct roles of bone morphogenetic proteins in osteogenic differentiation of mesenchymal stem cells. J Orthop Res [Internet]. 2007 May;25(5):665–77. Available from: https://onlinelibrary.wiley.com/doi/10.1002/jor.20359
47. Chen G, Deng C, Li YP. TGF-β and BMP signaling in osteoblast differentiation and bone formation. Int J Biol Sci. 2012;8(2):272–88.
48. Bosetti M, Boccafoschi F, Leigheb M, Cannas MF. Effect of different growth factors on human osteoblasts activities: A possible application in bone regeneration for tissue engineering. Biomol Eng. 2007;24(6):613–8.
49. Kang Y, Kim S, Bishop J, Khademhosseini A, Yang Y. The osteogenic differentiation of human bone marrow MSCs on HUVEC-derived ECM and β-TCP scaffold. Biomaterials [Internet]. 2012;33(29):6998–7007. Available from: http://dx.doi.org/10.1016/j.biomaterials.2012.06.061
50. Wang Q, Yang X, Wang G, Wan L, Wang S, Niu X, et al. Osteogenic growth peptide-loaded 3D-printed PCL scaffolds for the promotion of osteogenesis through the ERK pathway. Mater Des [Internet]. 2020 Aug;193(75):108811. Available from: https://doi.org/10.1016/j.matdes.2020.108811
51. Chung L, Maestas DR, Lebid A, Mageau A, Rosson GD, Wu X, et al. Interleukin 17 and senescent cells regulate the foreign body response to synthetic material implants in mice and humans. Sci Transl Med [Internet]. 2020 Apr 15;12(539). Available from: https://www.science.org/doi/10.1126/scitranslmed.aax3799
52. Shanbhag S, Kampleitner C, Mohamed-Ahmed S, Yassin MA, Dongre H, Costea DE, et al. Ectopic Bone Tissue Engineering in Mice Using Human Gingiva or Bone Marrow-Derived Stromal/Progenitor Cells in Scaffold-Hydrogel Constructs. Front Bioeng Biotechnol [Internet]. 2021 Nov 30;9(November):1–14. Available from: https://www.frontiersin.org/articles/10.3389/fbioe.2021.783468/full
53. Shim J-H, Moon T-S, Yun M-J, Jeon Y-C, Jeong C-M, Cho D-W, et al. Stimulation of healing within a rabbit calvarial defect by a PCL/PLGA scaffold blended with TCP using solid freeform fabrication technology. J Mater Sci Mater Med [Internet]. 2012 Dec

8;23(12):2993–3002. Available from: http://link.springer.com/10.1007/s10856-012-4761-9

54. Paris M, Götz A, Hettrich I, Bidan CM, Dunlop JWC, Razi H, et al. Scaffold curvature-mediated novel biomineralization process originates a continuous soft tissue-to-bone interface. Acta Biomater [Internet]. 2017 Sep;60:64–80. Available from: http://dx.doi.org/10.1016/j.actbio.2017.07.029

Supporting Information

Contact Osteogenesis by Biodegradable 3D-printed Poly(lactide-co-trimethylene carbonate)

Mohamad Nageeb Hassan*, Mohammed Ahmed Yassin, Ahmed Maher Eltawila, Ahmed Emad Aladawi, Samih Mohamed-Ahmed, Salwa Suliman, Sherif Kandil, and Kamal Mustafa*

Table S1: List of genes assessed in the current study.

Gene and code	Name	Role
GAPDH Hs02758991_g1	Glyceraldehyde-3-phosphate dehydrogenase	House-keeping gene
Runx-2 Hs01047973_m1	Runt-related transcription factor 2	Early osteogenic marker (for osteoblast differentiation)
ALPL Hs01029144_m1	ALP; Alkaline phosphatase, liver/bone/kidney	Early to intermediate osteogenic marker
COL1A2 Hs00164099_m1	COL1; Collagen, type I, alpha 2	Early to intermediate osteogenic marker
BMP-2 Hs00154192_m1	Bone morphogenetic protein-2	Early to intermediate osteogenic marker
SPP1 Hs00959010_m1	Osteopontin	Late osteogenic marker
BGLAP Hs01587814_g1	Osteocalcin; Bone gamma carboxyglutamate protein	Late osteogenic marker

Table S2: Printing parameters of PCL and PLATMC

Group	Pressure	Temperature [a)]	Printing speed	Printing Time	Feed
	[bar]	[ºC]	[mm sec^{-1}]	[min]	[g]
PCL	8.4	110	1.6	360	3.5
PLATMC	8.0	195	2.0 - 5.0	85	3.0

[a)] All polymers were pre-heated for 15 min before printing at 15-25 ºC beyond the actual recorded printing temperature.

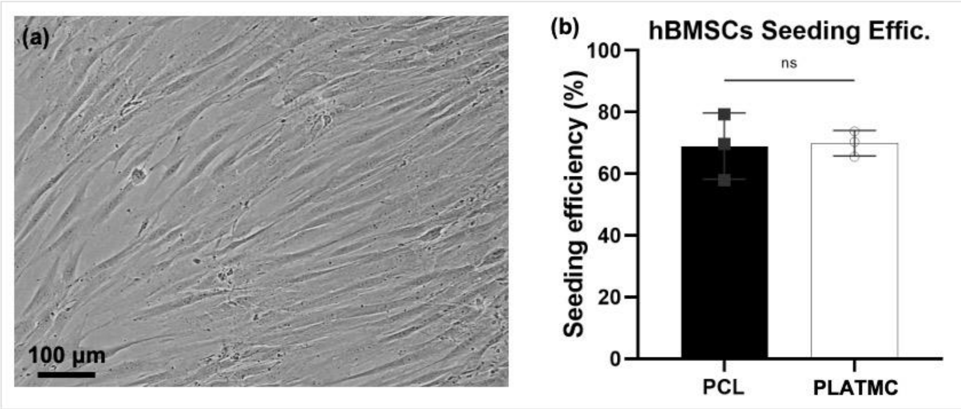

Figure S1: (a) morphology of the seeded hBMSCs at passage 4 (just before seeding) and (b) the quantification of seeding efficiency on PCL and PLATMC (b).

<u>Study IV</u>

M. N. Hassan, A. M. Eltawila, S. Mohamed-Ahmed, W. A. Ahmed, S. Suliman, S. Kandil, M. A. Yassin, and K. Mustafa. "3D-printed templates of hydroxyapatite blends: correlation between Ca release and osteoconduction *in vitro* and *in vivo*". *Submitted Manuscript.*

IV

Graphic design: Communication Division, UiB / Print: Skipnes Kommunikasjon AS

uib.no

ISBN: 9788230868911 (print)
9788230857458 (PDF)